Dissertation
submitted to the
Combined Faculties of the Natural Sciences and Mathematics
of the Ruperto-Carola-University of Heidelberg, Germany
for the degree of
Doctor of Natural Sciences

Put forward by
Dipl. Phys. Sabina Stephanie Pürckhauer
Born in Pirmasens
Oral examination: 31.10.2018

Characterising light concentrators for CTA and optimising the data selection to improve angular resolution and sensitivity

Referees: **Prof. Dr. Jim Hinton**
Prof. Dr. Stefan Wagner

Für
Willi Scherer (1931-2015)
Weil du gelebt hast,
weiß ich, was leben bedeutet.

und

Luise Scherer (1930-2018)
Weil du dich jeder Herausforderung
gestellt hast.

Zusammenfassung

Das Cherenkov Telescope Array (CTA) ist das bodengebundene Observatorium für Gammastrahlenastronomie der nächsten Generation mit einer in diesem Feld bislang unerreichten Empfindlichkeit. Diese Arbeit konzentriert sich darauf, die Empflindlichkeit von CTA im Hauptenergiebereich um 1 TeV zu optimieren. Im ersten Teil wird mit einem speziellen Testaufbau die wellenlängenabhängige Winkeleffizienz von Lichtkonzentratoren für FlashCam bestimmt. FlashCam ist ein Kamerasystem, das für die mittelgroßen Telescope von CTA bestimmt ist. Mit hexagonalen Konzentratoren mit drei reflektierenden Beschichtungen wird das Signal-zu-Rauschverhältnisses gegenüber einer Kamera ohne Lichtkonzentratoren um einen Faktor 2.2 verbessert. Durch das Variieren des Abstands zwischen Konzentrator und Lichtsensor ist eine Feinabstimmung der Winkeleffizienz möglich, die das Verhältnis um weitere 3%-5% steigert.
Im zweiten Teil wird die Winkelauflösung und die Sensitivität von CTA mit Hilfe von Simulationen untersucht. Durch die Optimierung unterschiedlicher Auswahlkriterien für eine bessere Datenqualität kann die Sensitivität um 20%-40% im Vergleich zu den Anforderungen von CTA verbessert werden, die Winkelauflösung sogar um 30%-40%. Mit diesen optimierten Auswahlkriterien werden Modelle der Radiogalaxie Centaurus A mit räumlich ausgedehnter Strahlung untersucht. Die verbesserte Winkelauflösung von CTA macht es möglich, zwischen unterschiedliche theoretische Strahlungsmodelle aufgrund ihrer vorhergesagten Strahlungsherde zu unterscheiden.

Abstract

The Cherenkov Telescope Array (CTA) is the next generation ground-based observatory for gamma-ray astronomy that will reach a performance unprecedented in the field. This thesis focuses on optimising this performance in the core energy range of CTA around 1 TeV. In a first part, the wavelength-dependent angular efficiency of light concentrators for the camera system FlashCam, proposed for the medium size telescopes of CTA, is determined with a dedicated test system. For hexagonal concentrators with three reflective coatings a signal-to-noise ratio enhancement of 2.2 compared to a camera without concentrators is observed. By varying the distance between concentrators and photo-sensors, a fine-adjustment of the angular efficiency increases this ratio by another 3%-5%.
In a second part, the angular resolution and the sensitivity of CTA are studied by means of simulations. By optimising different quality selection cuts on telescope data, sensitivity enhancements of 20%-40% compared to the CTA requirements are reached and 30%-40% for the angular resolution. With the optimised cuts, spatially extended emission models of the radio galaxy Centaurus A are investigated and it is found that the optimised angular resolution of CTA allows for different theoretical emission models to be discriminated based on the predicted emission regions.

Contents

"Oh no I've said too much,
I haven't said enough."

R.E.M., *Loosing my religion*, 1991

CHAPTER 1

Introduction

At the beginning of the 20th century, the observation of gas ionisation in closed containers intrigued physicists. The theoretical explanation attributing this effect to radioactive isotopes purely from within the crust and the atmosphere of our Earth was ruled out by Hess (1912). During seven balloon flights, he found that indeed the ionising radiation decreases for heights of several 100 m above ground, as expected. However, for even larger distances up to 5000 m, Hess observed a strong rise in ionisation rate. He concluded that an additional source of ionisation must exist outside our atmosphere. In 1936 he was awarded the Nobel prize for the detection of what we today call cosmic rays.

Cosmic rays are charged particles moving with relativistic speed. Their chemical composition is similar to the insterstellar matter (ISM) abundances, mainly Hydrogen and Helium cores and 1% of heavier nuclei. Another 2% of the observed cosmic rays are high energy electrons. Due to their charge, cosmic rays interact with electromagnetic fields on their way through the universe and their original direction is randomised quickly. On Earth, an almost isotropic spatial particle distribution is detected with an energy-dependent sidereal large-scale anisotropy of the order of 10^{-3} and small scale variations of 10^{-4} (Amenomori, 2017; Aartsen et al., 2017). While many authors agree on a diffuse cosmic ray flux generated by the distribution of sources within the galaxy as a cause for the large scale anisotropy, the origin of the small scale anisotropy is less clear. Currently discussed theories include structures in the magnetic field of the heliosphere created by the rotation of the Sun and the emitted solar winds, turbulences in the Galactic magnetic field as well as different diffusive and non-diffusive particle propagation mechanisms (Ahlers and Mertsch, 2017).

The cosmic ray energy spectrum shown in Figure 1.1 follows a power law with decreasing particle flux $E^{-\alpha}$ from a few GeV up to 10^{21} eV with $\alpha \approx 2.7$ below 10^{15} eV.

Even if the exact origin of cosmic rays is still a matter of debate, it is generally accepted that up to energies of 10^{15} eV they are generated within our galaxy. Baade and Zwicky (1934) proposed supernova explosions as the main source of particle acceleration in this energy regime. Indeed, supernova explosions produce energy outputs of 10^{44} J and are expected to occur with a rate of once every 30 years in the Milky Way. Even with acceleration mechanisms that convert only 10% of their energy into particle acceleration this would satisfy the power of 10^{34} W needed to sustain the cosmic ray population in our galaxy. The most studied acceleration mechanism is the diffusive shock acceleration of particles during the interaction

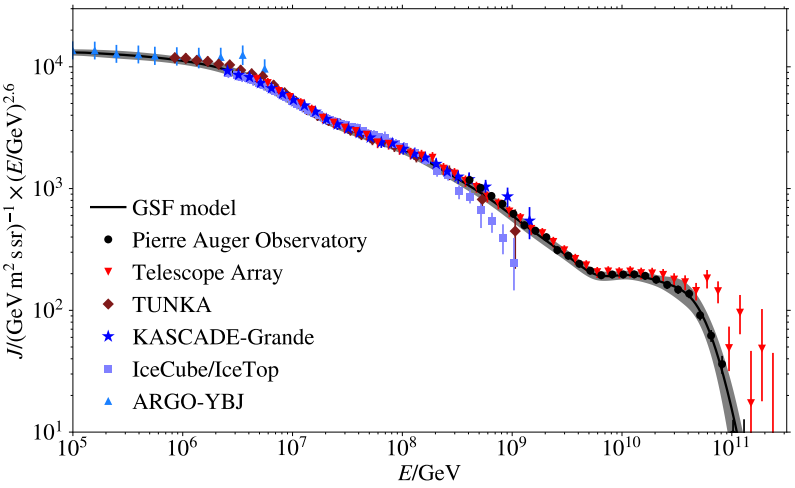

Figure 1.1 Cosmic ray all-particle flux over energy. The steeply falling flux was multiplied with $E^{2.6}$ to enhance two main spectral features known as the *knee* at $3 \cdot 10^6$ GeV and the *ankle* at $5 \cdot 10^9$ GeV. The solid curve is the GSF model (Dembinski et al., 2017), an empirical spline model fitted to raw data from multiple experiments. The GSF approach takes systematic uncertainties of the experiments into account and corrects energy scale offsets of different experiments within their uncertainties. The points represent energy-shifted data from Montini and Mari (2016), Rawlins and Feusels (2016), Apel et al. (2012), Schoo et al. (2016), Prosin et al. (2014), Korosteleva et al. (2007), Ivanov (2016), Valino (2016) and Aab et al. (2014).

of strong shocks with the surrounding ISM that is described in more detail in Section 1.1. This mechanism allows for protons to be accelerated up to 10^{14} eV (Lagage and Cesarsky, 1983) before the diffusion coefficient becomes larger than the radius of the shocked region and the particles are no longer contained in the acceleration region.
The accelerated cosmic rays that cross the shock front, interact with the unshocked medium and thereby create an amplification of the magnetic field on that side, that in turn confines the particles in the acceleration region for a longer time as described for example by Schure et al. (2012). A longer acceleration time naturally results in higher particle energies. As also more massive nuclei can be accelerated to higher energies, the steepening of the spectrum between the *knee* at $3 \cdot 10^{15}$ eV and the *ankle* at around $5 \cdot 10^{18}$ eV could be explained as a superposition of the different spectra of those components.
Other acceleration mechanisms include particle acceleration in electrical fields close to pulsars (Arons, 1981), reconnection of magnetic field lines of opposite polarity (de Gouveia Dal Pino and Kowal, 2015) or decay of highly massive particles (de Vega and Sanchez, 2003). Smaller contributions come from winds of Wolf-Rayet and certain hot, massive stars or even, at the lowest energies, from the solar winds.
The second spectral break at the ankle is nowadays interpreted as a second cosmic ray particle population. At those energies, the gyroradius r_g of a cosmic ray proton would be larger than 1 kpc, where r_g is calculated as

$$r_g = \frac{E}{|q|\mathrm{c}B} = 10^{-3} \left[\frac{\mathrm{nT \cdot pc}}{\mathrm{TeV}}\right] \frac{E}{B}, \tag{1.1}$$

with the relativistic energy E of the particle, its electric charge q , the speed of light c in vacuum and the galactic magnetic field B =0.3 nT. As this exceeds the thickness of the galactic disk, the proton would no longer be confined inside the galaxy and must be of

extragalactic origin. The most probable extragalactic cosmic-ray accelerators are shocks around active galactic nuclei (AGNs), gamma-ray bursts (GRBs) or cluster accretion shocks. At the highest energies, a cut-off in the flux spectrum was found by the Pierre-Auger Observatory (Abraham, 2008). One explanation of this flux suppression is the *GZK* effect predicted by Greisen (1966) and Zatsepin and Kuzmin (1966). According to this theory, protons with energies larger than a few 10^{19} eV are above the pion production threshold when interacting with the cosmic microwave background (CMB) while heavier nuclei at these energies tend to photo-disintegrate. Thus, cosmic rays in this energy range detectable on Earth must come from distances smaller than a few hundred Mpc, reducing the number of possible sources and hence the flux. For a more detailed review on cosmic ray origin see e.g. Drury (2012).
Gaining a deeper understanding of possible cosmic ray sources and the processes leading to the intense acceleration of cosmic rays will help us to gain a clearer picture of our universe. In this chapter, mechanisms of cosmic ray acceleration and gamma-ray production by cosmic rays are presented in Section 1.1. In Section 1.2 the physics of cosmic ray induced air showers are explained followed by a description of current detection methods in general and the Cherenkov Telescope Array in particular in Section 1.3.

1.1 Particle acceleration and γ-ray emission

Due to their charge, cosmic ray particles are sensitive to magnetic fields and their original direction will be obscured by scattering processes. While it is possible to detect cosmic rays on Earth, it is impossible to reconstruct their source positions directly. However, as the highly accelerated particles propagate through space they interact with the inter-stellar and inter-galactic matter and with the radiation fields around them, producing gamma rays by bremsstrahlung, synchrotron or inverse Compton emission. Unlike charged particles, gamma rays do not interact with magnetic fields and do still carry information about their creation site when detected on Earth. In this section, the diffusive shock acceleration, the most studied primary acceleration mechanism for particles in the vicinity of strong shocks, is described, together with the gamma ray production mechanisms that allow us to study the primary acceleration sites. The Formulas in this section are mostly modified from Longair (2011).

1.1.1 Diffusive shock acceleration

In 1949 Fermi proposed an acceleration mechanism based on the scattering of relativistic particles on irregularities in magnetised clouds. In this stochastic process, particles gain energy by head-on collisions with approaching clouds and lose energy by scattering on receding ones. As the probability of scattering on an approaching cloud is slightly higher, on average the particle is accelerated. As this energy gain is second order in $\frac{v}{c}$, where v is the average speed of the clouds, the mechanism became known as *second order Fermi acceleration.* However, this theory faces some difficulties in explaining the observed cosmic ray spectrum. The large acceleration time scales of the process lead to an increased time for energy loss due to ionisation while at the same time it is challenging to explain the universality of the cosmic ray spectral index by considering statistical processes in different sources.
A new theory was developed independently by Axford et al. (1977), Krymskii (1977), Bell (1978) and Blandford and Ostriker (1978). When relativistic particles cross non-relativistic shock fronts multiple times they can gain energy in effective head-on collisions on magnetic irregularities on either side of the shock front. This *diffusive shock acceleration* that could arise for example in the shocks of supernova explosions, is illustrated in Figure 1.2.

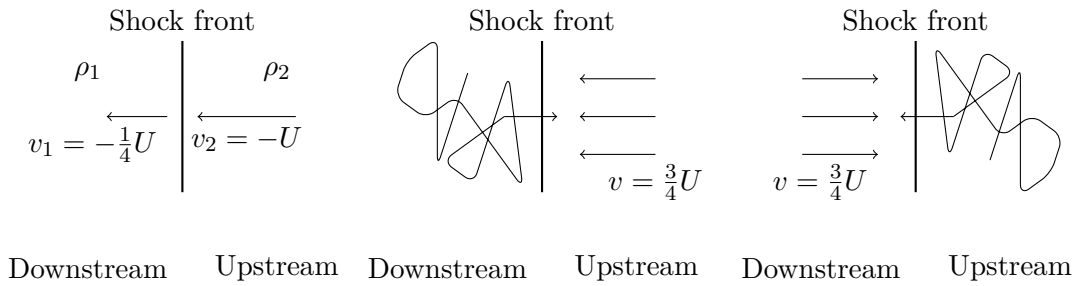

(a) Shock frame **(b)** Downstream frame **(c)** Upstream frame

Figure 1.2 Diffusive shock acceleration for a shock with velocity U, creating a density discontinuity. (a) In the rest frame of the shock the velocity in the downstream region is reduced by a factor 4 compared to the upstream velocity. (b) A cosmic ray particle loses its initial direction by isotropic scattering, but has a certain probability of crossing the shock front. In the downstream rest frame it sees the matter in the upstream region approaching and gains energy in head-on collisions. (c) In the upstream rest frame, the recrossing particle is approached by downstream matter and the particle regains energy in head-on collisions. The energy gain per cycle is $\left\langle \frac{\Delta E}{E} \right\rangle = \frac{4}{3}\frac{v}{\mathrm{c}}$.

As a shock front moves through space with a velocity U the passed-through medium is disturbed. In the rest frame of the shock front the undisturbed matter flows towards the front with a velocity of $-U$ and away from it with a smaller velocity (see Figure 1.2a).
The shock front represents a density discontinuity, where ρ_i are the densities and v_i the velocities of the particle distributions downstream and upstream of the front. *upstream* and *downstream* refer to the direction of the matter flow in this frame. Consequently, the *downstream* region is within the limits of the shock, *upstream* is outside. Mass continuity implies that the compression rate r of the perturbed gas downstream can be calculated via

$$\rho_1 v_1 = \rho_2 v_2 \tag{1.2}$$

$$r = \frac{v_2}{v_1} = \frac{\rho_1}{\rho_2} = \frac{\gamma + 1}{\gamma - 1}, \tag{1.3}$$

with the adiabatic coefficient γ of the ambient medium. For fully ionised mono-atomic plasmas, $\gamma = \frac{5}{3}$ and $r = 4$. Thus, the downstream medium flows away from the shock front with $v_1 = \frac{1}{4}U$. Magnetic irregularities appear on both sides. Downstream, they are created by turbulent motion within the shock, upstream, it is assumed that the highest energy cosmic rays introduce irregularities when crossing the shock front and producing Alfvén waves.
Cosmic ray particles are expected to move with speeds larger than the U. However, as a particle scatters on the magnetic irregularities downstream, it will lose its initial direction and the effective velocity in the direction of the shock is smaller. Nevertheless, with a certain probability it can cross the shock front to the upstream region due to its diffuse motion. In the downstream rest frame, the particle is approached by the ambient gas in the upstream region with $v = \frac{3}{4}U$. As for the second order Fermi acceleration, it gains energy in a head-on collision. In the upstream rest frame (see Figure 1.2b), the process is repeated when the scattered particle crosses the shock again in the downstream direction. For a non-relativistic shock and a relativistic particle with initial energy E, the average energy gain is

$$\left\langle \frac{\Delta E}{E} \right\rangle = \frac{4}{3}\frac{v}{\mathrm{c}}. \tag{1.4}$$

As the energy increases linearly with $\frac{v}{\mathrm{c}}$ this is known as *first order Fermi acceleration.*

There are two mechanisms to stop the acceleration of a particle. In each scattering process the particles take energy from the shock, thereby decelerating the shock. Also, once the initial energy that drives the shock propagation is used up, the shock front will slowly die out and the contained high energetic particles will leave the acceleration site. Additionally, during the lifetime of the shock, a particle in the upstream region will always be overtaken by the shock front after a certain time. A downstream particle, however, can fall further behind the shock front by scattering in a direction in which its effective velocity makes it impossible for the particle to recross the shock front and it escapes further downstream. Taking this escape probability into account, the energy spectrum of the accelerated particles is

$$N(E)\mathrm{d}E \propto E^{-2}\mathrm{d}E. \tag{1.5}$$

This power-law of index 2 is modified by diffusion and propagation mechanisms encountered on the particles' way to Earth and results in a spectrum similar to that found for the galactic cosmic rays in Figure 1.1. As this result is independent of the origin of the shock, the generality of the power-law index is plausible even when considering different primary sources. Additional effects that allow the particle to stay within the acceleration region for a longer time are topics of ongoing research. One example is magnetic fields amplifications Schure et al. (2012): The Alvén waves created by cosmic-rays crossing into the upstream region amplify the magnetic field there. This causes stronger scattering of the remaining cosmic-rays, confining them in the acceleration region over longer times. If this process is in spatial resonance between the wavelengths of the Alvén waves and the gyroradius of the cosmic-rays, field amplifications of $\frac{\delta B}{B_0} = 1$ can be reached, where δB is the amplification of the initial field B_0. Various linear and non-linear effects are proposed that lead to even higher amplifications of 10-100 outside the resonance regime (see Schure et al. (2012) for more details). A longer acceleration time results in a higher particle energy. However, the containment of particles becomes more difficult the higher the particle energy. As the resulting energy-dependent containment probability influences the power-law index of the spectrum a better understanding of acceleration processes can be gained by comparing the measured and predicted indices.
When the cosmic-rays escape from the acceleration region, they interact with surrounding matter and can create gamma-rays in different electromagnetic or hadronic processes. The most important interactions resulting in the emission of gamma-rays are Synchrotron radiation, inverse Compton scattering, Bremsstrahlung and pion decay.

1.1.2 Synchrotron radiation

As lower energetic cosmic rays bypass areas with high magnetic fields, the particles are deflected. Circular movement of particles around magnetic field lines produces synchrotron radiation. The average radiated power for a single particle with a mass m and $\beta = \frac{v}{\mathrm{c}}$ is

$$P_{\mathrm{syn}} = -\left(\frac{\mathrm{d}E}{\mathrm{d}t}\right) = \frac{4}{3}\mathrm{c}\sigma_{\mathrm{T}}\left(\frac{\mathrm{m_e}}{m}\right)^2 \beta^2\gamma^2 u_{\mathrm{B}} \tag{1.6}$$

where $\sigma_{\mathrm{T}} = \frac{8\pi}{3}\left(\frac{e^2}{\mathrm{m_e c^2}}\right)^2$ is the Thomson cross-section with the electron charge e and the electron mass $\mathrm{m_e}$ and $u_{\mathrm{B}} = \frac{B^2}{2\mu_0}$ the magnetic energy content with the magnetic moment μ_0. At the same energy, stronger emission is expected from lighter particles, as the emission is inversely proportional to the particle mass to the power of four (as gamma $\propto 1/\mathrm{m}$). Synchrotron emission is thus mainly observed for cosmic ray electrons. The cooling time for

electrons with $\beta \approx 1$ emitting synchrotron radiation is

$$t_{\mathrm{cool}} = \frac{E}{-\mathrm{d}E/\mathrm{d}t} \approx 10 \left[\mathrm{T^2 s}\right] B^{-2}\gamma^{-1}. \tag{1.7}$$

For 15 TeV electrons in the $3 \cdot 10^{-4}$ G magnetic field of the Crab Nebula, this cooling time is about 10 years, a factor of 100 shorter than the life time of the nebula. As still cosmic rays are detected from the direction of the Crab Nebula, SNRs must still accelerate particles long after the actual supernova explosion.

1.1.3 Inverse Compton radiation

The classical Compton effect describes the scattering of highly energetic photons on electrons during which part of the photon's momentum and energy is transferred onto the electron. At high energies, cosmic ray electrons can reverse this process when interacting with photon fields like the cosmic microwave background (CMB) and transfer energy onto the photon. The process is divided into two regimes: The *Thomson regime* if the initial electron energy in the centre of mass system of electron and photon is smaller than its rest energy and the *Klein-Nishina regime* at higher energies. The radiated energy for a single particle is

$$P_{\mathrm{IC}} = -\left(\frac{\mathrm{d}E}{\mathrm{d}t}\right) = \frac{4}{3}\mathrm{c}\sigma_{\mathrm{T}}\beta^2\gamma^2 u_{\mathrm{rad}} \qquad \text{Thomson} \tag{1.8}$$

$$P_{\mathrm{IC}} = -\left(\frac{\mathrm{d}E}{\mathrm{d}t}\right) \approx \frac{4}{3}\mathrm{c}\sigma_{\mathrm{T}}\beta^2\gamma^2 u_{\mathrm{rad}} \left[1 - \frac{63}{10}\frac{\gamma}{\mathrm{m_e c^2}}\frac{\varepsilon_{\mathrm{i}}^2}{\varepsilon_{\mathrm{i}}}\right] \qquad \text{Klein-Nishina} \tag{1.9}$$

with the energy content of the radiation field u_{rad} and the initial energy of the photon field ε_{i}. In the Thomson regime, the cooling time for an electron is

$$t_{\mathrm{cool}} = \frac{E}{-\mathrm{d}E/\mathrm{d}t} \approx 10^6 \left[\frac{\mathrm{m^3 s}}{\mathrm{J}}\right] u_{\mathrm{rad}}^{-1}\gamma^{-1}. \tag{1.10}$$

A 15 TeV electron interacting with the CMB, which has an energy density of $4{\cdot}10^{-14}\,\mathrm{J m^{-3}}$, has a cooling time of about 10^5 years.
In compact sources, electrons that generate synchrotron photons can inverse Compton scatter on those self-generated photon fields. This process is called *Synchrotron Self Comptonisation*.

1.1.4 Bremsstrahlung

Charged particles decelerated in electric fields around charged nuclei produce bremsstrahlung. The emitted energy for a single particle is

$$P_{\mathrm{Brems}} = 4 n_{\mathrm{n}} Z^2 \mathrm{r_e^2} \alpha \gamma \mathrm{m_e c^3} g \tag{1.11}$$

for an electron scattering on a nucleus with proton number Z and a density n_{n}. $\mathrm{r_e}$ is the classical electron radius, α the fine structure constant and g the Gaunt factor, which depends on the ionisation state of the nucleus. For a fully ionised gas the Gaunt factor is $g = ln(2\gamma) - \frac{1}{3}$ and the cooling time is

$$t_{\mathrm{cool}} = \frac{E}{-\mathrm{d}E/\mathrm{d}t} \approx 10^{22} \left[\mathrm{m^{-3} s}\right] \left(\ln(2\gamma) - \frac{1}{3}\right)^{-1} Z^{-2} n_{\mathrm{n}}^{-1}. \tag{1.12}$$

Assuming a region with the hydrogen particle density of the ISM of 1 particle per $\mathrm{cm^2}$, a 15 TeV particle would have a cooling time of 10^8 years. For regions with high densities of high-Z materials, this cooling time decreases.

1.1.5 Pion decay

The majority of cosmic rays are protons. Those protons can interact with other protons or ambient photon fields. If the energy of a cosmic ray proton is above a threshold energy of $E_{\mathrm{kin}} = 280\,\mathrm{MeV}$ or the photon energy $E_\gamma > 145\,\mathrm{MeV}$ in their centre of mass system, neutral pions can be generated. Those neutral pions can decay generating two high energetic gamma rays. The average energy of the generated photons is $E_\gamma \approx 0.1 E_{\mathrm{kin}}$. As the interaction cross section of proton-proton interaction is far larger than that of the proton-photon interaction, mostly pure hadronic interaction is expected. However, as the density of protons of the required energy is far smaller than than the photon density in the universe, the hadronic-electromagnetic process can even dominate in some areas.
For a mono-energetic pion distribution, the resulting photon energy spectrum is

$$P_\pi(E_\gamma, E_\pi) = \frac{2}{\sqrt{E_\pi^2 - m_\pi^2 \mathrm{c}^2}} \qquad \text{for } \frac{E_\pi}{2}(1-\beta_\pi) \leq E_\gamma \leq \frac{E_\pi}{2}(1+\beta_\pi). \tag{1.13}$$

The cooling time of the protons due to radiation losses is given as

$$t_{\mathrm{cool}} \approx \frac{1}{\kappa_{\pi^0} \mathrm{c} n_{\mathrm{H}} \sigma} \approx \frac{5 \cdot 10^{21}\,[\mathrm{m}^{-3}\mathrm{s}]}{n_{\mathrm{H}}}. \tag{1.14}$$

where $\kappa_{\pi^0} \approx 0.17$ is the inelasticity of the pion, $\sigma \approx 40\,\mathrm{mb}$ the interaction cross section and n_{H} the density of the surrounding material. For a proton density of $1\,\mathrm{cm}^{-3}$, compatible to the ISM, this cooling time corresponds to $0.2{\cdot}10^9$ years. Due to these long cooling times, the process is only visible in areas with high surrounding densities.

1.2 Extensive air showers

Cosmic rays and high energy photons that reach the Earth interact with molecules in the atmosphere. They lose energy by bremsstrahlung, pair production or hadronic interactions creating secondary particles. These secondaries can repeat the processes and a shower cascade is generated within our atmosphere. In this case photons are considered as electromagnetic particles as well. The actual form of *extensive air showers* (EAS) varies depending on whether the primary particle starting the cascade is electromagnetic or hadronic in origin.

1.2.1 Electromagnetic showers

A simple model for calculating the number of particles generated by an electromagnetic primary cosmic ray was established by Bhabha and Heitler (1937). If the initial energy of the primary particle is above a few GeV, bremsstrahlung and pair production are the only processes considered relevant:

$$\gamma \rightarrow \mathrm{e}^+ + \mathrm{e}^- \qquad \text{pair production} \tag{1.15}$$

$$\mathrm{e}^\pm \rightarrow \mathrm{e}^\pm + \gamma \qquad \text{bremsstrahlung} \tag{1.16}$$

This model is based on the assumption that the radiation length X_0^{pair} of the photon and the radiation length X_0^{brems} of an electron or positron are equal. As $X_0^{\mathrm{pair}} \approx \frac{9}{7} X_0^{\mathrm{brems}}$ with $X_0^{\mathrm{brems}} \approx 370\,\frac{\mathrm{kg}}{\mathrm{m}^2}$ this is a simplification. Furthermore for this model it is supposed that the initial energy in each process is distributed evenly between the two end products. A schematic drawing of the shower development is shown in Figure 1.3a.

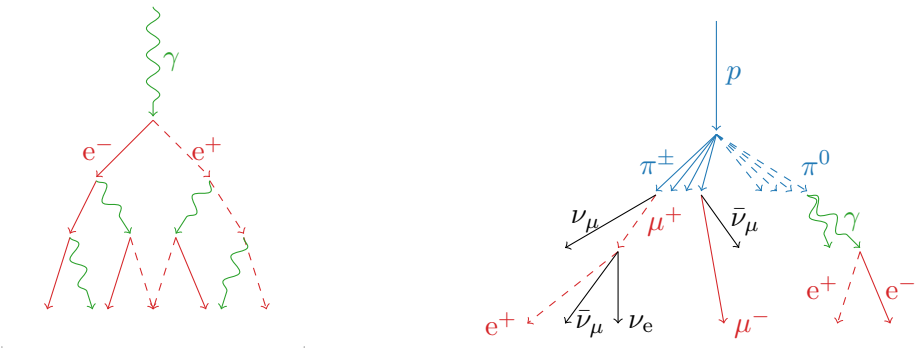

(a) Electromagnetic shower **(b)** Hadronic shower

Figure 1.3 Development of particle induced air showers. (a) In the atmosphere a primary photon creates an electron-positron pair. Those secondary particles can each emit a photon by bremsstrahlung. This process is repeated until the energy of the particles is below a threshold energy. (b) A proton interacting with the molecules in the atmosphere can undergo hadronic or electromagnetic processes and create several secondary pions of which neutral pions then decay into photons, charged pions into muons and neutrinos, all (except the neutrinos) creating further subshowers.

With these assumptions, a primary photon of initial energy E_0 will create an electron-positron pair after travelling the radiation lengths X_0. Both, the electron and positron will emit a photon by bremsstrahlung after another radiation length. This way, after travelling t radiation lengths, the initial photon will have created a particle cascade of 2^t secondary particles. As the energy is evenly distributed the energy of each particle will be

$$E(t) = \frac{E_0}{2^t}. \tag{1.17}$$

This process will last until a critical energy E_c is reached. Below this energy the electrons will lose their energy rapidly mainly via ionisation and the generated photons will no longer be energetic enough to create electron-positron pairs. The maximum number of generated particles at E_c and the depth X_max to which the shower penetrated into the atmosphere at this position can be calculated as

$$n_\mathrm{max} = 2^{t_\mathrm{max}} = \frac{E_0}{E_\mathrm{c}} \tag{1.18}$$

$$X_\mathrm{max} = t_\mathrm{max} X_0 = \frac{\ln(E_0/E_\mathrm{c})}{\ln 2} X_0 \tag{1.19}$$

The maximum number of generated particles is proportional to the initial energy. At larger penetration depths, the shower dies out slowly.
The opening angle of the cascade can be calculated assuming that after each process the particle with energy E deviates from the direction of its parental particle by $\vartheta = \mathrm{mc}^2 E^{-1}$. As the energy of the parental particle decreases, the maximum angular spread after t steps is

$$\vartheta \leqslant \sqrt{t}\frac{\mathrm{mc}^2}{E}. \tag{1.20}$$

As already stated, this model is only a simplification. For a more detailed understanding of the shower mechanics, more realistic interaction cross sections and accurate radiation lengths for bremsstrahlung and pair production need to be taken into account as well as the statistical energy distribution between the secondaries. Also ionisation losses play a small but significant role even before the critical energy is reached. Nowadays air showers are studied with detailed Monte-Carlo simulation codes such as CORSIKA (Heck et al., 1998).

1.2.2 Hadronic showers

The development of hadronic showers is more complex, as illustrated in in Figure 1.3b. The energy of cosmic-ray particles will in general be high enough to create several new particles in the atmosphere. Those secondaries, e.g. pions and kaons, again initialise new hadronic subshowers. In these cascades paarticles such as neutral pions decay into two photons that can create electromagnetic subshowers as described before. Charged pions decay into muons and neutrinos after a very short lifetime. The muons tend to penetrate deep into the atmosphere losing energy mostly by ionisation. Some of them also decay further into electrons and neutrinos and then these electrons create further subshowers. Hadronic showers are therefore characterised by the higher number of subshowers and the occurrence of muons on the ground. Additionally, while electromagnetic showers are very concentrated around the shower axis, hadronic showers have a far larger lateral spread due to the transverse momentum given to the secondary hadrons in strong interactions. Images of an electromagnetic and a hadronic shower simulated with CORSIKA are shown in Figure 1.4 for comparison.

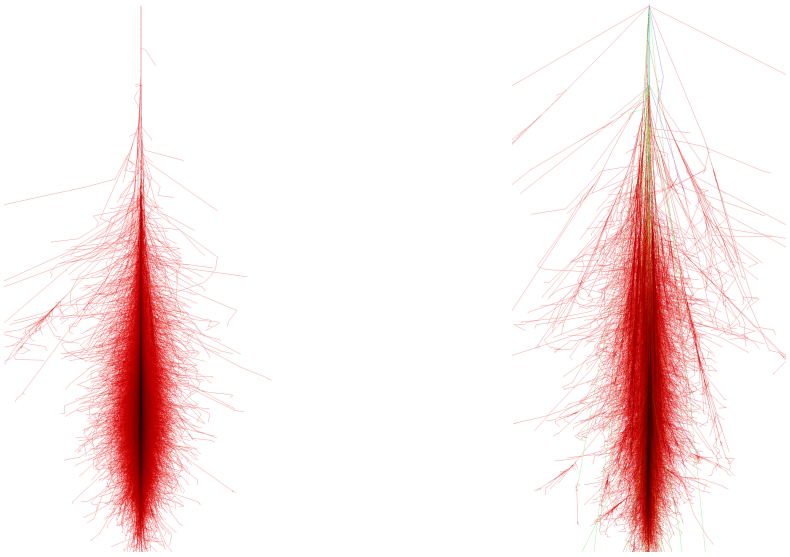

(a) Electromagnetic shower **(b)** Hadronic shower

Figure 1.4 A photon-induced air shower (a) and a proton-induced air shower (b) of an initial energy of 1 TeV simulated with CORSIKA. Each line corresponds to the track of one particle where red tracks corresponds to electrons, positrons or photons, green tracks to muons and blue tracks to hadrons. The electromagnetic shower is more concentrated around the primary particle direction while in the hadronic shower several subshowers are visible and the lateral spread is larger. At higher energies this effect becomes more prominent. Images taken from Schmidt (2017)

For experiments trying to localise the sources of TeV gamma-rays, hadronic showers are the dominant background. Even though those showers can be used to study the characteristics of the primary cosmic rays, as mentioned before they do not carry any information about their initial direction. It is possible to discriminate between hadronic and electromagnetic showers and to reduce this background, by using their different shower properties. However, in actual experiments other factors such as detector properties, night sky background, shower fluctuations or the energy dependent form of the showers can make it challenging to clearly differentiate the particle origin of a measured shower.

1.2.3 Cherenkov radiation

The secondary particles in the EAS cascades travel through the atmosphere with very high velocities. All charged particles that move within a dielectric medium such as the atmosphere emit electromagnetic waves. For particles with a speed v smaller than the wave propagation speed c, the waves will not interact (see Figure 1.5a). However, when moving through a medium with refractive index n the electromagnetic waves will propagate with a reduced phase speed $v_\mathrm{c} = \mathrm{c}n^{-1}$ while very energetic particles can move with higher velocity. As shown in Figure 1.5b, the waves will then interfere constructively and, following Huygen's principle, create a wave front that propagates away from the particle propagation direction under an angle ϑ_C with

$$\cos\vartheta_\mathrm{C} = \frac{\mathrm{c}}{vn}. \tag{1.21}$$

This *Cherenkov radiation* is named after P. Cherenkov who was the first to systematically study this unknown emission and was awarded with the Nobel Prize in 1958 together with Frank and Tamm (1937) who derived the theoretical description.

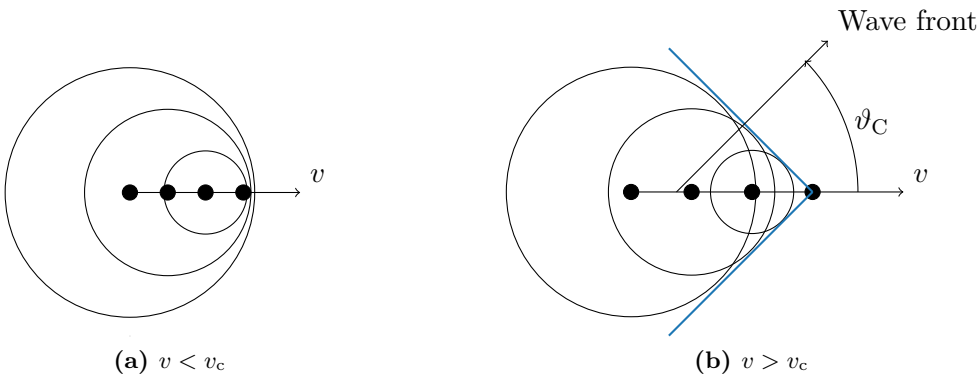

(a) $v < v_\mathrm{c}$ **(b)** $v > v_\mathrm{c}$

Figure 1.5 Principle of Cherenkov radiation. A particle moving through a dielectric medium produces electromagnetic waves. (a) If the particle velocity is smaller than the phase speed of light in the medium, the waves will not interfere. (b) At higher velocities the waves can interfere constructively creating a wave front of Cherenkov light that moves away from the particle propagation direction under an angle ϑ_C.

The minimum energy for a particle to emit Cherenkov radiation is

$$E_\mathrm{min} = \gamma_\mathrm{C} m\mathrm{c}^2 = \frac{m\mathrm{c}^2}{\sqrt{1-n^{-2}}} \tag{1.22}$$

For an electron in air, $E_\mathrm{min} \approx 20\,\mathrm{MeV}$ is much smaller than the critical energy of 79 MeV (Patrignani et al., 2016) of electrons in the vicinity of the molecules of the atmosphere at which the shower starts to die out, so most charged shower particles emit Cherenkov radiation. The continuous photon spectrum is given by the Frank-Tamm fomula to be

$$\frac{\mathrm{d}^2N}{\mathrm{d}x\mathrm{d}\lambda} = 2\pi\alpha\left(1 - \frac{1}{\beta^2 n^2}\right)\lambda^{-2}. \tag{1.23}$$

where dx is the path length the particle has travelled. Thus, more Cherenkov photons are expected at lower wavelengths. However, as our atmosphere is not transparent for wavelengths

below ~300 nm, the Cherenkov light intensity from EAS measured on Earth peaks at this wavelength before decreasing steeply towards longer wavelengths.
The Gladstone-Dale formula for gases implies that the refraction index varies with the density ρ of the atmosphere and thus with the altitude h as

$$n(h) - 1 \propto \rho(h) \propto e^{-h}. \tag{1.24}$$

Therefore, the particles of an air shower emit cones of light with different opening angles following Equation 1.21 (see Figure 1.6 left panel). Consequently, the Cherenkov light of the particles within an EAS creates rings of light with different radii on the ground. With the additional effect of multiple scattering of particles at low energies, a *pool of light* develops on ground level with an almost homogeneous light distribution. As the largest radius is reached at an altitude around 10 km, the size of this light pool is almost independent of the height of first interaction of the primary particle. The diameter of the light pool generated at an altitude of 1800 m a.s.l. will be around 250 m as shown in the right panel of Figure 1.6. The size shrinks with higher detection altitude. The emission of Cherenkov light from an EAS has a typical duration of around 5 ns.

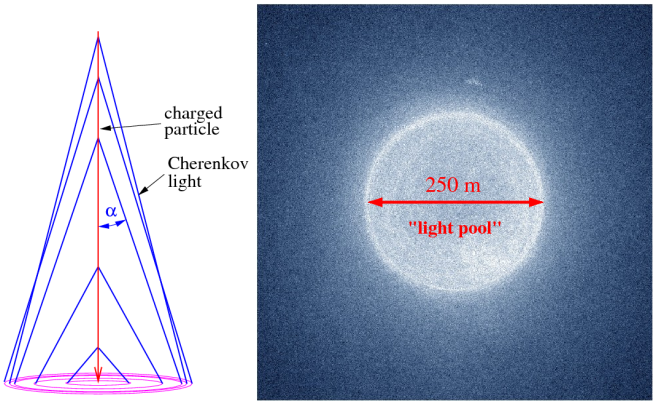

Figure 1.6 Cherenkov light emission of an EAS. Left: As the opening angle of light emission increases with decreasing altitude, rings of Cherenkov light are created on the altitude of detection. Right: Simulations of the Cherenkov light of a 1 TeV photon-induced air shower show an almost homogeneous light distribution within a 250 m diameter circular light pool at an altitude of 1800 m above sea level. Image taken from (Voelk and Bernloehr, 2009b).

1.3 Detection of very high energy photons

TeV astronomy is based on the detection of very high energy gamma-rays. Earth's atmosphere is not transparent for these photons, so up to an energy of 300 GeV measurements must be taken by space-based detectors such as the Large Area Telescope (LAT) on the Fermi satellite (Atwood et al., 2009). However, as the rate of photons drops at higher energies, detectors with even larger collection areas are needed which is not achievable in space. Therefore, ground-based detectors are built to observe the most highly energetic photons. There are two categories of ground-based TeV-photon detectors: Particle detectors and Imaging Atmospheric Cherenkov Telescopes (IACTs). Both cannot directly study the primary photons, but make use of EASs and the Cherenkov light emitted in different mediums.

1.3.1 Particle detectors

In 1938 P. Auger proved the existence of correlated EAS particles on the ground (Auger et al., 1939), only one year after the shower theory was established. Auger used temporal coincidences of measurements with charged particle counters at different distances to each other to prove the existence of air showers. He also repeated his measurements at different heights above sea level and found an agreement between the estimated number of particles in the shower with the predicted numbers from the Heitler model.
The results showed that high altitudes are crucial for the particle detection. The closer the detectors to the shower depth $X_{\max}$, the more particles can be measured and the better the energy reconstruction of the primary particle. Based on those ideas large particle detector arrays were built, the most recent ones being Milagro (McEnery et al., 2001), the IceCube Observatory (Tamburro, 2012), the Telescope Array (Abu-Zayyad et al., 2013), the Pierre-Auger observatory (Aab et al., 2015) with the upgrade AugerPrime (Aab et al., 2016) under construction, and the HAWC observatory (Abeysekara et al., 2017). The principle of *Water Cherenkov Telescopes* is hereafter described using the example of HAWC.
The High Altitude Water Cherenkov (HAWC) observatory located on top of the Sierra Negra volcano in Mexico at an altitude of 4100 m covers an area of 22000 m^2 with 300 tanks filled with 180,000 litre of water each. Each tank is equipped with four photo-multiplier tubes (PMTs). HAWC observes the sky of the northern hemisphere. Coincidently arriving charged particles of an EAS produce Cherenkov light in the water tanks which is detected by the PMTs. By counting the number of particles and studying their distribution throughout the array over time, the energy and direction of the primary particle can be derived.
The advantages of this method are a large field of view (FOV) of about 2 sr and a duty cycle of nearly 100%. Nevertheless, as the discrimination between hadronic and electromagnetic showers with this method is challenging, a sensitivity around 10% of the flux of the Crab Nebula over the full energy range improving for higher energies is reached.

1.3.2 Imaging Atmospheric Cherenkov Telescopes

IACTs are the second method of TeV photon detection. As shown in Figure 1.7, IACTs are telescopes with focusing mirror dishes. If positioned within the pool of light of an EAS they can reproduce a picture of the shower on their cameras. Also for the IACTs, the altitude is a crucial factor to get a good representation of the shower. The optimal altitude is low enough to ensure a large pool of light that corresponds to the maximal effective area of the telescopes, while being close to the shower maximum to get a large image on the camera. Most current IACTs are positioned at 1000-2500 m above sea level.
The telescope cameras are pixelated. Each pixel is a photon detector optimised for Cherenkov light. As the amount of light depends on the number density of the shower, the highest intensity is expected at $X_{\max}$ with gradually decreasing intensity above and below. The corresponding camera picture is approximately elliptical. From the elliptical images, the direction and energy of the primary particle can be reconstructed as well as the particle type. A more detailed description of the event reconstruction of IACTs is given in Chapter 4.
With this method the Whipple Observatory detected the first significant emission of photons above 0.7 TeV from the direction of the Crab Nebula in 1988 (Weekes et al., 1989). Afterwards, good results were achieved by single IACT projects like CANGAROO (Hara et al., 1993) and CAT (Degrange, 1994). However, with HEGRA (Mirzoyan et al., 1994) stereoscopic measurements with Cherenkov telescopes were performed for the first time, followed by H.E.S.S (Hinton, 2004), MAGIC (Lorenz and The MAGIC Collaboration, 2004) and VER-

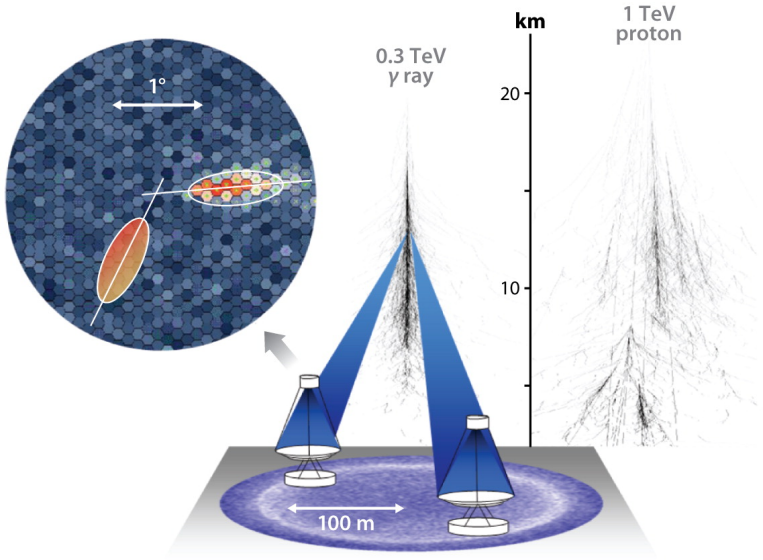

Figure 1.7 Principle of Imaging Air Cherenkov Telescopes (IACTs). EAS shower images are recorded by cameras of telescopes within the Cherenkov light pool. Form, alignment and intensity of the resulting images are used to reconstruct the primary particle type, its energy and original direction. Using several telescopes in stereoscopic mode and overlaying their images increases the direction reconstruction accuracy and reduces the background level. Image from Hinton and Hofmann (2009).

ITAS (Weekes et al., 2002). With the stereoscopic approach, large collection areas can be reached easily, by using the full pool of light. Additionally, the background can be reduced by comparing the temporally coincident images in different cameras and the reconstruction of the primary direction is improved by overlaying the shower images of several cameras. Even though the duty cycle is only about 1000 h/year as dark nights are needed to observe, and the measurements are sensitive to clouds and changes in the atmosphere, and the FoV is limited to a few degrees, very high sensitivities and angular resolutions are possible.

1.3.3 The Cherenkov Telescope Array

The Cherenkov Telescope Array (CTA) (The CTA Consortium, 2011) is an international project including 27 countries that is building the next generation IACT observatory. While current stereoscopic projects use up to 5 telescopes, CTA will have an array of 20 telescopes in La Palma and 100 telescopes Chile, observing both hemispheres. Different scientific goals are pursued in the two hemispheres: While CTA South will focus mainly, but not exclusively, on a detailed study of the Galactic Plane, CTA North will concentrate more on extragalactic sources of TeV gamma-ray emission. Due to the different targets and corresponding sensitivity requirements, an energy range between 20 GeV and 20 TeV is covered in the north and from 20 GeV to 300 TeV in the south. An artist's impression of CTA is shown in Figure 1.8.
Three major types of IACT telescopes are being developed. For the energy range below 200 GeV, a few Large Size Telescopes (LSTs) will be built at the centre of each array. The collection area of few closely positioned telescopes with large 23 m mirror diameters is sufficient due to the high rate of particles in this energy range even though they produce faint showers. The core energy range of CTA between 100 GeV and 10 TeV is covered by an outer array of Medium Size Telescopes (MSTs) with a dish diameters of 12 m and a spacing of approximately 100 m. In the Southern array, to cover even the highest energies, Small Size

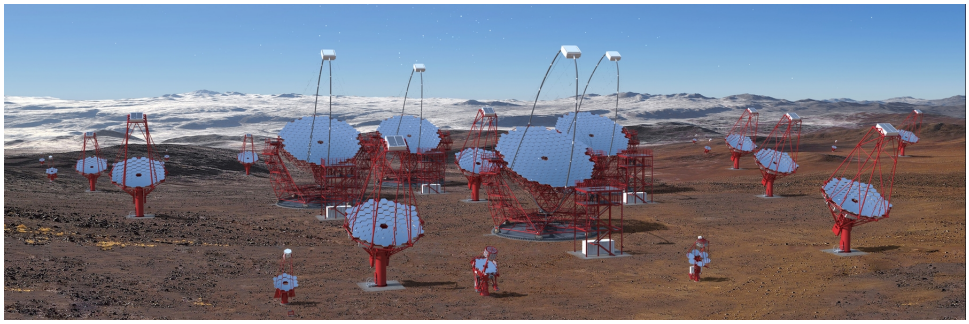

Figure 1.8 Artist's impression of the centre of CTA South by G. P. Diaz. CTA is based on about 100 telescopes distributed in two arrays to measure gamma-rays from sources on the southern and northern hemisphere. To cover the full energy range Large Size Telescopes, Medium Size Telescopes and Small Size Telescopes are used.

Telescopes (SSTs) with a dish diameter of 4 m are distributed over an area of several km^2. The most highly energetic showers are rare but bright and an even larger effective area is needed to collect as many showers as possible, but a sparse telescope distribution is sufficient. With this layout, CTA will reach sensitivities down to 10^{-13} erg cm^{-2}s^{-1}, a factor 10 better than current experiments (see Figure 1.9). The telescopes have a FoV between 5° and 10°, depending on the telescope type, and the whole array will observe with an energy resolution of 25% for energies below 100 GeV and even 10% for energies above 10 TeV. The angular resolution will be $< 0.1°$ for low energies and $< 0.05°$ for the highest.

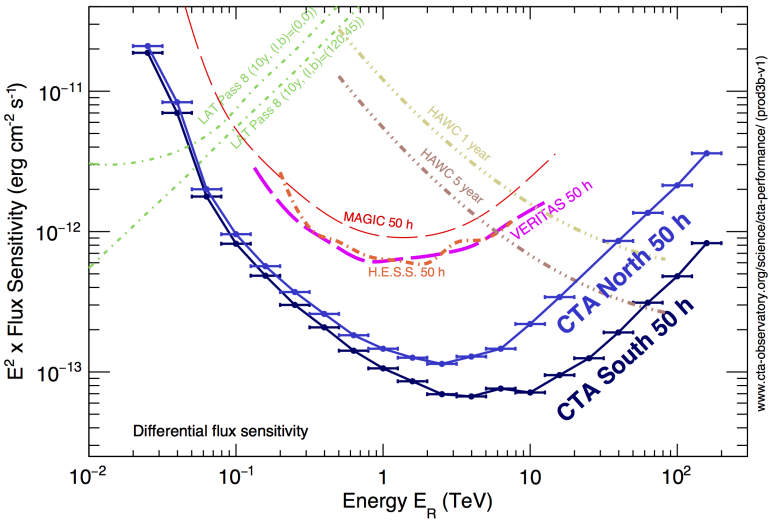

Figure 1.9 CTA sensitivity compared to current TeV photon detectors. Below 100 GeV Fermi LAT is optimised to detect photons with high sensitivity. In the core energy region both CTA South and CTA North will have a sensitivity an order of magnitude better than all current IACT projects with higher sensitivity for CTA South due to the higher number of telescopes required for the study of the Galactic Centre. Above a few tens of TeV the HAWC sensitivity becomes comparable to CTA.

CTA will be an open observatory granting external observers access to data and science tools to achieve the best possible scientific results. The research goals include the study of cosmic rays from various galactic and extra-galactic sources as well as the exploration of transient sources and the search for new physics in the form of dark matter (Acharya et al., 2017).

1.3.4 The Medium Size Telescope and FlashCam

The main focus of this thesis is on the performance of the MST telescopes. The MST project (Pühlhofer, 2017) consisting of telescope structure and two camera projects is currently run by an international team of 27 institutes distributed over 8 countries. A telescope prototype was constructed in Berlin, Germany, to prove that the current design is able to fulfil all CTA requirements and to study the long-term performance of the system. Figure 1.10 shows a picture of the prototype together with a schematic of the MST structure.

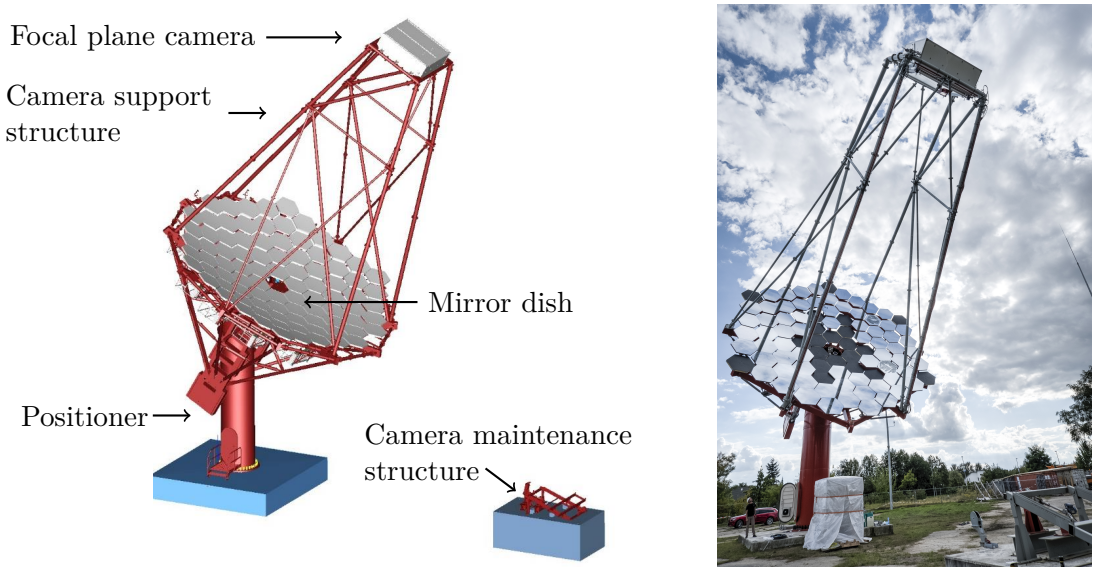

(a) Schematic **(b)** Prototype

Figure 1.10 Design of the MST prototype. (a) The MST telescope consists of a 12 m diameter segmented mirror dish that is mounted on a 9 m tall positioner. The focal plane camera is fixed at a distance of 16m from the dish centre, by the camera support structure. Drawing taken from Pühlhofer (2017). (b) The prototype of the MST telescope in Berlin-Adlershof was equipped with 68 mirrors during the FlashCam test mounting in September, 2017. Picture by C. Föhr.

The MST telescope is based on a modified Davies-Cotton design. Curved mirror segments are arranged on a spherical surface and superimpose their images on a camera mounted in the telescope's focal plane. For the MST, 86 hexagonally shaped mirrors with a flat-to-flat diameter of 1.2 m are mounted on a dish with a curvature radius of 19.2 m creating an effective mirror area of 88 m^2. This dish shape generates a focal plane at a distance of 16 m from its centre. All mirrors can be moved by motorised actuators for the high precision alignment needed to ensure a small point-spread function on the camera. As the camera housing would shadow the central mirror, the Davies-Cotton design uses only off-axis mirrors and the centre of the telescope dish is left empty. The available space is used to mount auxiliary devices such as a camera calibration device and a CCD camera used for mirror alignment control and telescope pointing calibration. Camera connected auxiliary devices such as the cooling system are set up next to the telescope structure on the ground. The pointing precision of the telescopes is within 7" with a reposition time to any possible source in the sky of < 90 s. CTA plans to have 25 MSTs observing in the southern and 15 in the northern hemisphere.
Two different cameras are in development for the MST telescopes: NectarCam (Glicenstein and Shayduk, 2017) and FlashCam (Pühlhofer et al., 2012). As this work mainly focuses on FlashCam, a short introduction to this camera is given hereafter. FlashCam is the first fully

digital Cherenkov camera. Its modular setup ensures an easy and cost efficient maintenance of all camera components. Even though all photo-detection and read-out modules are developed by the project members, they are based on commercial components. A schematic drawing and a picture of the camera prototype are given in Figure 1.11.

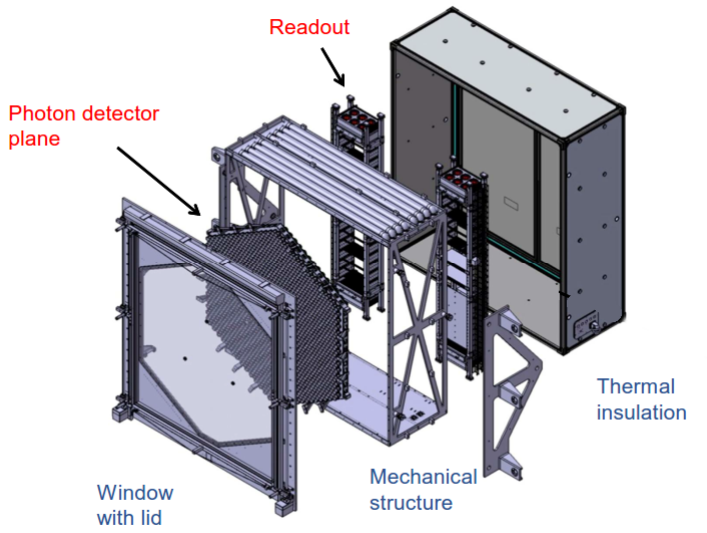

(a) Schematic

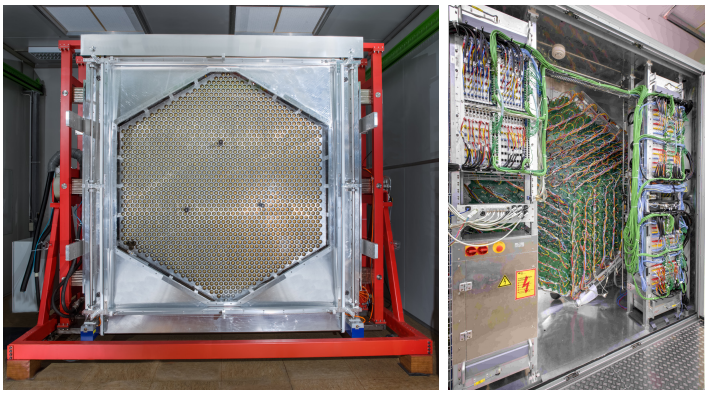

(b) Prototype front **(c)** Prototype back

Figure 1.11 Design of the FlashCam camera. (a) Light entering the modular camera is detected on the Photon Detector Plane and the digitised signal is processed in the readout boards. A 3x3x1 m^3 camera housing with a plexi glass protection window ensures thermal insulation. Diagram courtesy of the University of Zürich. (b) 1758 PMT pixels are visible on the front side of the FlashCam prototype camera. (c) Access to the PDP modules, readout electronic and safety cabins is possible is possible from the rear. Pictures taken by C. Föhr.

The quadratic camera housing has a length and height of 3 m and a depth of 1 m. It is sealed to provide thermal insulation and protection against sand and dust. Liquid cooling as well as a ventilation system are installed to ensure stable conditions within the housing. A plexi glass entrance window protects the sensitive optical camera components and can be closed with a lid during daytime. Light entering through this window is detected by 1758 PMT pixels. To reduce dead-space between the round PMT pixels light concentrators will be used. The PMT pixels are arranged in modules of 12 PMTs to fill the hexagonal Photon Detector Plane (PDP) of the camera. The modules include high-voltage supply and monitoring for

the PMTs, preamplifiers for the analogue signal and a Controller Area Network (CAN) bus interface for the handling of the PMTs (slow control). This way the photon detection is isolated from the further processing of the signal and can easy be exchanged with any other type of detector as long as the interfaces do not change.
The analogue PMT signal is transferred to the readout electronics via Cat. 6 twisted pair cables. On 84 Flash analogue to digital converter (FADC) modules the signals of two PDP modules each are then digitised by commercial 12-bit FADCs with a sampling rate of $250\,\mathrm{MS\,s^{-1}}$ to account for the $\mathcal{O}$(ns) duration of the Cherenkov flashes. (Field Programmable Gate Array (FPGA) integrated circuits acquire and buffer these signals. Compressed sums of neighbouring pixels are sent to trigger modules which continuously analyse the light distribution for compact, coincident short flashes. The trigger algorithms are set in the FPGA firmware and can be changed at any time. Trigger decisions of the individual trigger cards are controlled and synchronised by a master trigger board which finally decides whether the event data is transferred to a camera server located at the CTA computing facilities on site via 10 Gbit Ethernet connections. A dead-time free read-out rate of $>3.3\,\mathrm{GBytes\,s^{-1}}$ is possible.
A FlashCam prototype housing was built in Zürich and moved to Heidelberg, Germany, where it was equipped with PMTs and electronics. At Heidelberg, the long-term performance of FlashCam is being tested. The first results show that the dead-time free read-out rate of the camera is seven times higher than demanded by the CTA requirements, the charge and time resolution reaches the CTA goal performance and the temperature dependence of the signal chain is minimal and well-behaved (see Werner et al. (2017) for more details). This confirms that the FlashCam design allows for a stable high quality signal reconstruction that fulfils and partly outperforms all the requirements set by the CTA observatory.

This thesis is focused on the optimisation of the angular resolution and the sensitivity of CTA in the core energy around around 1 TeV where mainly the MSTs are operated.
The first part is dedicated to the characterisation of light concentrators for FlashCam. The tests performed on the FlashCam prototype up to now were concentrated on the verification of the camera design and the processes within the signal chain. One important part of the camera that is so far not tested in detail are the optical components in front of the PMTs such as the light concentrators and the protection window. Following the pact of design, all CTA cameras will be equipped with such concentrators as they are used in all current IACT projects like MAGIC or H.E.S.S.. They increase the light collection efficiency of a camera by reducing the amount of dead space between the pixels of a camera and decrease the level of night sky background light that is reflected from the ground or the telescope structure and would enter the camera from directions outside the telescope mirrors. In Chapter 2, a test system for optical camera components is presented that is especially optimised for angular and wavelength dependent measurements of light concentrators. Several measurements are performed to verify a dependable operation of the test system and its individual components. With this system, three light concentrator prototype coatings are characterised by their reflectivity and angular acceptance profile in Chapter 3. Accelerated ageing tests are performed in a climate chamber to verity the material durability of the coatings. Ray-tracing simulations are used to get a better understanding of the angular acceptance profiles and the influence of the light concentrator geometry on the illumination of the PMT surfaces. A dependency of the background suppression capability on the distance between the light concentrator and the PMT surface is presented that influences the signal-to-noise ratio of the camera and its benefit of this effect for FlashCam is discussed.
A completely different way of optimising the performance of CTA is discussed in a second

part of this thesis. In Chapter 4, two current IACT event reconstruction techniques are introduced that will be implemented in the CTA prototype software *ctapipe*: The standard Hillas reconstruction and the template based reconstruction algorithm ImPACT, which are both already successfully used in the standard event reconstruction of the H.E.S.S. experiment. By adapting the algorithms to the needs and requirements of the CTA telescopes, high angular resolutions and energy sensitivities over the whole energy range of CTA can be reached. A number of quality selection cuts is discussed and optimised cut sets for different scientific applications are developed that significantly increase the performance of CTA.
With the improved angular response of CTA, gained with this cut sets, scientific studies of the complex morphologies of extended sources can be performed with the highest accuracy ever in TeV astronomy. In Chapter 5, the radio galaxy Centaurus A is presented, an astronomical source that is of great scientific interest. The detectability of a possible source extension for this galaxy is studied by means of simulations. Different extensions indicate different TeV emission regions within the galaxy and a precise localisation of these regions will shed a new light upon particle acceleration and propagation within active galactic nuclei.

"All the small things
True care, truth brings"
blink-182, *All the small things*, 2000

CHAPTER 2

Optical test system

The FlashCam prototype contains different optical components such as the PMTs, the protection window and the light concentrators whose properties and durability need to be characterised and understood before the final deployment of the cameras on the CTA site. By testing different types of components and selecting those with the best performance in the sense of light throughput or detection, respectively, the overall performance of the cameras can be improved. By collecting more Cherenkov light, the signal to background ratio is increased so that light levels can be measured down to lower energy thresholds where the shower images become fainter. This leads to a better reconstruction of the gamma-ray events and therefore higher angular resolutions and flux sensitivities of the instrument.
Additionally, as failing components can lead to down-time of a camera and thus of a telescope during measurement time, unreliable components need to be identified and replaced. Influences of the components to the measured signal should be fully understood in order to correctly interpret the final astronomical data.
For this purpose, each component from the PMTs through the light concentrators up to the entrance window material is systematically tested. This way, it is ensured that only the best possible components with a fully understood performance are used for FlashCam and that data can be recorded by the camera in a reliable and stable way.
In this chapter, an optical test system is presented, optimised to determine the optical properties of light concentrators in combination with the FlashCam PMTs. After a general description, measurements verifying a dependable operation of the system are discussed.

2.1 Laboratory setup of the system

The optical test system is designed to determine the optical properties of camera related components. For this purpose, components are illuminated under different angles at different wavelengths and the light intensity after transmission is measured. A schematic is provided in Figure 2.1 and properties of the commercial components of the system are given in Table 2.1.
A stable light source with a well understood light field is necessary to minimise systematic errors. As Cherenkov cameras are designed for a spectral range from UV to visible light, a Xe arc lamp (Müller Elektronik, 75 W) with a broad spectrum between 250 nm and 800 nm is used in this setup. The lamp beam is directed into a remotely controllable monochromator

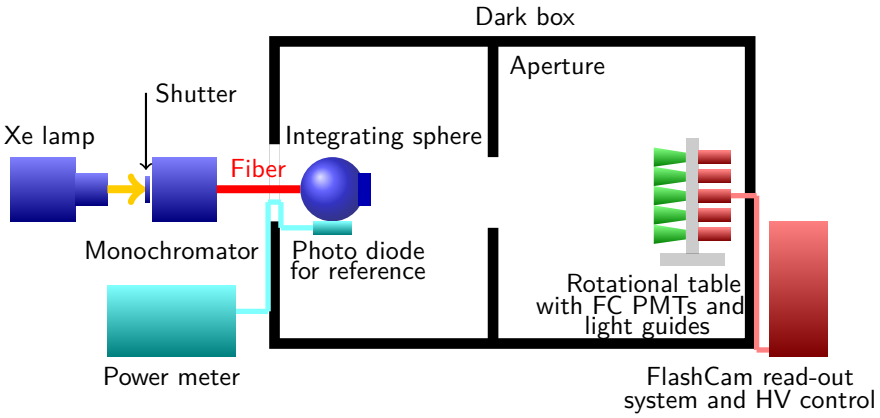

Figure 2.1 Schematic drawing of a test system for optical camera components. Light from a Xe arc lamp is focused into a monochromator for wavelength dependent measurements. The light is transmitted into a dark box with an optical fiber and coupled into an integrating sphere to produce a homogeneous light field. The light input is monitored with a reference diode and a power meter. On the other side of the box a FlashCam PDP module is mounted on a rotational stage to allow for angular dependent measurements. For light concentrator measurements, five concentrators can be attached to the front of five PMTs in vertical alignment for simultaneous measurements. The light is processed with the standard FlashCam signal chain. Image taken from Pürckhauer et al. (2017).

(Digicröm, CM112) which is used to scan the wavelength domain and can be closed with a shutter (Thorlabs, MFF101) for dark measurements (see Figure 2.2).
With an optical fiber, the light from the monochromator is transmitted into a dark box. To create a spatially homogeneous light field, it is coupled into a 13.5 cm diameter integrating sphere (SphereOptics) with a 6.4 cm diameter output port at the front, a 2.5 cm diameter input port on the side, and a 2.5 cm reference port on top of the sphere (see Figure 2.3). The sphere has a Spectralon® coating that provides a high reflectivity between 98% and 99.5% from the required UV up to the IR range. At the reference port a calibrated monitoring reference diode (Newport, 818-UV) is attached and read out by a powermeter (Newport, 2835).
At the far side of the dark box, a rotational stage (ZABER electronics, RSW60A) is mounted. For light detection a 12 pixel FlashCam PDP module is fixed on the stage with a dedicated holder, such that five pixels are vertically aligned with the rotation axis (see Figure 2.4a). During this work, PMTs will be referred to by their position with numbers from 1 to 5 where 1 correspond to the topmost and 5 to the lowest PMT. As the Cherenkov light peaks at around 350 nm, the PMTs (Hamamatsu R11920; 1.5 inch entrance window) were specially designed for CTA with an optimised quantum efficiency (QE) of up to 40% for wavelengths between 300 nm and 450 nm. The typical QE for those PMTs is displayed in Figure 2.4b.
Up to five optical test components are positioned in front of the PMTs. The PDP holder can be shifted on the stage such that the desired rotation axis of the component can be well aligned with the axis of the rotation table. A fine-adjustment of the distance between the test component and the PMTs in mm steps is also possible.
Inside the dark box, the distance between rotation axis and light source exit is 2.70 m. At 1.30 m from the light source a rectangular aperture is installed with a size of 20x30 cm^2 allowing for the five vertically aligned pixels of the PDP module to be fully illuminated while light scattered within the dark box is reduced. To further minimise light reflections and stray light the inner walls of the dark box are covered with black tissue and velvet.

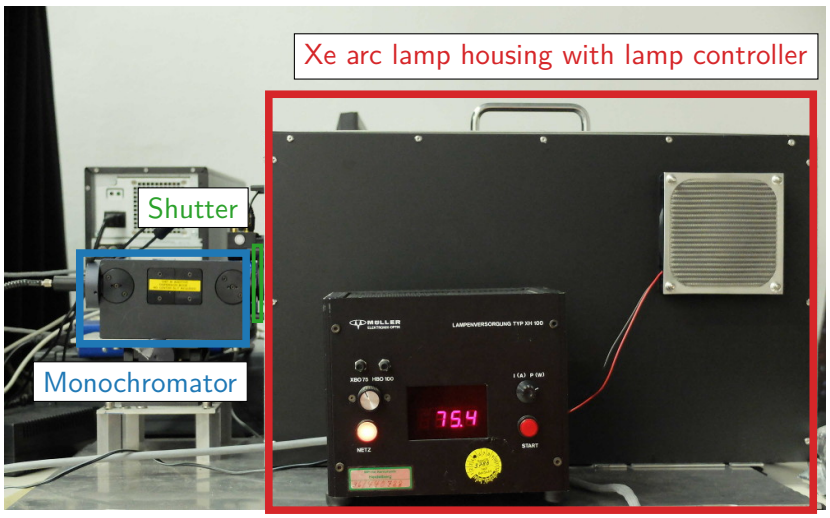

Figure 2.2 Light source setup outside the dark box. The Xe arc lamp is positioned within a special fan-cooled housing to avoid eye contact with the produced UV light and to decrease the generated heat. Exiting light is focused into a monochromator whose entrance slit can be closed with a shutter mounted on a flipper device. By means of an optical fibre the light is guided into a dark box.

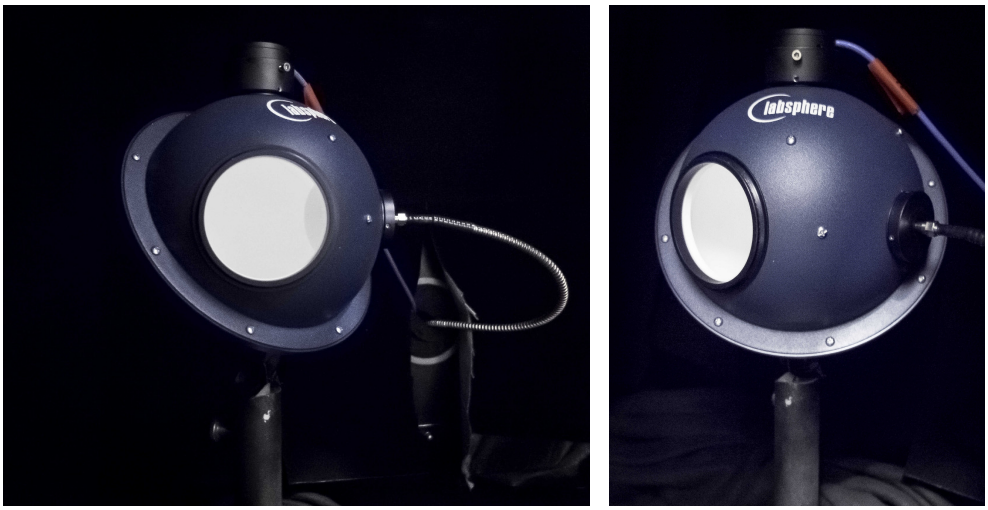

(a) Front view **(b)** Side view

Figure 2.3 Front and side view of the integrating sphere used to homogenise the light field. The light enters the dark box via the optical fiber that is attached to a port at the right side of the sphere and exits through the output port at the front. To prevent the light from leaving the sphere unscattered a baffle is installed in front of the entrance port. This baffle is barely visible in (a) on the right side of the exit window. At the top of the sphere a reference diode is installed.

Table 2.1 Nominal properties of the commercial devices used for the optical component test system taken from the corresponding data sheets.

Xe arc lamp, Müller Electronik (2011)	
Power	60-80 W
Stability	0.5 %
CM112 monochromator, Spectral Products (2006)	
Design	Czerny-Turner, dual-grating turret
Focal length	110 mm
Grating	1200 g/mm
Accuracy	±0.2 nm
2835-C power meter, Newport (1994)	
Accuracy (typical)	±0.1%
Noise	<1 pA
818-UV photo diode, Newport (1999)	
Spectral range	200-1100 nm
Max. power density	0.2 W/cm^2
Calibration uncertainty	2% 220-349 nm
	1% 350-949 nm
Linearity	±0.5%
RSW60A rotational stage, Zaber Technologies (2018)	
Angular resolution	234.375 $\cdot 10^{-6}$ °
Accuracy	0.14°

The PDP module is connected to a FlashCam readout system outside the dark box that consists of a CAN bus control system for high voltage (HV) and gain of the PDP module and a FlashCam FADC board. HVs between 700 V and 1500 V can be set for each PMT individually. For the test system 1200 V is chosen for the five vertically aligned PMTs. No voltage is set to all other PMTs which are used for noise reduction as will be explained later. The PMT signal, read-out by the FADC board, is analysed with the standard FlashCam software. FlashCam has a digitalisation rate of $250 \cdot 10^6$ samples. For this analysis 680 samples per trace are read-out. The light level is measured in *Least Significant Bits* (LSBs) equivalent to ADC counts. For reference, the value of no light signal (*zero baseline* or *dark measurement*) is set to about 200 LSB for each readout channel. Figure 2.5a shows a zero baseline trace. Variations within 0.5 LSB are due to the digitalisation of the signal. Dark measurements are taken before each measurement to correct for the small drifting of the value over time.
If light is transmitted into the dark box, each detected photon generates a photo-electron (p.e.) pulse on the trace as the PDP module is operated in DC mode (see Figure 2.5b). The baseline shift between dark and light measurement is proportional to the incident light intensity. For each measurement, the mean values of 500 single traces are averaged.
In parallel to the PMT measurements the reference diode at the integration sphere monitors the Xe lamp intensity at the set wavelength. The PMT data is normalised to that value to reduce the effect of time variabilities of the source. To determine optical properties of test components light intensities are measured for several angular positions and wavelengths.

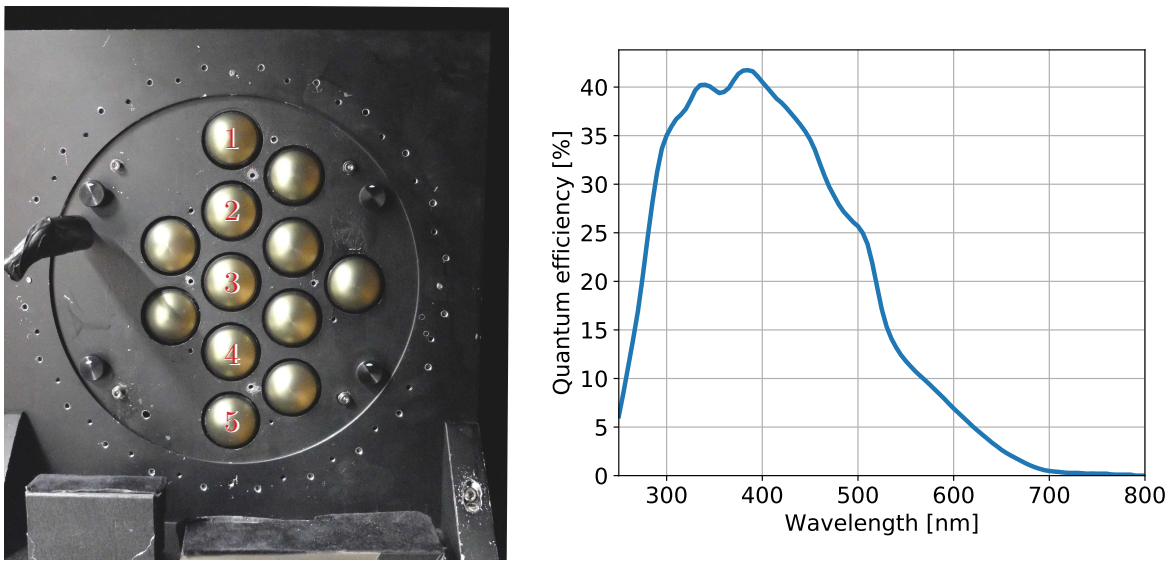

(a) PMT module **(b)** QE

Figure 2.4 FlashCam PDP module in mounting holder. (a) A FlashCam PDP module with 12 PMTs used for light detection in the test system is positioned inside a holder that vertically aligns five PMTs with the axis of the rotation table. (b) The typical quantum efficiency of the FlashCam PMTs peaks in the low visible wavelengths as does the Cherenkov light before decreasing steeply. Night sky background at higher wavelengths is suppressed. Measurements taken by S. Eschbach.

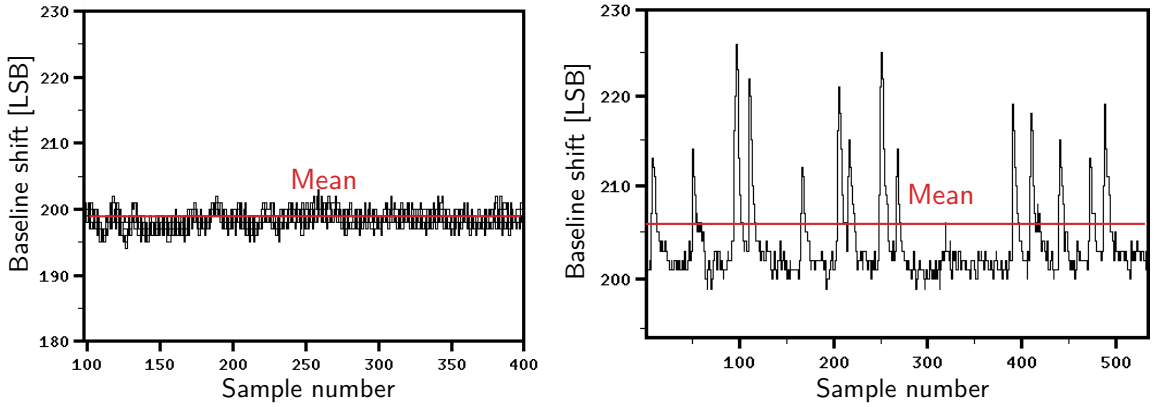

(a) No light detection **(b)** Light detection

Figure 2.5 Light intensity measurement with the PDP module. (a) The mean of the zero or dark baseline is set to 200 LSB for the each measurement. (b) If photons are detected by the PMTs, pulses are added to the zero baseline and the mean baseline is shifted proportional to the intensity of the incident light.

2.2 Noise and noise reduction techniques

The data analysis of the test system is based on averaging traces recorded by the readout system. An ideal dark trace should look like that shown in Figure 2.6a. There are no obvious features in the trace and a mean baseline of 200 LSB is found according to the settings.

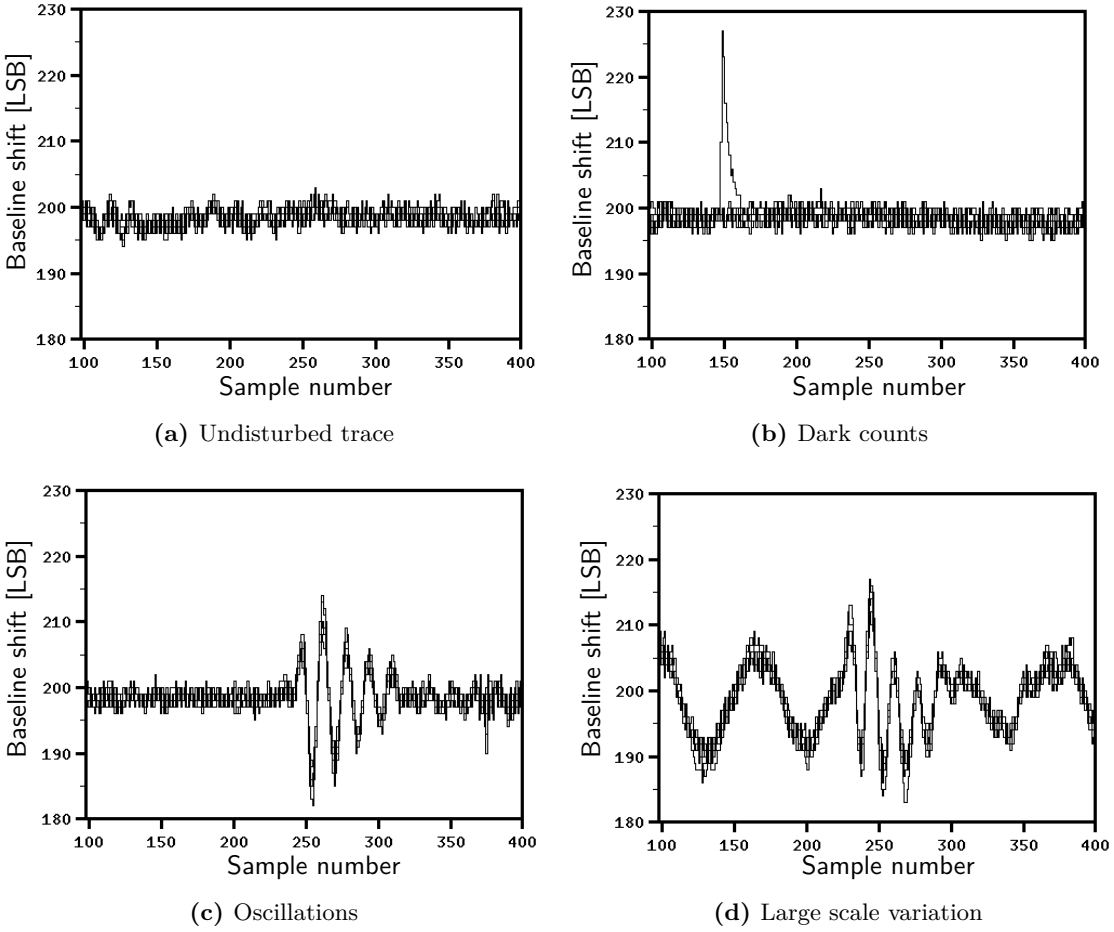

(a) Undisturbed trace

(b) Dark counts

(c) Oscillations

(d) Large scale variation

Figure 2.6 Trace types expected during a dark count measurement. Besides undisturbed traces (a), there can be signals of electrons generated by thermal noise (b), oscillations (c) or large scale variations (d). While most of these effects are reduced by averaging and baseline subtraction, the large scale variations add to the systematic error of the trace mean value and are rejected.

However, in some traces p.e. signals are detected by the PMTs even with the light beam blocked (see 2.6b). These events can either be due to photons that enter the dark box or to electrons that are produced inside the PMT material by thermal noise and then amplified as a signal p.e.. Their number add up to approximately 100 signals per dark measurement.
The number of p.e. in an illuminated measurement can be roughly estimated from the integrated area of a single electron peak at a specific PMT high-voltage and the measured baseline shift. Due to the low UV intensity of the Xe lamp, the lowest light intensity of this setup is measured at 250 nm where the ratio of dark electron signals to real p.e. at 1200 V is 10%. For higher intensity the percentage is smaller. Furthermore, as the number of random electron productions is approximately the same for all measurements, subtracting a mean dark baseline from all data will highly reduce the influence of those electron signals.

Oscillating distortions occur in some traces (see Figure 2.6c) and disturb the mean value calculation if they are not fully contained inside a trace. Their origin is not fully understood, however, they became less prominent after exchanging the PDP module. The new PDP module had a revised board layout and improved grounding. If a large number of traces is recorded, the effect of partly contained oscillations should average out.
Other traces show extensive large scale variations that lead to an error in the determination of the baseline shift especially at low light intensities as shown in Figure 2.6d.
The main purpose of the noise reduction described here is to reject the traces with large scale variations. This can be done by means of read-out channels of PMTs that are not used for the light detection. It is found that the baseline oscillations as well as large scale variations occur in the same samples of a trace in all channels independently of the HV settings. When comparing the minimum of a trace from a PMT with HV applied and the minimum of a HV-less PMT trace, a correlation is visible as shown in Figure 2.7. From this correlation a noise reduction algorithm is established to reject all traces for which one of the HV-less channels has a trace minimum that deviates more than 4 LSB from its zero baseline value. This way, traces with large distortions are excluded and the error on the mean value is decreased.

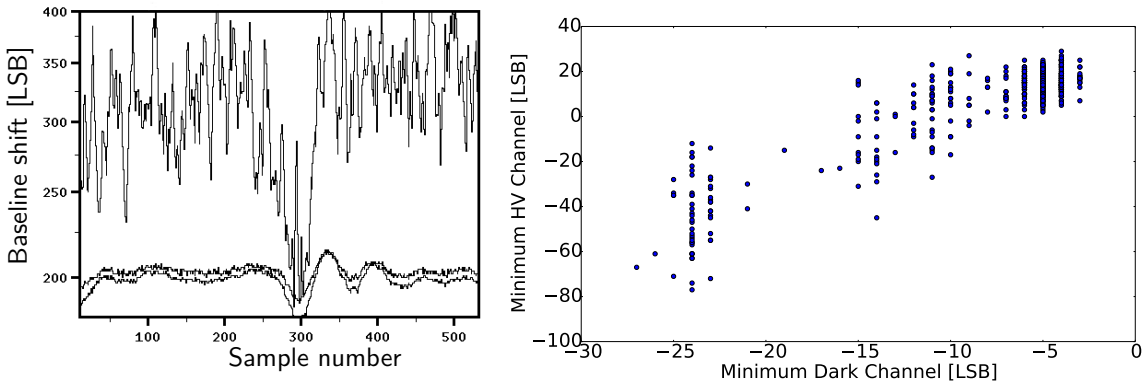

(a) Example trace **(b)** Correlation of minima

Figure 2.7 Correlation of noise features in PMT traces with and without HV applied. (a) Traces of two HV-less channels at 200 LSB and one HV channel at a higher baseline show a trace distortion at the same sample number. (b) The mimima of the traces of all HV-less channels and the minima of the traces of an HV channel are correlated. This is used for noise reduction.

2.3 Performance verification of the test system

Performance tests of all basic components of the test system have been performed to ensure the full functionality and the reliability of its results. These tests include

- Stability and homogeneity of the generated light field
- Accuracy of the monochromator
- Accuracy of baseline determination
- Linearity of the PMT-amplifier system.

Uncertainties and systematics found in these measurements that could influence the results of the system are also discussed.

2.3.1 Properties of the Xe lamp and the monitoring diode

As the results of the test system depend on the intensity of the light measured for a specific setup setting, the stability of the Xe lamp must be verified. For this purpose, the light intensity is measured over time with the reference diode at the integrating sphere at a wavelength with high initial light intensity. Two main features of the time variability are found. First, during a warm-up time of approximately 30 minutes the light intensity increases by 50% before reaching the stable configuration used during the measurements.
The light intensity after warm-up is shown in Figure 2.8. At 439 nm, an average value of $6.85{\cdot}10^{-8}\,\mathrm{W/cm^2/s}$ is found. Over a monitoring time of 1000 s, the intensity profile shows two types of variabilities. Small scale variations of the order of 0.6% between maximum and minimum output as between 300 s and 400 s are due to the reference diode measurement uncertainty. This uncertainty is included in the error calculation of the setup results.
The large scale variability within 2% is attributed to the actual Xe lamp and probably due to the internal heating cycle of the lamp. To minimize the influence of the Xe lamp variability on the results of the test system, the lamp output is monitored during component measurements and the results normalised to the monitoring values as described before. This process ensures Xe lamp independent light component measurements.

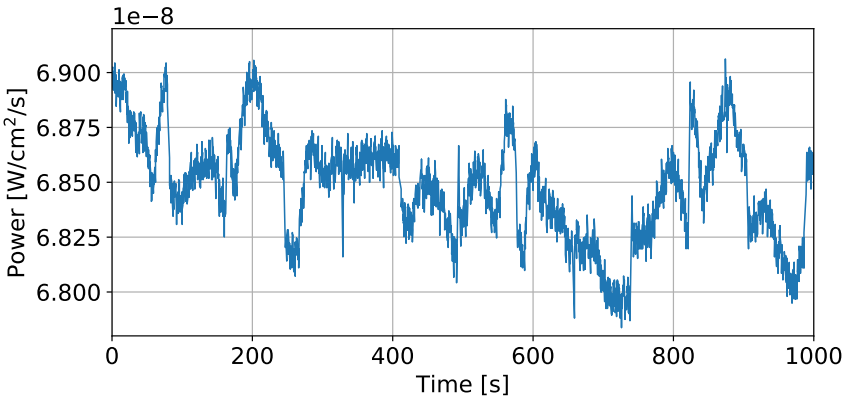

Figure 2.8 Time variability of the Xe lamp at 439 nm. During a measurement time of 1000 s the lamp output is stable within 2%. This includes variability of the actual lamp and measurement uncertainties of the monitoring diode.

2.3.2 Accuracy of the monochromator

A monochromator is used to select specific wavelengths. After mounting the device and aligning the Xe lamp, it was ensured that the wavelength selection of the monochromator works correctly. To do so, the monochromator is set to wavelengths between 250 nm and 800 nm in steps of 50 nm and the output of the fiber connected to the monochromator exit is measured with a JAZ handhold spectrometer. The measured spectral shape is Gaussian with a one sigma width of 5 nm (see e.g. Figure 2.9a). Hence, a step size of 5 nm is chosen for all future measurements. Otherwise, the mean value of the wavelength peak is a reliable measure of the selected wavelength with only an offset of 0.1 nm (see Figure 2.9b).
In measurements above 700 nm a second peak appeared beside the main peak in the reference spectrometer image. It is positioned at half the selected wavelength and increases in intensity with wavelength from 1% of the main peak at 700 nm to 86% at 800 nm as shown in Figure 2.9c

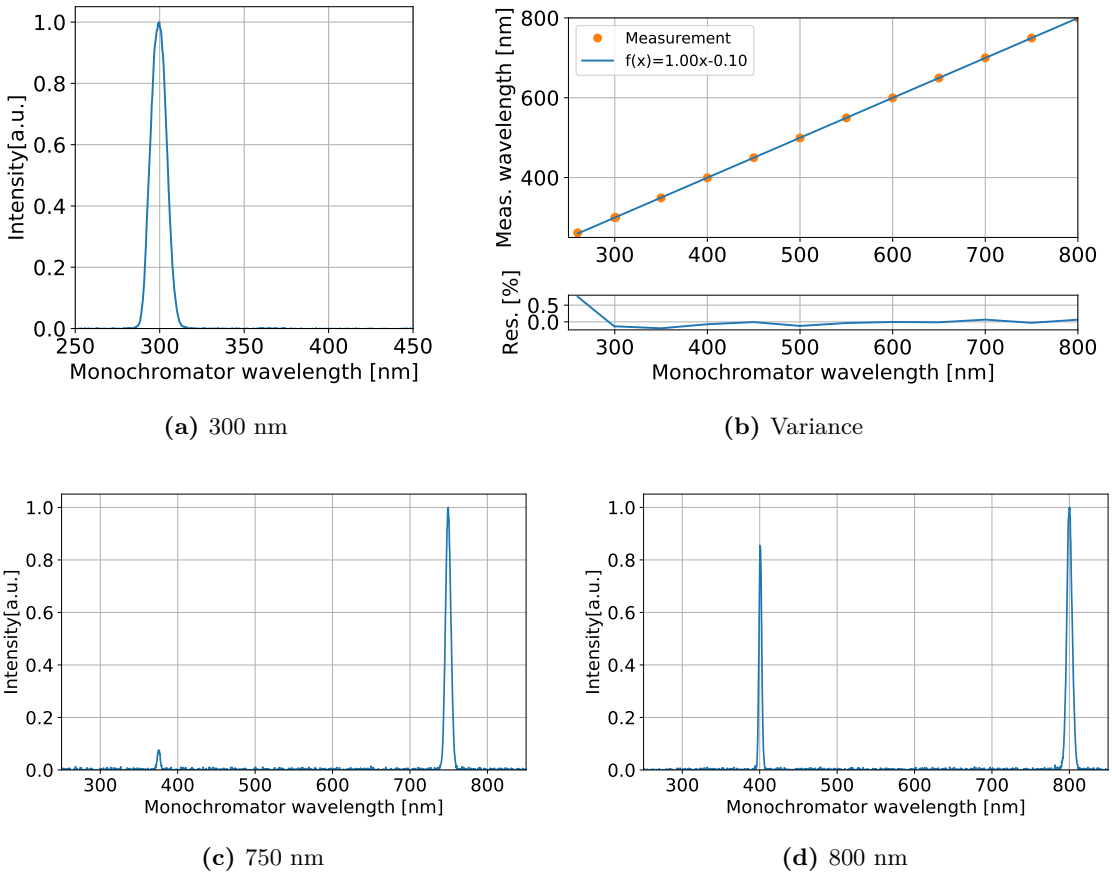

(a) 300 nm

(b) Variance

(c) 750 nm

(d) 800 nm

Figure 2.9 Output of the monochromator measured with a spectrometer at different wavelengths. (a), (c) and (d) The measured Gaussian profiles at have an average one sigma width of <5 nm. (c) and (d) At higher wavelength a second peak appears at the half the set wavelength with increasing intensity. This is an artefact of the reference spectrometer and does not influence the measurements. (b) Set and measured wavelength have an offset of only 0.1 nm.

and 2.9d. Reference measurements using the calibrated photo diode and a 420 nm coloured glass longpass filter show no systematic decrease in light intensity for higher wavelength as would be expected from the suppression of a second peak with increasing intensity. The additional peak is hence considered an artefact of the handheld spectrometer.
The wavelength selection of the monochromator drifted over a period of several months due to ageing of internal components and was calibrated with a longpass filter of known spectral shape every few months. A wavelength accuracy of <3 nm was ensured at all times.

2.3.3 Light field of the integrating sphere

The optical fiber couples the monochromator output into an integrating sphere. To test the homogeneity of the sphere's output beam, a photo diode is attached to a robot arm (Universal Robots, UR5) and moved around the sphere exit port in spherical shells with different radii (see Figure 2.10). The light intensity distribution found at a radius of 63 cm is shown in Figure 2.11. It is highest opposite the spheres exit port at 0° and decreases slowly for higher angles as light is blocked by the walls of the sphere housing. Within 5° the intensity decreases by 2%, within 10° by 5% and by a maximum of 9% over the full measured area.

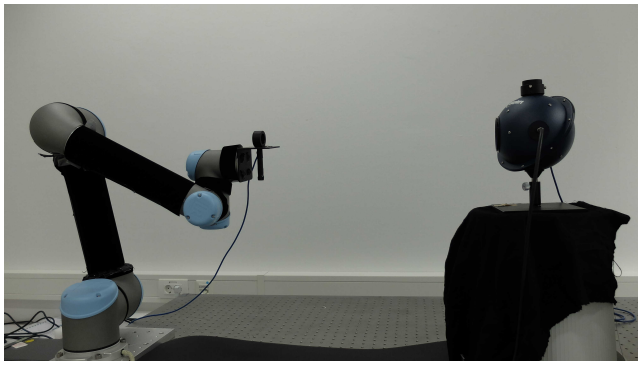

Figure 2.10 Robot arm setup to measure the homogeneity of the integrating sphere output. The calibrated photo diode is mounted on a robot arm that moves around the sphere's output port in spherical shells.

The PDP module of the test system is mounted opposite of the sphere's output port at a distance of 270 cm and occupy the central ±2° region of the light field. Inhomogeneities of this central region are within 0.4%.
As the PMTs are not positioned on a spherical shell but are vertically aligned an additional flux variation of 0.06% is expected between the highest and lowest PMT compared to the central PMT. This latter effect is neglected in the following.

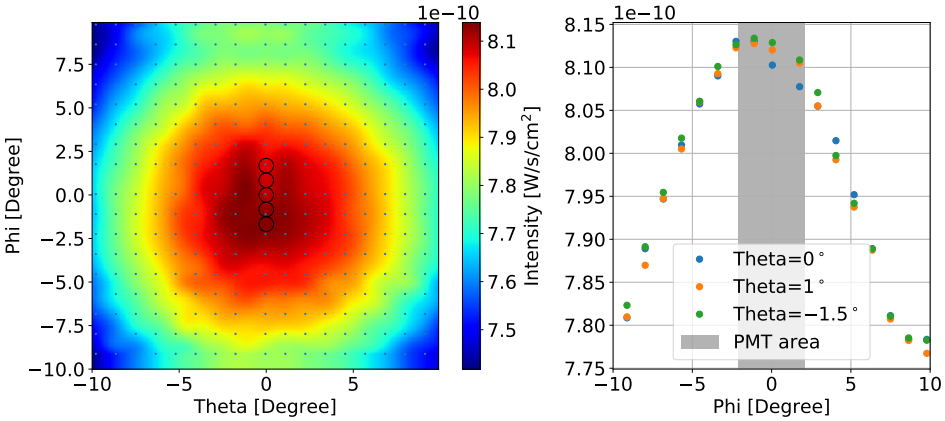

Figure 2.11 Intensity distribution of the integrating sphere output measured at a distance of 63 cm from the light source. The small dots in the left plot corresponds to the actual measurement positions while values inbetween are interpolated. The five black circles indicate the positions of the PMTs. On the right side slices at fixed ϑ values are compared. In the central region of ±2° where the PMTs are positioned the variations are within 0.4%.

The FlashCam PMTs are designed to detect very faint light sources. While this is necessary for the camera to observe Cherenkov air showers, the PMTs can be damaged by bright light. FlashCam can be operated up to a p.e. rate of 3 GHz/pixel where the probability of generating one p.e. by one incident photon depends on the quantum efficiency. Before applying high voltage to the PMTs in the test system it is thus crucial to determine the light intensity at the position of the rotation table to prevent damage on the sensitive devices. As the flux at this distance is too low to be measured with a photo-diode, the light field closer to the source needs to be measured and understood to predict the intensity at the PMTs.

Close to the integrating sphere, near-field effects influence the created light field. Only after a certain distance will the light intensity follow a regular r^{-2} behaviour expected for a simple point source. To determine this distance and the constant of proportionality, the intensity is measured at distances of 0 cm to 100 cm from the sphere at a wavelength of 530 nm.
In addition, a Geant4 (Agostinelli et al., 2003) Monte Carlo simulation of the integrating sphere is performed. Only a plain sphere with an exit port is simulated neglecting additional ports or internal structures and the inner surface is treated as a perfect Lambert emitter (Lambert, 1760). The photo diode is simulated as a circular plane with a radius of 0.56 cm corresponding to the sensitive area of the diode. Following Lamberts law the intensity emitted by each area element of the sphere is proportional to the cosine of the emitting angle ϑ

$$I(\vartheta) \propto \cos(\vartheta). \tag{2.1}$$

Photons that reach the simulated photo diode are weighted with the cosine of their emission angle to the inner sphere surface following Equation 2.1 and summed up.
The scaled result of the simulation is compared to the measurement in Figure 4.17. An ar^{-2} fit on the measurement data at r >30 cm results in

$$f(r) = \frac{8.93 \cdot 10^{-7}}{r^2} \frac{\mathrm{W}}{\mathrm{cm^4 s}}. \tag{2.2}$$

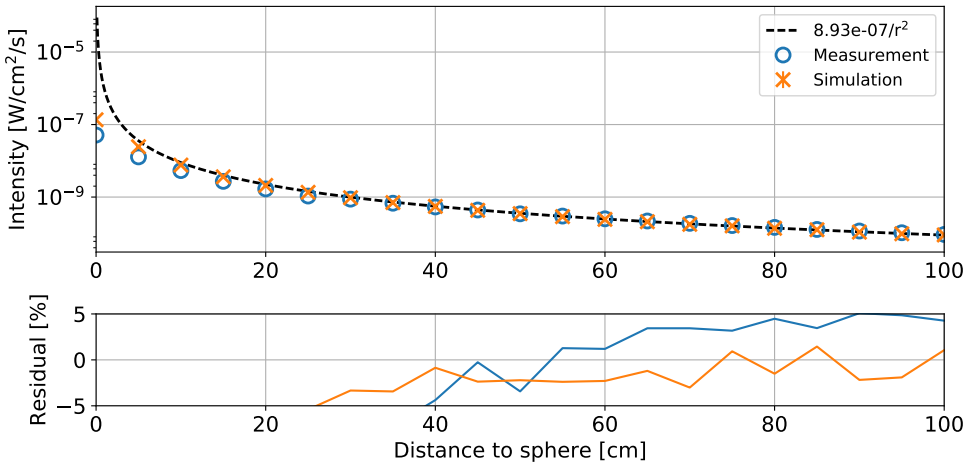

Figure 2.12 Distance dependent measured and simulated intensity profile of the light emitted by the integrating sphere. Close to the sphere the behaviour deviates from a simple r^{-2} fit as the inner geometry of the sphere has to be taken into account. Above 40 cm the intensity follows the expected point source behaviour and both measurement and simulation matches within 5%.

At small distances, simulation and measurement diverge from the applied fit due to near-field effects as the inner structure of the sphere becomes important. Photons cannot be reflected from the reference port, and the baffle, positioned in front of the entrance port, has a different distance to the diode than the sphere walls, so reflected photons have a different intensity.
At distances larger than 40 cm the fit function matches the measurements as well as the simulation within 5%. In the test system, the distance between the PDP module and the light source is 2.70 m. Following Equation 2.2 the intensity at the PMTs is $1.22 \cdot 10^{-11}\,\mathrm{Wcm^{-2}s^{-1}}$ for 530 nm photons. With the FlashCam quantum efficiency of 15.3% at that wavelength and a pixel size of 11.95 $\mathrm{cm^2}$, the expected p.e. rate is with $61.6 \cdot 10^6$ p.e./pixel/s still below the intensity criteria of 3 GHz/pixel. The flux at 400 nm will be about a factor 2 higher, however, there is no danger expected for the sensitive PDP module due to high fluxes.

2.3.4 Dark current and baseline precision

For a good signal-to-noise ratio, dark currents inside the dark box must be low. With the reference diode attached to the integrating sphere and the PMTs the remaining light level is measured while the entrance of the monochromator is blocked.
The intensity determined by the reference diode looking inside the integrating sphere corresponds to the mean light level inside the box. Values taken regularly during a period of about two months are shown in Figure 2.13. On average, the dark current within the box is $(1.10 \pm 0.82) \cdot 10^{-12}$ A. The intensity of the Xe lamp is smallest at 250 nm. At this wavelength, a mean current of $6.49 \cdot 10^{-10}$ A is found which is a factor 590 higher than the noise level. Near the peak intensity at 400 nm, an intensity of $7.33 \cdot 10^{-9}$ A is reached, a factor over 6000 larger than the noise. The Xe lamp monitoring is hence done with a very high signal-to-noise ratio and is considered undisturbed by the dark current in the box. Nevertheless, the dark current is recorded prior to each measurement and subtracted from the monitoring values.

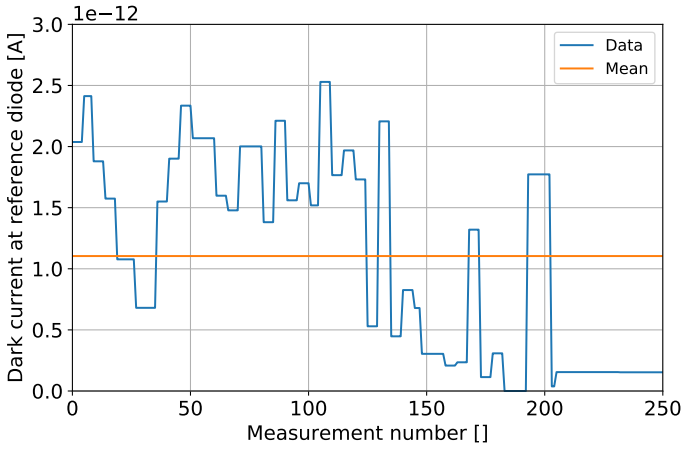

Figure 2.13 Dark measurements taken during a period of two months by the reference diode at the integrating sphere inside the dark box. The mean dark current is $1.10 \cdot 10^{-12}$ A.

The PMT measurement with blocked light source tests for direction dependant light incidence. A dark baseline reference value is recorded, before the light level is measured while rotating the PMTs between ±35°. Afterwards, the reference value recorded previously is subtracted. The results of the five vertically aligned PMTs can be found in Figure 2.14.
No significantly increased flux in any direction is visible, the dark box is thus considered light tight. The mean baselines of the different PMTs vary between ±0.2 LSB probably due to small variations in the high voltage settings of each PMT. To correct for this effect a dark baseline value is recorded and subtracted for each measurement run.
Another parameter can be deduced from this measurement. If the light level in the box is independent of the direction, the data shown in Figure 2.14 can interpreted as a timeline of a repeated measurement of the light level. The variations within each PMT measurement of typically ±0.1 LSB corresponds to the zero baseline determination. The lowest measured baseline shift of this setup is 0.7 LSB at 250 nm. A zero baseline uncertainty of 0.1 LSB corresponds to a 14% uncertainty in the light intensity determination. For wavelengths around the peak quantum efficiency, the error decreases to about 0.3%. The 0.1 LSB baseline uncertainty is included in the error calculation of the PMT light intensity measurements.

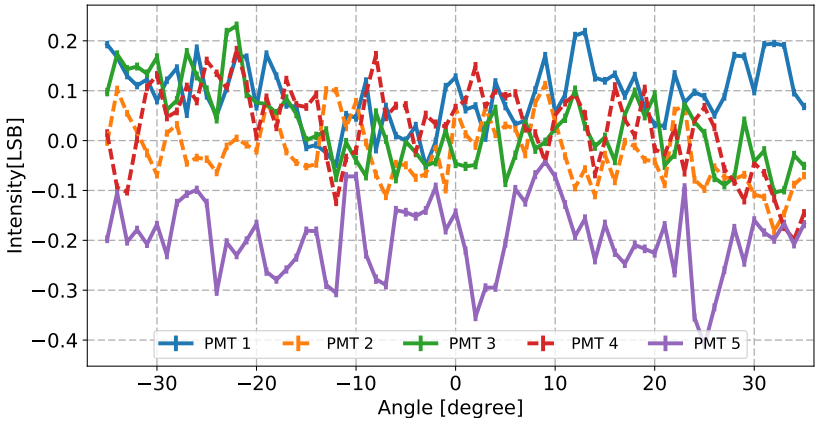

Figure 2.14 Dark measurements taken with the PDP module. The different curves corresponds to different positions on the PMT module from top to bottom. No direction dependent noise is measured. The baseline precision of the PMTs is within ±0.1 LSB.

2.3.5 Linearity of the PMT-amplifier system

At high photon fluxes and large high voltages the preamplified readout of the PMTs can become non-linear. To check if the experiment is run in an appropriate flux range, the light level measured by the PMTs is cross-checked with the incidence light level measured by the reference diode. The linearity of the reference diode is ±0.5% (see Table 2.1).
As the baseline shift for measurements with light concentrators is higher than with PMTs only, light concentrators are attached to the PDP module (a detailed description of light concentrators is given in Chapter 3). Furthermore, the PMTs are set to a high voltage of 1400 V. This corresponds to the maximum setting allowed by the PMT safety control for this setup. At higher voltages the light intensity will cause the high voltage of the PMTs to shut down automatically to prevent damage. The measurement is performed at 400 nm.
The intensity is increased slowly by opening an iris diaphragm placed in front of the monochromator exit and the baseline shift as well as the reference diode value are recorded. For reproducibility and possible hysteresis effects, the measurement is repeated with slowly closing diaphragm and falling intensity. The results of this linearity test are similar for all five vertically aligned PMTs. An example plot for the central PMT is shown in Figure 2.15. Data between 5 and 100 LSB baseline shift is fitted with a linear function and residuals are given in the lower panels in significance σ and per cent.
It can be noted that the linear fit has a non-zero offset even including fit errors. This offset varies between ± 3.5 LSB for the different PMTs. The origin of this offset is not known but suggests an uncertainty of the baseline determination that is larger than the baseline uncertainty found in the previous section. An improved baseline noise reduction algorithm is needed to gain a better understanding of the baseline shift at low intensities. In the following no claims are made for results based on baseline shifts below 5 LSB.
At baseline shifts larger than 120 LSB the data starts to deviate from the linear fit with residuals increasing slowly up to 10 σ or 5% at the highest intensities. This corresponds to the known non-linearity of the PMTs at high p.e. rates.
For the typical measured baseline shifts of the setup between 5 LSB and 100 LSB the output of the PMT-preamplifier system is linear within ±σ and no hysteresis effect is visible.

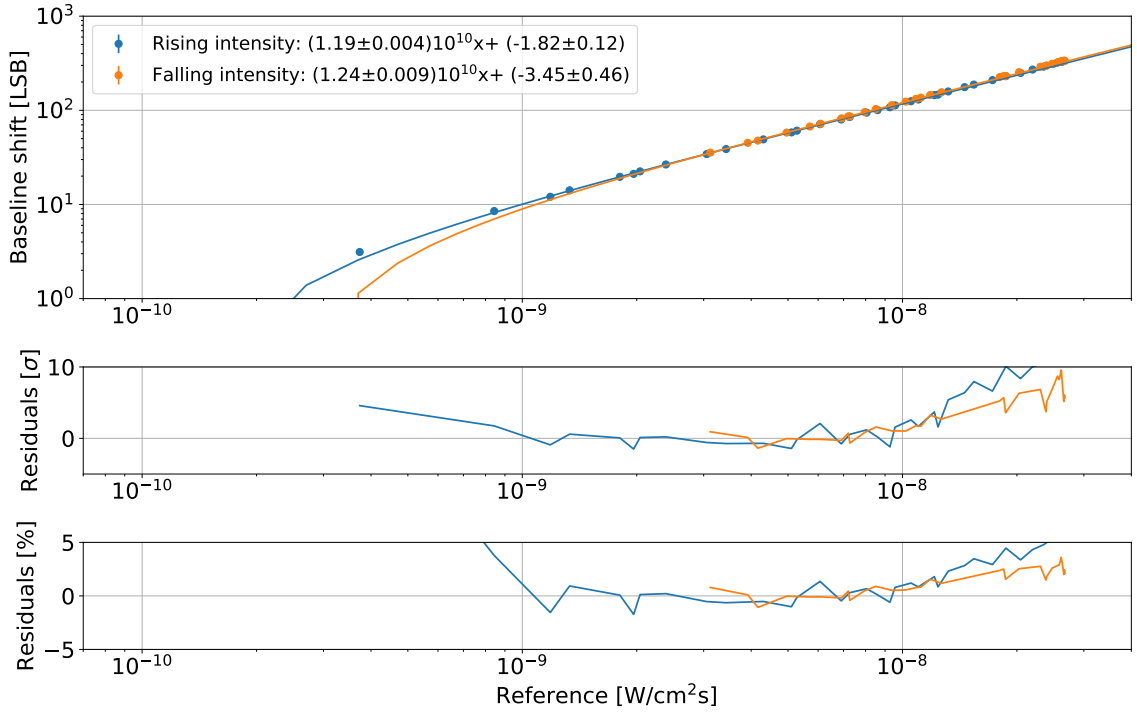

Figure 2.15 Linearity of the readout of the central PMT with respect to the reference diode. The PMT readout is linear over a large range of baseline shifts apart from an offset probably due to baseline noise. For baseline shifts above 120 LSB the PMT readout starts to become non-linear. The residuals are given in significance σ and in per cent.

From this chapter it is concluded that the performance of the described test system enables accurate optical component testing. The light source was confirmed to provide a homogeneous and predictable light field at the location of the PMTs. Uncertainties in the homogeneity are small, with a maximum of 0.4%. The light level of the Xe lamp setup is high enough to guarantee a good signal-to-noise ratio while being low enough not to damage the sensitive PMTs. For the monochromator a wavelength precision of < 3 nm was ensured during operation. The PMTs are operated in their linear range over the whole relevant wavelength range and intensity spectrum apart from the lowest intensities with a baseline precision of 0.1 LSB. The small uncertainties introduced by the baseline precision and the monitoring diode are included in the error calculation in the following. The error calculation in this work is based on the Python *uncertainties* package by Lebigot (2010).
This test system is especially optimised to measure the characteristic properties of light concentrators such as the wavelength-dependent reflectivity of their coatings or their angular acceptance profile. It is used in the next chapter to measure and compare light concentrators with three different prototype coatings for the use in FlashCam.

"Always look on the bright side of life"
Monty Python, *Always look on the bright side of life*, 1979

CHAPTER 3

Characterisation of light concentrators

Light concentrators increase the sensitive area of Cherenkov cameras by decreasing dead-space between pixels. Simultaneously they cut night sky stray-light that is backscattered from ground or the telescope structure. The concept of light concentrators used in current IACT experiments is based on the principle of Winston cones (Winston et al., 2005). A schematic drawing is shown in Figure 3.1.

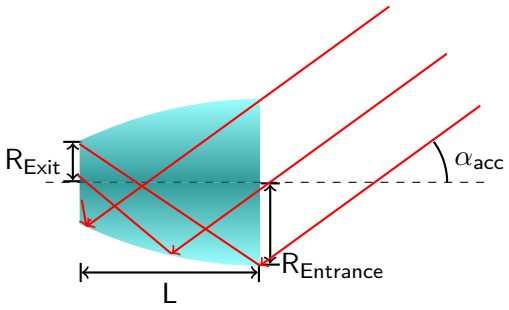

Figure 3.1 Light concentrator principle. Light entering the concentrator under an angle smaller than the acceptance angle α_{acc} is guided to the exit due to reflections on the inner surface. Light from larger angles is rejected to reduce stray light from outside the telescope mirrors. Image taken from Pürckhauer et al. (2017)

The geometrical form of light concentrators must be optimised for the application on a specific telescope. The angular light distribution on the camera that is expected from the mirrors depends on the diameter and form of the mirrors, the distance between mirror and camera and the arrangement and size of the pixels in the camera. Thereby, the form of the light concentrators must ensure to collect light from all angles under which light can be reflected from the mirror and to reject any light from larger angles as this adds to the background noise. For the MSTs, the geometry designed is optimised by Henault et al. (2013).
FlashCam features 1758 PMT pixels arranged in a 50 mm hexagonal grid. Each hemispherical PMT cathode has an outer diameter of 39 mm. In this grid this creates 45% of dead space between the pixels as clearly visible in Figure 3.2a. Hexagonal light concentrators with an outer flat-to-flat entrance diameter of 50 mm and a wall thickness of 0.5 mm provide the densest configuration and can reduce this dead-space to 4% (see Figure 3.2b).

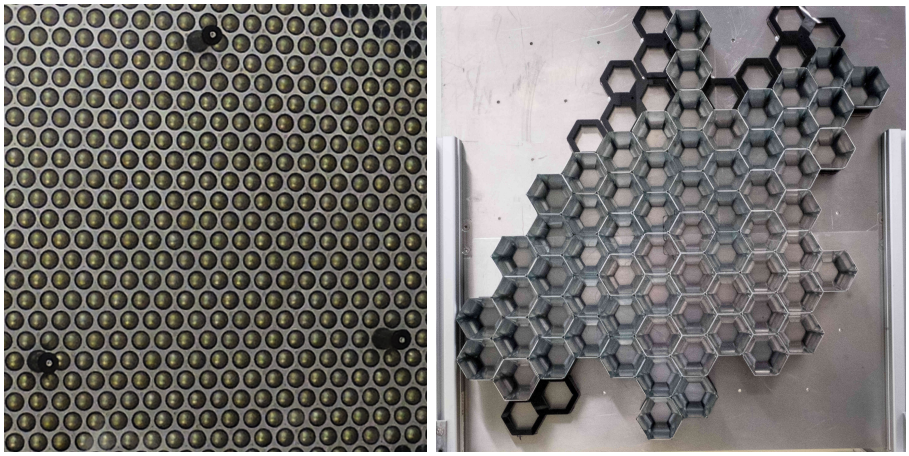

(a) Zoom of the PDP **(b)** Light concentrator configuration

Figure 3.2 Dead space minimisation by means of light concentrators. (a) On the FlashCam PDP dead space is visible inbetween the round PMT pixels where no light is detected. (b) The dead space is highly reduced by hexagonal light concentrators mounted with the 50 mm grid spacing on an aluminium plate for testing. The only remaining dead space is on the thin rims of the concentrators.

The exit window of the concentrator geometry is also designed to be hexagonal with a smaller outer flat-to-flat diameter of 25 mm. The reflective inner surface of the concentrators guides light that enters the concentrator under an angle smaller than an acceptance angle α_{acc} to the exit window. Light from larger angles is blocked by the outer geometry of the concentrator or reflected back outside by the inner surface. This behaviour is achieved by the parabolic form of each of the six segments of the hexagonal light concentrator. The parabola is defined by the Edge-ray principle described by Winston et al. (2005). Following this principle, the relation between height z of the concentrator and its flat-to-flat radius r is

$$\begin{aligned} 0 &= (rC + zS)^2 + 2R_{\text{Exit}}r(1+S)^2 - 2R_{\text{Exit}}zC(2+S)^2 - R_{\text{Exit}}^2(1+S)(3+S) \qquad (3.1)\\ S &= \sin\alpha \\ C &= \cos\alpha \end{aligned}$$

where α is the maximum input angle and R_{Exit} the exit radius of the concentrator. For the light concentrator design used for FlashCam a maximum input angle of $\alpha = 29.5°$ and an exit radius of $R_{\text{Exit}} = 12.2\,\text{mm}$ were chosen. The necessary entrance radius of $R_{\text{Entrance}} = 24.5\,\text{mm}$ is then reached at a height $z = 53\,\text{mm}$. With the geometry of the light concentrators fixed, the two light concentrators parameters crucial to ensure their functionality are the reflectivity of the inner coating and the reflectivity-dependent shape of the angular acceptance curve.
One goal of this work is to characterise three light concentrator prototype coatings from two different manufacturers. An Ultem® polyetherimide structure manufactured by Savimex forms the concentrator geometry and serves as support material for the coatings. Beside the geometrical support structure, Savimex contributes two coatings: a single layer aluminium coating (S) and a boosted multilayer aluminium coating (SB). The second manufacturer BTE provides a sputtered aluminium coating (BTE). All coatings have an additional protection layer of silicon oxide on top of the sensitive layers. The properties of the three coatings are summarised in Table 3.1 and a picture of sample light concentrators is given in Figure 3.3.

Table 3.1 Summary of the light concentrator coating types characterised in this work with a description of each coating and the number of concentrators tested per type.

Manufacturer	Name	Coating	Number of tested concentrators
Savimex	S	single layer aluminium + SiO_2	18
Savimex	SB	multi-layer aluminium + SiO_2	29
BTE	BTE	sputtered aluminium + SiO_2	27

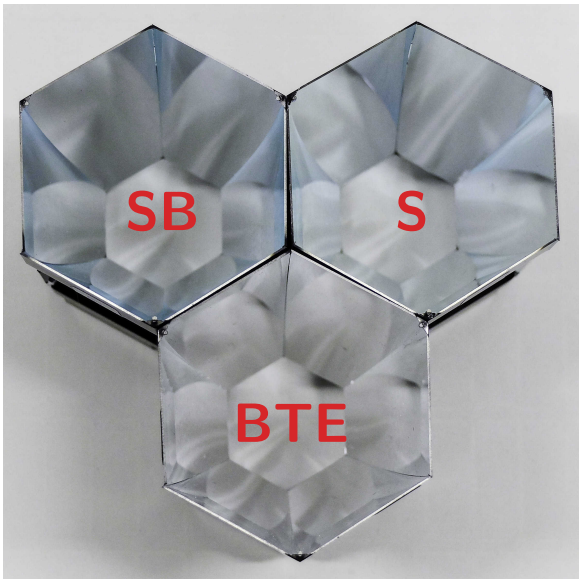

Figure 3.3 Sample light concentrators with different coatings seen from above. While the geometry is equal for all concentrators, the color of the Savimex coatings appear to be slightly bluey while the BTE coating is more silvery.

3.1 Measurement principle for light concentrators

To characterise light concentrators in the optical component test system, five concentrators can be attached to the five vertically aligned PMTs for simultaneous measurements. For the hexagonal FlashCam light concentrators special fixation were developed that can hold three concentrators, each (see Figure 3.4a). With three wings on the side of the exit window, the concentrators can be secured at the corners of the hexagonal structure so that the concentrators are aligned in a triangle as shown in Figure 3.4b. The fixations can then be screwed to the front of the PDP holder. With the fine adjustment screw the distance between light concentrator exit and PMT surface can be set. For FlashCam the nominal distance is 1 mm. To determine the efficiency of the light concentrators, measurements with light concentrators attached to the PMTs will be compared to measurements taken without. For comparability a mask can be installed in front of the PDP module to reduce the effective area of each PMT to the hexagonal area of the light concentrator exit window. This mask is shown in Figure 3.5. For measurements with light concentrators the PDP holder is positioned on the rotational stage so that the entrance windows of five concentrators are level with the rotation axis as shown in Figure 3.4. For measurements without concentrators the module is shifted forwards so that the mask is level with the rotation axis. This way the distance of the light source to the rotation center stays the same for mask and concentrator measurements.

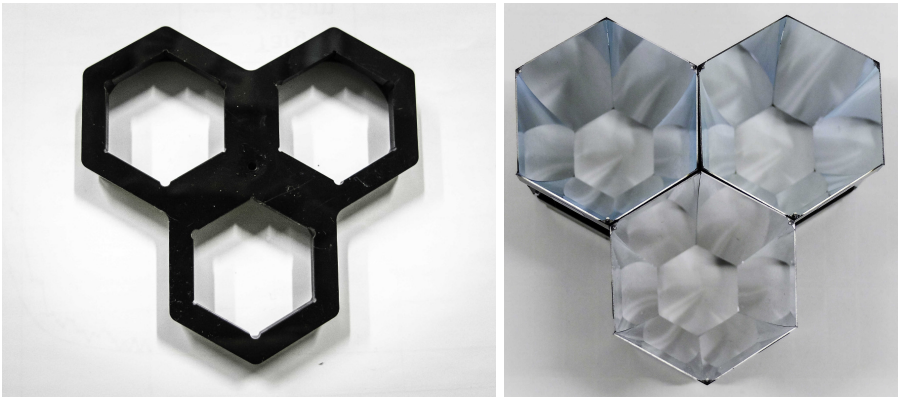

(a) Empty **(b)** Filled

Figure 3.4 Fixation for light concentrators. (a) Three light concentrators can be mounted in one fixation and are secured in place by means of the small indentations at the corners of the hexagonal structure. (b) If three light concentrators are installed their outer edges are almost perfectly aligned.

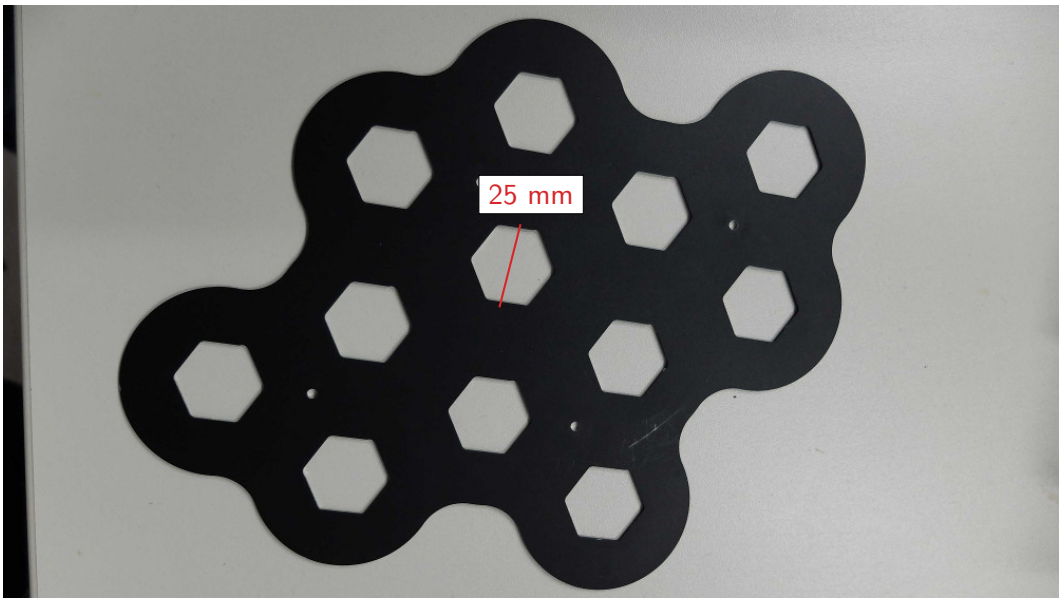

Figure 3.5 Hexagonal mask as reference for the light concentrator measurements. The mask restricts the effective area of the PMTs to the size of the exit window of the concentrators. This way measurements with and without light concentrators remain comparable.

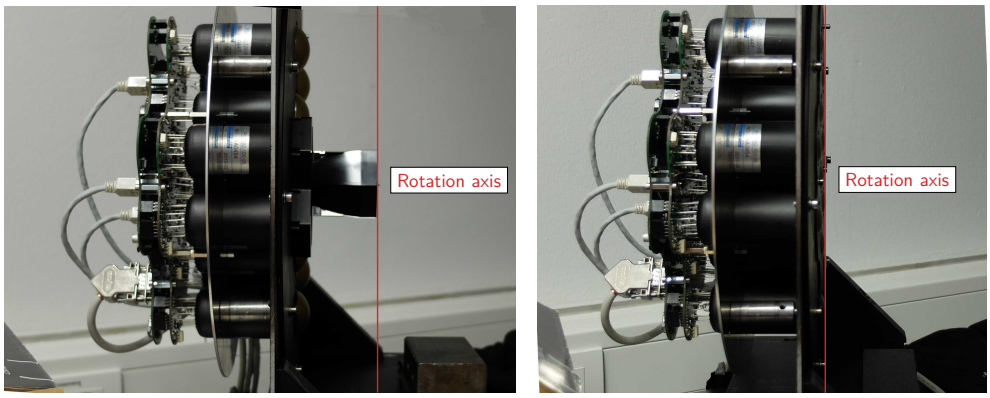

(a) Light concentrator **(b)** Reference mask

Figure 3.6 Positioning of the PDP module on the rotational stage. (a) For concentrator measurements the module is shifted backwards so that the concentrator entrance window is level with the rotational axis. (b) For reference measurements the module is shifted forwards so that the hexagonal mask is level with the rotational axis.

For measurements of the light concentrators' angular acceptance curve a dark measurement is performed at the zero position of the rotational stage where the entrance plane of the light concentrator is parallel to the integrating sphere output port. Afterwards, the light beam is unblocked and the main measurement is performed by moving the stage motor in steps of one degree from 35° to −35°. Measurements are taken at the five wavelengths 285 nm, 320 nm, 355 nm, 390 nm and 495 nm. Here, 285 nm and 320 nm are wavelengths on the rising edge of the Cherenkov spectrum but also of the QE (low detection rate, low Cherenkov flux), 355 nm and 390 nm correspond to wavelengths in the peak range (high detection rate, high flux) while 495 nm is already on the falling slope (low detection rate, low flux). By analysing measurements at these wavelengths a good understanding of the angular acceptance over the full Cherenkov regime is achievable.
A spectral behaviour measurement grants information about the reflectivity of the coatings. As for the angular dependent measurements, a dark measurement is performed at the zero position of the rotation stage before the main measurement is taken at the same stage position while the monochromator selects wavelengths between 250 nm and 800 nm in steps of 5 nm. Afterwards, the spectral measurement is repeated with the hexagonal mask.
The light spectral measurement is normalised to the reference mask measurement for each wavelength while the angular acceptance measurement is normalised to the reference value corresponding to the wavelength at which the angular measurement is taken. As the change of the light field due to rotation is hence not taken into account, all values are further normalised to the cosine of the rotation angle. This way the optical gain of the light concentrator in comparison to the mask measurement is calculated.

3.2 Simulation of light concentrators

To verify the results of the light concentrator measurements as well as to study further characteristic properties, a simulation is performed with the ray-tracing code ROBAST (Okumura et al., 2016). With this code it is possible to simulate the geometrical shape of light concentrators with the reflectivity of the coating as free parameter and to follow the path of photons through this given geometry.

3.2.1 Simulated light concentrator setup

The simulated light concentrator geometry follows the geometry described in the introduction of this chapter. With the build-in ROBAST function *AGeoWinstonConePoly* an n-sided polygon with a given entrance and exit radius and a parabolic inner surface following Equation 3.1 can be created. An illustration of the simulated geometry is shown in Figure 3.7. Choosing a z-axis for the concentrator along its height, two rotation axes are defined: A *concentrator rotation axis* parallel to the z-axis and a *light rotation axis* perpendicular to it. As the width of the light concentrator in the light rotation direction varies depending on the concentrator rotation, the width of the angular acceptance curve will also be influenced by this latter rotation. In the following two extreme cases are analysed. In the *edge configuration* the concentrator is rotated in a way that the light rotation axis is orthogonal to two flat sides of the hexagon, in the vertex configuration the concentrator is rotated by 30° so that the light rotation axis connects two corners. The two rotations together with the corresponding light rotation axes are shown in Figure 3.7d and 3.7e. The broadest angular acceptance is expected for the edge configuration due to the largest effective radius from corner to corner with respect to the shortest effective radius between two flat sides in the vertex configuration.

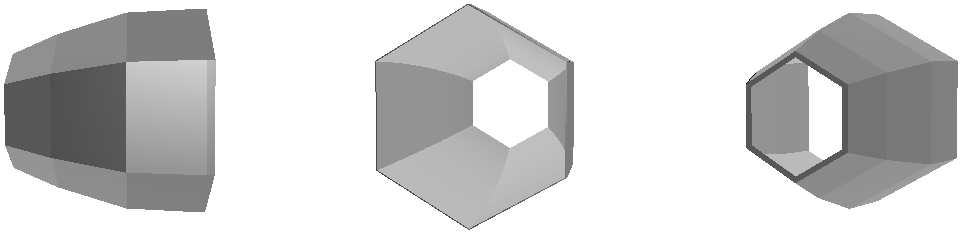

(a) Side view **(b)** Front view **(c)** Rear view

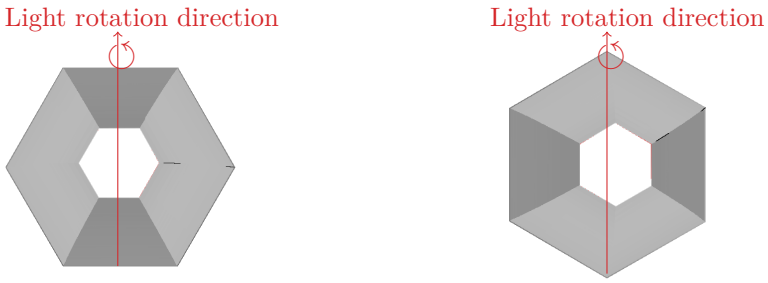

(d) Edge configuration **(e)** Vertex configuration

Figure 3.7 Simulated light concentrator geometry from different viewing angles. The inner surface follows Equation 3.1. Two main rotational configurations, edge and vertex, will be analysed, which are rotated to each other around the concentrator height axis by 30°.

For the ray-tracing, a wavelength dependent reflectivity of the light concentrator material can be defined. To simulate the angular acceptance as closely as possible to the measurements, for each coating type the average reflectivity found in the spectral measurements at the zero position of the rotational table will be used.

For the light detection a PMT is simulated corresponding in geometry to the PMTs used in the laboratory test system. This PMT consists of three parts: A glass window that protects the sensitive parts of the PMT, the actual sensitive cathode as well as a rear part containing the dyodes and other electronic components of the PMT. Both glass window and cathode are hemispherical with a curvature radius of 21 mm and 20 mm and a radius of the circular base of 19.8 mm and 15 mm, respectively. The rear part of the PMT is simulated to prevent photons from entering the PMT geometry without passing through the light concentrator. Its geometrical form is a tube with an inner radius of 15 mm, an outer radius of 19 mm and a length of 20 mm. A distance of the nominal 1 mm is chosen between the light concentrator exit an the PMT glass window.
Additionally, a cover shield is placed around the light concentrator to suppress stray photons. Both, PMT rear part and cover shield are simulated as non-reflective materials in order to exclude any further effects of backscattered photons. A full sketch of the simulated setup is displayed in the upper panels of Figure 3.8 for the vertex configuration.

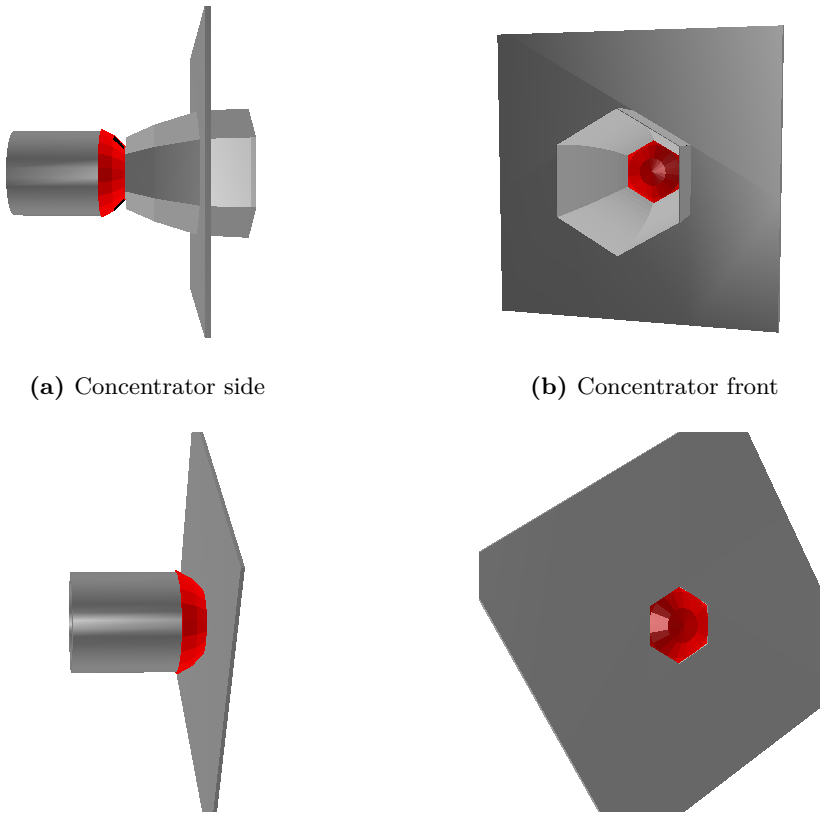

(a) Concentrator side **(b)** Concentrator front

(c) Reference mask side **(d)** Reference mask front

Figure 3.8 Full simulated setup of light concentrator, reference mask and PMT for the vertex configuration. (a) and (b) The light concentrator setup includes the light concentrator, the PMT as well as a protection shield for stray light. (c) and (d) The reference mask setup is used for normalisation.

Corresponding to the laboratory measurement, apart from the light concentrator, also the reference mask is simulated. A 36 cm^2 big plate of 1 mm thickness is created with a hexagonal opening matching the form of the exit window of the light concentrator and placed in front of the PMT (see lower panels of Figure 3.8). Both, light concentrator and reference mask can be rotated arbitrarily around the concentrator rotation axis.

As a particle source a circular source plane is created with a radius of 6.35 cm, corresponding to the integration sphere exit. Contrary to the laboratory setup, the position of the light concentrators is keep stable while the source plane moves along a circular orbit with a radius of 270 cm around the light concentrator entrance. The normal of this plane always faces the entrance. Photons are emitted from random positions within this plane under random directions. The particle source is moved on the orbit for angles ϑ between 0° and 40° in steps of 0.5° where 0° corresponds to the position opposite of the light concentrator entrance. At each angular position 10^7 photons are emitted.
With this setup, a ray-tracing simulation of the measurement processes can be realised.

3.2.2 Weighting and normalisation of detected photons

Only photons that reach the PMT surface are further studied. Each photon is weighted with an anode sensitivity depending on the incidence angle of the light on the PMT surface. This relative anode sensitivity measured by Okumura et al. (2015) with a blue LED and a PMT reduced by a mask to a 5 mm central spot is shown in Figure 3.9.

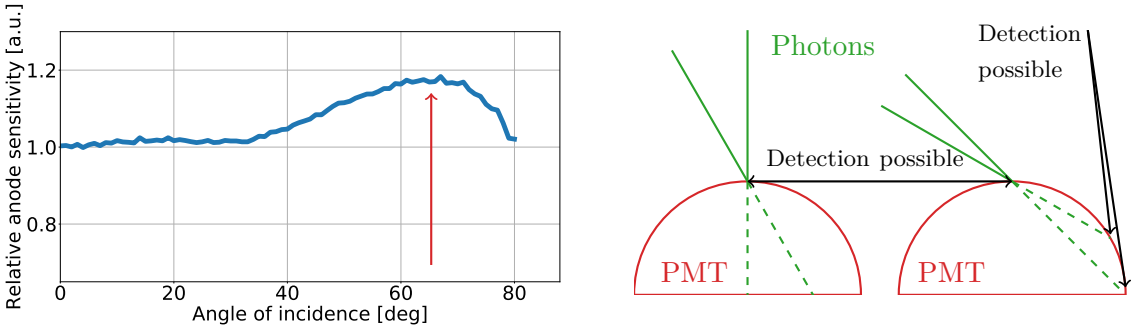

(a) Anode sensitivity

(b) Possibilities of detection

Figure 3.9 Relative anode sensitivity depending on the incidence angle w.r.t the PMT surface normal. (a) The anode sensitivity measured by Okumura et al. (2015) at the PMT center increases between 40° and 80°. The red arrow marks the geometrical beginning of a second detection possibility. (b) This is mainly caused by the spherical shape of the PMT cathode. While photons with small incidence angles have only one possibility to be detected, photons with larger angles have a second detection possibility when passing through the cathode undetected at the first interaction point. The geometrical effect is probably smeared out by effects in the glass window.

It is normalised to the sensitivity at 0° and shows an increase between 40° and 80° with a maximum at 65°. This bump structure is mainly due to the geometrical form of the PMT. As shown in Figure 3.9b photons entering the center of the hemispherical PMT surface under small angles are detected by the cathode with a probability depending on the QE of the PMT. While this is also true for photons entering under larger angles, photons can also pass through the the cathode layer undetected and reach the cathode layer again where they have a second possibility to be detected. Their detection probability is therefore higher. For the given PMT geometry the minimum angle for the photon to cross the PMT and reach the

cathode a second time is

$$\alpha = \arctan\left(\frac{\mathrm{R_{Base}}}{\mathrm{R_{Curvature}} - \sqrt{\mathrm{R^2_{Curvature}} - \mathrm{R^2_{Base}}}}\right) = 65.7^\circ \tag{3.2}$$

where $\mathrm{R_{Base}}$ is the radius of the cathode base area and $\mathrm{R_{Bending}}$ its curvature radius. This angle α corresponds to the peak of the bump structure in the anode sensitivity. The broadening of the peak is probably due to light scattering in the PMT's glass window.
Because the exact scattering mechanisms in the glass window are not known, in this simulation the PMT glass window is considered perfectly transparent for the incident light and neglected. As a simplification it is further assumed that the anode sensitivity measured at the center of the PMT is true on the whole PMT surface. Each photon is then weighted with the anode sensitivity at the impact angle between the incidence direction of the photon and the surface normal of the cathode at the impact position.
To calculate the optical gain of the light concentrators the weighted number of photons in a light concentrator simulation is normalised to the corresponding number in the reference mask simulation at 0° and the cosine of the azimuth angle of the light source position. This way the optical gain found in the laboratory measurement and the simulation can be compared.

3.3 Results of the spectral measurements: Effective reflectivity

The optical gain of a light concentrator setup does not only depend on the reflectivity of the concentrator coating material, but also, due to the non-uniform anode sensitivity, on the impact position and direction of the reflected photon on the cathode surface. To determine the *effective reflectivity*, the spectral response of the three different light concentrator coatings is studied. Spectral measurements are performed as described in Section 3.1 for all light concentrators at 0°. Additionally, for a subset of three concentrators per coating the measurement is repeated at 5°, 10° and 15°. An effective reflectivity is defined, related to the optical gain, via:

$$R = \mathrm{Optical\,gain}\frac{R^2_{\mathrm{Exit}}}{R^2_{\mathrm{Entrance}}}, \tag{3.3}$$

where R_{Entrance} and R_{Exit} are the flat-to-flat inner distances of the concentrator's entrance and exit window. The results are summarised in Figure 3.10. Baseline shifts for wavelengths below 280 nm and above 550 nm are outside the confidence limit set by the linearity test.
All three coatings have a very high effective reflectivity of $\geq$80% over the full spectral range even at higher angles which ensures the functionality of the light concentrators. The spectral shape is similarly constant for all coatings apart from wavelengths between 300 nm and 425 nm. The difference is most prominent at 0° light incidence: While the optical gain drops for the Savimex coatings, the BTE coating remains nearly constant. This effect decreases from almost 10% at 0°, to 5% at 5° and 2% at 10° before completely vanishing for 15°.
Due to policies of the coating companies the exact production mechanisms of the coatings are not known. As a result it is challenging to determine the origin of the drop in the spectral response at small angles. One possible explanation could be interference effects of grazing incidence photons interacting with multiple thin aluminium layers. Another possibility are absorption effects in differently thick protective SiO_2 layers. However, as the drop is most

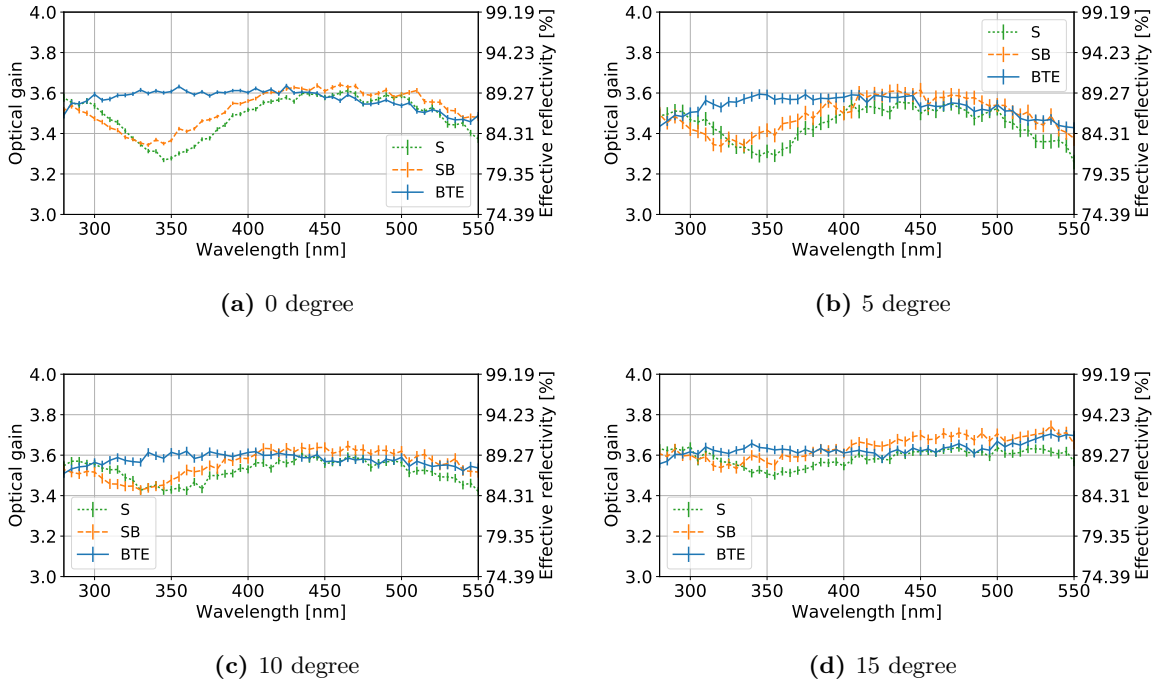

(a) 0 degree

(b) 5 degree

(c) 10 degree

(d) 15 degree

Figure 3.10 Spectral response of the prototype coatings. Averages over measurements with different concentrators of each coating type are shown for different angles between 0° and 15°. For large wavelengths or angles the spectra are similarly constant for all coatings. Between 300 nm and 425 nm the effective reflectivity drops by up to 10% depending on the angle for the Savimex coatings in comparison to the BTE coating.

significant at 0°, where the telescope mirrors will be shadowed by the camera housing, and washes out for larger angles, the effective reflectivity of all three prototype coatings fulfils the requirements for the FlashCam light concentrators.
Nevertheless, it is interesting to compare the average deepness of this drop for the coatings, so the mean effective reflectivity in the wavelength regime between 300 nm and 400 nm at 0° is further studied. As the anode sensitivity could vary from one PMT to the other and influence the results of the effective reflectivity, the concentrators of the different coating types are distributed randomly over the five PMTs of the PDP module. The mean effective reflectivities on different PMT positions are summarised in Table 3.2.

Table 3.2 Mean effective reflectivity for the three prototype coatings averaged over measurements with different concentrators between 300 nm and 400 nm for individual PMT. As PMT 3 was equipped with the same monitoring light concentrators in all measurement it is left out in this study.

PMT	1	2	4	5	average
S	84.4±0.4	83.2±0.6	84.1±0.5	84.3±0.5	84.1±0.2
SB	85.2±0.5	84.8±0.4	85.4±0.4	85.4±0.4	85.2±0.2
BTE	89.6±0.4	89.2±0.5	88.8±0.4	89.8±0.5	89.3±0.2

The effective reflectivites measured by the individual PMTs match within the statistical errors. In average, the reflectivity is 84% for the S, 85% for SB and 89% for the BTE coating. Outside the drop region, the effective reflectivity of all coatings is above 85%.

3.4 Results of the angular measurements

In a second step, the angular response of the light concentrators is studied. Contrary to the reflectivity, the angular acceptance depends on the rotation of the light concentrators with respect to the concentrator rotation axis: The angular acceptance curve of a light concentrator in edge configuration is expected to be broader than the curve from a concentrator in vertex configuration (see Section 3.2.1). Angular measurements are taken in edge configuration for all concentrators. Additionally, for one concentrator per coating, the PDP holder is rotated by 30° and a measurement is performed for the concentrator at the central PMT position. A small asymmetry induced by the repositioning of the PDP holder between measurements is corrected for each measurement (see Section 3.7.3)
From each angular acceptance curve two characteristic parameters are determined, the acceptance angle and the slope steepness, as shown exemplary for measurements of one light concentrator in both rotation configurations in Figure 3.11.

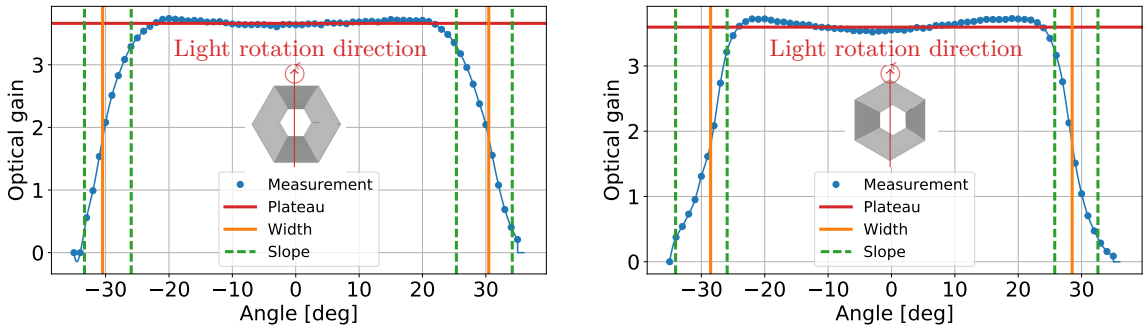

(a) Edge **(b)** Vertex

Figure 3.11 Example of angular acceptance curves for a concentrator in edge and vertex configuration. The rotation configurations and the corresponding light rotation axes are shown in the inlet of each plot, respectively. Two parameters are taken from each curve: The acceptance angle defined as the half width at 50% of the average plateau height between ±15° and the slope steepness for a decrease from 90% to 10% of this plateau height.

As expected, the angular acceptance curves differ for the two concentrator rotations. To gain quantitative parameters the curves are interpolated with a cubic method. The plateau height of the angular acceptance curve is defined as the average of the rather stable values between ±15°. With this definition, the slope steepness then corresponds to the angular range in which the acceptance curve decreases from 90% to 10% of this plateau height. It is a good measure of how good light from angles larger than the acceptance angle is cut off completely. For the acceptance angle itself the two angles at which the curve reaches 50% of the plateau height are determined. The acceptance angle is then defined as half the angular distance between those two points. This angle specifies the angular range from which light can enter into the light concentrator to be detected by the PMT.
These parameters are determined for all light concentrators at 285 nm, 320 nm, 355 nm, 390 nm and 495 nm. The results are discussed in the following. Also, for the edge configuration the dependency of the measurements on the distance between light concentrator exit window and the PMT surface will be analysed in the course of this section.

3.4.1 Cut-off steepness

The slope of the angular acceptance curve in which the curve decreases from 90% to 10% of its plateau value is a measure of how good light from angles larger than the acceptance angle is cut off. Figure 3.12 displays the slope width averaged over all concentrators of each prototype coating in edge configuration at the five main wavelengths.

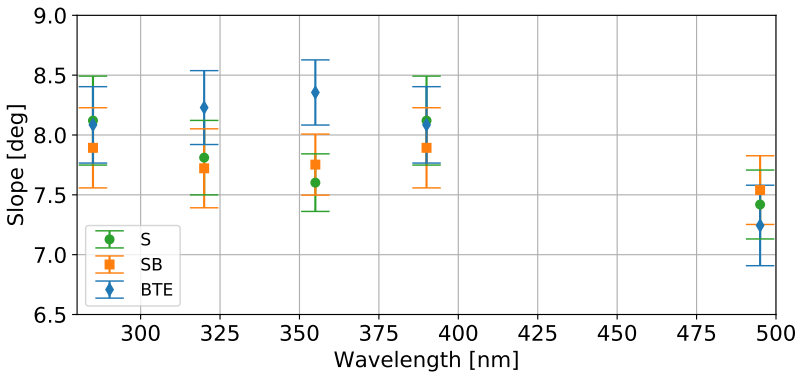

Figure 3.12 Slope steepness of the angular acceptance curve averaged over measurements with different concentrators of each coating in edge configuration. The errorbars corresponds to one standard deviation. A similar slope width between 7° and 8.5° is found for all light concentrators at the five measured wavelengths.

In this configuration, the slope steepness for all light concentrators is found between 7° and 8.5° at all measured wavelengths. While the S and SB coating are stable within errorbars for all wavelengths, the slope width of the BTE coating seems to decrease for 495 nm. At this wavelength, baseline shifts at 0° light incidence are small for all concentrators. The furthermore large angle at which the 10% plateau height is reached adds to the uncertainty of this data point. The wavelength averaged results of the slope width determination for both rotations are summarised in Table 3.3.

Table 3.3 Slope steepness averaged over the five measured wavelength for the three prototype coatings. For the edge configuration all available light concentrators are measured, while the results of the vertex configuration are based on one measurement per coating type per wavelength.

	Edge			Vertex		
	S	SB	BTE	S	SB	BTE
Slope [°]	7.8±0.3	7.8±0.2	8.1±0.5	6.7±0.2	7.2±0.1	6.7±0.3

From this table, it can be deduced that the slope steepness of all light concentrators in edge rotation configuration is compatible within errorbars. For the vertex rotation the SB coating shows a 7% larger mean steepness than the S and BTE coating. Overall, the angular acceptance of a vertex rotated concentrator decreases about 10% to 20% faster than that of an edge rotated one. Those two rotations corresponds to the extreme cases of light incidence possible in real telescope operation.

3.4.2 Acceptance angle

The second key parameter, the acceptance angle, is calculated as the half width of the angular acceptance curve at 50% of the plateau height and as explained before strongly depends on the rotation of the light concentrator with respect to the concentrator rotation axis. In Figure 3.13 the acceptance angle averaged over measurements of different concentrators of one coating type is shown for five wavelengths for the edge configuration. Wavelength averaged values for both rotation configuration are given in Table 3.4.

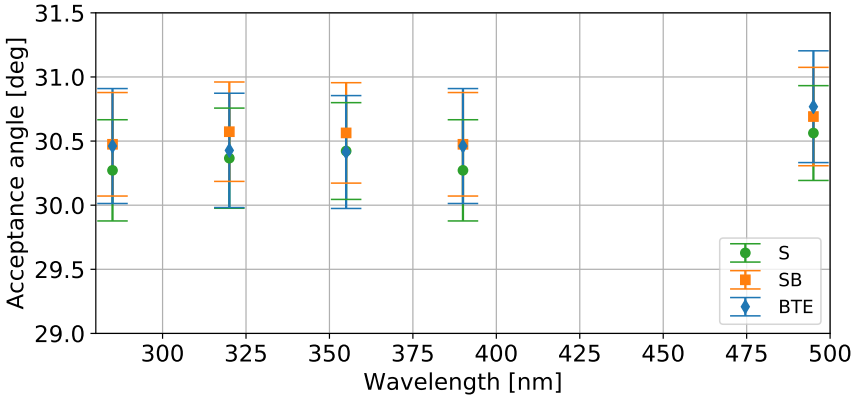

Figure 3.13 Acceptance angle averaged over measurements with different concentrators of each coating at five wavelengths in edge configuration. The errorbars corresponds to one standard deviation. The width for all light concentrators is equal within errorbars over the full wavelength range with a mean value of 30.5°.

Table 3.4 Acceptance angles of light concentrators averaged over measurements at five wavelengths. For the edge configuration all light concentrators are measured, while the results of the vertex configuration are based on one measurement per coating type per wavelength.

	Edge			Vertex		
	S	SB	BTE	S	SB	BTE
Acceptance angle [°]	30.4±0.1	30.5±0.1	30.5±0.1	29.5±0.2	29.4±0.1	28.5±0.1

An acceptance angle of about 30.5° is found for the light concentrators in edge configuration, independent from the wavelength and the coating type. In the vertex configuration the acceptance angle is about 1° smaller for the Savi coatings. For the BTE coating an even 2° smaller acceptance profile is found in the vertex configuration.
The acceptance angle of a light concentrator should be optimised to collect the full signal focused onto the camera by the telescope mirrors while simultaneously suppress stray light background coming from outside the mirror dish. The amount of signal seen by a camera pixel is proportional to the mirror area visible to that pixel. The angular distribution of mirror area visible from an averaged pixel position for an MST telescope is shown in Figure 3.14.
No light is reflected into a pixel around 0° as the camera shadows this light with its housing. For larger angles the visible mirror area increases linearly. Around 17° the pixel starts to look over the edge of the mirror dish and to pick up background, so the effective visible area decreases. Finally, at 27° all light detected by a pixel comes from outside the mirror dish.

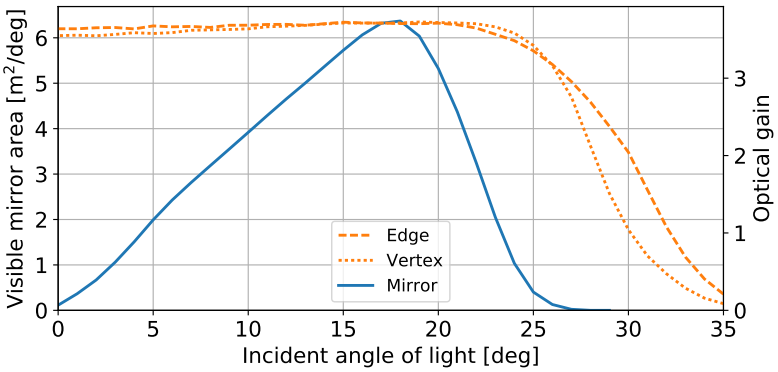

Figure 3.14 Visible mirror area for an average pixel position on the MST camera under specific light incidence angles. Light around 0° is shadowed by the camera housing. The amount of visible mirror area increases linearly until the pixels begin to see outside the mirror. Above 17° the distribution falls off steeply and vanishes for 27°. Angular acceptance curves from edge and vertex rotation show that the acceptance angle is 2°-3° wider than the maximum possible light incidence angle.

Optimal light concentrator geometries should provide acceptance angles that cut the light collection efficiency at the vanishing tail of the mirror area distribution. For both angular acceptance curves shown in Figure 3.14 for edge and vertex rotation, the light concentrator equipped pixels will collect the full mirror signal and only a 2°-3° wide ring of possible stray light from outside the mirror. Background from larger angles will be cut efficiently.

3.4.3 Distance test: Variation of the optical efficiency

The nominal distance between the light concentrator exit window and the PMT surface is 1 mm. Different distances effect the angular acceptance curve as the path of the photons through the light concentrator geometry changes. To check the mounting accuracy needed to generate reproducible results, concentrators with different coatings are installed at different distances from direct contact up to 3 mm at the inner three PMTs and angular measurements are recorded at the five main wavelengths. A reference plate measurement is performed at the standard distance and the data is processed as before. The resulting angular acceptance curves for concentrators at 355 nm are shown on the left side of Figure 4.17.
For all measured distances the plateau height and the slope width of the angular acceptance curves remain unchanged. However, the width of the acceptance curve shrinks. This effect is analysed more systematically in the right side of Figure 4.17. At distances below 1 mm the behaviour of the concentrators varies among the concentrators of different coatings. While the SB coated concentrator seems to be stable, the other two concentrators already show a decrease of the angular acceptance angle for all measured wavelengths.
For larger distances the acceptance angle starts to decrease systematically by 1° per mm. This effect is coating independent and allows for the acceptance angle to be adjusted by varying the distance between light concentrator exit and PMT. The acceptance angle of the measured light concentrators found in Section 3.4.2 is 2°-3° larger than the maximum angle of light reflection from the MST telescope mirrors. For an optimised acceptance angle, the light concentrator geometry could be adjusted. This would mean large effort, time and costs of simulating new geometries, manufacturing of sample concentrators and retesting. By enlarging the distance between light concentrator and PMT by only few mm, the same can be achieved in a much easier and cost efficient way if the camera design allows for this change.

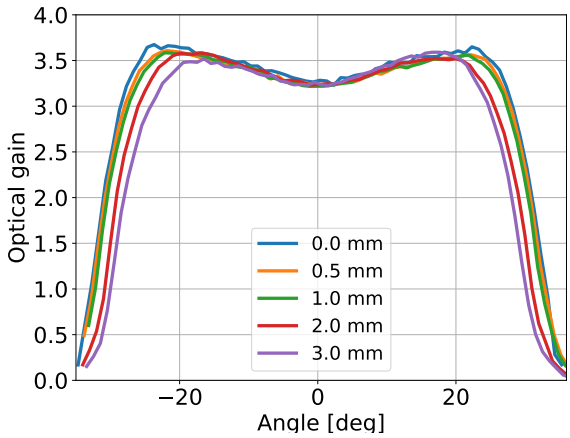

(a) S coating, 355 nm

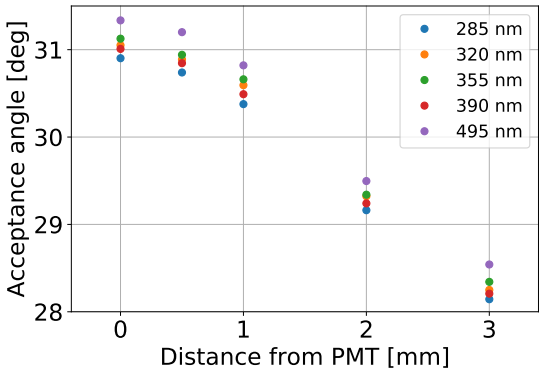

(b) S coating

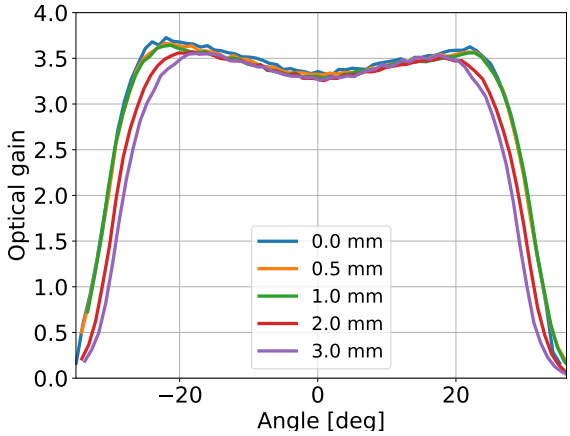

(c) SB coating, 355 nm

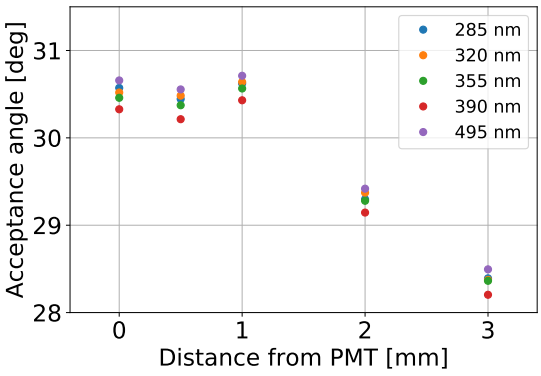

(d) SB coating

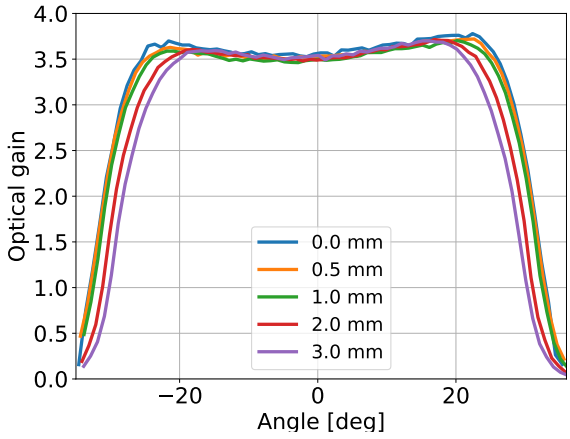

(e) BTE coating, 355 nm

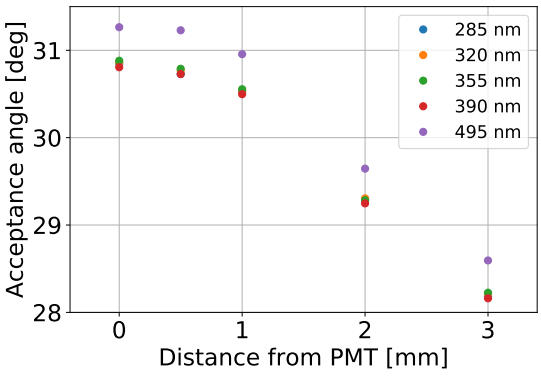

(f) BTE coating

Figure 3.15 Angular acceptance of concentrators with different coatings at different distances between concentrator exit and PMT surface for five wavelengths. On the left, acceptance curves taken at 355 nm are shown for the selected distances, while on the right, the acceptance angle is plotted over distance for all wavelengths. For distances of $\geq$1 mm the acceptance angle shrinks about 1°/mm.

3.5 Results of the ray-tracing simulations

The measured light concentrator acceptance curves can be compared to the results of the ray-tracing simulation described in Section 3.2. This way, the accuracy of the model used in the simulation is tested. The model consists not only of the concentrator geometry but includes also the coating reflectivity. For this simulation, this coating reflectivity is set to the average effective reflectivity found for each coating in the spectral measurements at the corresponding wavelength under central light incidence. As a simplification, the reflectivity is considered independent of the light incidence angle. In Figure 3.16, the comparisons between the measured and the simulated acceptance curves are shown for the different coatings at five wavelengths and both rotation configurations.
For the BTE coated light concentrators in both rotation configurations, the simulated angular acceptance profiles are compatible with the measured profiles averaged for different concentrators at the five main wavelengths. The simple model assumption that the angular acceptance only depends on the light concentrator geometry and the effective reflectivity at 0° light incidence is thus sufficient for those concentrators.
The case is different for the S and SB coating. While the simulated angular profiles are still close to the averaged measurements at 285 nm and 495 nm, the deviations are larger for wavelengths in the effective reflectivity drop region between 300 nm and 400 nm (see Figure 3.10). In general, the exaltations at ±25° are underestimated by the simulation by up to 5% in edge rotation and even up to 10% for vertex rotation for both coatings. As this divergence is not visible for the BTE coated concentrators, this cannot be a geometry effect. Consequently, in this region the angular dependence of the effective reflectivity must be more complex, so that the simplifications made in the simulation model are no longer valid.
Nevertheless, as the model is compatible with the angular acceptance measurements of BTE coated light concentrators, in the following further concentrator properties are studied with this simulation setup. These properties include a more detailed analysis of the distance dependent angular acceptance found in Section 3.4.3 and the illumination pattern on the PMT surface created by the photons travelling through the light concentrator geometry.

3.5.1 Corrleation between distance and acceptance angle

In Section 3.4.3 a correlation between the light concentrator exit window distance from the PMT surface and the corresponding acceptance angle was found. This correlation is again studied within the simulation. Exemplary simulated angular acceptance curves for an edge rotated BTE coated light concentrator at 355 nm are shown in Figure 3.17 together with the respective measurement at the nominal 1 mm distance. Additionally the acceptance angle of those curves is plotted against the distance. The results match those of other wavelengths.
The simulation confirms the dependency of the acceptance angle on the distance between the PMT surface and the light concentrator exit window. Not only are the simulated angular acceptance curves compatible with the measurements taken for distances up to 3 mm, but an even further decrease in acceptance angle is found for larger simulated distances. A linear fit to the acceptance angles of the simulated acceptance profiles up to 6 mm distance determines an angular decease of 1.3° per mm. As already concluded for the measurements, this distance dependency admits easy fine-adjustments of the angular acceptance angle and as a consequence of background reduction.

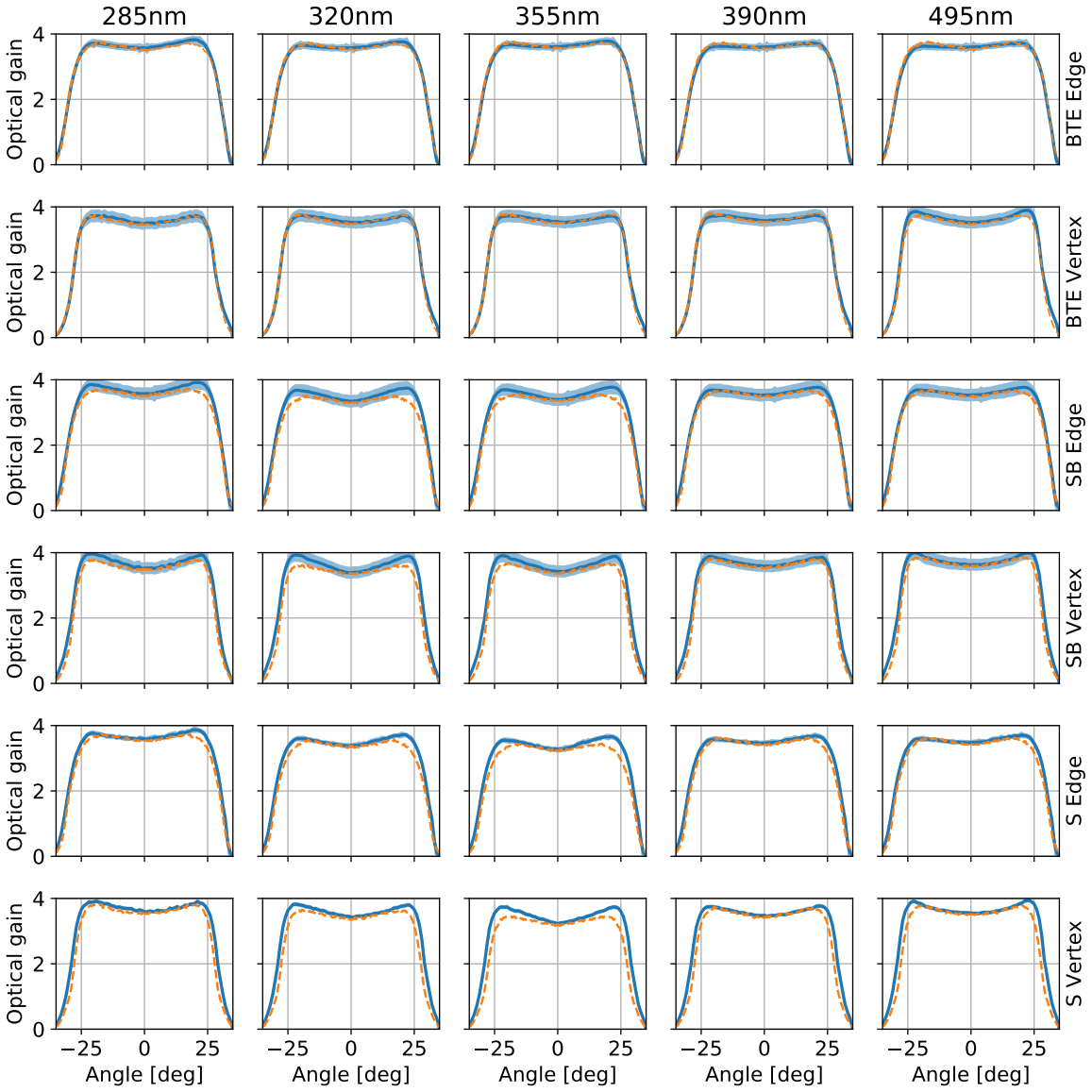

Figure 3.16 Comparison between measured (blue band indicates the average over different concentrators of the same coating and the standard deviation) and simulated (orange dashed line) angular acceptance curves. Acceptance curves are shown for five wavelengths and combinations of the three coatings and the concentrator rotation configuration. The simulated acceptance profile of the BTE coated light concentrators in both rotations is compatible with the measurements. Outside the reflectivity drop region between 300 nm and 400 nm (see Figure 3.10) the same holds true for the S and SB coated concentrators. However, within this drop region the plateau exaltation of the angular profile cannot be reproduced by the simulation. In the extreme case of the vertex rotated SB concentrators at 355 nm, the simulated acceptance at $\pm 20°$ is 10% lower than the measurement.

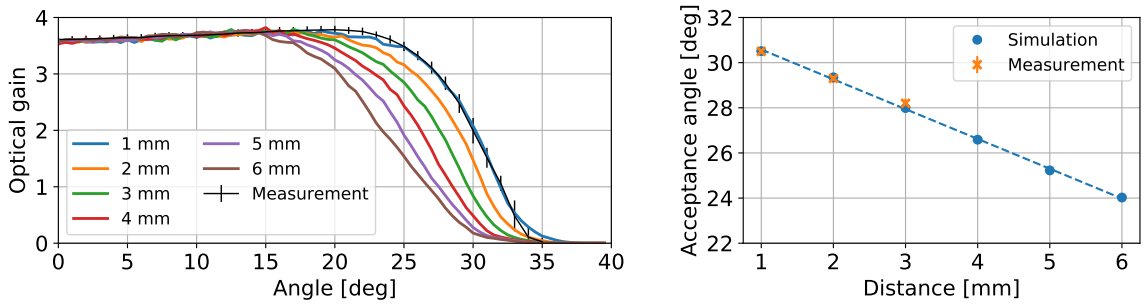

(a) Angular acceptance curves **(b)** Acceptance angle comparison

Figure 3.17 Simulation of the angular acceptance dependency on the concentrator-PMT distance. (a) The simulated angular acceptance curves for edge rotated BTE concentrators at 355 nm match the measurements at 1 mm distance and decrease in width for increasing distances. (b) Measured and simulated acceptance angles match up to 3 mm. For larger distances the simulation show a further decrease. The dashed line corresponds to a linear fit on the simulated acceptance angles.

3.5.2 Illumination of the PMT surface

The response of the PMTs varies with the impact position and angle of the photons on the hemispherical surface. It is therefore interesting to know how the light concentrator influences the illumination pattern on the PMT. For this purpose, the patterns created by simulated photons are analysed. Results for different light incidence angles are given in Figure 3.18.

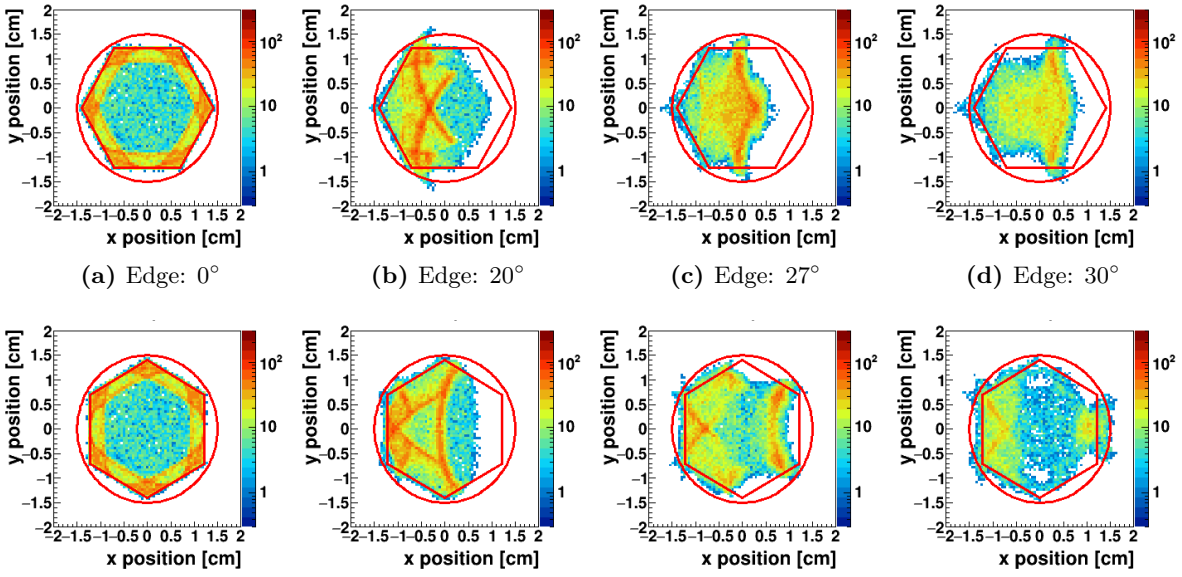

(a) Edge: 0° **(b)** Edge: 20° **(c)** Edge: 27° **(d)** Edge: 30°

(e) Vertex: 0° **(f)** Vertex: 20° **(g)** Vertex: 27° **(h)** Vertex: 30°

Figure 3.18 Illumination patterns created on the PMT surface by photons entering the light concentrators under different angles for both rotations. The red hexagon indicates the exit window, the red circle the minimal sensitive cathode area. Photons are concentrated around the exit window for small angles and gradually reflected towards the cathode center for larger angles. Beyond 27° the distribution shifts again to the rim of the PMT.

At 0° light incidence photons are concentrated around the edges of the light concentrator exit window. For larger angles, photons on the right rim are shadowed by the concentrator while more photons are reflected under larger angles from the left concentrator wall and their impact position shifts towards the PMT center. There, the maximum photon density is reached at 27° for the edge and at 20° for vertex rotation. Afterwards the total number of detected photons decreases and the distribution becomes more homogeneous. Finally, the distribution shifts again towards the PMT rim before vanishing completely.
During camera operation the incidence light distribution is expected to follow the visible mirror distribution shown in Figure 3.14. As there is no preferred light rotation axis in the camera, a simulation is performed in edge rotation with photons emitted from ±35° in the standard light rotation direction and perpendicular to it. Their number is weighted with the expected light distribution. The resulting illumination pattern is shown in Figure 3.19a.

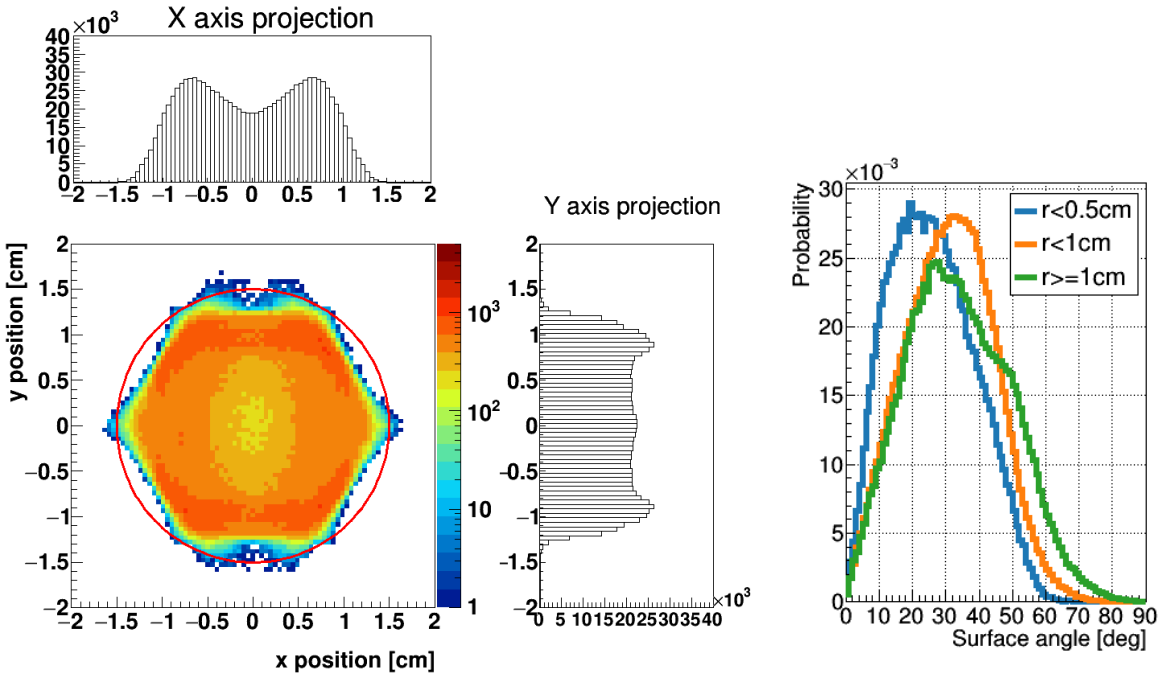

(a) Illumination pattern **(b)** Incidence angles

Figure 3.19 Average illumination of the PMT surface. (a) PMT illumination pattern from photons following the expected light distribution of the MST telescope. Inside the hexagonal exit window the PMT surface is fully illuminated. (b) The distribution of light incidence angles w.r.t the PMT surface for different distances r from the PMT center shifts to larger peak angles for larger distances.

Apart from small areas outside the exit window the full PMT surface is illuminated. While few photons are found around the window edges, the inner region shows a high impact rate. The very center is thereby less illuminated as the main illumination is expected between 15° and 20° where the maximum photon density in edge rotation is not yet reached while it is just reached for the vertex rotation.
Finally, the distribution of photon impact angles to the PMT surface normal is studied for impact positions within concentric rings of 0.5 cm, 1 cm and the 1.5 cm radius. For the PMT center the peak of hte almost Gaussian distribution is at 25°, while it shifts to 35° for the intermediate ring. The outer ring seems to consists of a main peak centred around 25° and a smaller peak at 45°, the latter describing the photons along the exit window rim.

3.6 Ageing tests with environmental influences

Another important coating property is the long term durability of the materials. Once installed on the Cherenkov camera, the light concentrators are behind an acrylic glass window which protects the sensitive parts against dust and other external sources of damage. The camera has temperature and humidity sensors and the conditions within the camera body are kept stable at 20°C with an humidity below 10%. However, during storage or unexpected power cuts the light concentrators can be exposed to different temperatures and humidity variations which could influence the their performance over longer time periods.
Two sets of light concentrator with one concentrator per coating each are placed inside a climate chamber. The temperature is cycled between 0° and 50° within 4 hours, the humidity from 10% to 90% within 5 hours as sketched in Figure 3.20. A full combined temperature and humidity cycle takes 20 hours.

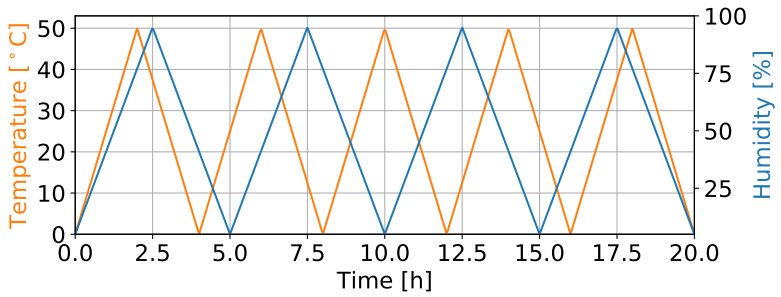

Figure 3.20 Temperature and humidity cycles in the climate chamber. The temperature varies between 0° and 50° with a period of 4 hours, the humidity between 10% and 90% in 5 hours.

The climate chamber treatment of the two sets are started with a time difference of 90 days. In irregular time intervals effective reflectivity, slope and acceptance angle are remeasured. One reference light concentrator that is kept under clean, dry and cool conditions is measured each time together with the climate chamber samples.
Figure 3.21 shows the change in the average effective reflectivity between 300 nm and 400 nm of the coatings over a period of 450-550 days. Two gaps in the plotted data corresponds to major changes in the test system: After 25 days the PDP module was exchanged and the monochromator recalibrated, after 490 days a new reference light concentrator was chosen.
Apart from a jump in reflectivity around 120 days that is also visible for the reference concentrator and is assumed to be setup dependent, over the course of 550 days, the reflectivity of all three prototype coatings seems to decrease by 4% only. This shows the degrading of the reflective coating quality due to ageing.
Acceptance angle and slope of the angular acceptance curves are presented for 355 nm in Figure 3.22. The results match those of the four other wavelengths. A broadening of 0.5° in acceptance angle is visible before the first setup change for both, sample and reference concentrators, due to an improved distance setting between PMTs and light concentrator. Otherwise, the acceptance angle remains stable within $31° \pm 0.3°$, except for one BTE coated concentrator that has a lower acceptance angle from the beginning and stabilises at $30° \pm 0.1°$. The same holds true for the slope region. For all concentrators the slope width is stable around 8.5° for concentrators with BTE coating or around 7.5° for the Savimex coatings, respectively. No significant ageing effect in terms of acceptance angle or slope width is found for any coating. Variations are within the systematic effects of the setup.

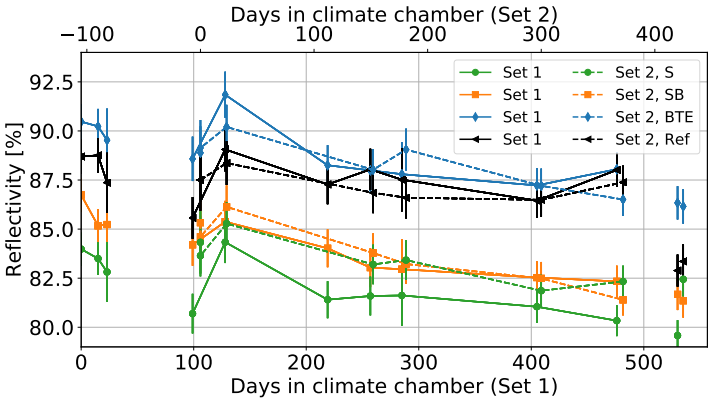

Figure 3.21 Changes in the average effective reflectivity between 300 nm and 400 nm of the prototype coatings in the climate chamber. The two gaps corresponds to major setup changes. A decrease of 4% in performance over a period of over 500 days due to ageing of the materials is detected.

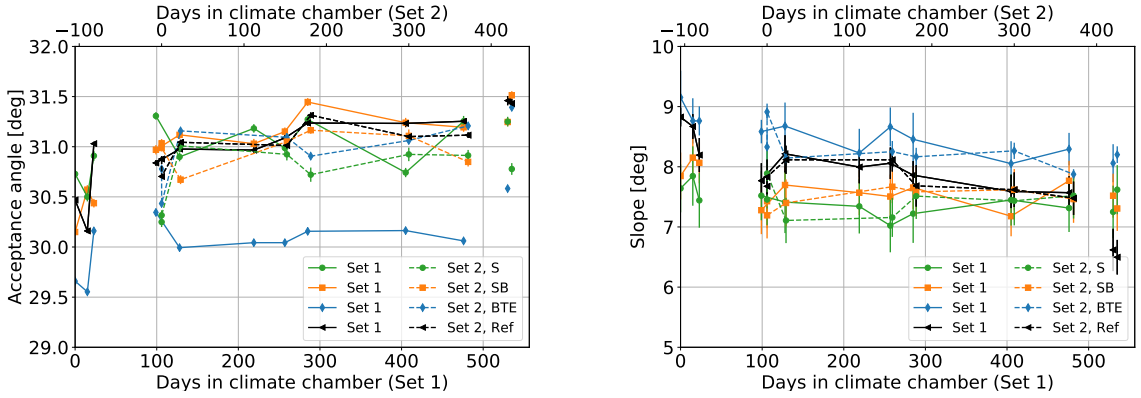

(a) Acceptance angle **(b)** Slope steepness

Figure 3.22 Variation of the acceptance angle and the slope width at 355 nm for the three coating types during climate chamber treatment. Both slope and acceptance angle remain constant apart from a broadening of 0.5° in acceptance angle due to a new alignment of PMTs and concentrators.

In summary, after over 500 days in the climate chamber only a 4% decrease in effective reflectivity is found for the three prototype coatings. If one temperature cycle corresponds to one day, this is equivalent to 2000 days or 5.5 years in storage or a camera without temperature control. Obviously, as the cameras have internal air-conditioning, the durability of the coatings during camera operation will be excellent even for longer time scales.

3.7 Study of systematics

The measurements of the key parameters of the light concentrators can only be correctly interpreted when the systematics of the measurement procedure are understood. Systematic errors of the test system were already discussed in Section 2.3. In this section systematic uncertainties as the reproducibility of a measurement, the variation of measurements of concentrators of the same coating, the asymmetry of the angular acceptance curves and the effect of the small inhomogeneity of the light field are examined.

3.7.1 Reproducibility of the measurements

To assess the reproducibility 20 monitoring light concentrator measurements are analysed. The monitoring concentrator was always attached to the central PMT position. As an indicator of the reproducibility, the relative spread of the optical gain values in the spectral measurements is determined. The result is shown in Figure 3.23.

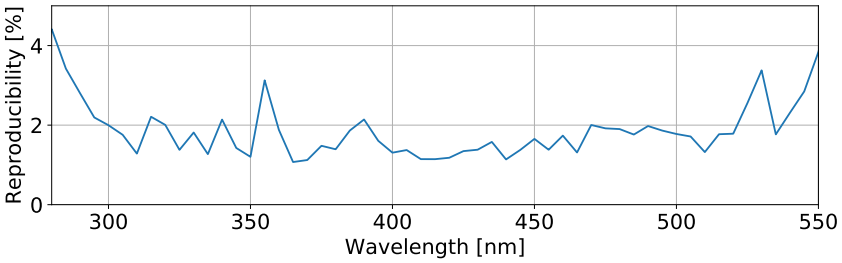

Figure 3.23 Reproducibility uncertainty determined from monitoring light concentrator measurements over the full wavelength range. The typical reproducibility between 280 nm and 550 nm is below 2% of the measured mean optical gain.

As expected, the reproducibility depends on the flux intensity. Below 300 nm and above 550 nm, the QE is low as is the photon flux and the optical gain determination is sensitive to small variations. In the high flux regime between 300 nm and 500 nm the reproducibility uncertainty is typically below 2% of the measured mean gain.

3.7.2 Variability within one coating type

Apart from the reproducibility of single light concentrator measurements, the variability of concentrators of the same coating type is investigated. The relative spread of those measurements is shown in Figure 3.24. For comparison the one concentrator reproducibility is given.

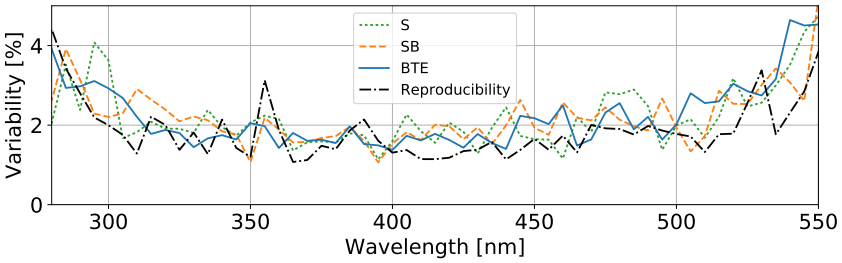

Figure 3.24 Variability of measurements of concentrators of the same coating type. A typical variability of 1.2% of the measured optical gain is found.

The variation in optical gain within one coating type are only slightly larger than the reproducibility of a single concentrator measurement. Taking the mean value of the variations in the wavelength range between 280 nm and 550 nm and assuming that the variability of concentrators with the same coating is independent of the reproducibility, a variability of 1.2% is found for all coatings.

3.7.3 Asymmetry of the acceptance curve

With a perfect setup, the results of an angular acceptance curve should be symmetric around zero. Unfortunately, in the measurements performed during this work a small offset of $\pm 1.5°$ was detected. This asymmetry is induced by the shifting of the PDP holder when switching between light concentrator and reference mask measurements. A position misalignment of the order of 1 mm already leads to a curve asymmetry of 1.1°. This effect is corrected by shifting the angular acceptance curve such that the two angles at which 50% of the curve plateau is reached, match. The cosine normalisation of the curve is performed after the asymmetry correction. An acceptance curve before and after correction is shown in Figure 3.25.

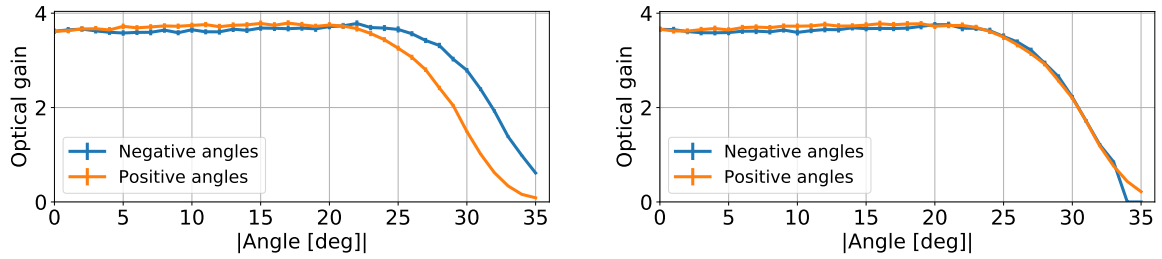

(a) Before correction **(b)** After correction

Figure 3.25 Angular acceptance curve folded around the zero position of the rotation table. (a) Without correction an asymmetry between positive and negative angles of 1° can be seen. (b) After corrections the curves in the two angular regimes agree within errorbars.

3.7.4 Diverging incidence angle

For the angular acceptance measurements, light is expected to enter the concentrator from a fixed angle. However, in the test system, the light from the integrating sphere is not emitted in a parallel beam. As the distance between the extended exit port and the PMTs is 2.7 m, a widening of the beam of up to 1° is possible. This effect is also included in the simulations. To test the influence of the diverging light source on the final result, a simulation with beamed light emission from the integrating sphere is performed. The results are compared to the original simulation with diverging light field and are shown in Figure 3.26.

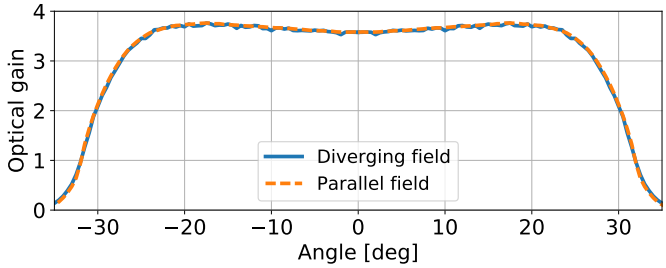

Figure 3.26 Angular acceptance curves from parallel or diverging light emission. Width differences of the two curves are within 0.1°.

Both angular acceptance profiles are compatible. Width differences of $\leq 0.1°$ could be due to statistical fluctuations or an effect of the diverging light field.

3.7.5 Inhomogeneity of the light field at the light concentrator position

For the effective reflectivity or the angular efficiency of a light concentrator the measured optical gain is renormalised with the ratio of the light concentrator entrance area to its exit area or the mask reduced PMT surface. In a perfectly homogeneous light field, this is equivalent to the ratio of the flux integrated over the light concentrator or the PMT surface. In Section 2.3.3 an inhomogeneity of $\leq 0.4\%$ was found. More precisely, the inhomogeneity averaged over each reduced PMT surface is 0.28%, for the larger light concentrators 0.35%. In an extreme case this would mean that 0.28% of the PMT and 0.35% of the light concentrator entrance are not illuminated at all while the light distribution on the remaining area is homogeneous. The error induced by this inhomogeneity can be calculated via

$$\Delta\mathrm{Eff} = 1 - \frac{R^2_{\mathrm{Exit}}}{R^2_{\mathrm{Entrance}}} \cdot \left(\frac{R^2_{\mathrm{Entrance}}}{R^2_{\mathrm{Exit}}} \right)_{\mathrm{red}}, \tag{3.4}$$

where *red* marks the areas reduced by the not illuminated parts. The resulting efficiency is 0.07% lower than the measurement which is much smaller than the statistical errors.

3.8 Signal and night sky background

All results from this chapter can be merged in the calculation of the signal to noise ratio of Cherenkov light detection by means of the MST mirrors. The detected signal will be proportional to the Cherenkov flux from the cosmic-ray induced air showers while the background noise depends on the night sky background (NSB) flux. Both flux spectra are shown in Figure 3.27 for La Palma, Spain, where the northern CTA observatory will be positioned.

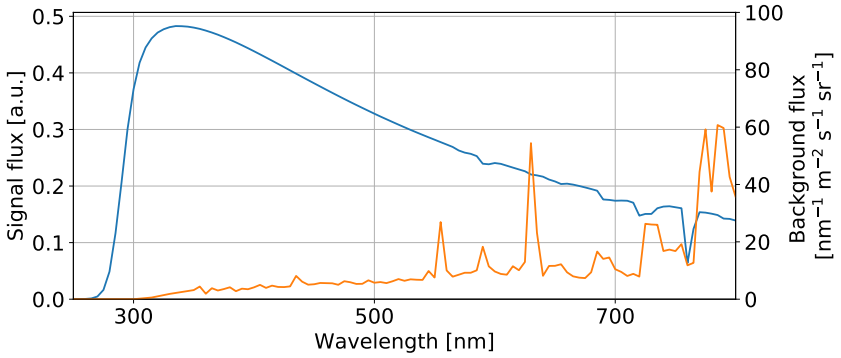

Figure 3.27 Expected Cherenkov flux and NSB for La Palma, Spain. The Cherenkov spectrum peaks between 300 nm and 400 nm while the NSB increases slowly for higher wavelength showing emission lines from elements such as oxygen and sodium in the otherwise continuous spectrum. Data taken from Benn and Ellison (1998).

The Cherenkov light signal reaches the camera only as light reflected from the telescope mirrors following the light distribution shown in Figure 3.14. The NSB flux effects the signal detection in two different ways: A direct background component is focused onto the camera surface by the telescope mirrors in the same way as the Cherenkov signal while an indirect component of NSB light is reflected from ground or parts of the telescope structure and enters the camera plane as diffuse stray light from outside the mirrors. Both, background and signal, are wavelength and angular dependent as they have to pass through the different optical components of the camera before being detected.

3.8.1 Performance of the light concentrators

The expected photo-electron rates in the camera, are calculated via the following equations.

$$\begin{aligned}\mathrm{Signal}(\lambda) &= \mathrm{F_{Signal}}(\lambda) \cdot \mathrm{T_{Window}}(\lambda) \cdot \mathrm{PDE_{PMT}}(\lambda) \\ &\quad \cdot \epsilon \cdot \int \mathrm{E_{LC}}(\vartheta, \lambda) \cdot \mathrm{dA_{Mirror}}(\vartheta)\mathrm{d}\vartheta \end{aligned} \tag{3.5}$$

$$\begin{aligned}\mathrm{NSB_{direct}}(\lambda) &= \mathrm{F_{NSB}}(\lambda) \cdot \mathrm{T_{Window}}(\lambda) \cdot \mathrm{PDE_{PMT}}(\lambda) \\ &\quad \cdot \epsilon \cdot \int \mathrm{E_{LC}}(\vartheta, \lambda) \cdot \mathrm{dA_{Mirror}}(\vartheta)\mathrm{d}\vartheta \cdot \mathrm{c_{hex}} \cdot \int_0^{\alpha_\mathrm{A}} \int_0^{2\pi} \mathrm{d}\Omega \end{aligned} \tag{3.6}$$

$$\begin{aligned}\mathrm{NSB_{indirect}}(\lambda) &= \mathrm{a} \cdot \mathrm{F_{NSB}}(\lambda) \cdot \mathrm{T_{Window}}(\lambda) \cdot \mathrm{PDE_{PMT}}(\lambda) \\ &\quad \cdot 2\pi \int \mathrm{A_{LC}} \cos(\vartheta) \cdot \mathrm{E_{LC}}(\vartheta, \lambda) \cdot \mathrm{dA^{rel}_{Ground}}(\vartheta) \cdot \mathrm{c_{hex}} \cdot \sin(\vartheta)\mathrm{d}\vartheta \end{aligned} \tag{3.7}$$

where:

- $\mathrm{F_{Signal}}(\lambda)$, $\mathrm{F_{NSB}}$: Incoming photon fluxes as shown in Figure 3.27
- $\mathrm{T_{Window}}(\lambda)$: Transmission of the acrylic glass protection window as shown in Figure 3.28a (angular dependency neglected)
- $\mathrm{PDE_{PMT}}(\lambda)$: Photo-detection efficiency, a product of the QE shown in Figure 2.4 and an assumed collection efficiency of 95% (angular dependency neglected)
- $\epsilon = 0.96$: Coverage ratio of the light concentrator pixel size to the maximal possible pixel size in the camera grid
- $\mathrm{E_{LC}}(\vartheta)$: Efficiency of the light concentrators
- $\mathrm{dA_{Mirror}}(\vartheta)$: Light distribution following the differential mirror area in Figure 3.14
- $\mathrm{c_{hex}} \cdot \int_0^{\alpha_\mathrm{A}} \int_0^{2\pi} \mathrm{d}\Omega$ with $\mathrm{c_{hex}} = 2\frac{\sqrt{3}}{\pi}$: Hexagonal solid angle as the NSB is uniformly distributed over the full visible patch of sky; The integral is limited to the angular size $2\alpha_A = 0.179°$ of the light concentrator seen from the mirror in 16 m distance
- a: Albedo of the ground from which the NSB is reflected
- $\mathrm{A_{LG}} \cos(\vartheta)$: Pixel size corresponding to the concentrator entrance window area
- $\mathrm{dA^{rel}_{Ground}}(\vartheta)$: Relative amount of ground seen by the pixel described in Figure 3.28b

For the light concentrator efficiency, one data set of angular acceptance curves is recorded for all wavelengths between 250 nm and 600 nm in steps of 5 nm in edge configuration. As this configuration produces the broadest angular acceptance curve, the resulting rates are the maximum rates expected for FlashCam in the MST telescopes for the La Palma sky. For a more detailed study the angular dependent integrals of the three different components calculated for light concentrators efficiencies at 355 nm are displayed in Figure 3.29.
These integrals show clearly the two effects of light concentrators on a Cherenkov camera. As the processing of light is equal for signal and direct NSB, their integrals behave equally. Both saturate at 30° at a value a factor 2.7 larger than that of a bare PMT for the signal and even 7.7 for the direct NSB. This is due to the larger sensitive area created by the light

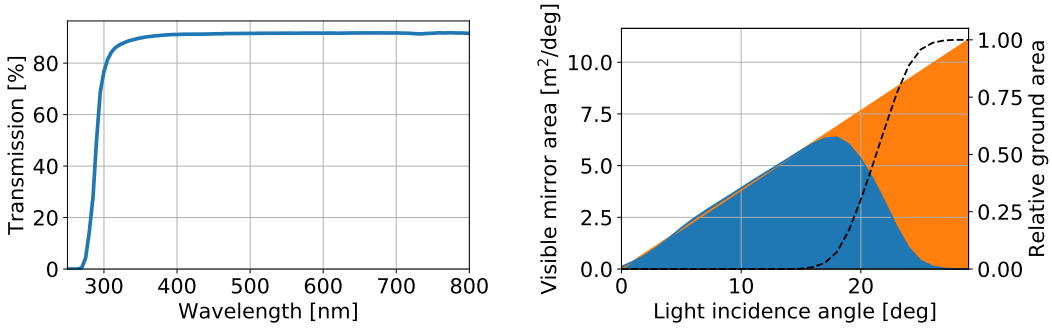

(a) Transmission **(b)** Visible ground

Figure 3.28 Camera related auxiliary functions for the calculation of signal and background rates. (a) Transmission of the acrylic glass window that insulates the camera and protects the sensitive camera components from environmental influences. (b) Differential mirror and ground area visible at an average pixel position. The differential amount of visible mirror area (blue) increases linearly for angles up to 15° before starting to decrease. From the difference between this area and a further linear increasing area (orange), the amount of visible ground (black dashed line) can be calculated.

concentrators and the associated solid angle. Variations between the different coatings are small. The SB coated concentrator show only a $\leq$1% lower light detection than the BTE coated one, the detection of the S coated concentrators is 5% smaller.
The angular integral of the indirect NSB component represents the noise reduction ability of the light concentrators. While the detection of stray-light by the PMT raises steadily for larger angles, the integral of the light concentrators starts to saturate above 30°. At 90° the noise is reduced by the light concentrators by a factor of 2.6. Again, the differences between the coatings are small. BTE and SB coated concentrators provide the smallest amount of indirect NSB, while the angular integral of the S coated concentrators is 5% larger.
All resulting photo-electron flux rates after wavelength integration are summarised in Table 3.5. For the calculation of the indirect NSB rate an albedo of 0.25 is expected for the telescope location by the CTA observatory.

Table 3.5 Signal and NSB rates calculated from measured light concentrator efficiencies. For the indirect NSB an albedo of 0.25 is assumed. The signal is normalised to the BTE signal rate.

Coating type	Signal [a.u.]	direct NSB [MHz]	indirect NSB [MHz]	Total NSB [MHz]
S	0.97	181	63	244
SB	0.98	180	57	237
BTE	1	185	58	243
PMT	0.37	23	141	164

Light concentrators of any coating rise the total NSB rate to 240 MHz, about 40% higher than for a bate PMT. However, due to the larger sensitive area the detected signal is increased by 60%. The signal to noise ratio can be calculated via

$$\text{Signal to noise} = \frac{\text{Signal}}{\sqrt{\text{NSB}_{\text{direct}} + \text{NSB}_{\text{indirect}}}}.$$

In total, the relative increase of the signal-to-noise ratio of the camera with light concentrators in comparison to a camera with only PMTs camera is strongly enhanced by a factor of 2.2.

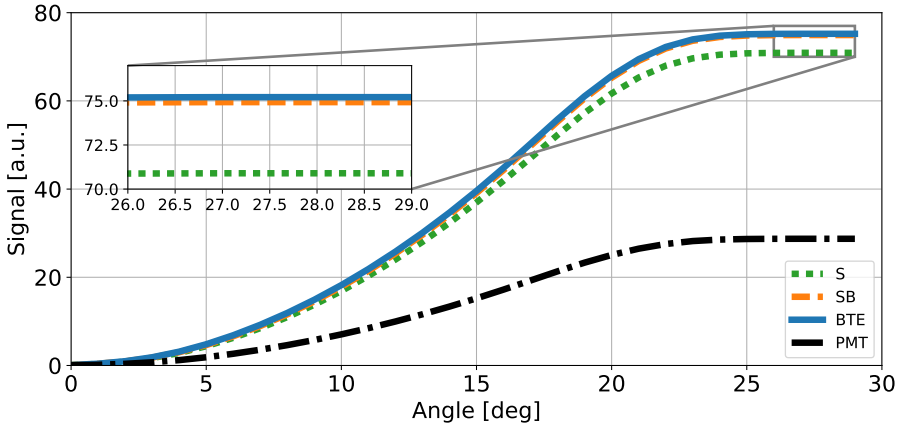

(a) Signal

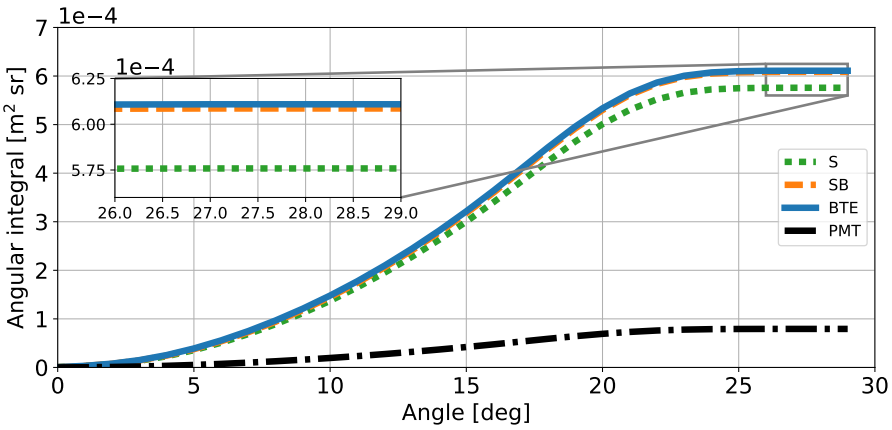

(b) Direct NSB

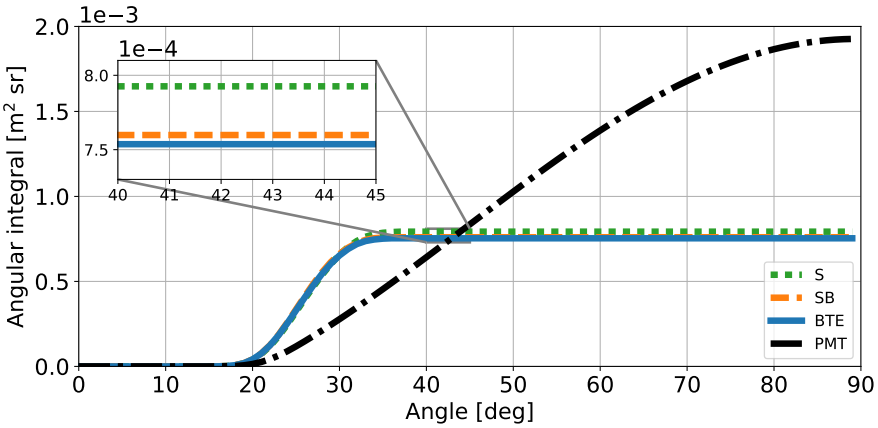

(c) Indirect NSB

Figure 3.29 Angular integrals for the calculation of the signal and the background rates detected by a camera pixel at 355 nm. (a) The signal is increased by a factor 2.7 for light concentrators in comparison with a bare PMT due to the larger sensitive area. (b) For the direct NSB background the increase factor is even 7.7 due to the difference in the solid angle. (c) Indirect NSB is reduced by the usage of light concentrators above 30°. Differences between the coatings are small.

3.8.2 Optimisation via the distance-acceptance angle correlation

In Section 3.4.3 a correlation between the acceptance angle and the distance between light concentrator exit and PMT surface was found. Each mm additional distance decreases the angle by approximately 1°. This way, the signal-to-noise ratio can be further optimised. For this study, the simulated distance dependent efficiency curves from Section 3.5.1 are used. Angular integration curves for signal and indirect NSB are shown in Figure 3.31. The integral of the direct NSB is equivalent to the signal integral.

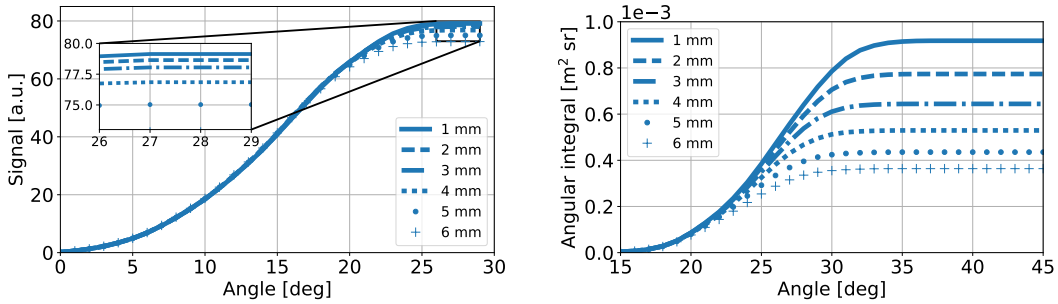

(a) Signal **(b)** Indirect NSB

Figure 3.30 Effects of smaller angular acceptance widths through increased PMT-light concentrator distances on the angular integrals for signal and NSB. While the signal decreases only slightly up to maximum 7%, the indirect NSB can be reduced by 20% per mm additional distance.

The smaller acceptance width barely effects the signal (and the direct NSB). In each mm step the relative decrease in light detection doubles from 0.5% at 2 mm up to 7% at 6 mm. However, the effect is more dramatic for the indirect NSB component. For each mm step, the angular integral is reduced by approximately 20%.
Assuming the same angular acceptance profile for all wavelengths and just renormalising the efficiency at 0° to the effective reflectivity of the spectral measurements allows to calculate the background rates by means of the simulated profiles. Obviously, this fine-adjustment depends on the pixel position on the camera. So far an average pixel position was assumed. Now, the visible mirror area for the innermost and outermost pixels will also be taken into account. Figure 3.31 shows the change in signal and total background for the different positions.

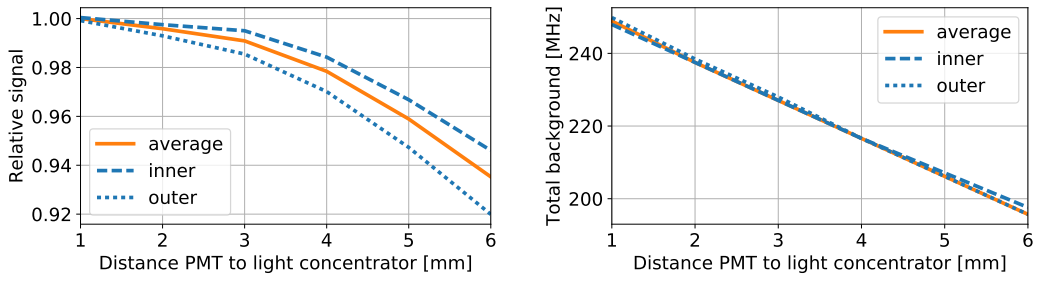

(a) Signal **(b)** NSB

Figure 3.31 Signal and total NSB background rates with increased light concentrator-PMT distance for different pixel positions. While the signal is only reduced by up to (7±1)%, the full background can be decreased by up to (26±1)%.

As discussed before, for the average pixel position the signal decreases up to 7% at 6 mm. For the background a reduction between 4% at 2 mm and 26% at 6 mm is achievable. Results from the outermost and innermost positions are within ±1% of those of the average position. The resulting signal-to-noise ratios can be found in Figure 3.32 normalised to the ratio at 1 mm distance for the average pixel position. At distances above 3 mm, the ratios seems to saturate as the angular acceptance starts to cut away few per cent of the signal from the mirrors. However, even for lower distances a 3%-4% higher signal-to-noise ratio can be gained with simultaneously 10% less background noise in each pixel. This provide an easy way to fine-adjust the signal-to-noise ratio of FlashCam if an additional space of 1-2 mm is available in the camera for moving the PDP modules.

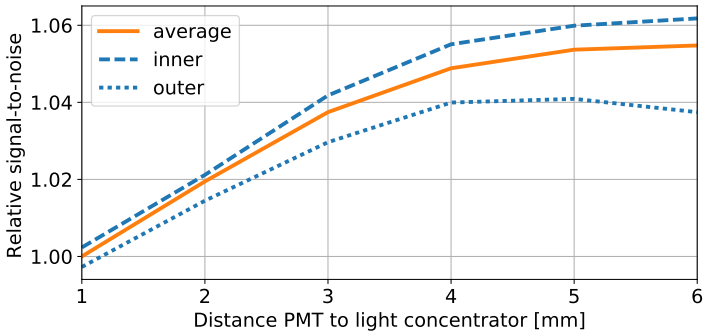

Figure 3.32 Distance dependent signal to noise ratio normalised to the ratio at 1 mm of the average pixel position. A maximum increase in signal to noise ratio of 4% for the outer, 5% for the average and even 6% for the inner pixel positions is possible.

3.9 Conclusion and outlook

By means of the specially developed optical components test system that uses a FlashCam PDP module and the actual FlashCam signal chain, light concentrators with three prototype coatings have been characterised. All three coatings show a similarly high effective reflectivity of typically above 85% for the angular and wavelength regime relevant for Cherenkov telescopes. A relatively steep cut-off of 8° and a maximum acceptance angle of 30.5° ensures full signal collection from the mirrors by simultaneously reducing ground reflected NSB from outside the telescope dish. Due to the diminution in dead space between pixels and this background suppression, a signal to noise ratio improvement of a factor of 2.2 can be achieved. By increasing the distance between the PMT surface and the light concentrator exit window by only a few mm, the acceptance angle can be decreased to cut more stray light. As a consequence, the signal to noise ratio can be even further optimised by 2% to 6%.
During climate chamber treatment of over 500 days, an ageing of the reflective material of only 4% is detected. This relates to over 5 years of operation without temperature control. Air-conditioning in the camera will lead to an even higher durability of the coatings.
A ray tracing simulation best matches the measurements of BTE coated light concentrators indicating that their angular acceptance profile is dominated by the concentrator geometry. In this model, the effective reflectivity at central light incidence is the only free parameter. With this simulation, the correlation between light concentrator-PMT distance and the acceptance angle is verified. Additionally the illumination pattern of the PMT surface is derived which may help in understanding the resulting PMT response during camera operation.

Regarding reflectivity and durability, all three prototype coatings are of high quality and fulfil the specifications for CTA cameras. As the BTE coating provides the highest signal collection, the FlashCam group decided to use this coating for the two preproduction cameras that are, as of summer 2018, in preparation. An additional 1-2 mm distance between light concentrator exit and PMTs is being considered.
In a next step, the available light concentrators will be installed on the photon detection plane of the prototype FlashCam camera in Heidelberg. A picture of the current status is shown in Figure 3.33. The FlashCam subgroup responsible for the prototype testing will now study influences of the light concentrators on the camera operation such as signal time-spreads expected from the illumination pattern of the PMT surface.

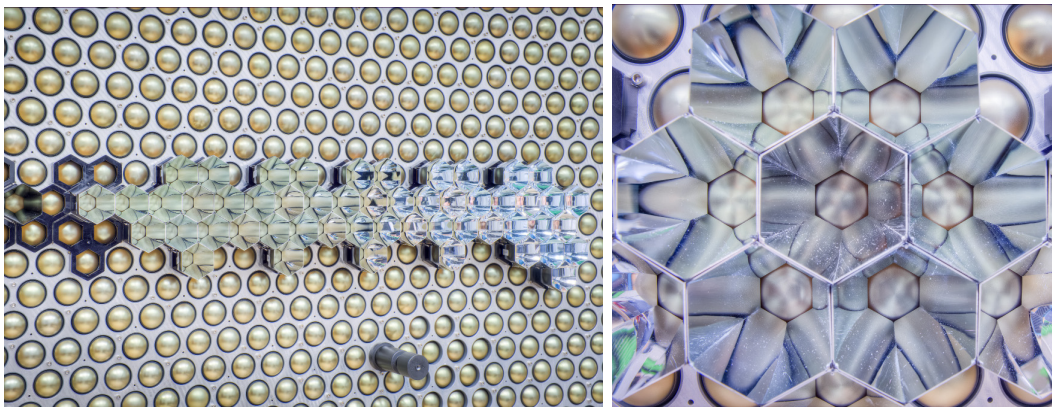

(a) Concentrators on PDP **(b)** Zoom

Figure 3.33 Status of light concentrator mounting on the prototype FlashCam camera (summer 2018). The characterised light concentrators are currently installed on the PDP so that influences of the concentrators on the camera output can be studied.

Furthermore, the climate chamber treatment of the sample concentrators is continued. Because the storage temperatures at the telescope sites could be even more severe than simulated up to now in the climate chamber, a new climate cycling with temperature variations between $-15°$ and $50°$ was recently started. As before, the key parameters of the concentrators will be regularly monitored. First results show no further degradation of the coating quality.
In summary, light concentrators will highly improve the signal light collection and as a result the data quality of FlashCam. This quality is wanted and needed to achieve the scientific goals in the core energy range of CTA between 100 GeV and 10 TeV. With the increased signal to noise ratio the observation time needed for high significance detection of TeV sources can be reduced offering an opportunity for more or more detailed studies of the most violent events in our universe.
To improve the performance not only of the MSTs but the whole CTA array, a different approach is needed. CTA uses the experiences gathered in IACT projects over the last 30 years and develops telescope structures, optomechanics, software as well as reconstruction algorithms to advance the current state of the art. In the next chapter, the CTA reconstruction procedures are presented and optimised quality selection cuts are developed that improve the angular resolution of CTA to a level never reached in TeV astronomy before.

"Open your eyes,
look up to the skies and see."

Queen, *Bohemian rhapsody*, 1975

CHAPTER 4

Optimisation of the angular resolution of CTA

Two important properties of an TeV gamma-ray instrument are the flux sensitivity and the angular resolution. While the first describes the lower flux limit above which gamma-ray emission from a source can be detected, the latter quantifies the ability to resolve the actual structures of the emission regions. Even so both, the spectral and the angular performance of the future CTA observatory, are studied in this chapter, the main focus will be on the angular resolution. Current TeV instruments such as the Large Area Telescope (LAT) on board the Fermi satellite, the IACT H.E.S.S. experiment or the particle detector array HAWC reach angular resolutions between 0.5° and 0.05° or 5'-30' (see Figure 4.1).

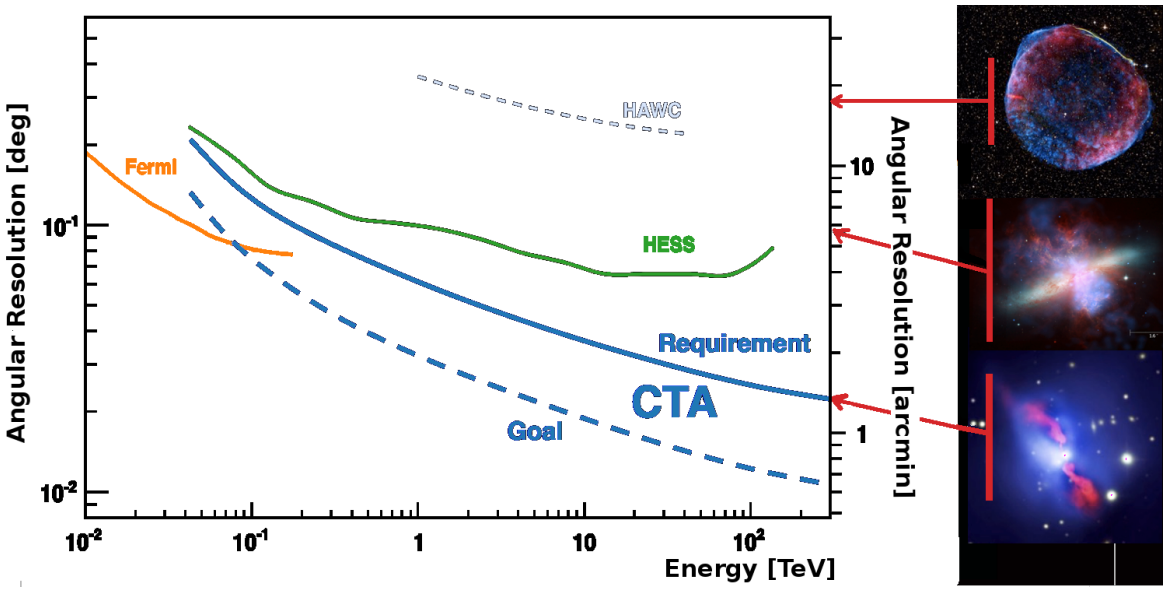

Figure 4.1 Expected angular resolution of CTA compared to other current gamma-ray observatories. While HAWC is able to detect supernova remnants like that of SN1006 (right panel, top), Fermi and H.E.S.S. can resolve smaller sources such as the galaxy M82 (right panel, center). The goal of CTA is to improve the resolution by an order of magnitude to be able not only to detect those sources as well as smaller ones like the galaxy cluster Hydra A (right panel, bottom), but also to study their morphology in more detail as currently possible. Images from Chandra, HST and Spitzer.

During the H.E.S.S. galactic plane survey (Abdalla et al., 2018b), it was found that most TeV source are not point-like but extended. With the current resolution the extension of large TeV sources such as supernova remnants (SNR) or pulsar wind nebulae (PWN) with typical sizes of tens of arcminutes (Green, 2014; Abdalla et al., 2018c) are visible. To study the structures of these extended sources in detail and to understand where exactly in those objects the TeV emission is produced, better angular resolutions are needed.
Recently, Holler et al. (2017) reported an extension of the Crab nebula of 54" obtained by re-evaluation of H.E.S.S. data with a better understanding of their point-spread function and thus a better angular resolution. This analysis opened up the field of TeV source studies in the sub-arcminute regime. With the CTA goal resolution such extended source morphologies can be studied with an even higher accuracy and inner structures and the actual TeV emission sites can be determined much more precisely. Also small sources such as clusters of galaxies, star forming galaxies and bright stars of few arcseconds that are visible at TeV energies can be detected. This will lead to a better understanding of the acceleration and propagation mechanisms of cosmic-rays inside and outside our own galaxy. Morphological interesting objects such th closest radio galaxy Centaurus A, for which an inner structure is predicted (Abdalla et al., 2018a) but not yet resolved will be promising targets of CTA in the future.
One way to achieve the required performance of CTA is the optimisation of the event reconstruction algorithms that determine the EAS properties. In general, the reconstruction is based on the analysis of the quasi-elliptical images of the showers recorded by the telescope cameras. From the calibrated and cleaned images specific characteristics are determined that are compared to the results of extensive simulations of EAS and camera responses in order to reconstruct the primary direction of the shower inducing particle, the extrapolated impact position of the shower on ground, the primary energy as well as the particle type.
In this chapter, the simulations needed to perform the event reconstruction will be presented. Afterwards, a step-by-step description of the reconstruction process is given. Two different reconstruction algorithms are discussed in detail and their performance is shown. This performance can be optimised by quality selection cuts on the recorded data. Different preselection and postselection cuts that enhances the angular resolution and the flux sensitivity of CTA will be established in the course of this chapter.

4.1 Air shower simulations

All current reconstruction approaches rely on knowledge about EAS gained in extensive Monte-Carlo and ray-tracing simulations. These simulations are performed in two steps (Bernloehr, 2008). First, air showers are generated with the Monte-Carlo based CORSIKA (Heck et al., 1998) code. Initial particles of different energies and zenith angles are generated and their path through the atmosphere is simulated including all relevant effects such as bremsstrahlung, pair production, energy loss due to ionisation, multiple scattering, bending of the particle tracks due to the geomagnetic fields and annihilation of particles. Each secondary particle is tracked successively in the same way. Altitude-dependent density and optical extinction models are used for the atmosphere expected at the telescope operation site. For all charged particles the Cherenkov light produced along the particle's path is determined. Examples of showers produced in CORSIKA can be found in Figure 1.4. To study the shower properties in detail several 10^6 primary particles per energy are simulated.
In a second step, the photons are used as input for a full *sim_telarray* ray-tracing simulation of the telescope optics. Telescope properties such as the form, the focal length and the reflectivity of individual mirror segments including effects of random misalignments can be

taken into account. The photons are traced to the focal plane where their way through the camera optics is simulated. For each photon a detection probability is calculated including the shadowing of the camera housing and the telescope structure, the optical efficiency of the light concentrators, the quantum and collection efficiency of the PMTs and possible variations of theses values within the camera. Also transit time jitters of photo-electrons through the PMTs to the anode due to variations of the applied high-voltages are considered. A background noise in form of a fixed NSB p.e. rate is added to each pixel also processed by the optical response of the camera. For the NSB photons additionally afterpulsing is included, created by ions within the PMTs that are accelerated towards the photo-cathode. Those signals are usually cut by selecting a time window around the faster ns photon signal, however, previously detected NSB photons could create an afterpulsing signal during the detection period of a Cherenkov photon and the effect can therefore not be neglected.
Finally, the detected signal is traced through the camera electronics passing through the digitisation process that takes into account the variations of the photon arrival times and transit time jitters. The sum over all photons in each pixel creates patterns on the camera that are then analysed by the different trigger algorithms of each Cherenkov camera. An array-wide telescope trigger in the end searches for timely coincidences between the signals of the individually triggered cameras.
This way, camera images for different telescope types and specific energies, zenith angles and impact distances are generated. Such simulations were able to accurately reproduce the performances of IACT projects, for example of the H.E.S.S. experiment.
Simulations are crucial for the data analysis of IACTs. They are used to generate look-up tables of typical image parameters created by showers with specific characteristics, to train neural networks or to produce image templates that are compared to measured images. Without the high accuracy reached by the simulations, the reconstruction of the main shower properties such as the shower energy or the particle identity would be impossible.

4.2 Event reconstruction with ctapipe

For the performance analysis described in this chapter, the pipeline prototype software *ctapipe* (Kosack et al., 2017) is used. Contrary to most previous software prototypes, *ctapipe* follows a top-down code writing approach in which the main functionalities are written in the programming language *python* and only specific time critical parts of the software are implemented in *C++*. This approach was chosen because *python* offers a user friendly implementation environment in which many basic functionalities are already available in established libraries. Additionally, it is a widely used programming language not only within astronomy but also in other scientific fields and industry so that a large community of users is interested in the implementation and maintenance of stable and high quality functions and libraries. The steps taken from the raw data to the final astronomical data are now discussed in detail.
As explained in Section 1.3.2, particle induced air showers create almost elliptical images in an IACT camera (see Figure 4.2a for more details). If a camera triggers, the raw data of those images is transmitted to a common data server. After calibration, the images contain the number of measured p.e. in each pixel. The images are cleaned with a two-level *tail cut* (Daum, 1997) that keep the signal of only those pixels whose intensity is above a first limit and who have at least one neighbouring pixel containing more p.e. than required by a second lower limit. This way, the significant signal remains while night sky background noise and isolated pixels with high signal amplitude are largely discarded.

From the cleaned images, the moments of the ellipses are calculated. Those *Hillas parameters* were introduced by Hillas (1985) for single IACTs and later adapted for multi-telescope projects (see e.g. Hofmann et al. (1999)). Usually six parameters are used: The centre of gravity (COG) of the image, length and width of the ellipse, the orientation of the image in the camera frame, the distance of the COG to the camera centre and the amplitude corresponding to the total signal contained within the ellipse (see Figure 4.2b).

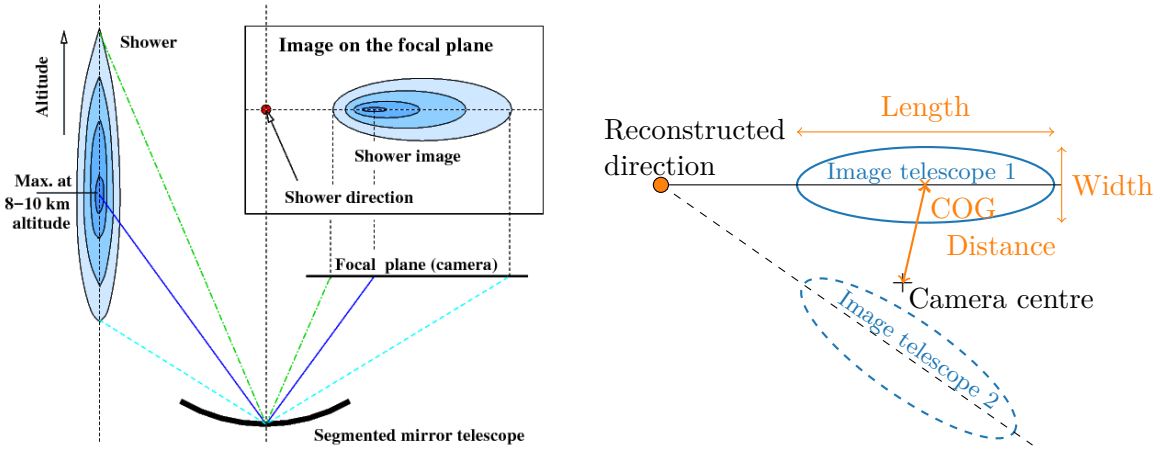

(a) Camera image **(b)** Hillas parameters

Figure 4.2 Parameterisation of the Cherenkov shower images. (a) The Cherenkov light from EAS creates an elliptical image in the focal plane camera of a telescope. Image by Voelk and Bernloehr (2009a). (b) The elliptical images can be described by Hillas parameters including the centre of gravity, width and length of the image and the distance of the COG to the camera centre. A shower image from a second telescope is overlaid in this picture to show how the reconstruction of the shower direction is performed. Image reproduced from Aharonian et al. (2006).

Quality cuts on the data ensure that the event reconstruction is based on images with clearly visible signal properties. Using only high amplitude images in which the full signal shape is contained and not truncated by the camera FOV will obviously lead to better reconstruction. However, a low number of images can increase the reconstruction error. A good trade-off between a careful selection of high quality shower data and high event statistics is crucial.
With different algorithms, the direction of the primary shower particle, the impact position of the shower core on the ground and the primary energy are reconstructed from the remaining events. Two reconstruction mechanisms will be presented later in this section.
Cherenkov telescopes not only detect gamma-ray induced air showers but also a background created by hadronic showers that outnumber the gamma-rays by a factor of 10^4. Efficient and stable background identification is important for high sensitivity. As leptonic and hadronic showers develop differently in the atmosphere (see Section 1.2), the images created in the camera and the Hillas parameters differ (see Figure 4.3). While e.g. gamma-induced showers have a small lateral distribution resulting in a smaller width and a larger length of the signal, hadronic showers are more often spread out over the camera. Also muons leave characteristic ring features in the image classifying an event as hadronic. Based on such differences, various background rejection methods were developed for different reconstruction algorithms.
From the reconstructed data, *event lists* are created containing all relevant event information of a dedicated observation period. With the corresponding instrument response functions provided by CTAO, observers can then perform detailed studies of TeV gamma-ray sources.

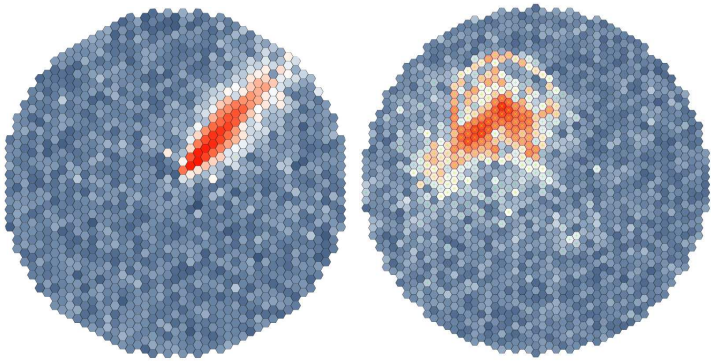

Figure 4.3 Camera images of a gamma-ray and a proton shower. In general, gamma-ray showers (left) are more concentrated around the shower axis generating elongated signals with small widths. Cosmic-ray showers (right) are more diffuse due to their increased substructure.

4.2.1 Hillas reconstruction

With the Hillas reconstruction algorithm, source direction and energy of a primary EAS particle as well as the particle type are determined from the Hillas parameters. For the source direction, the main axes of the elliptical images of different cameras are compared in a common camera reference frame as shown in Figure 4.4. Their intersection point provides an estimate of the source direction. An event that is captured by N cameras will result in $\frac{1}{2}N(N-1)$ points. The source direction is then estimated as an average over all intersection points weighted with the sine of the intersection angle and the image amplitude.
The same approach is used for the reconstruction of the impact position. This position describes where the extrapolated shower axis reaches the detector plane. For the calculation of this point, the axes connecting the camera centre and the COG of the selected images are studied in a common array-wide coordinate system that is tilted perpendicular to the array pointing direction. The process is shown in Figure 4.4. As for the source position these axes will intersect and an amplitude and intersection angle weighted average is calculated.
In this work, for the Hillas energy reconstruction of each event a Gradient Boosting Regressor is employed that uses Boosted Decision Trees (BDTs). BDT (Hoecker et al., 2007) regressors or classifiers are based on binary decision trees (see Figure 4.5). At each node of the tree the best split criteria for a training sample of events is determined to either discriminate between two classes of events (classifier) or to estimate a specific value by minimising an error function for a target variable (regressor). This process is repeated until a predefined minimum number of events or a limit in the error function is reached. To improve the performance and to reduce the effect of statistical fluctuations in the training set, several decision trees are trained with the same set of events applying higher weights to those misclassified in a previous tree. The answers of the resulting forest of decision trees are combined by averaging.
For the Hillas energy reconstruction, the decision trees are trained with a set of image amplitudes, impact distances and widths and lengths of the Hillas ellipses of events simulated as described in Section 4.1. The final shower energy is found as the average of the individual telescope results weighted with the square root of the amplitude.
A major challenge in TeV gamma astronomy is the discrimination between EAS generated by gamma-rays from astrophysical sources and those by hadronic cosmic rays. BDT classifiers trained on simulated gamma and hadron events can calculate a probability of an event to be gamma-like. Probability distributions for several energies are shown in Figure 4.6. For each bin of simulated energy a cut value is defined that contains 80% of the gamma-ray events.

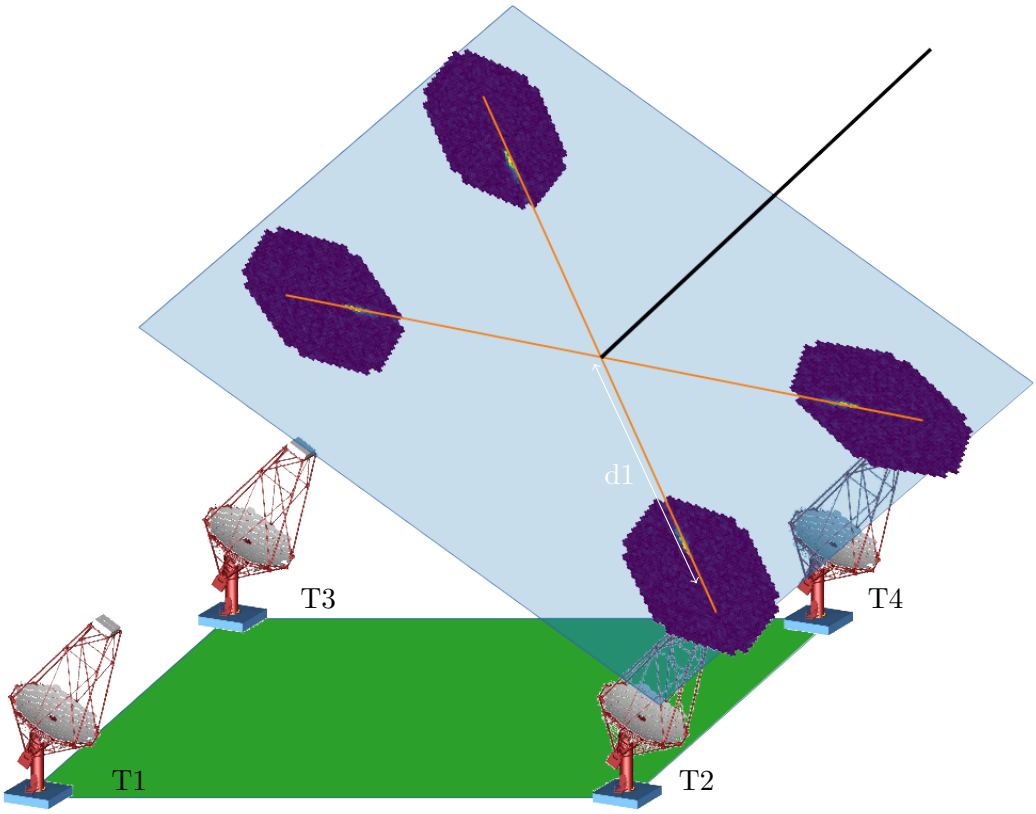

Figure 4.4 Calculation of the impact distance with the Hillas reconstruction algorithm. The extrapolated axes (orange) between camera centre and COG of the signal for several cameras are studied in a tilted array-wide coordinate system (blue). The intersection point signifies the position at which the shower axis (black) reaches the detection plane. The impact distance (white) is the distance between this point and the telescope position.

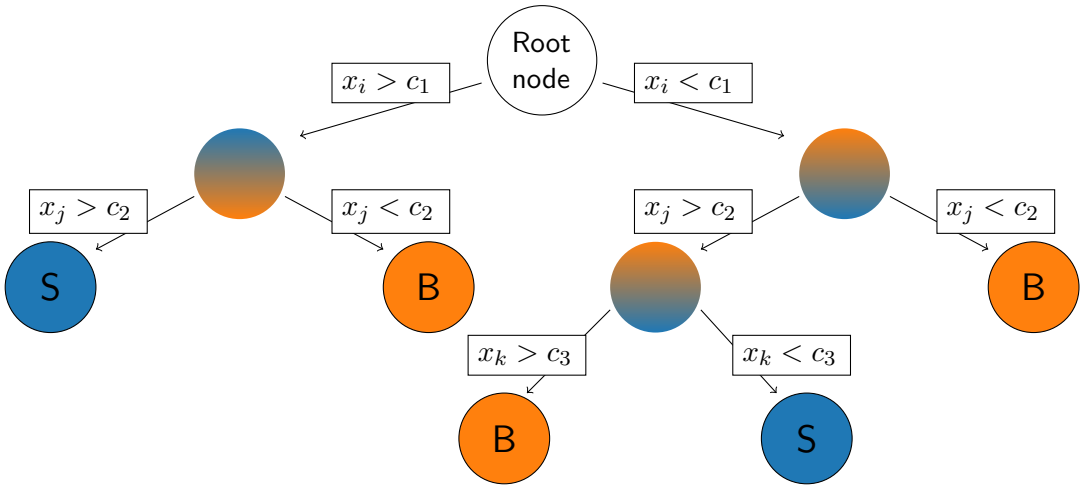

Figure 4.5 Schematic of a decision tree. For a root set of events with specific parameters $\vec{x}$, a split criterion c_1 is determined based on a parameter x_i to discriminate between signal (S) and background (B). This is repeated successively for the subsets of events until a stopping criterion is reached. The results stated at the leafs on the bottom of the tree are combined to a final classification value. Image reproduced from Hoecker et al. (2007).

In the event reconstruction events this cut is then used on the reconstructed energy that depending on the data quality deviates from the simulated energy. Nevertheless, depending on the energy, a discrimination of 90% of the hadron background is achievable while 80% of the gamma events are retained. As images at larger energies are typically larger and easier to parametrise, this classification works better for higher energies.

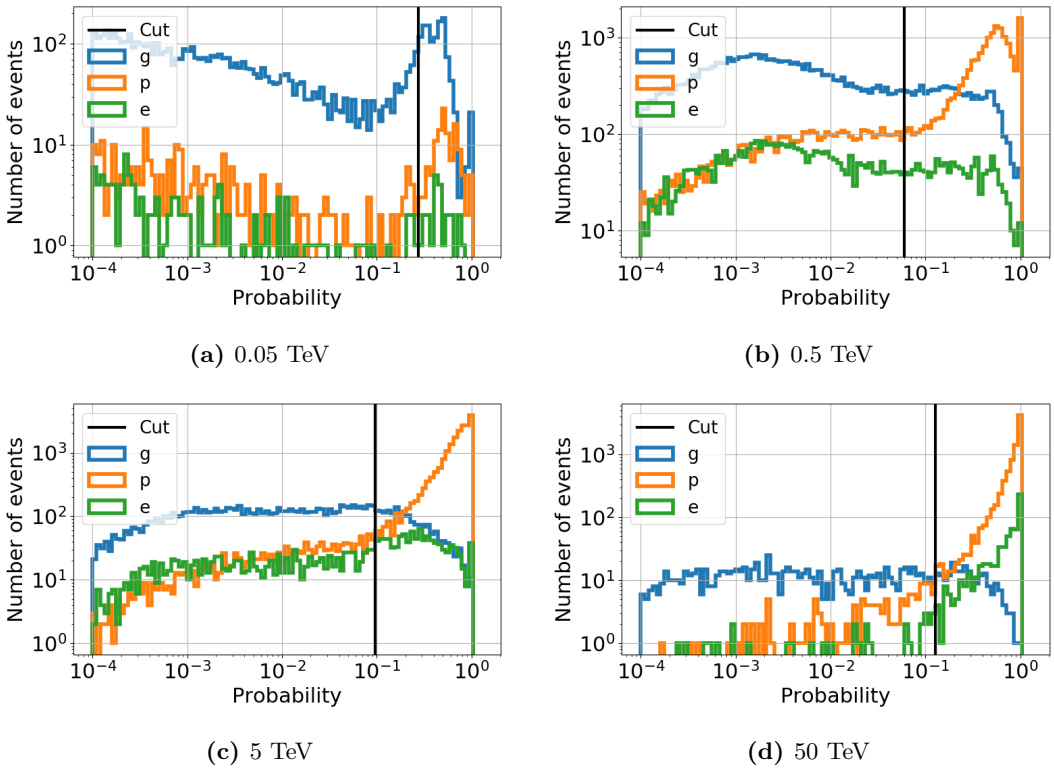

(a) 0.05 TeV **(b)** 0.5 TeV

(c) 5 TeV **(d)** 50 TeV

Figure 4.6 Background rejection by a probability distribution cut. BDTs classify events into signal and background. A cut on the 80% containment of the gamma events reduces the hadronic background in the reconstruction. This classification works better for higher energies.

The Hillas reconstruction proved to be stable and reliable in obtaining the main properties of EAS and was used with variations in all IACT projects (Hofmann et al., 1999). However, as the shower images in the IACT cameras are slightly asymmetric, the ellipse parametrisation is only an approximation and image information is lost during the reconstruction.

4.2.2 ImPACT reconstruction

A more complex reconstruction method was developed by Le Bohec et al. (1998) and improved by de Naurois and Rolland (2009). It uses a semi-analytical model to predict the light distribution on Cherenkov telescopes cameras depending on the direction and energy of the shower inducing particle, the height of the first interaction in the atmosphere, the impact distance of the telescopes and the telescope response. From the predictions, image templates are generated and compared to the recorded images in a multi-dimensional likelihood fit. This approach uses the full provided image information and significantly improved the reconstruction performance for EAS showers. However, it becomes unstable at the highest energies as there, fluctuations in the shower beyond the purely statistical fluctuations become relevant, but are not predictable by the models.

Instead of a semi-analytical model, the Image Pixel-wise fit for Atmospheric Cherenkov Telescopes (ImPACT) by Parsons and Hinton (2014) uses Monte-Carlo simulation generated templates that represents images taken by perfect cameras and fits them to the recorded camara images in the same likelihood fitting approach as in the model-based reconstruction. To generate those templates a grid of energies, impact distances, zenith and azimuth angles is chosen as input parameters. A full CORSIKA simulation of air showers at the different energies and direction angles and a *sim_telarray* simulation for the impact distances are performed for all telescope types as described in Section 4.1. The resulting camera images are binned for different values of the maximum particle emission height $X_{\max}$ of the showers in the atmosphere and stacked for a set of input parameters. In this work, for the first time a neural network approach is used for fitting of the light intensity distribution surface in the camera. For a fixed two-dimensional grid, the fitted surface is evaluated and stored as a template. Templates with low photon statistics are discarded. Four examples of templates with different input parameters are shown in Figure 4.7 and a comparison between a template and a simulated camera image is displayed in Figure 4.8.

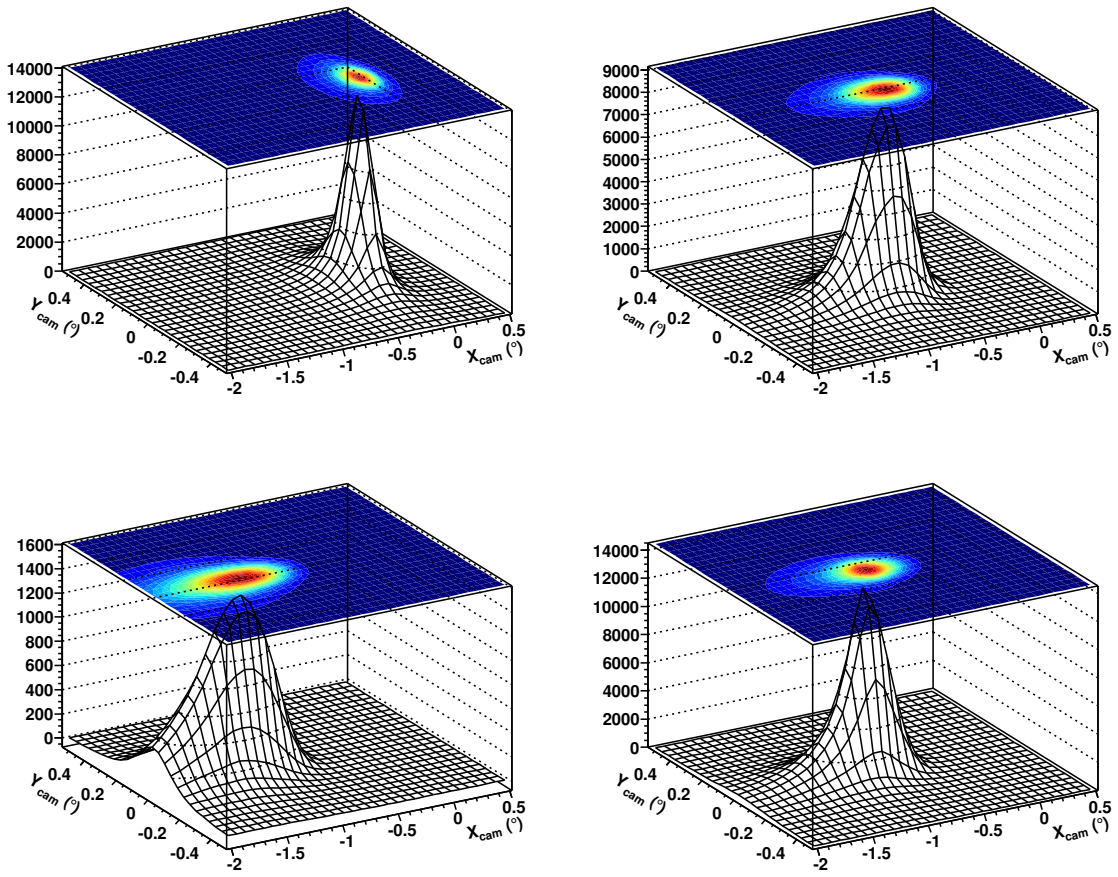

Figure 4.7 Templates for an 1 TeV gamma-ray induced air shower at different impact distances and shower depth. The plots on the top left, top right and bottom left show a shower with $X_{\max} = 300\,\mathrm{g\,cm^{-2}}$ and impact distances of 20 m, 100 m and 200 m, respectively. For the template on the bottom right, $X_{\max}$ is $400\,\mathrm{g\,cm^{-2}}$ and the impact distance is 100 m. The heights of the histograms are given in p.e. per square degree. Image from Parsons and Hinton (2014).

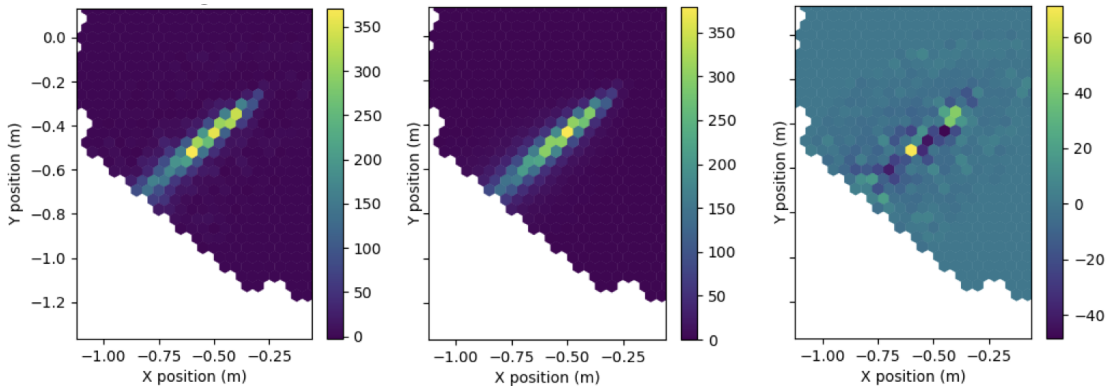

(a) Image **(b)** Template **(c)** Residual

Figure 4.8 Comparison between shower image and template. The shower (a) is very well predicted by the template (b). No significant signal remains in the residual image (c). Images by D. Parsons.

For the reconstruction, the templates are oversampled depending on the camera used for detection to match the resolution due to the camera pixel size. To compare the recorded camera images of an observation to the templates, a likelihood fit is applied. For any position in the input parameter space, the signal likelihood of the templates to the images can be calculated for each pixel in each telescope. The likelihood of a signal s in one pixel of a measured image compared to an expected signal μ of a corresponding pixel in a template image can be described as a convolution of the Poisson distribution of the n photo-electrons generating the signal and the resolution of the detecting photomultiplier. The latter is typically expressed as a Gaussian distribution with a width of $\sqrt{\sigma_p^2 + n\sigma_\gamma^2}$ where σ_p is the width of the pedestal distribution that describes electronic noise as well as the NSB photons while σ_γ is the width of a single photo-electron peak. The likelihood can then be written as

$$\mathrm{P}(s|\mu, \sigma_p, \sigma_\gamma) = \sum_n \frac{\mu^n e^{-\mu}}{n!\sqrt{2\pi(\sigma_p^2 + n\sigma_\gamma^2)}} \exp\left(-\frac{(s-n)^2}{2(\sigma_p^2 + n\sigma_\gamma^2)}\right) \tag{4.1}$$

For large expectations $\mu > 5$ the Poissonian distribution can be approximated by a Gaussian function and the convolution of the two Gaussian components results again in a Gaussian.

$$\mathrm{P}(s|\mu >> 0, \sigma_p, \sigma_\gamma) \approx \frac{1}{\sqrt{2\pi(\sigma_p^2 + \mu(1+\sigma_\gamma^2)}} \exp\left(-\frac{(s-\mu)^2}{2(\sigma_p^2 + \mu(1+\sigma_\gamma^2)}\right) \tag{4.2}$$

In the current version of *ctapipe* only this Gaussian limit is used. Also, at high energies and large impact distances the statistical fluctuations in the shower decrease due to the large number of particles, so that intrinsic shower fluctuations become relevant. These intrinsic fluctuations are not accounted for in the current likelihood function.
The resulting value is converted into a variable that asymptotically follows the behaviour of a χ^2 variable of a typical fitting routine. This pixel log-likelihood is

$$\ln \mathrm{L} = -2 \cdot \ln \mathrm{P}(s|\mu, \sigma_p, \sigma_\gamma) \tag{4.3}$$

The log-likelihood value is calculated and summed up for each image pixel of all telescopes to create an event likelihood for the initial shower parameters. In a six-dimensional fit of

the zenith and azimuth angle of the source direction, the energy, the interaction height $X_{\max}$ and the impact position this likelihood is minimised using the MINUIT (James and Roos, 1975) routine. For this purpose, the MIGRAD subroutine uses the Davidson-Fletcher-Powell formula (C. Davidon, 1991; Fletcher and Powell, 1963), that follows the gradient of the likelihood surface function to reach its minimum. Errors for each parameter are calculated from the width at $(\ln L - \ln L_{\min}) = 1$, assuming a parabolic form of the likelihood surface around the minimum at $\ln L_{\min}$ as shown in Figure 4.9.

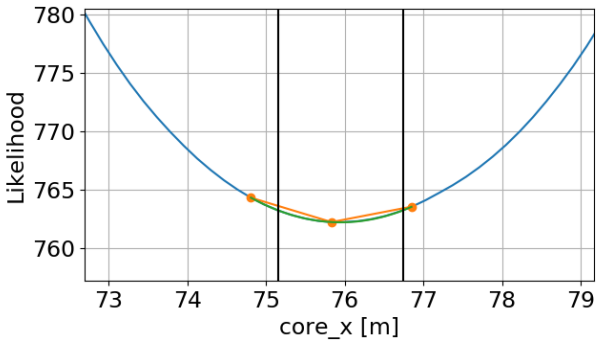

Figure 4.9 Calculation of the likelihood fitting error. For a fixed parameter (x coordinate of the shower core position), the likelihood surface (blue) should behave like a parabola around the minimum. A parabola (green) is fitted through three points on the surface (orange) chosen by stepping a fixed distance away from the minimum. The error corresponds to the width at $\ln L_{\min} + 1$ (black).

The convergence of this fitting procedure strongly depends on its initial seeding as the fit could otherwise converge to a local minimum occuring frequently in the log-likelihood surface. The ImPACT reconstruction therefore uses the results of the classical Hillas reconstruction as seeding positions for the fit. Improvements could be made by better seeding.
Finally, to judge the quality of the reconstructed parameters a *Goodness of Fit* (GOF) value is calculated for each fit:

$$\mathrm{GOF} = \frac{\sum_i [\ln L(s_i, \mu_i) - < \ln L > |\mu]}{\sqrt{2 \cdot \mathrm{NdF}}} \tag{4.4}$$

$$< \ln \mathrm{L} > |_\mu = \int \mathrm{d}s \ln \mathrm{L}(s|\mu, \sigma_p, \sigma_\gamma) \times \mathrm{P}(s|\mu, \sigma_p, \sigma_\gamma) \qquad \mu <= 5 \tag{4.5}$$

$$< \ln \mathrm{L} > |_\mu = 1 + \ln(2\pi) + \ln(\sigma_p^2 + \mu(1 + \sigma_\gamma^2)) \qquad \mu > 5, \tag{4.6}$$

where $< \ln \mathrm{L} > |_\mu$ is the average log-likelihood for a given set of μ, σ_p and σ_γ and NdF the number of free parameters in the fit procedure.
The distribution of GOF values for all events is expected to be Gaussian with a mean of zero and an RMS of unity. As mentioned before at high energies, intrinsic shower fluctuations become relevant. As this is not included in the likelihood function, this leads to larger differences between recorded and template images and creates tails in GOF distribution as seen for the gamma-ray showers in Figure 4.10
As the templates are generated for gamma-ray induced air showers, stronger deviations are expected for hadronic showers with their wider lateral distribution and increased amount of substructure. The higher GOF values in the fitting procedure can be used as a background discriminator. Examples of GOF distributions for proton and electron events are also shown in Figure 4.10. As for the probability calculated by the BDTs for the Hillas reconstruction, an

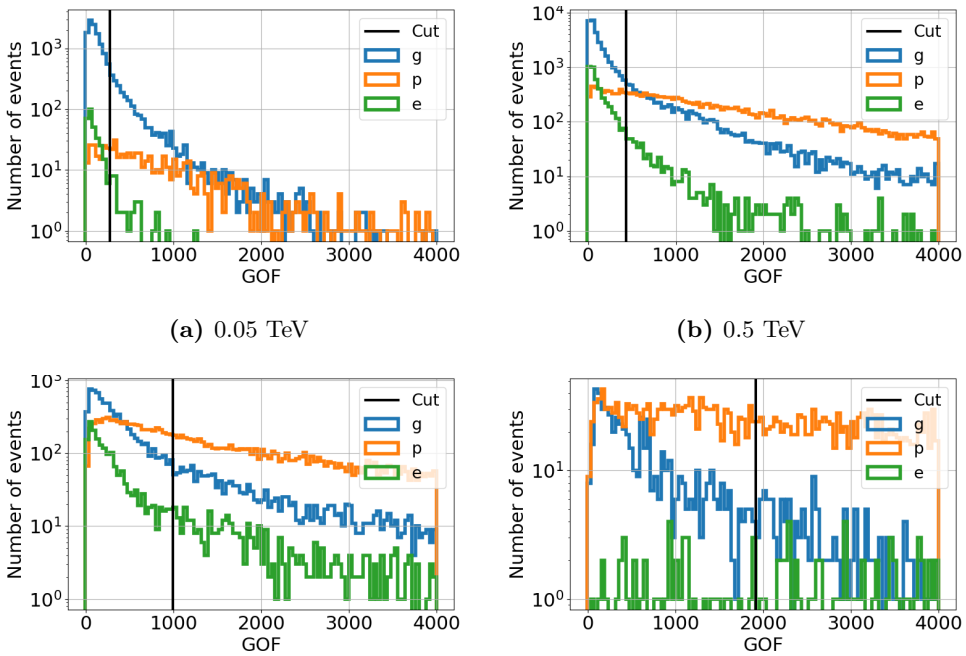

(a) 0.05 TeV **(b)** 0.5 TeV

(c) 5 TeV **(d)** 50 TeV

Figure 4.10 Background rejection by a GOF distribution cut. As the templates are generated from gamma-ray shower simulations, the GOF value increases for hadron events. A cut on the 80% containment of the gamma events reduces the hadronic background in the reconstruction.

80% containment cut is determined based on the GOF distribution in each bin of simulated energy. By applying this cut to the reconstructed energy during the event reconstruction, depending on the energy, a suppression of 95% of the hadronic background is possible.
Due to larger deviations of the templates at higher energies, the background classification works better at low energies. While it provides a better event classification than the BDT approach of the Hillas reconstruction below 2 TeV, at higher energies the opposite is observed. To make up for this point, in the following the GOF classification will be used for reconstructed energies below 2 TeV, the BDT classification above.

4.3 Quality selection cuts

The determination of shower parameters relies on the correct determination of the Hillas parameters and the quality of the combined reconstruction of different camera images. Preselection of the images based on the Hillas parameters and postselection of reconstructed parameters based on the telescope position and multiplicity or the estimated reconstruction uncertainties can improve the results. In this work, the optimisation of selection cuts is performed by means of simulations. Details of the simulation are given in Table 4.1.
The telescope layout used in this study (see Figure 4.11) is close to the final CTA layout proposed for the Southern hemisphere and includes the three types of telescopes described in Section 1.3.3. In total, the array contains 3 LSTs, 24 MSTs and 73 SSTs (the final array will have 4 LSTs, 25 MSTs and 70 SSTs, see Hassan et al. (2017)). Apart from the full-array performance, the performance of subarrays containing only one telescope type are studied individually. The telescope pointing is set to an azimuth of 180° and a zenith of 20°.

Table 4.1 Parameters for the CORSIKA Monte-Carlo shower simulation of gamma-rays, electrons and protons and the calculation of the differential flux sensitivity.

Variable	γ	e	p
Simulated detection area $A_{\mathrm{sim,p}}$ [km^2]	19.6	28.3	28.3
Number of simulated events $N_{\mathrm{sim,p}}$ [10^9]	0.13	3.5	2.6
Observation time t_{obs} [h]	50	50	50
Simulated energy range [TeV]	0.003-330	0.004-600	0.003-320
Index of simulated particle spectrum	-2	-2	-2

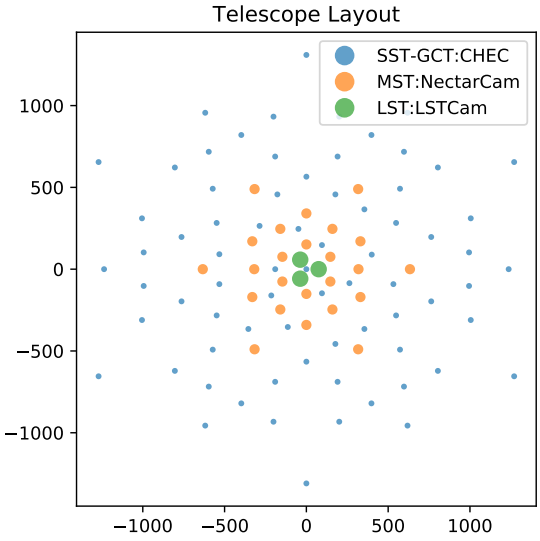

Figure 4.11 Simulated telescope array layout. This layout includes 3 LSTs, 24 SSTs and 73 SSTs and is close to the final layout of CTA South. In the simulation, the LSTs are equipped with LSTCams, the MSTs with NectarCams and the SSTs with CHEC cameras. For the SSTs the GCT telescope structure is assumed that has a Davis-Cotton layout. Distances are given in meters.

As a benchmark for the optimisation the expected angular resolution and the differential flux sensitivity of CTA is determined. To calculate the angular resolution, the selected events are sorted into a histogram with 20 logarithmic energy bins E_{bins} between 0.01 TeV and 100 TeV. For each energy bin the angular difference between the reconstructed and the simulated source direction is again plotted in a histogram. While these histograms correspond to the energy-dependent one-dimensional Point-Spread Function (PSF) of the system, the angular resolution is defined as the 68% containment radius of the events in the PSF (see Figure 4.12). In an actual observation, apart from an *on* measurement of a region of interest, multiple *off* measurements around the source location are recorded to estimate the background. There are different ways to chose the regions within an image that are defined as signal and background region. One typical method is the *reflected background method* (see e.g. (Berge et al., 2007)): An *on* region is chosen around the source of interest that has a certain offset to the telescope pointing direction. Several *off* regions are then selected of the same size as the *on* region and reflected around the pointing direction to get an estimate of the background in this region. This method is sketched in Figure 4.13. As the acceptance in the FOV of an instrument is

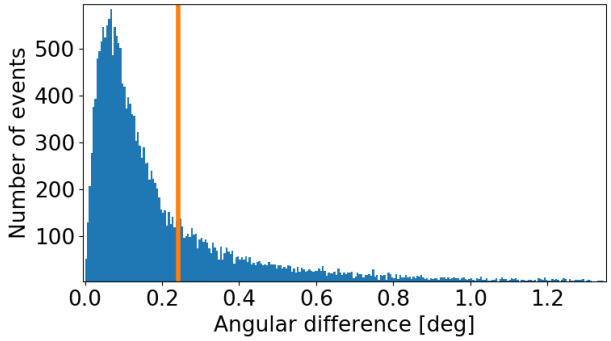

Figure 4.12 Calculation of the angular resolution. For each energy bin, a histogram of the angular distance between reconstructed and simulated direction is created. The orange line corresponds to the 68% containment radius of this histogram and defines the angular resolution at this energy.

assumed to be radial symmetric, this method excludes influences of the FOV position on the signal and background determination. The value α specifies the relative acceptance of the on to the off regions. Assuming this method, for the presented analysis a value $\alpha = 0.2$ is chosen. This would correspond to one *on* and 5 *off* regions.

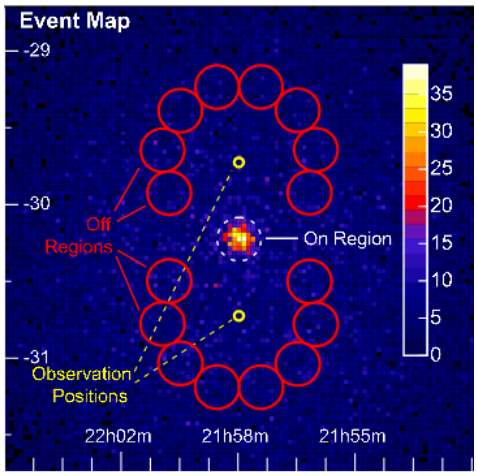

Figure 4.13 Reflected region method as an example for background estimation in an observation. An *on* region around a source of interest is reflected around the observation position to select *off* regions with the same radial distance to the FOV centre. The area close to the *on* region is omitted to reduce influence from source photons. Image taken from (Berge et al., 2007).

The differential flux sensitivity signifies the minimum flux detectable by the telescope array with a 5σ significance over background at a specific energy bin. To calculate this sensitivity, the significance of a source detection over background noise is determined via Equation 17 of Li and Ma (1983):

$$S = \sqrt{2}\left\{N_{\text{on}} \ln\left[\frac{1+\alpha}{\alpha}\left(\frac{N_{\text{on}}}{N_{\text{on}}+N_{\text{off}}}\right)\right] + N_{\text{off}} \ln\left[(1+\alpha)\left(\frac{N_{\text{off}}}{N_{\text{on}}+N_{\text{off}}}\right)\right]\right\}^{1/2} \tag{4.7}$$

where N_{on} is the number of events classified as signal and N_{off} of those classified as background. The number of events in the simulations of a specific environment are calculated via:

$$N(E) = \int_{\mathrm{E_{bins}}} F(E) A_{\mathrm{eff}}(E) t_{\mathrm{obs}} \tag{4.8}$$

$$A_{\mathrm{eff}}(E) = A_{\mathrm{sim}} \frac{N_{\mathrm{passcuts}}(E)}{N_{\mathrm{sim}}} \tag{4.9}$$

Angular cuts on the size of the *on* region are discussed in Section 4.3.2. The rates are determined for all particle types with A_{eff} the effective collection area and N_{passcuts} the number of events after selection cuts. The fluxes assumed for each particle are

$$F_{\gamma}(E) = 3 \cdot 10^{-7} E^{-2.5} \, [\mathrm{TeV}^{-1}\mathrm{m}^{-2}\mathrm{s}^{-1}] \tag{4.10}$$

$$F_{\mathrm{p}}(E) = 0.215 E^{-2.67} \, [\mathrm{TeV}^{-1}\mathrm{m}^{-2}\mathrm{s}^{-1}\mathrm{sr}^{-1}] \tag{4.11}$$

$$F_{\mathrm{e}}(E) = 105 \cdot 10^{-6} E^{-\Gamma_1} (1 + (\frac{E}{E_b})^{\frac{1}{\zeta}})^{-(\Gamma_1 - \Gamma_2)\zeta} \, [\mathrm{TeV}^{-1}\mathrm{m}^{-2}\mathrm{s}^{-1}\mathrm{sr}^{-1}] \tag{4.12}$$

with $\Gamma_1 = 3.04$, $\Gamma_2 = 3.78$ and $\zeta = 0.12$ in the H.E.S.S. electron spectrum (Kerszberg et al., 2017) in Equation 4.12. Further values are specified in Table 4.1. The differential flux sensitivity is then calculated via a scaling factor for the flux that ensures an at least 5 σ detection of a source for a given energy bin.
Both, angular resolution and flux sensitivity strongly depend on the accuracy of the event reconstruction. Additionally, the sensitivity can be very sensitive to the number of events that pass the quality selection cuts. Therefore, they are useful figures of merit to compare the quality of the selection cuts for the Hillas and the ImPACT reconstruction algorithms.
Standard selection cuts for CTA are chosen extrapolating from the cuts used in the H.E.S.S. experiment. The cuts will be described in more details in the next section. The angular resolution reached by applying these standard cuts to the Hillas and ImPACT reconstruction is shown in Figure 4.14 for the full telescope layout. It is compared to the required performance of CTA. The performance requirement are derived from Monte-Carlo simulations in an approach similar to the one used in this work. The Hillas reconstruction is used, however, strong selection cuts are already applied to reach this high performance (Hassan et al., 2017).

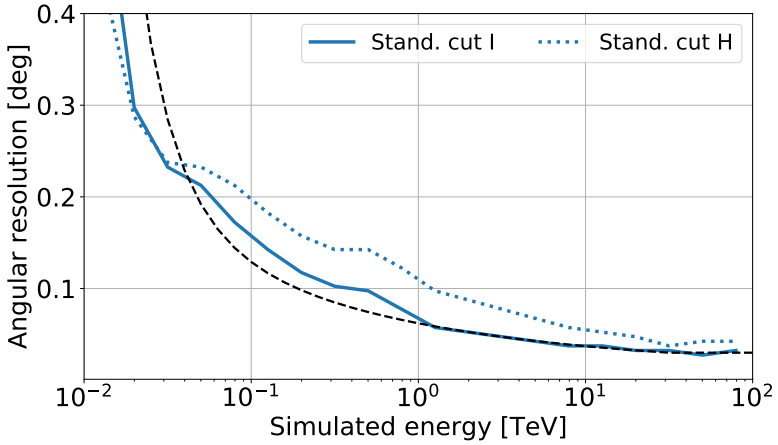

Figure 4.14 Angular resolution after applying standard cuts. The black dashed line identifies the CTA requirement. With the same cuts, the ImPACT (I) performance deviates from the requirements by maximum 30% while for the Hillas (H) method the resolution needs to be improved by 50%.

It can be seen that already with the ImPACT standard cuts, the angular resolution of the ImPACT reconstruction fulfils the CTA requirements over almost the whole energy range. Small improvements are needed for energies between 50 GeV and 1 TeV, where the angular resolution is too high by 10%-30%. For the Hillas reconstruction, the requirements are only fulfilled below 50 GeV with the loose ImPACT standard cuts. Above this energy, the average deviation from the requirements is 50%. The influence of different quality selection cuts on both performances is discussed in the next section.

4.3.1 Optimisation of the preselection cuts

Preselection cuts on Cherenkov images are applied to the amplitude, the number of significant pixels and the distance of the image COG to the camera centre prior to the event reconstruction. To optimise the standard cuts and to see the impact of these cuts on the Hillas algorithm, the angular resolution and the fraction of events after different selection cuts are compared to the standard cut performance.

Amplitude cut

The amplitude of a Cherenkov image is the sum over the signal in all significant pixels after tail cut cleaning. Brighter images are in general recorded by telescopes closer to the shower axis. Reconstruction of these events is more reliable than those of a telescope further away with fainter signal. The standard amplitude cut A is 92.7 p.e. for an LST, 90.6 p.e. for an MST and 29.4 p.e. for an SST camera. These values are obtained by rescaling the cuts used in the H.E.S.S. experiment to fit the expected level of NSB on the corresponding operation site for the different sized telescopes. Variations from A to $2.5A$ are studied here. In Figure 4.15 the results for the different amplitude cuts are shown.
The amplitude cut affects the energy regime below 1 TeV as low energetic showers are typically fainter than their higher energetic counterparts. Average improvements reached for the LST subsystem in the energy range between 50 GeV and 1 TeV are summarised in Table 4.2. With a $2.5A$ cut, the average LST performance of the ImPACT analysis can be improved by 22%, the Hillas performance by 20%. However, already an $1.5A$ cut rejects more than 50% of the events. Due to the high event loss, the standard cut is considered the best compromise between performance and event statistics for both algorithms.

Table 4.2 Average improvement of the angular resolution of the LST subsystem by different amplitude cuts compared to the standard cut for the Hillas and the ImPACT reconstruction in the energy range between 50 GeV and 1 TeV. The maximal event loss caused by each cut is also stated.

	ImPACT	Hillas	
Cut [A]	$\left\langle \frac{\text{AngRes}}{\text{AngRes}_{\text{Std}}} \right\rangle$	$\left\langle \frac{\text{AngRes}}{\text{AngRes}_{\text{Std}}} \right\rangle$	$\left(1 - \frac{N}{N_{\text{Std}}}\right)_{\text{max}}$
1.5	0.90	0.92	0.53
2.0	0.83	0.85	0.85
2.5	0.78	0.80	0.95

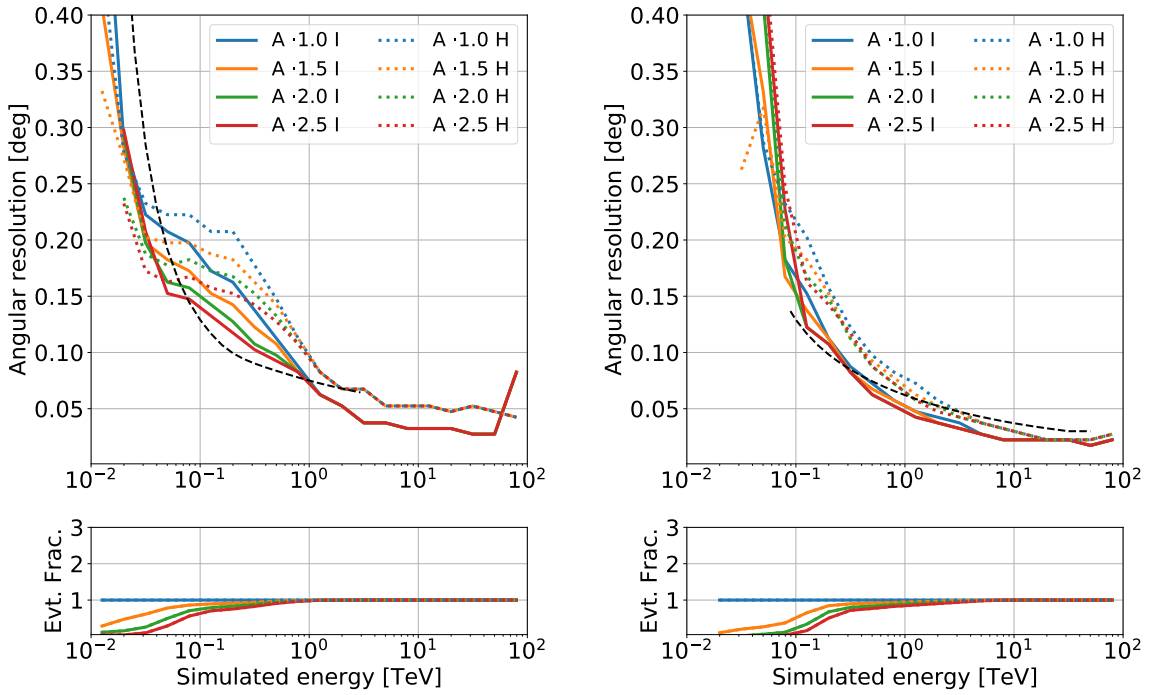

(a) LST **(b)** MST

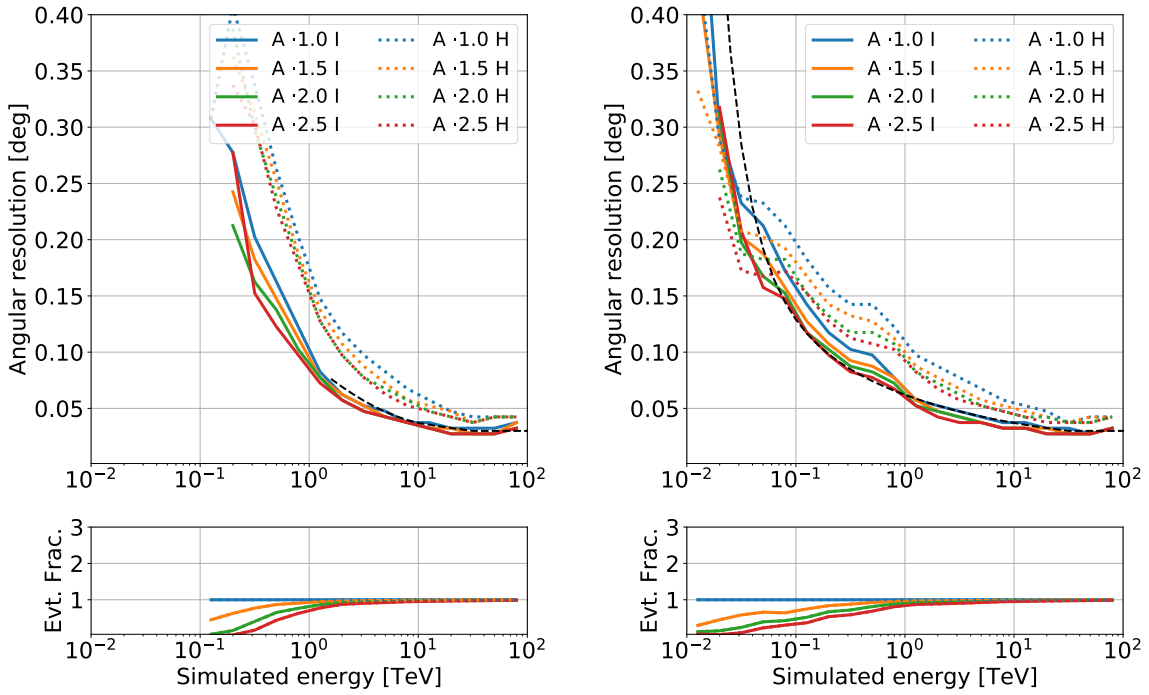

(c) SST **(d)** Full array

Figure 4.15 Angular resolution after a cut on the signal amplitude for different telescope array subsystems for ImPACT (I) and Hillas (H) reconstruction. The black dashed line identifies the CTA requirement. In the lower panel of each plot, the number of events is compared to the number after applying the standard cut. With higher amplitude cuts the low energy regime can be improved.

Pixel cut

The pixel cut operates on the number of significant pixels after image cleaning. Width and length calculation of the roughly elliptically shaped signal becomes easier and more reliable the more pixels are involved. The standard cut P is 5 pixels for LST and 4 pixels for MST and SST cameras. Cuts of 3 to 6 pixels are studied and the results are shown in Figure 4.16. The pixel cut only influences the lowest energies. Faint showers at low energies only illuminate a small number of pixels. Performances improvements for the LST telescopes are indicated in Table 4.3. By increasing the pixel cut to 6, the angular resolution could be optimised by few percent for energies between 20 GeV and 300 GeV for both reconstruction mechanisms. Then again, while the cut barely affects the number of selected events for the MSTs and SSTs, a looser 3 pixels cut for the LSTs triples the amount of low energy events.

Table 4.3 Average improvement of the angular resolution of the LST subsystem by different pixel cuts compared to the standard cut for the Hillas and the ImPACT reconstruction in the energy range between 20 GeV and 300 GeV. The maximal event loss caused by each cut is also stated.

	ImPACT	Hillas	
Cut [pixel]	$\left\langle \frac{\text{AngRes}}{\text{AngRes}_{\text{Std}}} \right\rangle$	$\left\langle \frac{\text{AngRes}}{\text{AngRes}_{\text{Std}}} \right\rangle$	$\left(1 - \frac{N}{N_{\text{Std}}}\right)_{\text{max}}$
3	1.05	1.05	2.00
4	1.03	1.04	1.50
6	0.93	0.94	0.57

Distance cut

While the COG of an image moves outwards from the camera centre, the probability of the signal to be truncated by the camera FOV increases. Hillas parameters from truncated signals lead to larger reconstruction uncertainties. The standard distance cut is 75% of the field of view (FOV) of a camera corresponding to 1.74° for LST, 3° for MST and 3.55° for SST cameras. Distance cuts between 65% and 80% of the FOV are shown in Figure 4.17.
The distance cut affects the high energy performance of the arrays. High energetic showers are brighter and can be detected even at large impact distances. Their images thus more likely move outside the FOV. While the MSTs are barely influenced, above 10 TeV the SST performance matches the requirements for the Hillas method with an 65% cut while the ImPACT resolution even exceeds the requirements with the same cut by about 30% without loosing more than 20% of the events. Improvements for different cuts are shown in Table 4.4.

Table 4.4 Average improvement of the angular resolution of the SST subsystem by different distance cuts compared to the standard cut for the Hillas and the ImPACT reconstruction in the energy range above 10 TeV. The maximal event loss caused by each cut is also stated.

	ImPACT	Hillas	
Cut [% FOV]	$\left\langle \frac{\text{AngRes}}{\text{AngRes}_{\text{Std}}} \right\rangle$	$\left\langle \frac{\text{AngRes}}{\text{AngRes}_{\text{Std}}} \right\rangle$	$\left(1 - \frac{N}{N_{\text{Std}}}\right)_{\text{max}}$
65	0.72	0.78	0.20
70	0.8	0.89	0.12
80	1.12	1.12	1.08

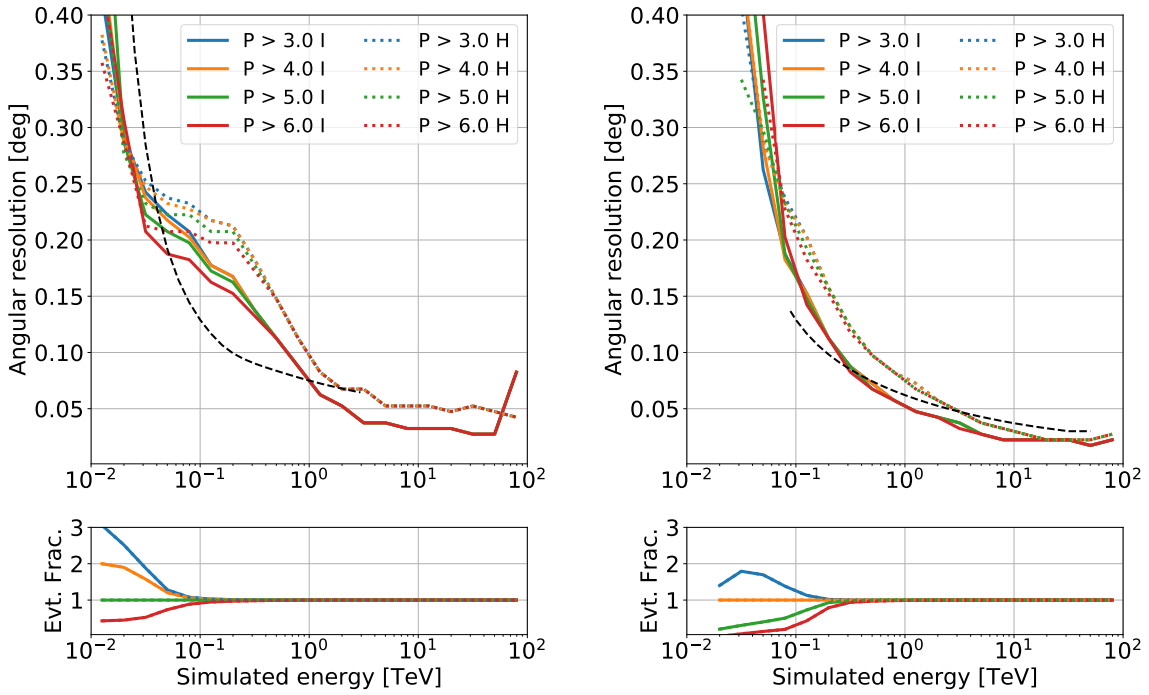

(a) LST **(b)** MST

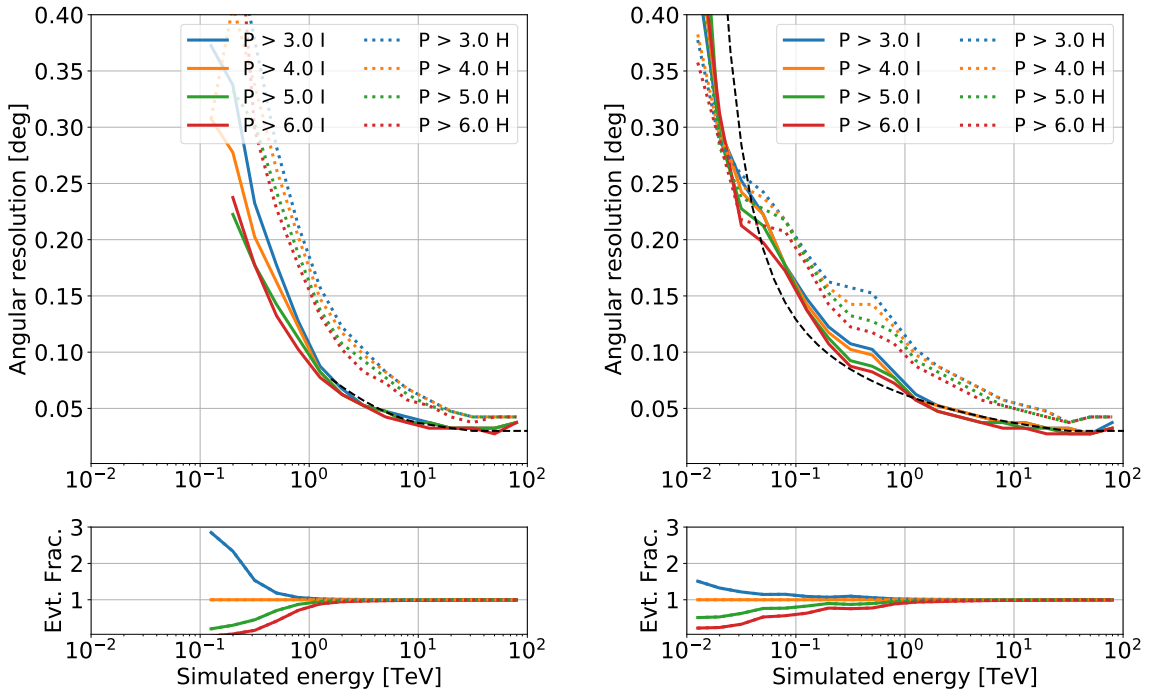

(c) SST **(d)** Full array

Figure 4.16 Angular resolution after a cut on the number of significant pixels in a camera after image cleaning for different telescope array subsystems for ImPACT (I) and Hillas (H) reconstruction. The black dashed line identifies the CTA requirement. In the lower panel of each plot, the number of events is shown compared to the number after applying the standard cut. With higher pixel cuts the low energy regime can be improved.

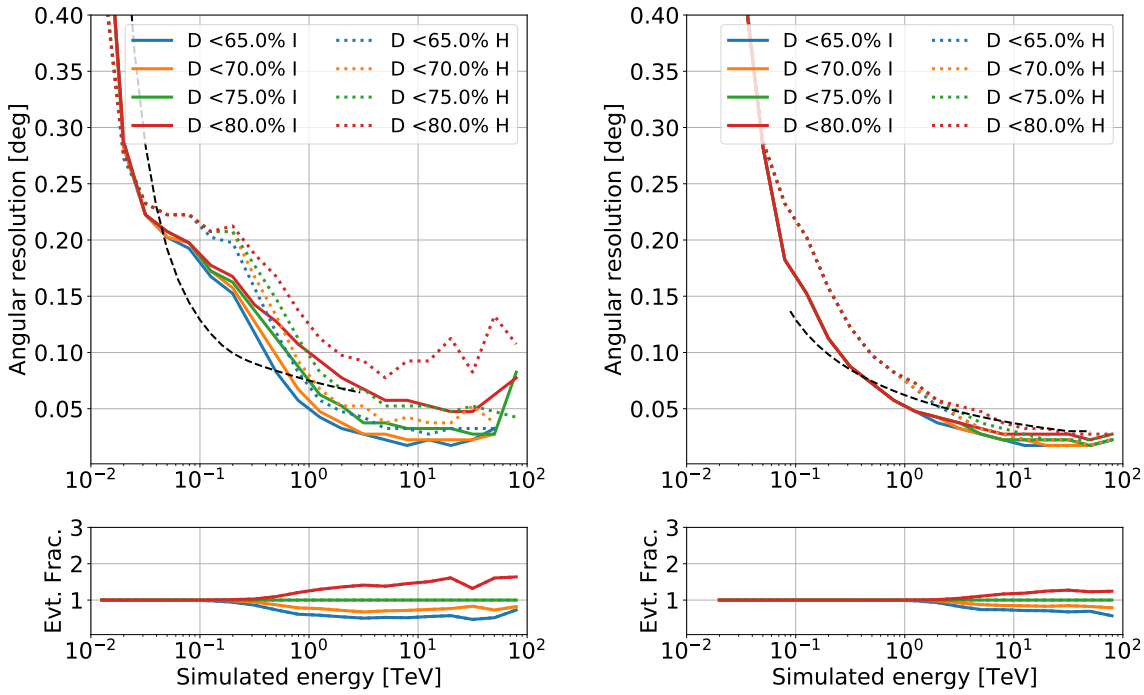

(a) LST **(b)** MST

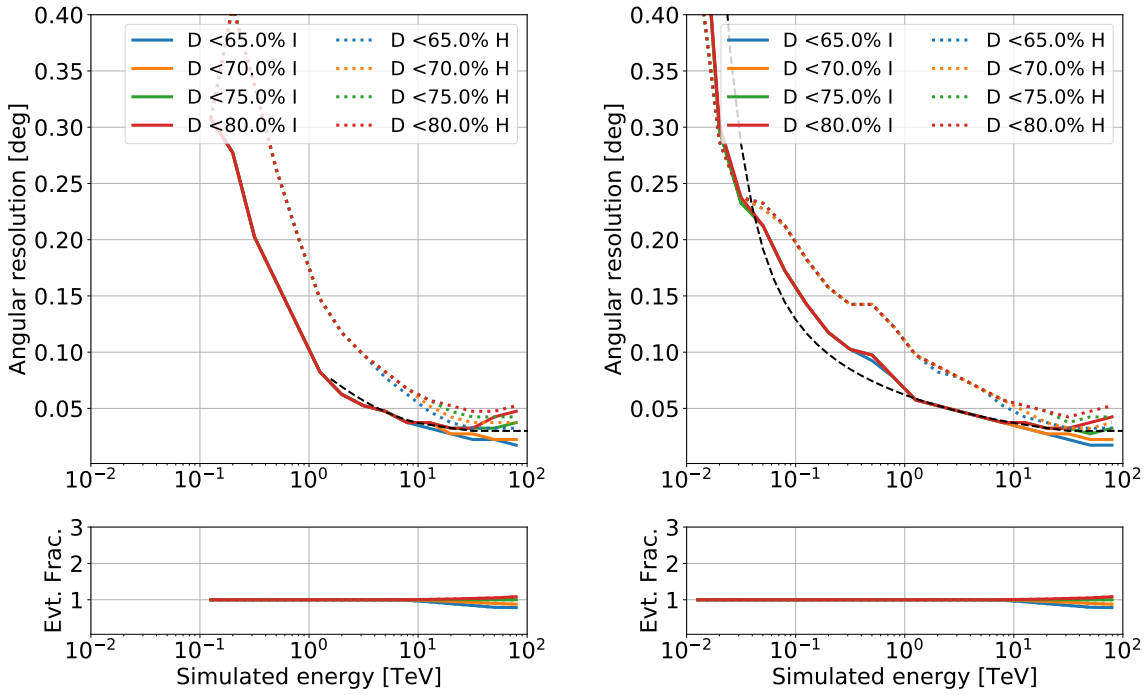

(c) SST **(d)** Full array

Figure 4.17 Angular resolution after a cut on the distance between COG and camera centre for different telescope array subsystems for ImPACT (I) and Hillas (H) reconstruction. The black dashed line identifies the CTA requirement. In the lower panel of each plot, the number of events is shown compared to the number after applying the standard cut. With lower distance cuts the medium to high energy regime can be improved.

Conclusion

Based on this study, the preselection cuts are changed: For the LSTs the pixel cut is loosened from 5 to 3 pixels and for the SSTs a stronger distance cut of 65% FOV instead of 75% is applied. The final preselection cut set is summarised in Table 4.5. Additionally, Figure 4.18 shows a comparison of the angular resolution with the optimised and the standard cut for the Hillas and the ImPACT reconstruction.

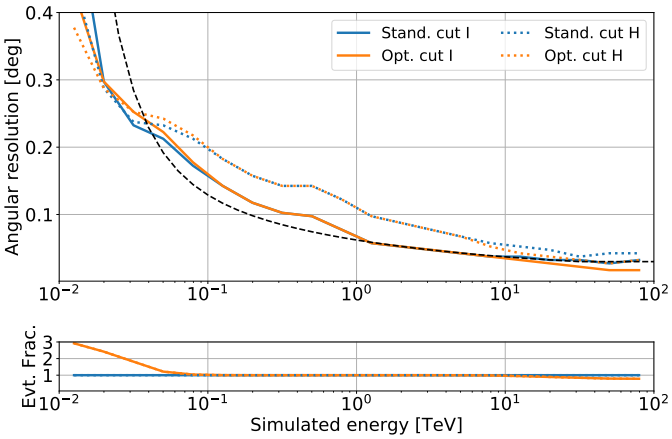

Figure 4.18 Angular resolution after an optimised preselection cut for ImPACT (I) and Hillas (H) reconstruction. The black dashed line identifies the CTA requirement. In the lower panel, the number of events is shown compared to the number after applying the standard cut. With the optimised cut, the lowest and the highest energy performance is improved.

Table 4.5 Final set of preselection cuts for the Hillas and ImPACT reconstruction. The values marked in red are changed compared to the standard cuts based on the results of this section.

Cut	LST	MST	SST
Amplitude [p.e.]	92.7	90.6	29.4
Pixel	3	4	4
Distance [% FOV]	75	75	65

With these cuts, the performance decreases up to 10% for both reconstruction mechanisms below 100 GeV but still exceeds the requirements. However, the number of events increases by a factor of 3. Above 10 TeV the requirements are now reached by both algorithms, the ImPACT resolution even exceeds them by 30%. The medium energy range can be further enhanced by applying postselection cuts on the data.

4.3.2 Optimisation of the postselection cuts

The reconstruction of EAS shower parameters can be further optimised after the event reconstruction by applying postselection cuts on the determined parameters. This includes cuts on the angular distance of the reconstructed source direction from the expected source position, errors of the likelihood fitting, the distance of the shower core position to the centre of the telescope array or the number of telescopes providing shower images. As this highly influences the number of selected events, these cuts are studied by means of both, the angular resolution and the flux sensitivity.

Background suppression cuts

For the detection of a point source, emission is expected from an area the size of the point spread function of the instrument. Contrary, the cosmic-ray background is rather homogeneously distributed over the full FOV. To reject as much background as possible, a cut on the angular distance of the reconstructed source direction to the expected source position, based on an 80% containment radius of the PSF, is performed. For extended sources, the slopes of the PSF distribution are relevant. Thus, for these sources a fixed containment radius of 0.2° is chosen based roughly on the median source size distribution found in the H.E.S.S. galactic plane survey (Abdalla et al., 2018b). Events outside this radius are rejected. In a real observation the selected angular area would correspond to the *on* region.
If only background events close to the source position (equivalent to the telescope pointing direction in this simulation) are considered, the number of events that needs to be simulated increases dramatically. To use the observation runs described before, the background events are instead cut for a fixed region of radius 2° around the telescope pointing and the corresponding events N_{passcuts} in the sensitivity calculation in Equation 4.9 are weighted with the area ratio of the two regions:

$$N^{\text{new}}_{\text{passcuts}}(E) = N^{\text{old}}_{\text{passcuts}}(E)\frac{r^2_{\text{cont}}}{\text{cut}^2_{\text{fixed}}},$$

with the containment radius r_{cont} of the gamma-ray showers and the cut $\text{cut}_{\text{fixed}}$ applied to the background events. The sensitivities for both angular cuts are shown in Figure 4.19.
To further improve the background suppression the error estimation of the likelihood fit can be exploited. Whenever the likelihood surface around the minimum can not be approximated by a parabola for an input parameter (see Figure 4.9), the event is marked. By excluding the marked events, 87% of the signal events remain while 55% of the proton and electron background is rejected. The effect is shown for the ImPACT sensitivity in Figure 4.19 and for the angular resolution in Figure A.2 in Appendix A.
With a flux sensitivity between $10^{-10}\,\text{TeV}\,\text{cm}^{-2}\text{s}^{-2}$ and $10^{-13}\,\text{TeV}\,\text{cm}^{-2}\text{s}^{-2}$, the performances of both reconstruction methods and both angular cuts are in the same range as the CTA requirements for the detection of a point source. The peak in the MST sensitivity at 2 TeV clearly shows the transition from the GOF to the BDT background classification for the ImPACT approach. Neither of the angular cuts is enough to fulfil the requirements. Average deviations of the performance from the requirements are given in Table 4.6.

Table 4.6 Improvements of the sensitivity and the angular resolution of the ImPACT and the Hillas reconstruction compared the the requirements after applying background cuts and a point-like and an extended angular cut. Numbers in brackets signify the results for an additional error cut.

	ImPACT			Hillas		
	Point-like	Extended		Point-like	Extended	
Telescope	$\left\langle \frac{\text{Sens}}{\text{Req}} \right\rangle$	$\left\langle \frac{\text{Sens}}{\text{Req}} \right\rangle$	$\left\langle \frac{\text{AngRes}}{\text{Req}} \right\rangle$	$\left\langle \frac{\text{Sens}}{\text{Req}} \right\rangle$	$\left\langle \frac{\text{Sens}}{\text{Req}} \right\rangle$	$\left\langle \frac{\text{AngRes}}{\text{Req}} \right\rangle$
LST	2.64 (2.27)	2.53 (2.29)	(1.11)	300	7.45	1.43
MST	2.48 (2.15)	5.56 (4.36)	(0.78)	2.32	4.93	1.09
SST	3.16 (2.19)	5.38 (4.27)	(0.78)	4.27	5.10	1.37
Full array	3.47 (2.76)	6.81 (5.70)	(0.91)	6.85	7.75	1.37

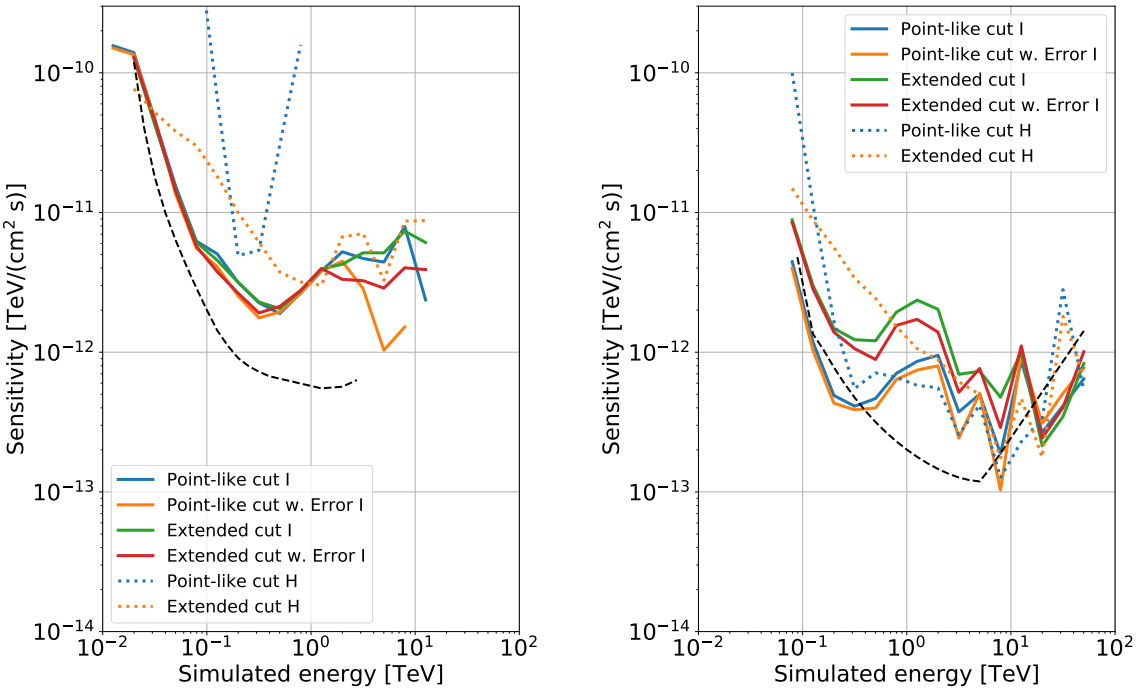

(a) LST **(b)** MST

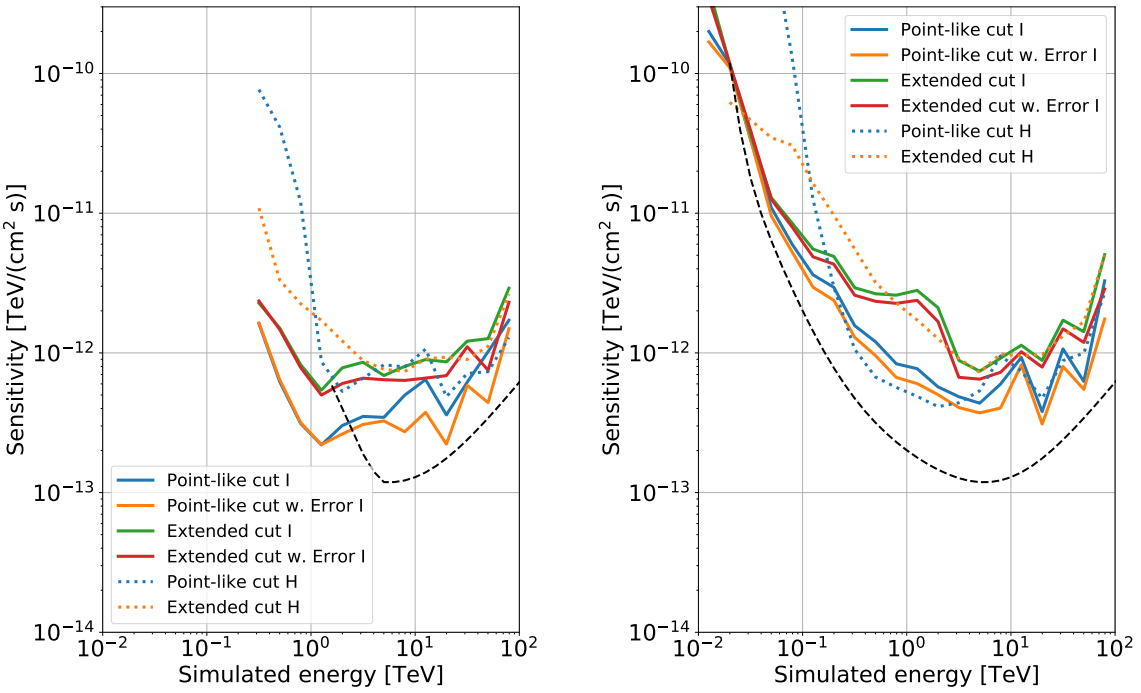

(c) SST **(d)** Full array

Figure 4.19 Flux sensitivity after a cut on the angular distance of the reconstructed direction from the telescope pointing and on the fitting error for different telescope array subsystems for ImPACT (I) and Hillas (H) reconstruction. The black dashed line identifies the CTA requirement. The point-like angular cut leads to better energy sensitivities than the extended angular cut for both reconstruction algorithms as expected.

For the ImPACT method, a factor 3.5 between the point-like sensitivity performance and the requirements and a factor of almost 7 for the extended cut performance is found. The error cut improves this performance telescope-depended by 15% to 45%. Above 1 TeV, the Hillas sensitivity is comparable to the ImPACT results, however, at low energies it is up to one order of magnitude above the requirements. For the angular resolution, the same background cuts are applied than for the sensitivity. This rejects some of the badly reconstructed events when they appear to be hadron-like and hence improve the overall resolution. For the ImPACT reconstruction additionally the error cut is applied. With these cuts, the angular resolution found with the ImPACT reconstruction is in average about 10% better than the requirements. However, in the energy range between 50 GeV and 1 TeV still a deviation of 20% is visible. The angular resolution after Hillas reconstruction improves highly for the MSTs, but is otherwise still 30% worse than the requirements.

Core cut

The shower core position describes where the extrapolated shower axis intersects with the detection plane. Showers with core positions close to the centre of the array can be detected by many telescopes. Further out, less telescopes are able to record the shower and the signal amplitude decreases. Core distance cuts C of 250 m to 500 m from the array centre are studied for the LSTs and of 250 m to 1000 m for all other systems. Figure 4.20 shows the cut efficiency for the sensitivity with an additional point-like angular cut. The corresponding angular resolution curves can be found in Figure A.1 in Appendix A.
It can be seen immediately that the performance of the flux sensitivity decreases for core distance cuts of less than 1000 m for the both reconstruction methods. This is due to the low event statistic. As the image selection is already optimised, this cut only unnecessarily decreases the number of events that have a high enough quality to be reconstructed.
The angular resolution is less sensitive to the number of events. With a 750 m cut the ImPACT resolution exceeds the requirements by 30%, with a 250 m cut even by 45%. Also the Hillas resolution is greatly improved, especially in the medium and high energy regime. Overall improvements of 5% for a 750 m cut and 30% for a 250 m cut are possible. However, only few percent of the events remain. Because of the high event loss, this cut will not be included in the set of postselection cuts hereafter.

Multiplicity cut

The telescope multiplicity defines the minimum number of telescopes that have to record a shower image for an event to be reconstructed. CTA is a stereoscopic instrument, therefore the multiplicity must be at least 2. As the final shower parameters are averages over the parameters reconstructed by individual telescopes, the more telescopes have seen the same event, the smaller will be the reconstruction uncertainty. Effects of multiplicities M between at least 2 and at least 5 telescopes on the flux sensitivity are shown in Figure 4.21 in addition to a point-like and in Figure 4.22 to an extended angular cut. Figure A.2 in Appendix A shows the corresponding angular resolution. It should be noted that due to the telescope layout used for this study, LST multiplicities above three are not possible.
The multiplicity cut has a large influence on the flux sensitivity. Especially, between $M \geq 2$ and $M \geq 3$ the performance is increased. This is due to the fact, that if the elongated signals in two telescopes have parallel main axes, the reconstruction of the source direction becomes challenging. These cases are excluded by an $M \geq 3$ cut. Performance improvements reached by this $M \geq 3$ are summarised for the different telescopes in Table 4.7.

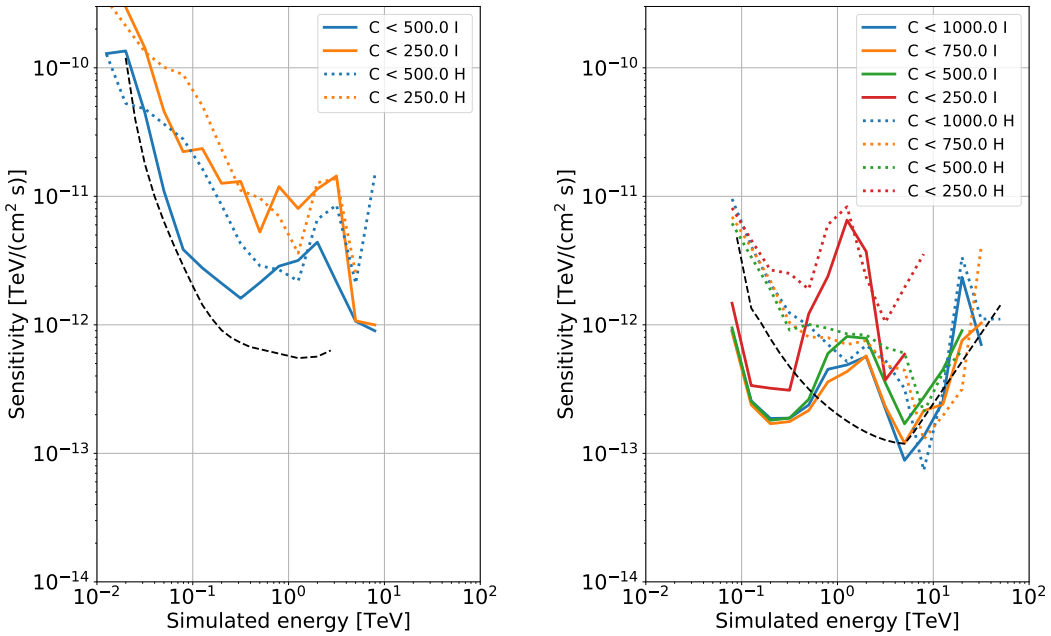

(a) LST

(b) MST

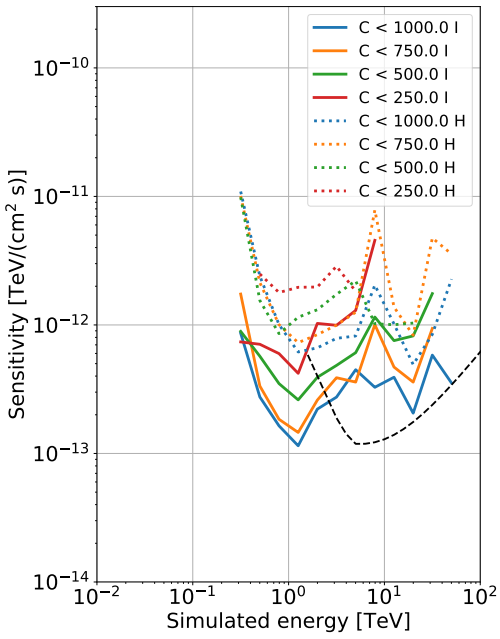

(c) SST

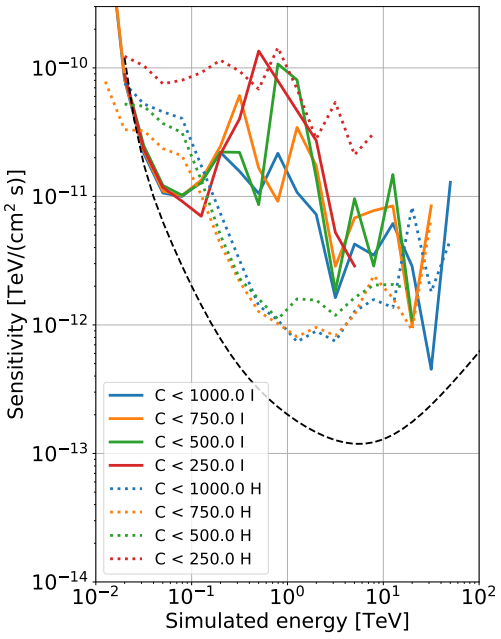

(d) Full array

Figure 4.20 Flux sensitivity after a cut on the distance between the shower core position and the array centre for different telescope array subsystems for ImPACT (I) and Hillas (H) reconstruction. A point-like angular cut is applied. The black dashed line identifies the CTA requirement. Due to the high loss of events, the performance decreases for cuts harder than 500 m for the LSTs and 1000 m for all other telescope subsystems.

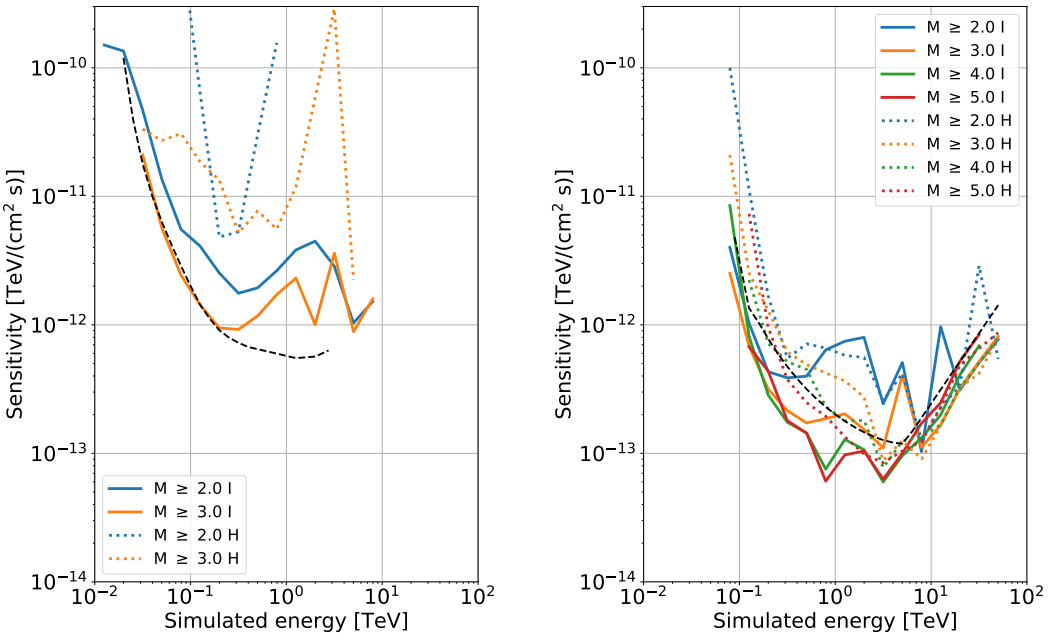

(a) LST **(b)** MST

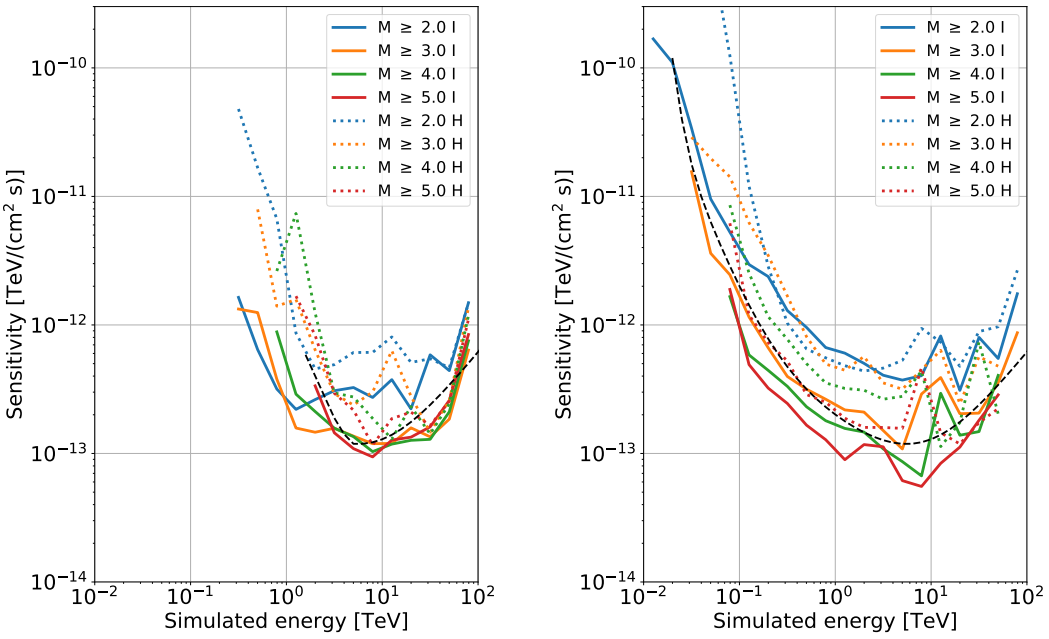

(c) SST **(d)** Full array

Figure 4.21 Flux sensitivity after a telescope multiplicity cut for different telescope array subsystems for ImPACT (I) and Hillas (H) reconstruction. A point-like angular cut on 80% of the angular resolution is applied. The black dashed line identifies the CTA requirement. The multiplicity cut improves the performance over the full energy range. With a harder cuts the requirements can be matched over almost the full energy range by the ImPACT reconstruction.

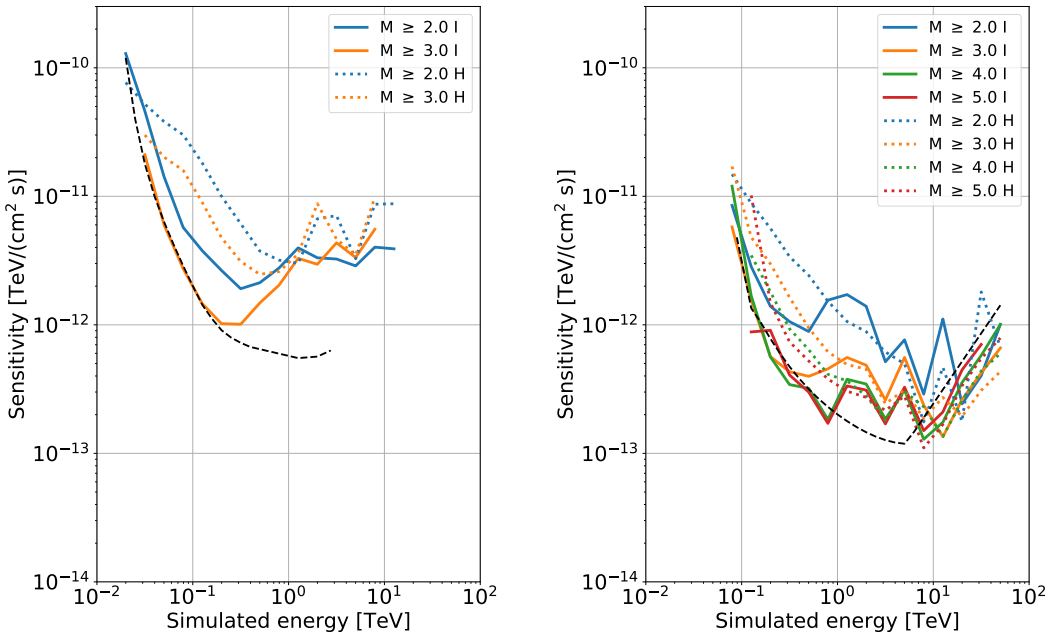

(a) LST

(b) MST

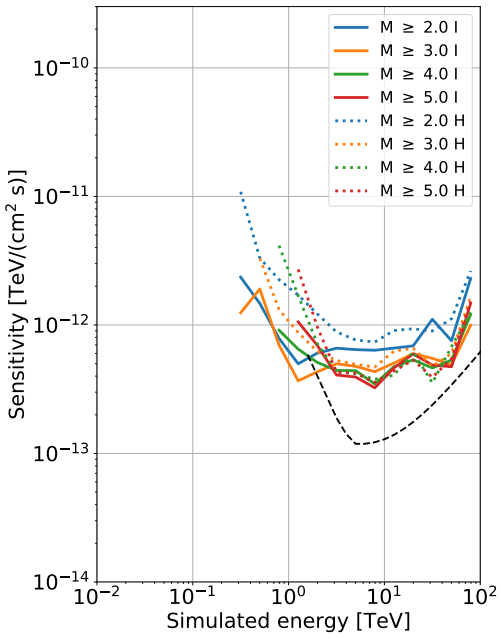

(c) SST

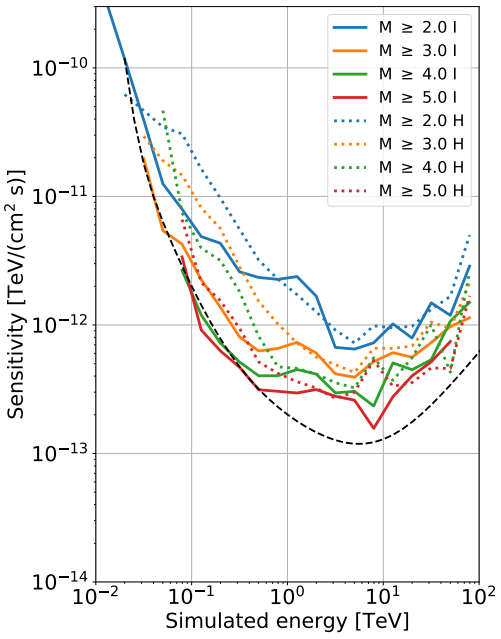

(d) Full array

Figure 4.22 Flux sensitivity after a telescope multiplicity cut for different telescope array subsystems for ImPACT (I) and Hillas (H) reconstruction. A fixed extended angular cut of 0.2 deg is applied. The black dashed line identifies the CTA requirement. The multiplicity cut improves the performance over the full energy range. With a harder cuts, the point-like requirements can be met up to an energy of 300 GeV by the ImPACT reconstruction.

For the point-like angular cut, the LST sensitivity reaches the requirements up to an energy of 200 GeV, the MST and SST performance even over the full energy range. The same sensitivity is found for the Hillas method but for this purpose a $M \geq 5$ cut is needed.

Table 4.7 Improvements of the sensitivity and the angular resolution of the ImPACT and the Hillas reconstruction compared to the requirements after applying a multiplicity cut of $M \geq 2$ and an additional point-like or extended angular cut.

	ImPACT			Hillas		
	Point-like	Extended		Point-like	Extended	
Telescope	$\left\langle \frac{\text{Sens}}{\text{Req}} \right\rangle$	$\left\langle \frac{\text{Sens}}{\text{Req}} \right\rangle$	$\left\langle \frac{\text{AngRes}}{\text{Req}} \right\rangle$	$\left\langle \frac{\text{Sens}}{\text{Req}} \right\rangle$	$\left\langle \frac{\text{Sens}}{\text{Req}} \right\rangle$	$\left\langle \frac{\text{AngRes}}{\text{Req}} \right\rangle$
LST	1.03	1.10	0.77	8.61	4.36	1.12
MST	1.02	2.14	0.68	1.54	2.98	0.95
SST	0.88	2.87	0.70	2.02	3.26	1.19
Full array	1.20	2.67	0.75	5.90	4.36	1.11

Also for the extended cut the point-like requirements can be fulfilled for the ImPACT reconstruction up to an energy of 300 GeV for the LSTs with three telescopes, for the MSTs even up to 700 GeV and above 10 TeV. The average SST performance can be improved by over 80% with the same cut. For the Hillas algorithm, enhancements of 60%-80% can be reached. The greatest improvement is reached for the angular resolution. Already with a simple $M \geq 3$ cut, the ImPACT resolution exceeds the requirements over the whole energy range of in average 25%. With this cut, the Hillas performance still deviates from the requirements in average by 10% percent in the energy range between 50 GeV and 1 TeV. Higher cuts of $M \geq 5$ are needed to match the requirements. As the performance of the telescope multiplicity cut is highly energy dependent, likewise energy-dependent cuts needs to be considered.

4.3.3 Energy dependent postselection cuts

From the results of the last section, energy-dependent optimised multiplicity cuts can be selected. To find the best compromise between good angular resolution and high flux sensitivity, these parameters are compared at fixed energies for different multiplicity cuts in special plots. Examples are shown for the full telescope array at specific energies in Figure 4.23. Other energies and subsystems can be found in Figure B.1 to Figure B.4 in Appendix B.
For higher cuts, the angular resolution and the sensitivity become smaller and thus better. However, as soon as the number of events due to the selection cuts drops too low, the sensitivity starts to worsen again and the cut curves shown here increase. The best performance of the event reconstruction is expected at these turning points.
Three different cut sets are chosen from the cut performance curves. For the *HighN* set, cuts are selected that provide the best compromise between angular resolution and flux sensitivity while keeping at least 30% of the events. Contrary, for the *Opt* set the best combined performance reachable is found, independent of the number of events, while for the *AngOpt* set additional priority is given to a high angular resolution. All cut sets are deduced from the full array performance for both reconstruction algorithms and both angular cuts. The resulting 12 cut sets are presented in Figure 4.24. It should be noted that due to the high optimisation the number of events can be low. With few events, small variations of the cut value already largely change the sensitivity, which can lead to quite different multiplicity cuts in neighbouring energy bins.

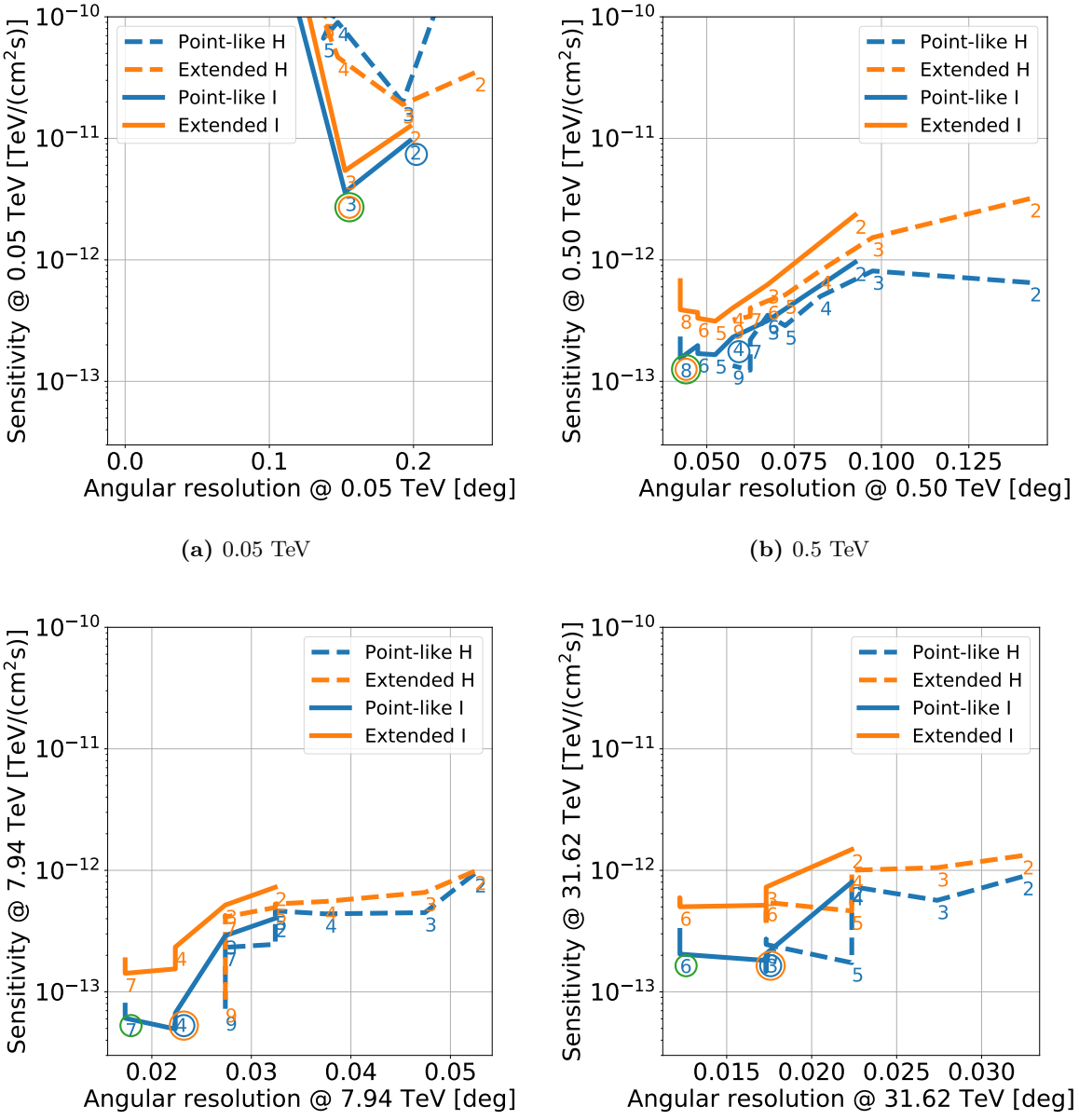

(a) 0.05 TeV

(b) 0.5 TeV

(c) 7 TeV

(d) 30 TeV

Figure 4.23 Cut-dependent angular resolution and sensitivity at fixed energies for ImPACT (I) and Hillas (H) reconstruction. For both reconstruction mechanisms and both angular cuts the performance variation is shown with solid or dashed coloured lines, respectively. At each step the corresponding multiplicity cut is specified by the small number below the line. If the performance does not change, the higher cut number is omitted. As small resolutions and sensitivity are desired, priority is given to values in the lower left corner. Multiplicity cuts selected for the *HighN* cut are shown in blue, for the *Opt* cut in orange and for the *AngOpt* cut in green circles.

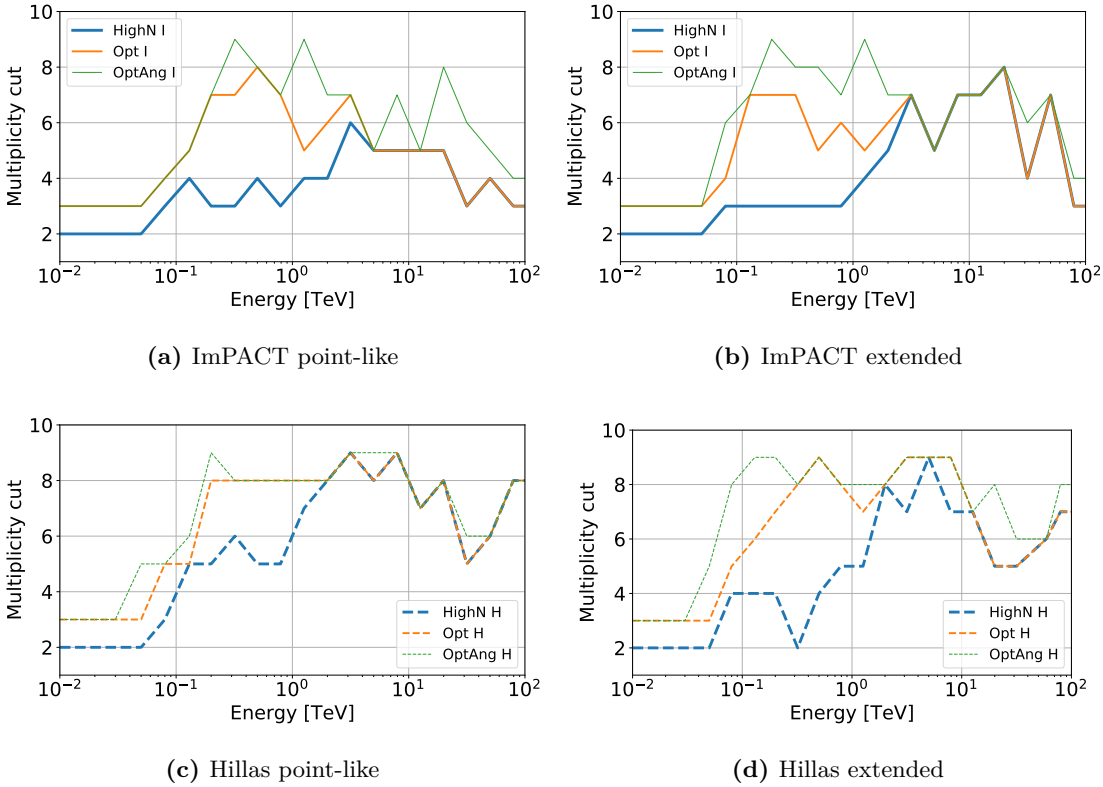

(a) ImPACT point-like

(b) ImPACT extended

(c) Hillas point-like

(d) Hillas extended

Figure 4.24 Multiplicity cut sets for the ImPACT (I) and the Hillas (H) reconstruction and both angular cuts. In general, the *Opt* cut set always stays between the *HighN* and the *OptAng* cut set.

For the *HighN* set of the ImPACT reconstruction an $M \geq 2$ telescope cut is applied to the lowest energies where the effective area is low and an $M \geq 3-4$ cut to the highest to collect most of the rarest high energy events. In the medium energy range the multiplicity can reach up to $M \geq 6$ for the point-like and $M \geq 8$ for the extended angular cut with still a good event statistics. Higher cuts are used in the OptAng cut set with a maximum of $M \geq 9$ telescopes in the medium energy range (the maximum number studied in this analysis). The *Opt* cut set stays within the limits of these two cuts. For the Hillas reconstruction, in general higher cuts are needed to reach a similarly high performance resulting in a lower event statistics. Sensitivity and angular resolution curves resulting from the different cuts are shown in Figure 4.25 and the improvements are summarised in Table 4.8.

Point-like flux sensitivity

The point-like flux sensitivity exceeds the requirements for the ImPACT reconstruction with all cut sets over the whole energy range below 30 TeV. With the *HighN* cuts, the flux sensitivity is enhanced by 20% in average compared to the requirements. As intended, the *Opt* an *AngOpt* cuts increase this performance even further. The average improvement is 40%. With its higher cuts, the sensitivity reached by the Hillas reconstruction with the *Opt* and *AngOpt* cut sets is comparable to the ImPACT performance for energies above 500 GeV. For the *HighN* cuts, the results especially at low energies are less good, even though they also exceeds the requirements over almost the whole energy range.

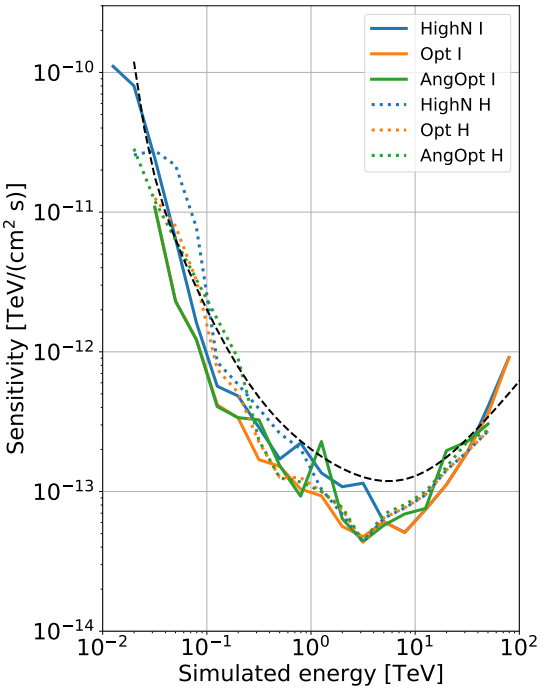

(a) Point-like

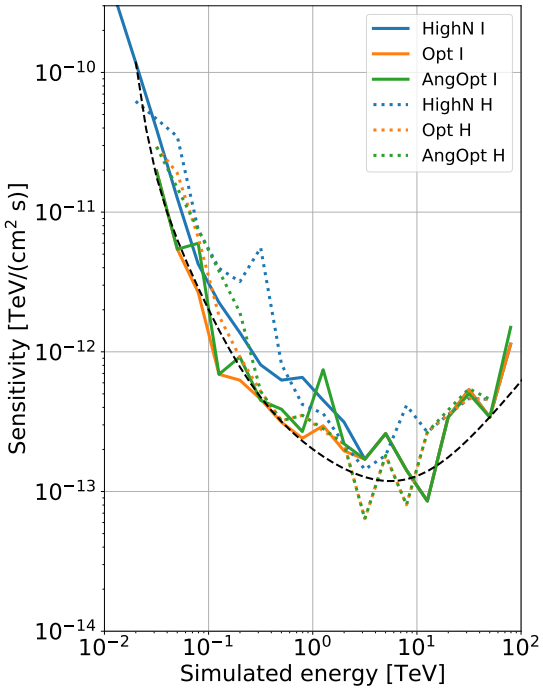

(b) Extended

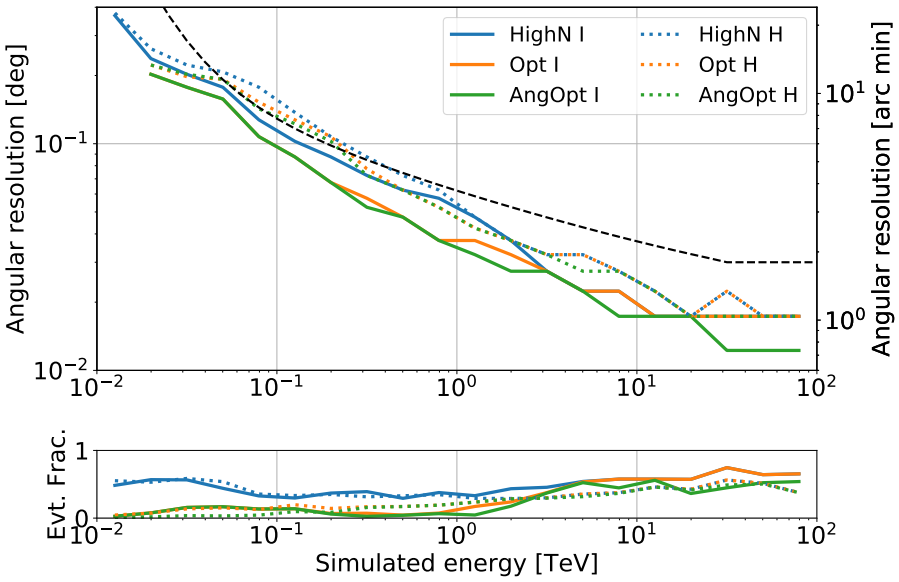

(c) Angular resolution

Figure 4.25 Angular resolution and flux sensitivity after optimised postselection cuts for ImPACT (I) and Hillas (H) reconstruction . The black dashed line identifies the CTA requirement. The flux sensitivity of the three cut sets applied additionally to a point-like (a) and an extended (b) angular cut as well as the angular resolution (c) exceed the CTA requirements for a point-like source detection over almost the whole energy range. In the lower panel of (c), the number of events is shown compared to the number after applying the standard cut.

Table 4.8 Improvements of the sensitivity and the angular resolution of the ImPACT and the Hillas reconstruction compared to the requirements after applying optimised multiplicity cuts together with a point-like and an extended angular cut.

	ImPACT			Hillas		
	Point-like	Extended		Point-like	Extended	
Telescope	$\left\langle \frac{\text{Sens}}{\text{Sens}_{\text{Std}}} \right\rangle$	$\left\langle \frac{\text{Sens}}{\text{Sens}_{\text{Std}}} \right\rangle$	$\left\langle \frac{\text{AngRes}}{\text{AngRes}_{\text{Std}}} \right\rangle$	$\left\langle \frac{\text{Sens}}{\text{Sens}_{\text{Std}}} \right\rangle$	$\left\langle \frac{\text{Sens}}{\text{Sens}_{\text{Std}}} \right\rangle$	$\left\langle \frac{\text{AngRes}}{\text{AngRes}_{\text{Std}}} \right\rangle$
HighN	0.79	1.78	0.70	0.97	2.79	0.82
Opt	0.58	1.27	0.61	0.66	1.53	0.76
AngOpt	0.60	1.55	0.57	0.63	1.52	0.75

Extended flux sensitivity

As a very low number of background events affects the calculation of the Li-Ma significance, the performance curves become very unstable at higher energies. However, it is clearly visible, that up to 500 GeV, the flux sensitivity of the ImPACT reconstruction with an extended angular cut is able to match the requirements for a point-like source detection for the *Opt* and *AngOpt* cuts. Outside this region, deviations are of the order of 30% to 50%. The performance of the Hillas reconstruction with higher multiplicity cuts are comparable.

Angular resolution

Already with the *HighN* cut, the ImPACT angular resolution outperforms the requirements below 2 TeV by 20% and by even 40% at higher energies while the number of events stays within 30%-50% of the initial number. The *Opt* and the *AngOpt* cut increase the average improvement to 40%. Between 50 GeV and 200 GeV the Hillas performance is still 5% above the requirement, then improves continuously, until it becomes comparable to the ImPACT results above 10 TeV.

Conclusion

With the *HighN*, *Opt* and *AngOpt* cut sets not only can the CTA requirements for the angular resolution be exceeded, but also the CTA goal resolution can be matched (see Figure 4.1). In addition to the flux sensitivity that outperforms the requirements for the detection of a point-like source by 20%-40%, this will allow sources with sizes of less than 1 arcminute can be detected and studied. Also analyses of the inner structures of large, extended source morphologies will be possible, that will allow us to investigate the origins of cosmic-rays induced TeV emission on even smaller scales. By detecting the exact location of the emission, theoretical models of particle acceleration and propagation in different sources can be verified or rejected, which will enhance our understanding of these processes. The ability of CTA to refrain theoretical predictions due to its increased angular resolution will be tested in the next chapter by simulating observations of the radio galaxy Centaurus A.

"And it's the stars,
The stars that shine for you
And it's the stars,
The stars that lie to you, yeah"

Stone Sour, *Through the glass*, 2006

CHAPTER 5

Impact on scientific source studies

With the optimised quality selection cuts found in Chapter 4 the performance of CTA exceeds the requirements and allows for detailed studies of TeV gamma-ray sources inside and outside of our galaxy. With the two different angular cuts, not only point sources but especially the morphological complex structures of extended sources can be investigated and resolved.
To understand the impact of the improved performance on the results of such scientific studies, source observations can be simulated using the *Instrument Response Functions* (IRFs) of CTA. These functions describe the relation between the physical quantities of a gamma-ray and the quantities measured by an astrophysical instrument in a given configuration. This configuration can for example include the pointing direction, the number of triggered telescopes, the offset angle of the observed source to the FOV, the observation conditions (observation time, atmospheric conditions, etc.) and of course the quality selection cuts. The IRF components, effective area, energy dispersion, point-spread function and background rate can be directly generated from the calculation of the angular resolution and the flux sensitivity explained in Section 4.3. The expected IRFs for CTA resulting from the optimisation of the quality selection cuts are presented in this chapter.
These IRFs are then used to perform source simulations with the high-level data analysis software *ctools* with different spatial models. Simulated count maps are created which can be analysed like real astronomical data to show the scientific power of CTA with the new IRFs. With this approach, the closest radio galaxy, Centaurus A, is studied, an object of high scientific interest in TeV astronomy. By current instruments, this source is resolved only as a point-sources, however, several authors predict a fascinating structure that can lead to a better understanding of particle acceleration and propagation within the highly active centres of galaxies. A detailed introduction to Centaurus A is given in Section 5.3 and the ability of CTA to resolve a source extension in the direction of the distinct jets is discussed.

5.1 Instrument response function

The IRFs include the effective area, the energy dispersion, the PSF as well as a background estimation and are used to predict the response of the instrument for the observation of a specific source. In the following the individual functions are described and corresponding example curves for the *HighN* cut set are shown in Figure 5.1.

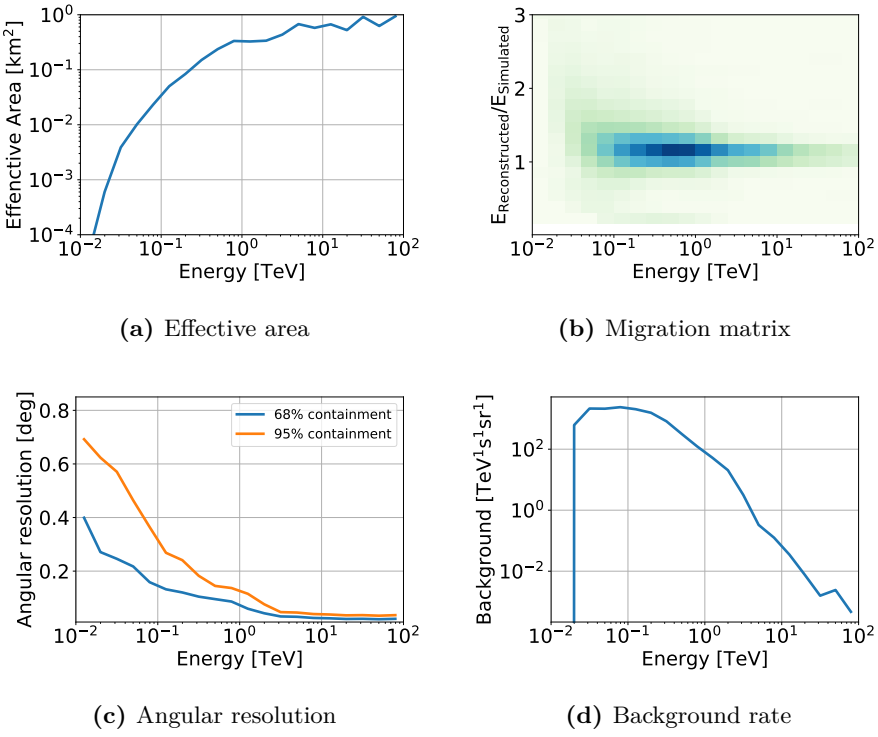

(a) Effective area **(b)** Migration matrix

(c) Angular resolution **(d)** Background rate

Figure 5.1 IRFs for the HighN cut set optimised for the detection of a point source consisting of the (a) effective area, the (b) energy migration matrix as a parametrisation of the energy dispersion, the (c) angular resolution from a parametrisation of the PSF and the (d) expected background rate.

5.1.1 Effective area

The effective area of a Cherenkov telescope describes the detection probability for a set of gamma-ray showers on ground. This probability depends on the sensitivity of the instrument at a certain energy and the number of events that pass the quality selection cuts. The effective area shown in Figure 5.1a is calculated directly via Equation 4.9 for energies between 0.01 TeV and 100 TeV. With its maximum around 1 km^2 it is comparatively small. This is due to the fact that recorded events from showers that fall further outside in the array are highly suppressed by the selection cuts, which leads to a smaller effective area, but a higher reconstruction accuracy. While typically the effective area is given as a function of the offset angle of a source position from the centre of the FOV, for this work, a constant effective area is assumed over the whole FOV. This is valid in the case of this analysis as the sources will be simulated at the centre of the FOV with sizes far smaller than 1°

5.1.2 Energy dispersion

The energy dispersion defines the deviation of the reconstructed energy of observed events from the true energy, known from simulations. A *migration matrix* can be calculated as a two-dimensional histogram of the simulated energy and the ratio of reconstructed to simulated energy. If normalised correctly, each slice of fixed simulated energy corresponds to a probability density of how well the energy is reconstructed. For a perfect reconstruction, the migration matrix would be unity for all simulated energies. As shown in Figure 5.1b for the *HighN* cut set, the deviations of the reconstructed energies from unity are small.

5.1.3 Point spread function

In Figure 4.12 of the last chapter the calculation of the one-dimensional PSF was shown. For the IRFs these PSF histograms are normalised such that for each angular bin the integrated probability $\frac{\mathrm{d}P}{\mathrm{d}\Omega}$ with $\Omega = 2\pi\vartheta\mathrm{d}\vartheta$ is unity. The form of these histograms that comes directly from the Monte-Carlo simulations define the general form of the PSF. The probability signifies how far a reconstructed direction in the sky might deviate from its true position due to uncertainties in the reconstruction. A 68% containment radius of the probabilities, results in the angular resolution in Figure 5.1c that corresponds to the *HighN* curve in Figure 4.25.

5.1.4 Background rates

The expected background rates for a source observation follow Equation 4.11 and Equation 4.12 for the proton and the electron fluxes, respectively. They are in general normalised to the observation time, the effective area of the telescope array and the solid angle covered by the FOV. In this work, the combined background rate for protons and electrons shown in Figure 5.1d is assumed to be constant over the full FOV. As the sources studied in this chapter are small compared to the FOV, this simplification should not influence the results.

5.2 Source simulation with ctools

CTA has two prototype software solutions for the high level data analysis of Cherenkov showers: *gammapy* (Donath et al., 2015) and *ctools* (Knödlseder et al., 2013). While *gammapy* is based mainly on *python* code and libraries, *ctools* is written in *C++* with no dependencies on external libraries. Both approaches come with their individual advantages and disadvantages, however, their final results should be compatible. In this chapter, *ctools* is used to simulate TeV sources and to perform fits of these sources to recover the model parameters. Different models are available for the spatial distribution as well as the energy spectrum of a source. To understand the steps performed in a *ctools* simulations, a Gaussian elliptical source with a semi-major axis of $r_{\mathrm{max}} = 0.05°$, a semi-minor axis of $r_{\mathrm{min}} = 0.01°$ and a power-law energy spectrum is simulated. The models used to create this morphology and spectrum are:

$$I(E) = A\left(\frac{E}{E_0}\right)^{-\Gamma} \qquad \text{Energy spectrum} \qquad (5.1)$$

$$M_{\mathrm{spatial}}(\vartheta,\phi) = e^{-\frac{\vartheta^2}{2r_{\mathrm{eff}}^2}} \qquad \text{Spatial model} \qquad (5.2)$$

$$r_{\mathrm{eff}} = \frac{r_{\mathrm{min}} r_{\mathrm{max}}}{\sqrt{(r_{\mathrm{min}}\sin(\phi-\phi_0))^2 + \sqrt{(r_{\mathrm{max}}\cos(\phi-\phi_0))^2}}} \qquad (5.3)$$

For the energy spectrum a flux normalisation of $A = 1.49 \cdot 10^{-13}\,\mathrm{cm^{-2}s^{-1}TeV^{-1}}$, a reference energy $E_0 = 1\,\mathrm{TeV}$ and a spectral index of $\Gamma = 2.52$ is chosen. In the spacial model, a fixed rotation angle of the ellipse of $\phi_0 = 45°$ is used. The resulting model is shown in Figure 5.2a. To simulate an actual source observation, the model is convolved with the PSF of the instrument provided by the IRFs (see Figure 5.2b). Furthermore, the dependency of the observations on a random Poissonian distribution of n detected photons is taken into account. With different seedings, statistically independent images can be created and studied. Finally, a background depending on the IRF background rate is added.

By specifying the observation conditions such as the telescope pointing direction, the observation time, the FOV radius and of course the IRFs, the expected number of counts per pixel given the model are calculated. The final counts map of this example is shown in Figure 5.2c.

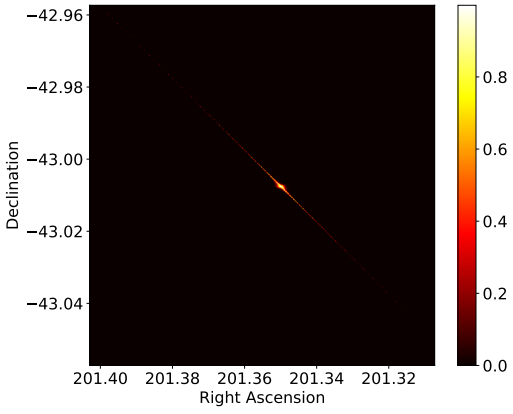

(a) Source model

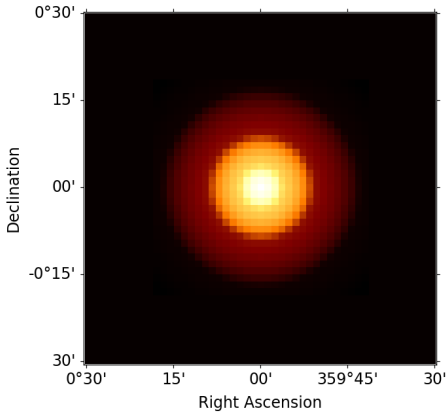

(b) PSF

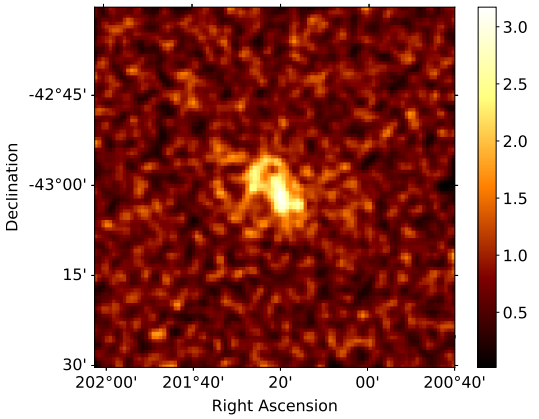

(c) Simulated source

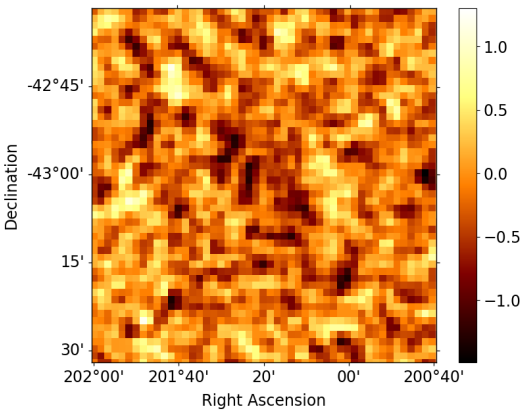

(d) Residual map

Figure 5.2 Simulation of an elliptical Gaussian distributed source with a semi-major axis radius of 0.05° and a semi-minor axis of 0.01°. For the simulation the model (a) is convolved with the PSF (b) to predict the number of detected photons in a counts map (c). After fitting, the residual map (d) should not show any significant features.

To recover the model parameters, the simulated counts maps are fitted. In this case, the same model is used for the fit as for the simulation. In ctools, an unbinned likelihood fit is performed similar to the procedure described in Section 4.2.2. The quality of the fit can be tested by analysing the residual map after subtracting the fit result from the counts image. For a good fit, the residual image should only show Poissonian noise in all pixels. This is shown for the example counts map in Figure 5.2d.
With this procedure, different complex source scenarios can be realised and studied. This will not only lead to a better understanding of the instrument itself, but will also allow prediction of the ability of CTA to discriminate between different theoretical models of a specific source by analysing the morphology. This is discussed hereafter for the radio galaxy Centaurus A.

5.3 Centaurus A

Centaurus A (Cen A) (Israel, 1998) is a radio galaxy at a distance of 3.8 Mpc from the Earth. As the closest known active galactic nucleus (AGN), it is one of the most studied objects with observations mainly in the radio, infrared, X-ray and gamma-ray bands. Classified as a type I Fanaroff-Riley radio galaxy due to its moderate luminosity, in the AGN unification model (Urry and Padovani, 1995), Cen A corresponds to a BL Lacertae object emitting a jet that is not aligned with the line of sight of an observer.
Cen A exhibits a complex morphology. A radio image of the structure is given in Figure 5.3. In total Cen A has an angular size of $8° \times 4°$. From a compact core containing the central black hole with a mass of $3\text{-}12 \cdot 10^7\ M_\odot$, a jet is emitted that is visible in the Northern direction over a length of 4.5 pc. A counter-jet probably exists but is not visible as the Doppler-boosting of the jet motion favours the jet moving in the direction of an observer. The inner jet then connects to a central jet region with a length of 1.35 kpc and then widens into the inner lopes extending outwards up to 5 kpc, a Northern middle lope with a size of 30 kpc and finally the giant outer lobes with an extension of up to 250 kpc.

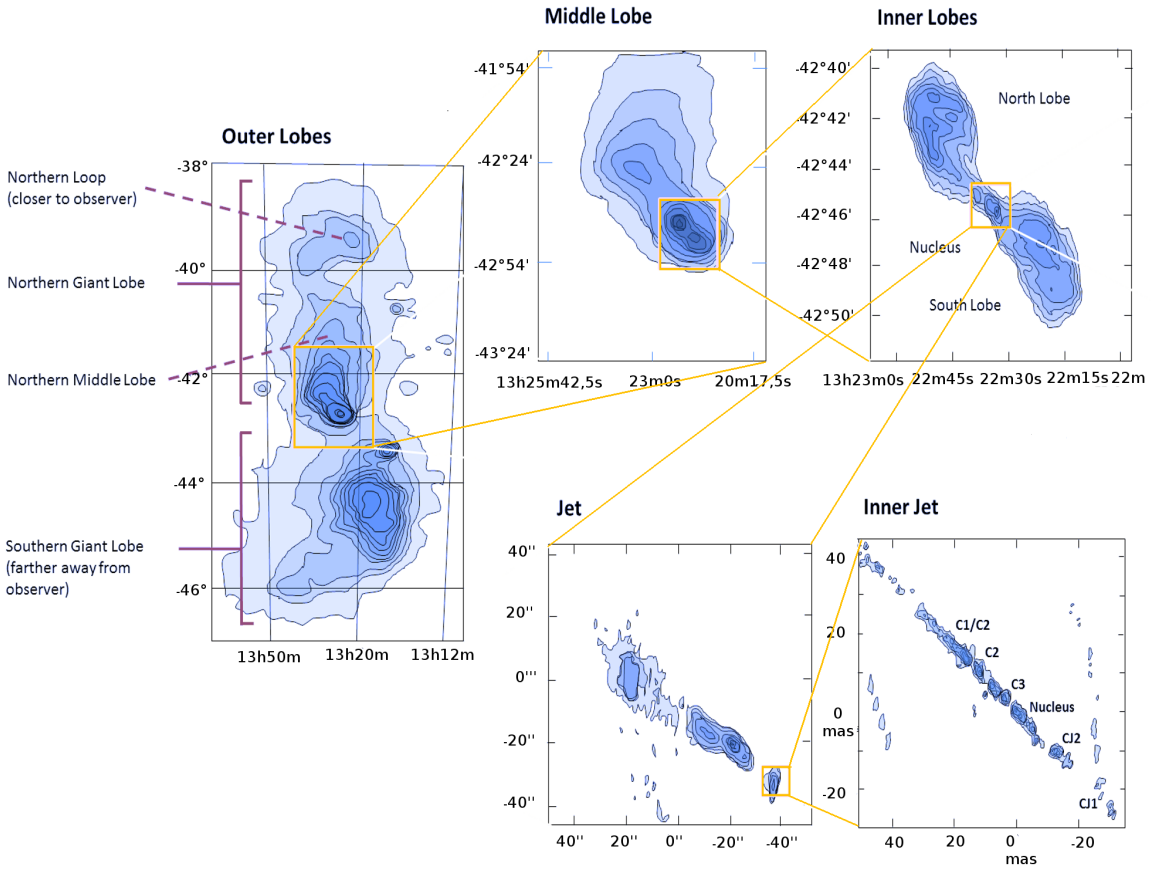

Figure 5.3 Radio image of Cen A. Cen A shows a complex morphology with scales from several degrees (outer lobes) down to few milli-arcseconds (inner jet). Image reproduced from Israel (1998) colourised by MoreInput (2015).

5.3.1 The gamma-ray picture of Centaurus A

Very high energy gamma-rays were discovered from the core region of Cen A by H.E.S.S. (Aharonian et al., 2009). This gamma-ray core region contains the central core object, the inner jets of pc-scale, the central kpc-scale jet and the inner lobes. Due to the limited angular resolution of H.E.S.S. of 0.1° this region was detected as a point source (see Figure 5.4).

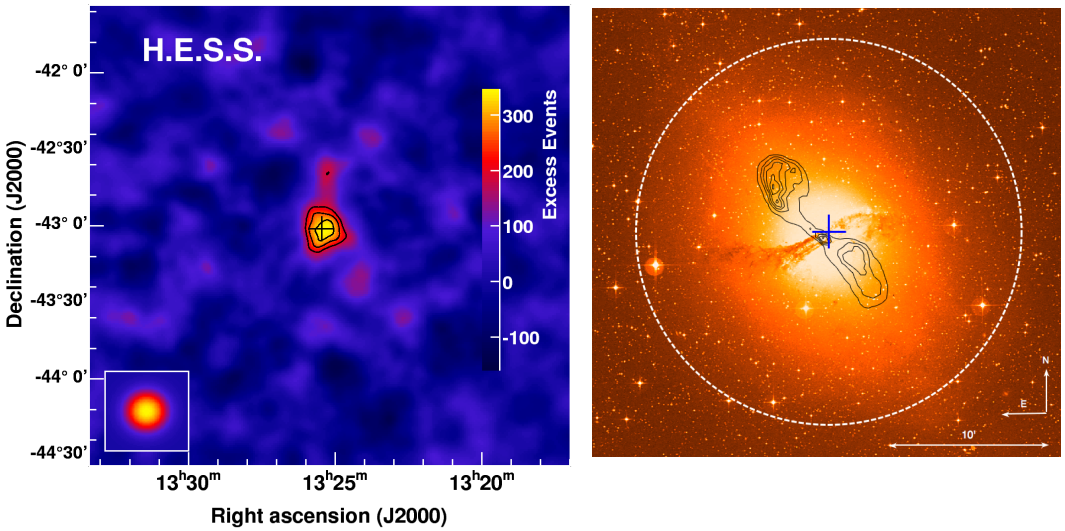

(a) H.E.S.S. detection **(b)** Optical counterpart

Figure 5.4 Optical, radio and gamma-rays observations of Cen A. (a) Due to its limited angular resolution of about 0.1°, H.E.S.S. detected the TeV emission from Cen A as point-like. (b) In the optical image by the 48-inch Schmidt telescope and the overlaid VLA radio image the host galaxy and the inner lopes of Cen A are visible within the 95% confident limit (white dashed line) of H.E.S.S. . Images from (Aharonian et al., 2009).

More recent studies by Abdalla et al. (2018a) of combined data from H.E.S.S. and Fermi-LAT revealed a hardening in the energy spectrum above 2.8 GeV and a spectral energy distribution (SED) that hints at a second gamma-ray emitting component additionally to the emission of a synchrotron self Comptonisation (SSC) component at lower energies (see Figure 5.5). Especially BL Lactea objects in general exhibit characteristic SSC dominated SEDs. These SEDs show a first broad X-ray peak originating from the synchrotron emission and a second broad gamma-ray peak due to the inverse Compton emission. The origin of the second double-peaked SSC component at the highest energies of Cen A is yet unknown. Possible explanations are proposed by different authors and are characterised by different sites of TeV emission. A selection of these theories is sketched here:

- Rieger and Aharonian (2008) proposed a centrifugal (pulsar-like) electron acceleration in radiative inefficient accretion disks around the central black hole. Accelerated electrons can upscatter ambient photon-fields via the inverse Compton effect. In this scenario, TeV emission is expected from a point-source at the black hole position of Cen A.
- Abdalla et al. (2018a) (and references therein) favour interactions between particles of the inner pc-scale jet with ambient matter, e.g. Synchrotron Self Comptonisation of particles moving along the jet in separate clumps or photon-meson interactions of accelerated protons. Emission is expected from the inner milli-arcseconds of the core.

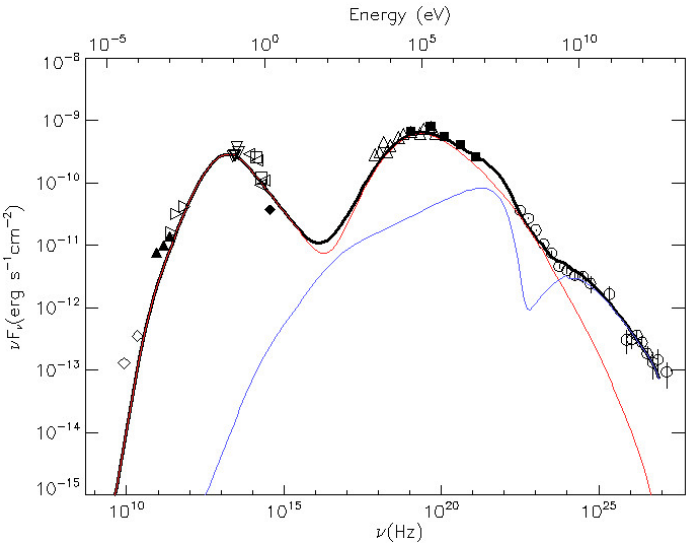

Figure 5.5 Spectral energy distribution of Cen A. The SED shows the typical double maxima structure of SSC in the sub-GeV regime (red). A second SSC component (blue) is found at higher energies. The black curve corresponds to the sum of the two components. Image taken from Abdalla et al. (2018a) with data points from TANAMI (⋄), SEST (▲), JCMT (▷), MIDI (▽), NAOS/CONICA (◁), NICMOS (□), WFPC2 (⧫), Suzaku (△), OSSE/COMPTEL (■) and Fermi/H.E.S.S (◯).

- Brown et al. (2017) suggest a population of millisecond pulsars that can form in the inner regions of galaxies in large number as the density is high. Their combined TeV emission is therefore expected from the inner kpc around the Cen A core and a spherical symmetric source extension of 10 arcminutes would be expected.
- Hardcastle and Croston (2011) propose that particles accelerated in the kpc central jet interact via the inverse Compton effect with ambient photon fields like the CMB or starlight from the host galaxy. In this scenario, an extended emission would be expected elongated along the jet axis for about 45 arcminutes.
- Brown et al. (2017) favour a spike in the dark matter density close to the galactic core that could result in TeV emission by self-annihilation of the particles. A radially symmetric emission would be expected from the central core region.

With the higher angular resolution of CTA, the actual sites of TeV emission can be determined more precisely than ever before. This will help to discriminate between the different theories listed above and to gain deeper knowledge about the processes within AGNs in general and Cen A in particular. To determine how accurate CTA can localise this emission sites, different spatial emission models of Cen A are simulated and studied by means of the optimised IRFs.

5.3.2 Simulation of Cen A

Cen A is simulated with *ctools* as described in Section 5.2. The energy spectrum corresponds to the spectrum found for very high energies in Abdalla et al. (2018a). Assuming that the extension of Cen A in South-West to North-East direction is not resolvable even with the higher angular resolution of CTA, a minor radius $r_{\mathrm{min}} = 0.01°$ is chosen for the elliptical model, while the major radius r_{max} is varied between 0.01° and 0.2° along the central jet axis. Ellipses of different sizes are compared to the Cen A radio image in Figure 5.6.

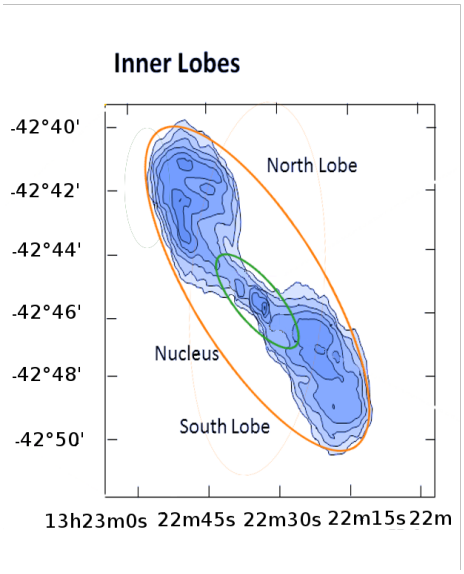

Figure 5.6 Simulated source extensions compared to the radio contours of the inner lobe structure of Cen A. The green ellipse corresponds to a source extension with a semi-major axis of $r_{\mathrm{max}} = 0.03°$, the orange to $r_{\mathrm{max}} = 0.1°$. The semi-minor axis r_{min} is not to scale.

As before, for the background, the IRF rates are used. Observation times between 5 h and 50 h are simulated. To obtain statistically solid results, 100 realisations of Possionian fluctuations in the counts maps are used per setting. The resulting counts maps are fitted with the models stated in Section 5.2. As this study is dedicated to the detection of a source extension, for simplicity, in the fit, the well established power-law spectrum of Cen A is fixed.
All simulated source extensions are smaller or equal to the angular cut of 0.2° for which the IRFs for extended sources are optimised. Therefore, it is not expected that those IRFs bring any benefit to the source detection in this specific case. Consequently, in the following analysis, the IRFs for a point-like source detection using the ImPACT and the Hillas reconstruction method with with the *HighN*, *Opt* and *AngOpt* cut optimisation are compared.
The source fitting results are shown in Figure 5.7. Due to the individual optimisation of the cut sets for the ImPACT and the Hillas event reconstruction, the determined source extension averaged over 100 iterations of simulating and fitting a model are very similar for the two reconstruction approaches. For the *HighN* optimisation the mean value of the fit results is biased towards larger sizes by about 20% over the whole energy range. For the *Opt* set, this bias is reduced to 10%, for the *AngOpt* set it is even lower. Cen A is one of the weakest known TeV sources, the flux level is therefore expected to be low. While the *HighN* cut is optimised to keep at least 30% of the events, the two other sets apply harder cuts, highly reducing the number of detected events. The low event statistic increases the uncertainty in the reconstruction of the source sizes. With the higher angular resolution of the *Opt* and *AngOpt* optimisation, the parameters of the ellipses can be determined with a higher precision, making it easier for the fit to recover the correct extensions.
The standard deviation of the size determination decreases for longer observation times as expected. However, it also increase from the *HighN* to the *Opt* and the *AngOpt* cut set as the event statistics decreases. The significance of a source detection is defined by the ratio of the reconstructed source size to one standard deviation of the result. For the present analysis, a significance level of at least 5 is required to claim the detection of an extended emission from the centre of Cen A. This significance is studied in detail in Figure 5.8 and Figure 5.9

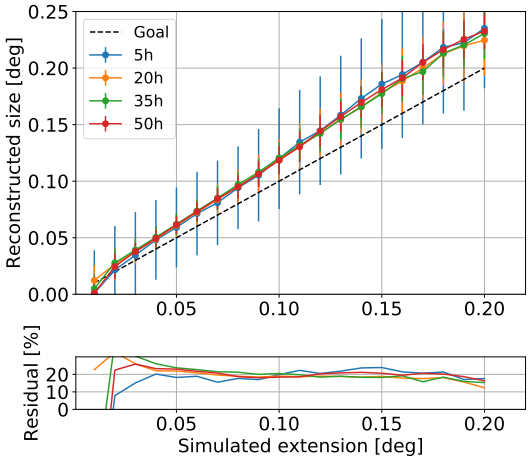

(a) HighN ImPACT

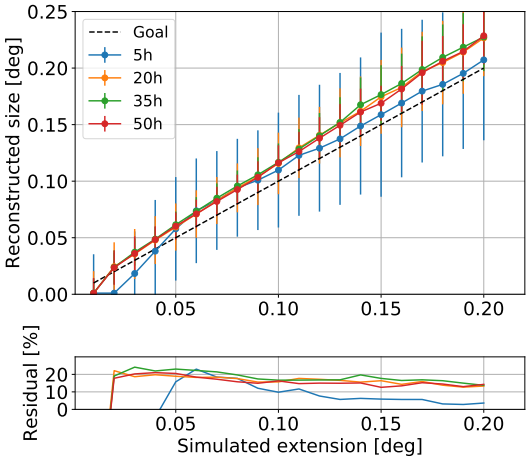

(b) HighN Hillas

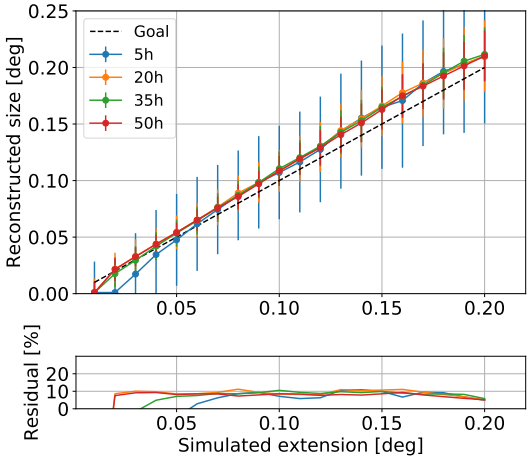

(c) Opt ImPACT

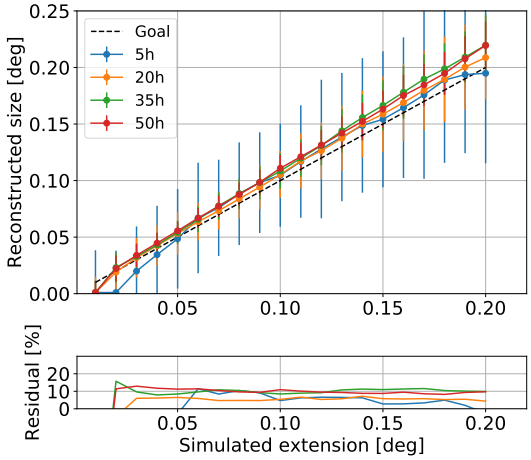

(d) Opt ImPACT

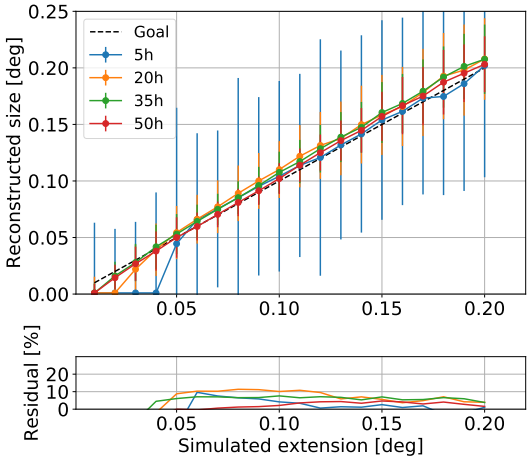

(e) AngOpt ImPACT

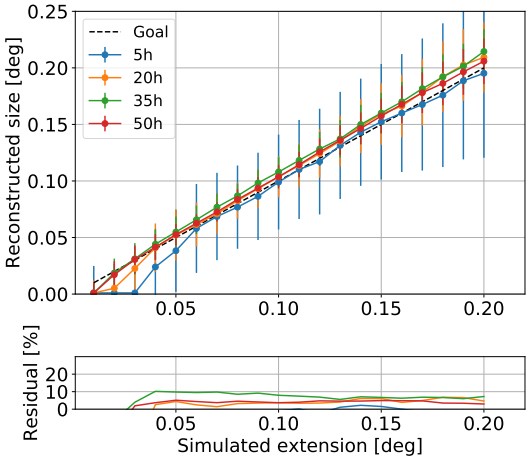

(f) AngOpt ImPACT

Figure 5.7 Results of the source size fitting of Cen A for different extensions with the different cut sets for Hillas and ImPACT reconstruction. With a higher angular resolution, the deviation of the mean reconstructed size from the real source becomes smaller. Statistical errors for short observation times are large due to the low event statistic expected from Cen A.

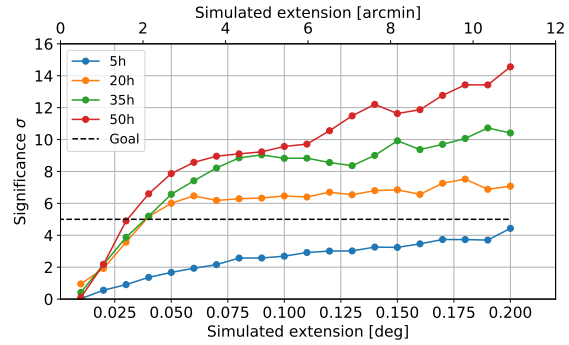

(a) HighN ImPACT

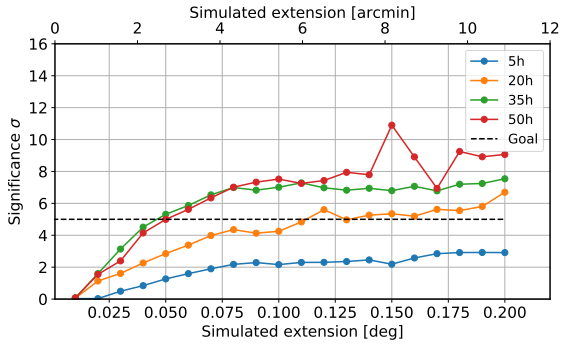

(b) HighN Hillas

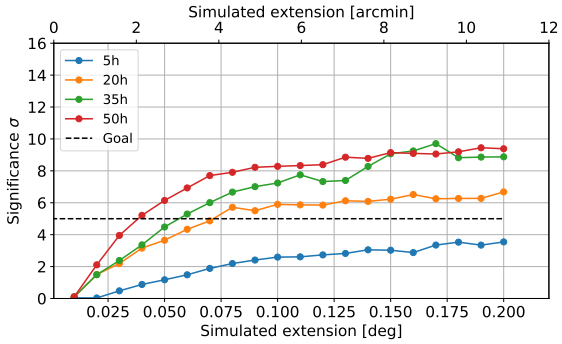

(c) Opt ImPACT

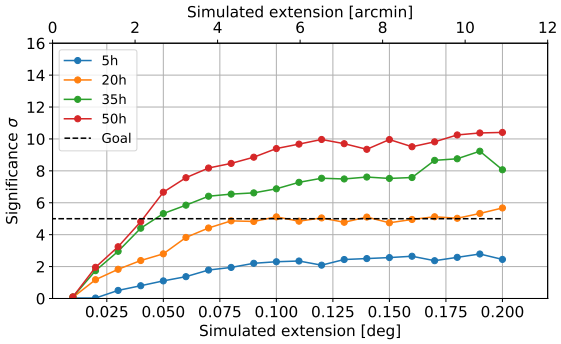

(d) Opt Hillas

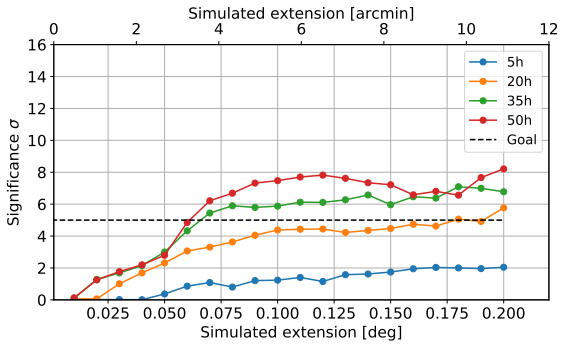

(e) AngOpt ImPACT

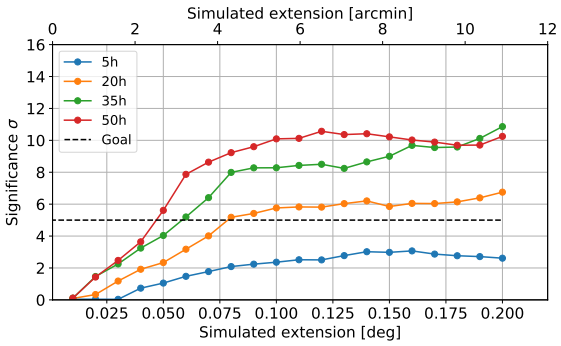

(f) AngOpt Hillas

Figure 5.8 Significance of the Cen A extension detection for different cut sets for the ImPACT and the Hillas reconstruction. Due to the higher event statistics, in general the ImPACT reconstruction reaches a higher significance that the Hillas reconstruction.

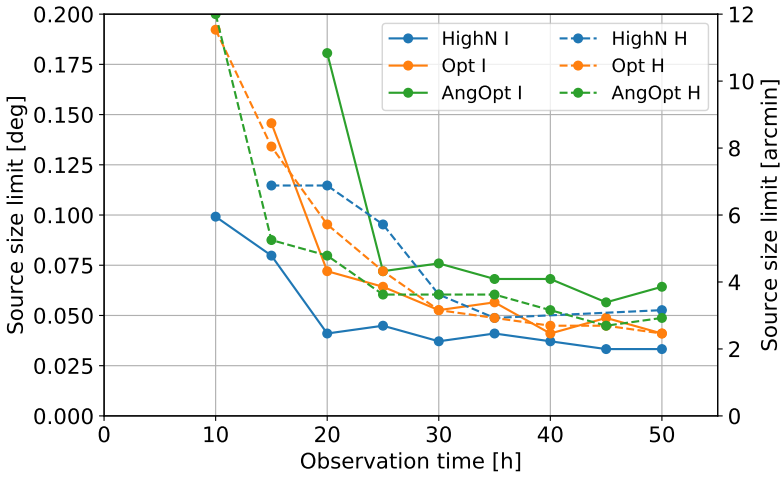

Figure 5.9 Lower size limit for a significant detection of a source extension over the observation time for the optimised cut sets with the ImPACT (I) and the Hillas (H) reconstruction. Due to the low flux, the full potential of the optimised cuts cannot be exploited.

The *HighN* optimisation achieves a significant detection with the ImPACT reconstruction already for an observation time above 20 hours for source sizes below 0.05° or 3 arcminutes, respectively. With an observation of 50 hours even a source of 0.03° or 1.8 arcminutes size can be detected with the required significance. The higher cuts needed for the Hillas reconstruction to reach the same angular resolution and sensitivity decreases the detected flux further, so that finally significant source detections are possible for a 20 hours observation above source sizes of 0.12° or for a 50 hours observation for source sizes of 0.05°.
Due to the low event rate, the *Opt* cut provides a lower significance for the same observation times. Nevertheless, significant source detection is possible above 0.04° for both reconstruction methods with an observation time of 50 hours.
Finally, the *AngOpt* cut set is purely optimised to provide the best angular resolution. Consequently, it produced the lowest deviation of the mean reconstructed size to the real source size. This benefit comes with a very low event rate and so the significance for Cen A-like sources is reached for sizes above 0.06° for the ImPACT analysis and 0.05° for Hillas reconstruction. With none of the cut sets the required significance limit can be reached for an observation time below 10 hours with neither reconstruction mechanism.
The looser cuts needed for the ImPACT event reconstruction compared to the classical Hillas analysis, result in a higher event statistics at the same very high angular resolution and flux sensitivity. With this high resolution, significant determinations of the TeV emission sites of Cen A can be provided. Even though the accuracy is not high enough to distinguish between emission scenarios that predict an emission from the inner core of Cen A such as the centrifugal electron acceleration, the dark matter scenario and the inner pc scale jet interactions that would emit within the inner arcminute around the core, it is clearly possible to detect any extended emission from millisecond pulsars in the inner 10 arminutes or the outer jet extending up to 45 arcminutes. Longer observation times may decrease the lower limits discussed here, so that a study of the inner arcminute around the core of Cen A might be feasible after all. However, already with the resolution predicted by this analysis, source observations with CTA will greatly improve our understanding of the particle acceleration and propagation processes in AGNs.

5.4 Conclusion and outlook

Quality selection cuts on the data recorded by CTA highly improve the performance of the instrument. Already the preselection cuts on the signal amplitude, the number of significant pixels and the distance of the image centroid to the camera center enhance the angular resolution at energies above 1 TeV by 30%. With an angular cut on the data and a simple telescope multiplicity cut, the CTA requirements for the point-like flux sensitivity can be fulfilled over almost the whole energy range and the angular resolution even exceeds the requirements by 25% in average. With the Hillas reconstruction, a similar performance can be reached, however, much harder selection cuts are needed, which results in lower event statistics and thus longer observation times.
For the ImPACT analysis, three sets of optimised energy-dependent multiplicity cuts for the detection of a point source and an extended source, each, are established: The *HighN* cut provides the best angular resolution and sensitivity while still keeping at least 30% of the events, the *Opt* cut uses higher cuts to result in the best compromise performance between angular resolution and sensitivity without taking into account the number of events and the *AngOpt* cut provides the highest angular resolution independent of the number of events or the sensitivity. With these optimised cut sets, the sensitivity for the detection of a point-source is 20% better than required for the *HighN* cut and even 40% for the *Opt* cut and the *AngOpt* cut. For an extended angular cut, optimised for source extensions above 0.2°, a sensitivity can be reached that fulfils the requirements for the detection of a point-source at energies below 1 TeV and otherwise deviates by only 50% in average.
The main improvement is, however, gained for the angular resolution. With all three optimised multiplicity cuts an average improvement between 30% and 40% over the requirements can be reached. At the highest energies angular resolutions below 1 arcminute are possible. With this angular resolution, possible source extensions of the radio galaxy Centaurus A are found to be detectable with a significance level above 5 σ down to sizes of 4.9 arcminutes with the *AngOpt* cut and even 1.8 arcminutes with the *HighN* cut in a 50 hours observation. Other lower limits of a source extension detectable with the ImPACT and the Hillas reconstruction are summarised in Table 5.1 for selected observation times.

Table 5.1 Lower source extension limit (in degree/arcminutes) for a 5 σ significance detection for the three cut sets with ImPACT and the Hillas reconstruction for different observation times.

	ImPACT			Hillas		
Observation time [h]	20	35	50	20	35	50
HighN	0.04/2.4	0.04/2.4	0.03/1.8	0.13/7.8	0.05/3	0.05/3
Opt	0.08/4.8	0.06/3.6	0.04/2.4	0.1/6	0.05/3	0.05/3
AngOpt	0.08/4.8	0.07/4.2	0.06/3.6	0.18/10.8	0.07/4.2	0.07/4.2

As Centaurus A is one of the weakest known TeV sources, the firm detection of an extension of arcminute scale at the given flux level is very promising for future CTA observations in general. For sources with a stronger TeV emission, the full potential of the *AngOpt* cut could be exploited and the size limits can be lowered even further. However, even with the current limits the available theoretical models explaining the emission of Cen A – so far is only measured as a point-source – can be restrained. This opens up a window into the processes of particle acceleration and propagation in the centres of AGNs of an accuracy never reached in TeV astronomy before.

Nevertheless, further improvements can be made. The data processing software *ctapipe* and especially the event reconstruction approaches are still under development. Changes and optimisations can be expected before the official start of CTA operation. Possible improvements include a better seeding and more advanced minimisation algorithms for the ImPACT likelihood fit as well as new and improved image templates. Intrinsic fluctuations of the EAS can be studied in more detail and included into the likelihood calculation. Also the BDT background rejection can be updated to include the GOF parameter of the ImPACT fit, which could then improve especially the high energy performance of the background classification. All these changes will directly influence the quality of the shower parameter reconstruction and thus improve the angular resolution and the flux sensitivity to even higher levels.
Also further optimisation cuts can be studied. A fit on the parameter uncertainties calculated by the MINUIT likelihood minimisation was investigated during this work, but found to be unstable. More effort can be invested into fixing this instability, so that a rejection cut depending on the fit uncertainty estimates can be developed. Suppressing events with large errors on the reconstructed source direction and energy, could significantly improve the recovered shower parameters and hence the performance of CTA.
Concluding, it can be said, that the expected performance of the future CTA observatory makes it a very promising instrument to explore the universe at the highest energies. An angular resolution and a flux sensitivity of at least one order of magnitude better than current instruments, will be especially useful for the planned Galactic plane survey. From the H.E.S.S. survey (Abdalla et al., 2018b) it is interpolated that with a higher sensitivity and resolution hundreds of new sources in the galactic plain could be detected. The main part will be extended sources like pulsar wind nebulae and supernova remnants, but also a range of small-scale sources. With a high statistics on TeV source populations, a new insight in the general behaviour of different source classes will be possible. Together with detailed studies of the complex morphologies of extended sources inside and outside of our Galaxy, this will bring us closer to solving the mystery of the cosmic-ray origin.

APPENDIX A

Angular resolution curves for postselection cuts

Core cut

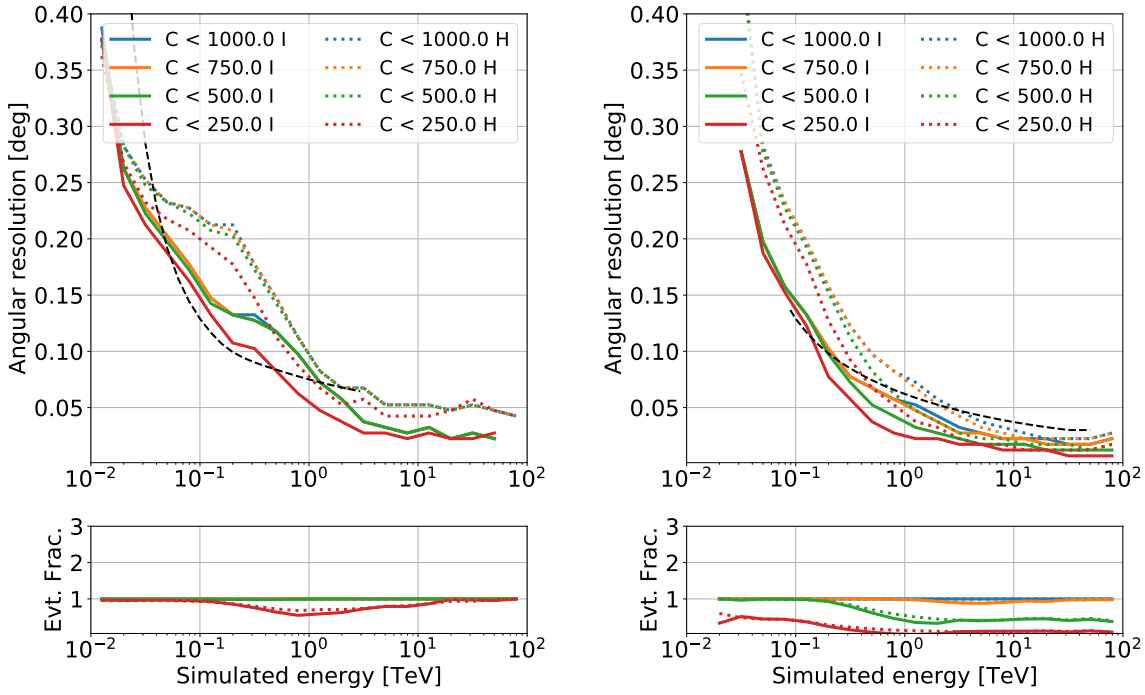

(a) LST **(b)** MST

Figure A.1 Angular resolution after a cut on the distance between the shower core position and the array center for different telescope array subsystems for ImPACT (I) and Hillas (H) reconstruction. The black dashed line identifies the CTA requirement. In the lower panel of each plot, the number of events is shown compared to the number after applying the optimised preselection cuts. With higher core distance cuts the medium and high energy regime can be improved.

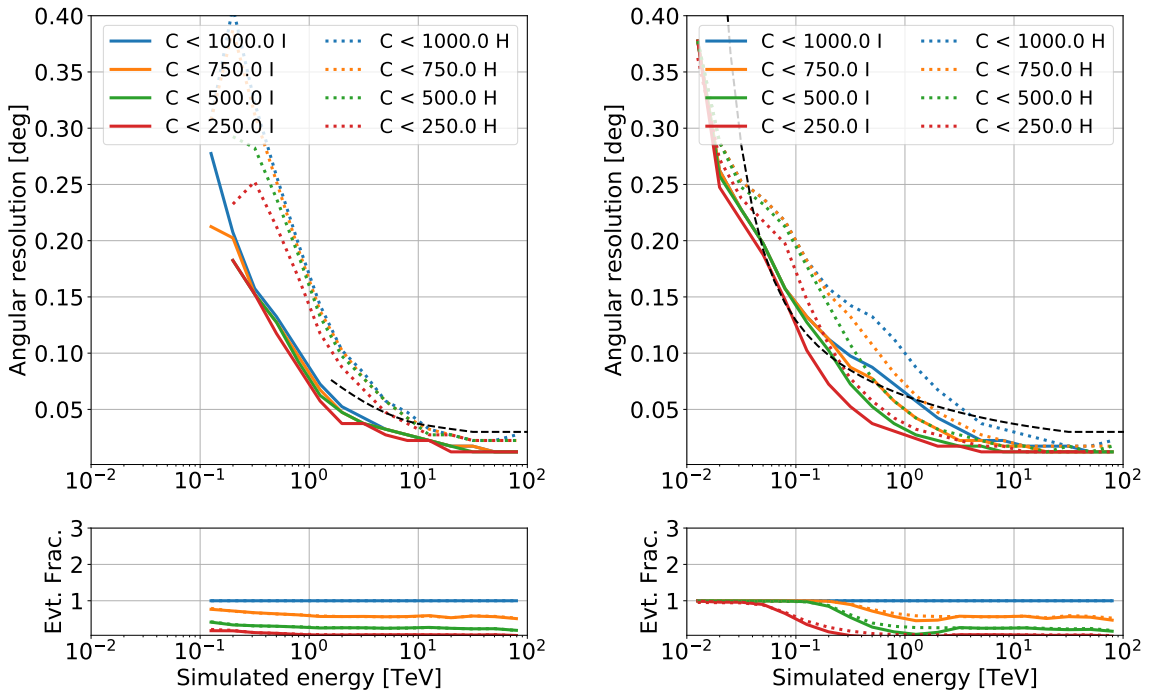

(c) SST **(d)** Full array

Figure A.1 Angular resolution after a cut on the distance between the shower core position and the array center for different telescope array subsystems for ImPACT (I) and Hillas (H) reconstruction. The black dashed line identifies the CTA requirement. In the lower panel of each plot, the number of events is shown compared to the number after applying the optimised preselection cuts. With higher core distance cuts the medium and high energy regime can be improved (Continued).

Multiplicity cut

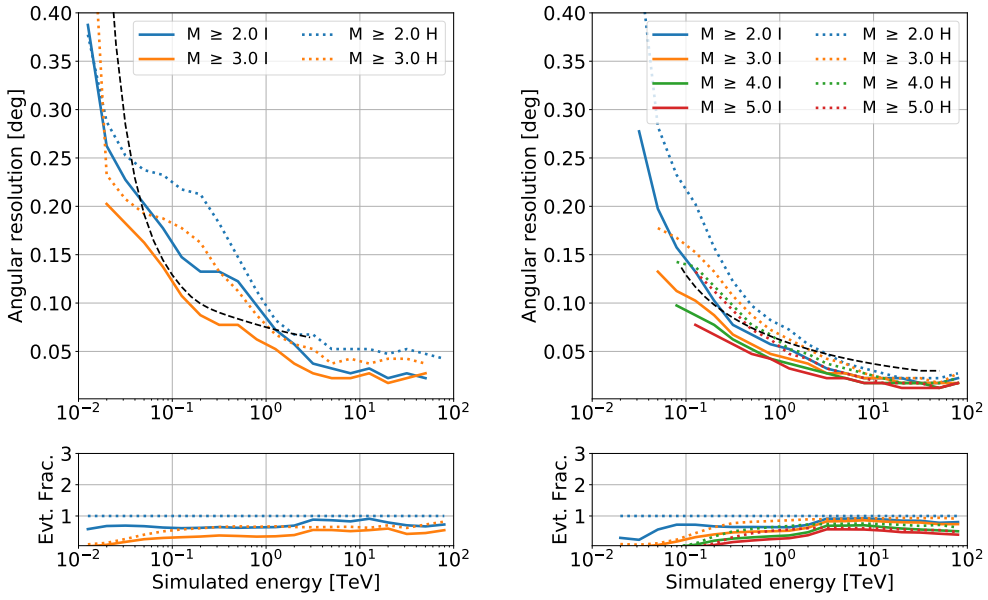

(a) LST

(b) MST

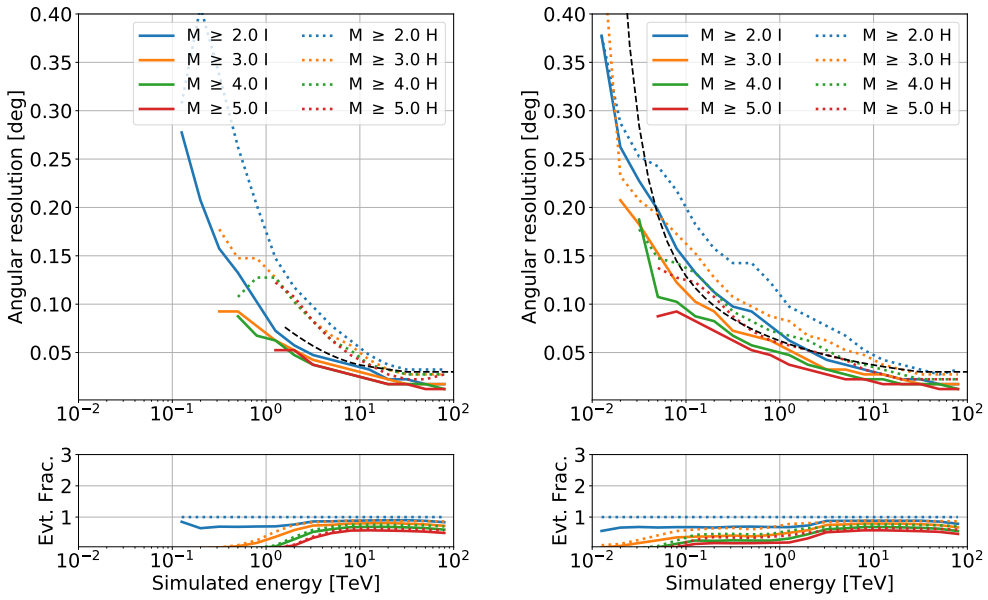

(c) SST

(d) Full array

Figure A.2 Angular resolution after a cut on the telescope multiplicity for different telescope array subsystems for ImPACT (I) and Hillas (H) reconstruction. The black dashed line identifies the CTA requirement. In the lower panel of each plot, the number of events is shown compared to the number after applying the optimised preselection cuts. With higher telescope multiplicity cuts the full energy regime can be improved. The $M \geq 2$ cut also shows the performance of the background and error cut.

APPENDIX B

Energy dependent cut performance

LST: Optimised postselection cut

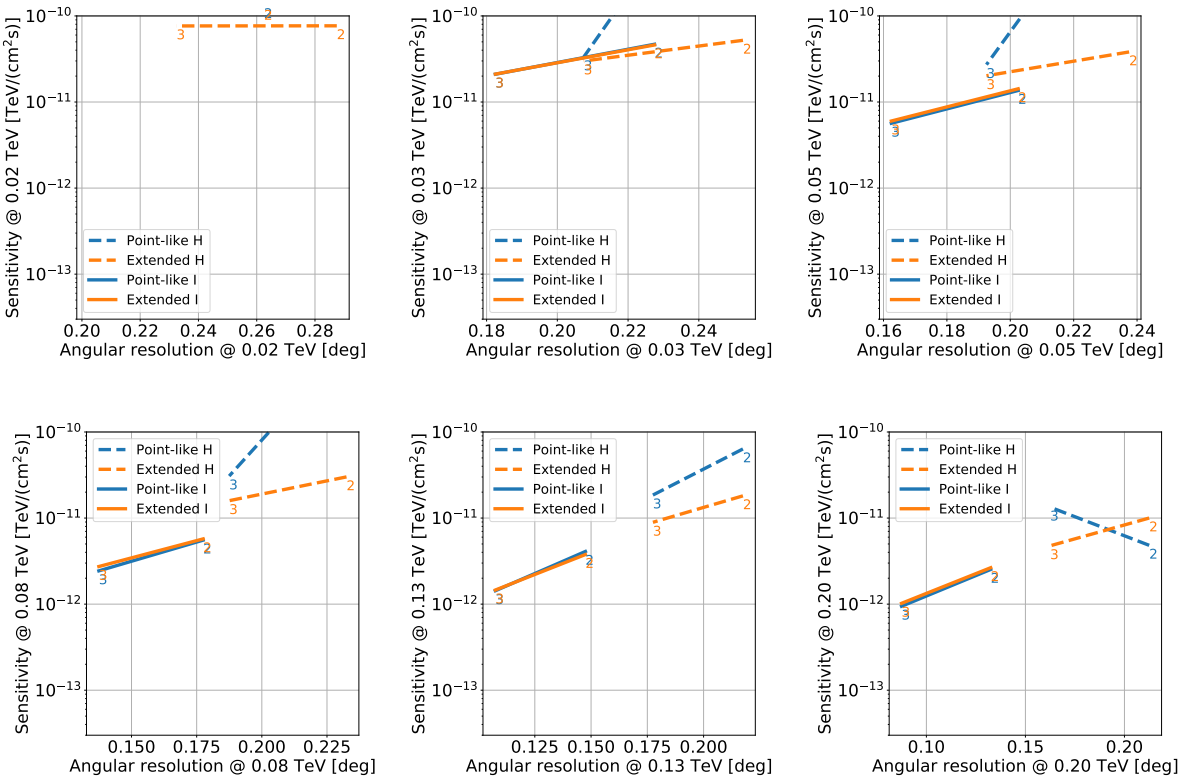

Figure B.1 Cut-dependent performance at fixed energies for LSTs for ImPACT (I) and Hillas (H) reconstruction. At each step the corresponding multiplicity cut is specified by the number below the line. If the performance does not change, the higher cut number is omitted. As small resolutions and sensitivities are desired, priority is given to values in the lower left corner.

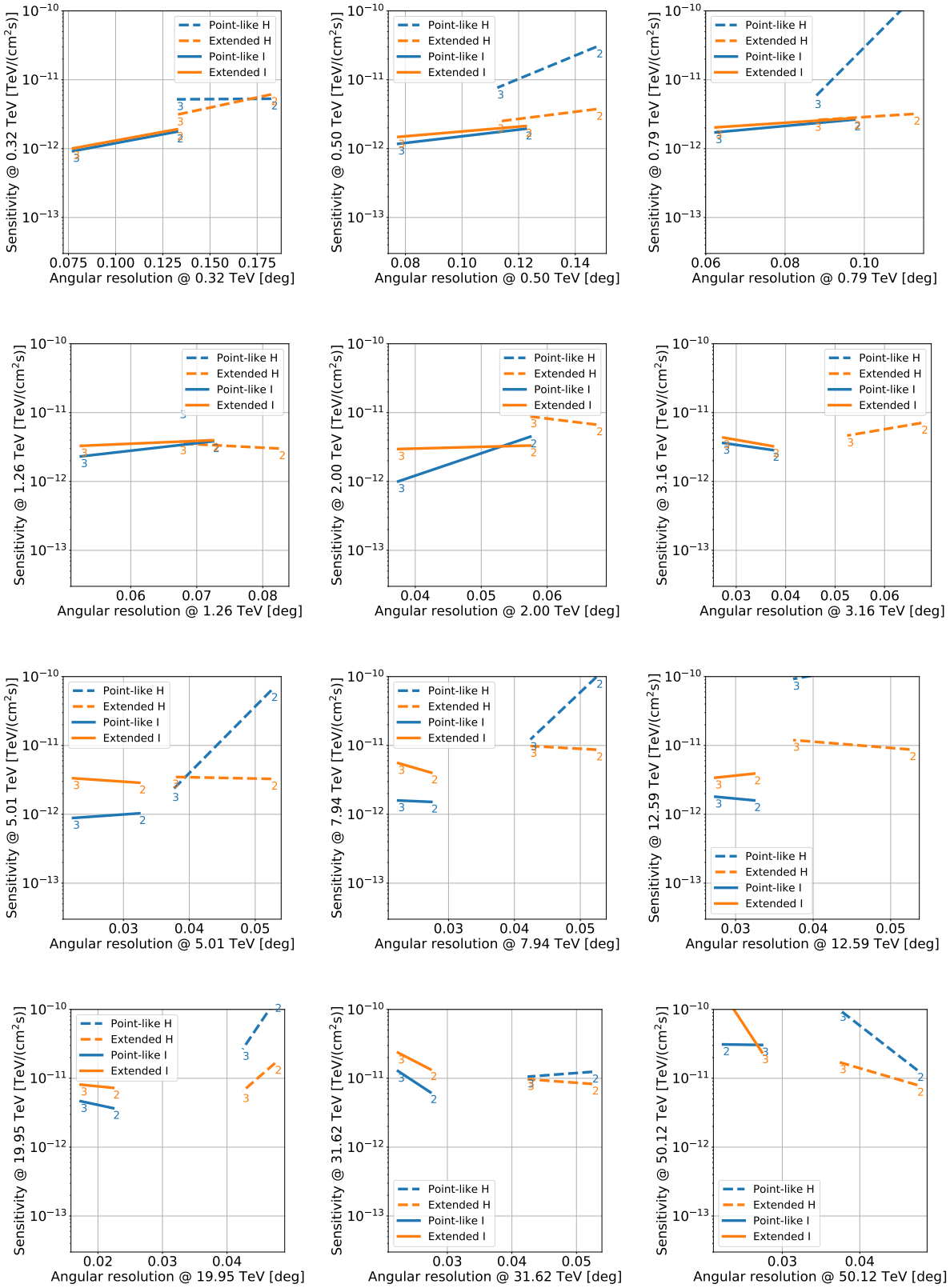

Figure B.1 Cut-dependent performance at fixed energies for LSTs for ImPACT (I) and Hillas (H) reconstruction. At each step the corresponding multiplicity cut is specified by the number below the line. If the performance does not change, the higher cut number is omitted. As small resolutions and sensitivity are desired, priority is given to values in the lower left corner (Continued).

MST: Optimised postselection cut

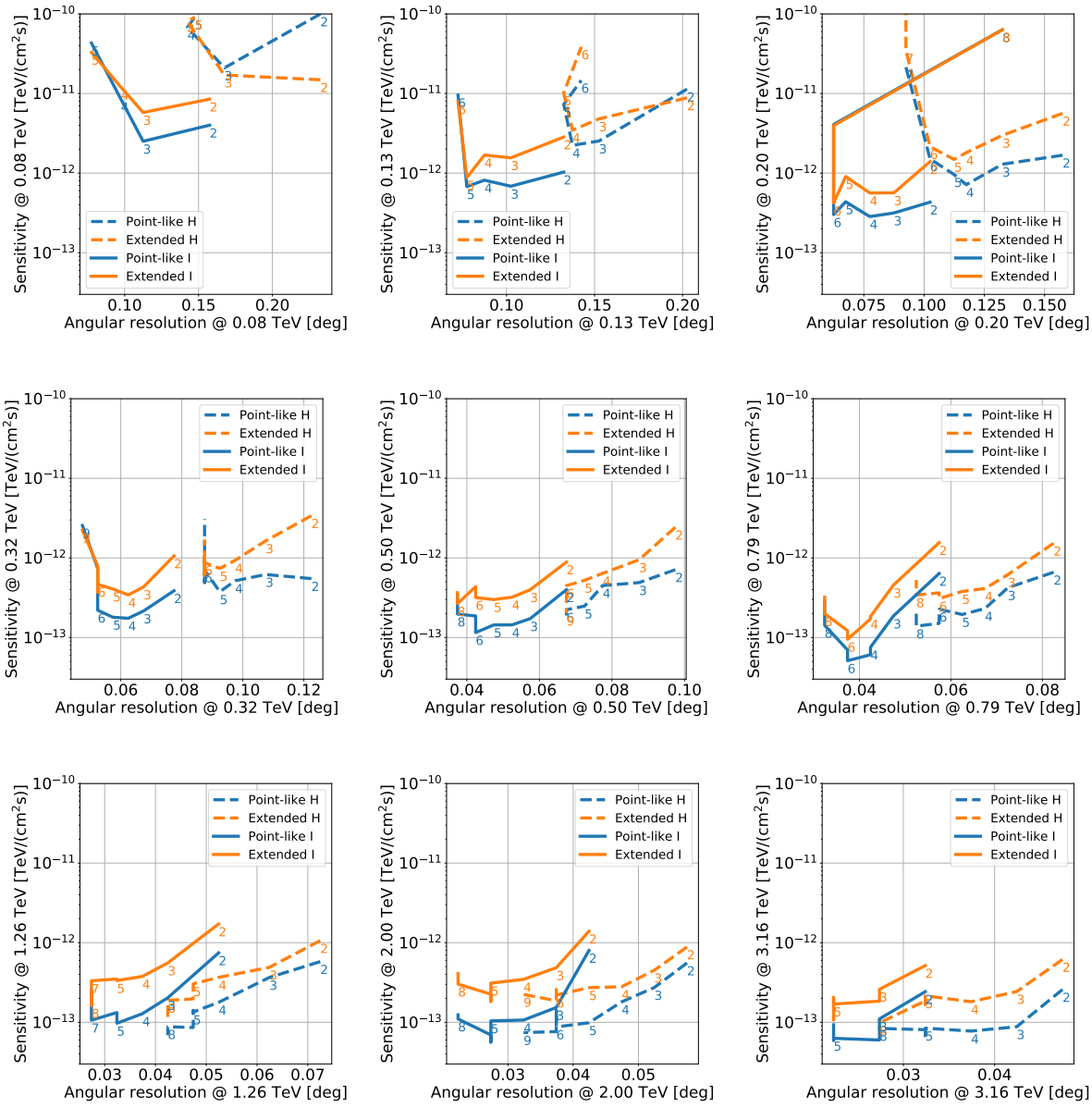

Figure B.2 Cut-dependent performance at fixed energies for MSTs for ImPACT (I) and Hillas (H) reconstruction. At each step the corresponding multiplicity cut is specified by the number below the line. If the performance does not change, the higher cut number is omitted. As small resolutions and sensitivity are desired, priority is given to values in the lower left corner.

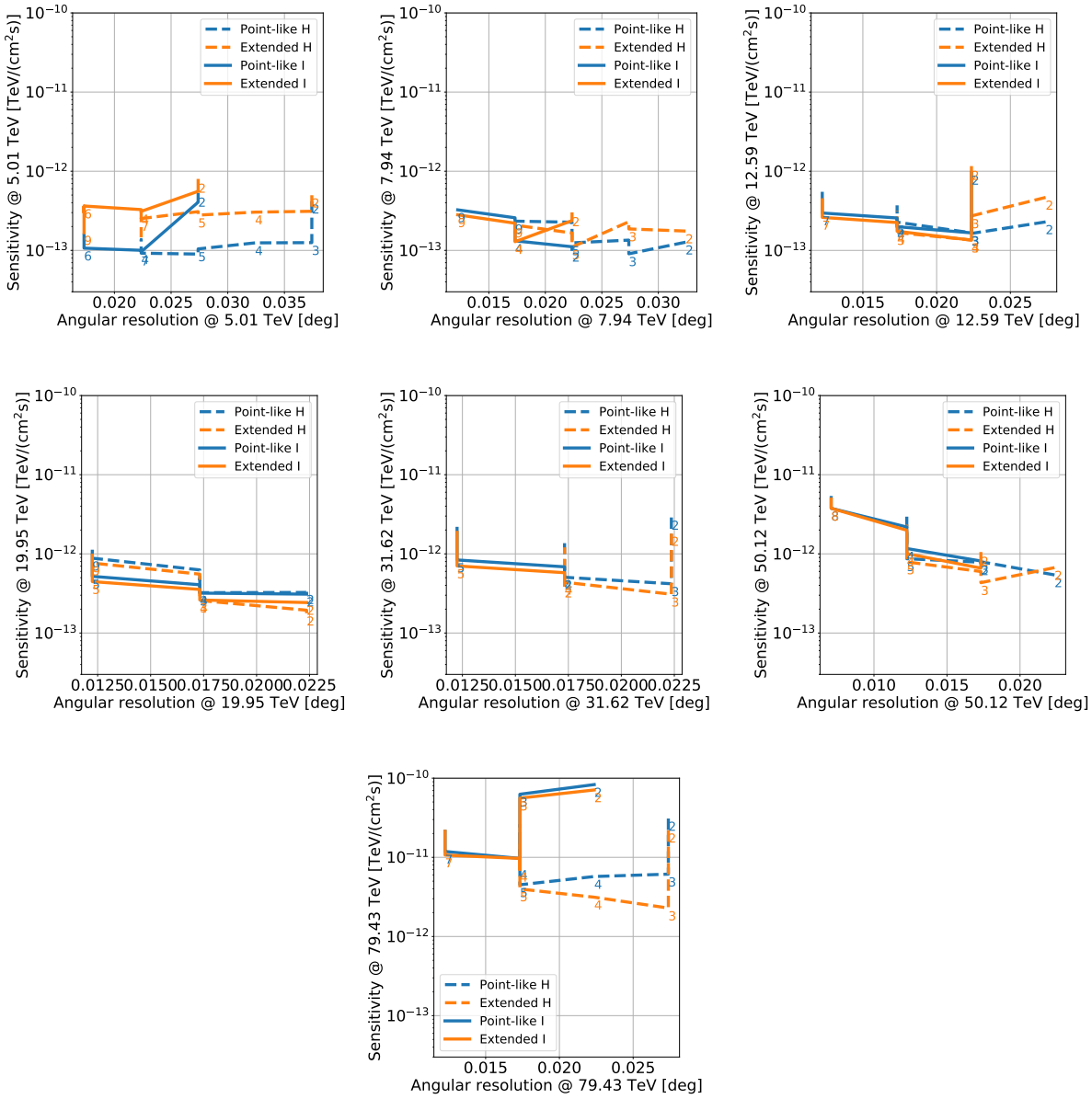

Figure B.2 Cut-dependent performance at fixed energies for MSTs for ImPACT (I) and Hillas (H) reconstruction. At each step the corresponding multiplicity cut is specified by the number below the line. If the performance does not change, the higher cut number is omitted. As small resolutions and sensitivity are desired, priority is given to values in the lower left corner (Continued).

SST: Optimised postselection cut

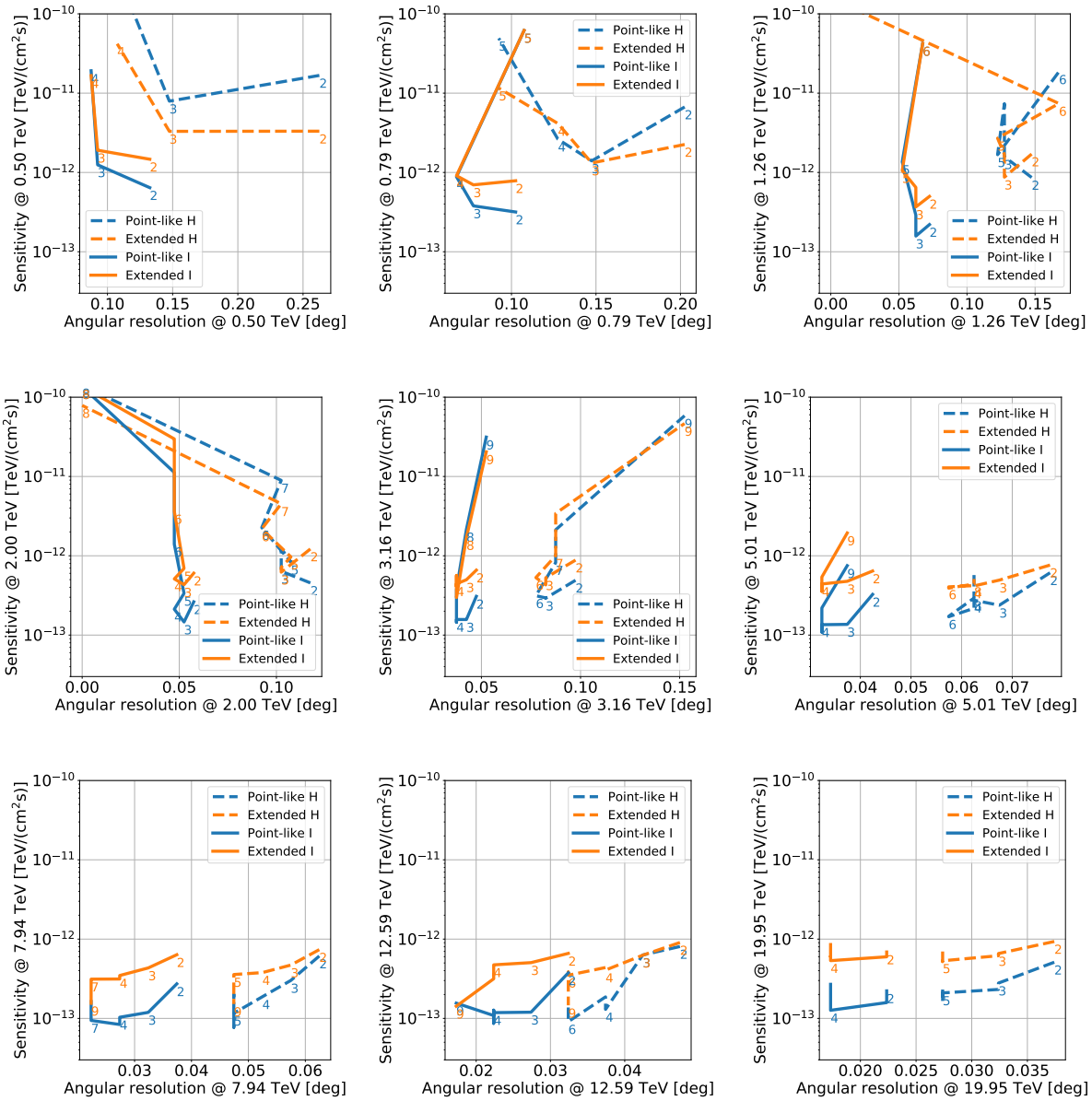

Figure B.3 Cut-dependent performance for SSTs for ImPACT (I) and Hillas (H) reconstruction. At each step the corresponding multiplicity cut is specified by the number below the line. If the performance does not change, the higher cut number is omitted. As small resolutions and sensitivity are desired, priority is given to values in the lower left corner.

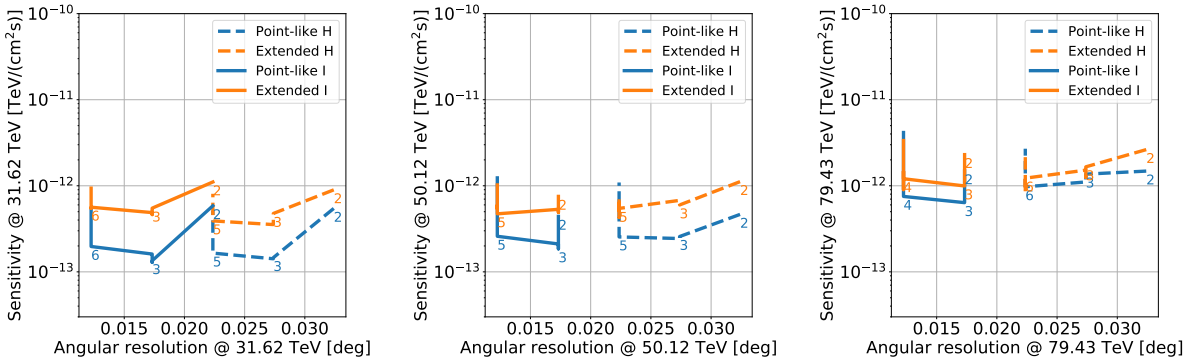

Figure B.3 Cut-dependent performance at fixed energies for SSTs for ImPACT (I) and Hillas (H) reconstruction. At each step the corresponding multiplicity cut is specified by the number below the line. If the performance does not change, the higher cut number is omitted. As small resolutions and sensitivity are desired, priority is given to values in the lower left corner (Continued).

Full array: Optimised postselection cut

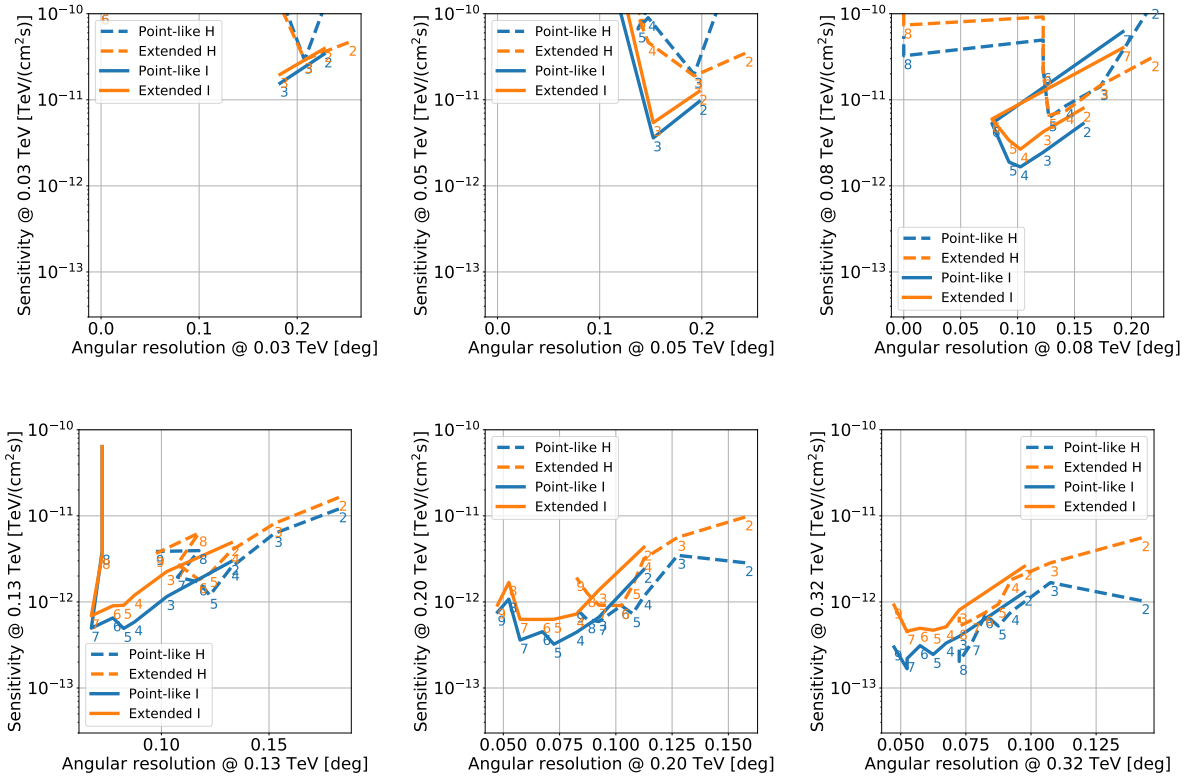

Figure B.4 Cut-dependent performance at fixed energies for the full array for ImPACT (I) and Hillas (H) reconstruction. At each step the corresponding multiplicity cut is specified by the number below the line. If the performance does not change, the higher cut number is omitted. As small resolutions and sensitivity are desired, priority is given to values in the lower left corner.

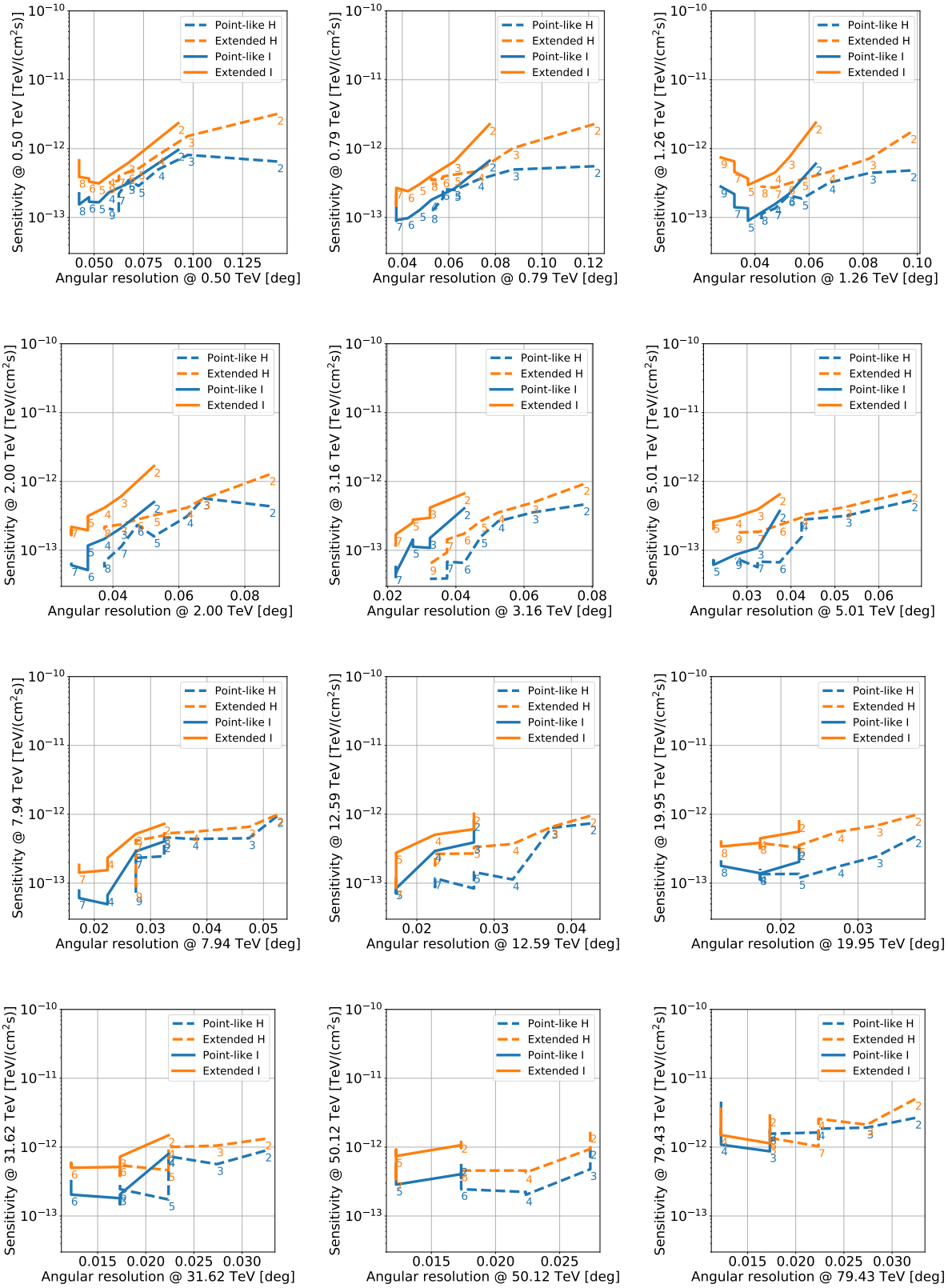

Figure B.4 Cut-dependent performance at fixed energies for the full array for ImPACT (I) and Hillas (H) reconstruction. At each step the corresponding multiplicity cut is specified by the number below the line. If the performance does not change, the higher cut number is omitted. As small resolutions and sensitivity are desired, priority is given to values in the lower left corner (Continued).

Optimised cut sets: Tables

Table B.1 Optimised multiplicity cut sets for the ImPACT reconstruction.

	Point-like			Extended		
Energy [TeV]	HighN	Opt	AngOpt	HighN	Opt	AngOpt
0.01	2	3	3	2	3	3
0.02	2	3	3	2	3	3
0.03	2	3	3	2	3	3
0.05	2	3	3	2	3	3
0.08	3	4	4	3	4	6
0.13	4	5	5	3	7	7
0.20	3	7	9	3	7	9
0.32	3	7	9	3	7	8
0.50	4	8	8	3	5	8
0.79	3	7	7	3	6	7
1.26	4	5	9	4	5	9
2.00	4	6	7	5	6	7
3.16	6	7	7	7	7	7
5.01	5	5	5	5	5	5
7.94	5	5	7	7	7	7
12.59	5	5	5	7	7	7
19.95	5	5	8	8	8	8
31.62	3	3	6	4	4	6
50.12	4	4	5	7	7	7
79.43	3	3	4	3	3	4

Table B.2 Optimised multiplicity cut sets for the Hillas reconstruction.

	Point-like			Extended		
Energy [TeV]	HighN	Opt	AngOpt	HighN	Opt	AngOpt
0.01	2	3	3	2	3	3
0.02	2	3	3	2	3	3
0.03	2	3	3	2	3	3
0.05	2	3	5	2	3	5
0.08	3	5	8	4	5	8
0.13	5	5	9	4	6	9
0.20	5	8	9	4	7	9
0.32	6	8	8	2	8	8
0.50	5	8	8	4	9	9
0.79	5	8	8	5	8	8
1.26	7	8	8	5	7	8
2.00	8	8	8	8	8	8
3.16	9	9	9	7	9	9
5.01	8	8	9	9	9	9
7.94	9	9	9	7	9	9
12.59	7	7	7	7	7	7
19.95	8	8	8	5	5	8
31.62	5	5	6	5	5	6
50.12	6	6	6	6	6	6
79.43	8	8	8	7	7	8

List of Figures

List of Tables

Bibliography

A. Aab et al. Depth of maximum of air-shower profiles at the Pierre Auger Observatory. II. Composition implications. *Physical Review*, D90(12), 2014. doi: 10.1103/PhysRevD.90.122006. arXiv:1409.5083 [astro-ph.HE].

A. Aab et al. The Pierre Auger Cosmic Ray Observatory. *Nuclear Instruments and Methods in Physics Research Section A: Accelerators, Spectrometers, Detectors and Associated Equipment*, 798:172 – 213, 2015. doi: 10.1016/j.nima.2015.06.058. arXiv:1502.01323 [astro-ph.IM].

A. Aab et al. The Pierre Auger Observatory Upgrade - Preliminary Design Report. 2016. arXiv:1604.03637 [astro-ph.IM].

M. G. Aartsen et al. Combined Analysis of Cosmic-Ray Anisotropy with IceCube and HAWC. In *Proceedings, 35th International Cosmic Ray Conference (ICRC)*, 2017. arXiv:1708.03005 [astro-ph.HE].

H. Abdalla et al. The gamma-ray spectrum of the core of Centaurus A as observed with H.E.S.S. and Fermi-LAT. 2018a. arXiv:1807.07375 [astro-ph.HE].

H. Abdalla et al. The H.E.S.S. Galactic plane survey. *Astronomy & Astrophysics*, 612:A1, 2018b. doi: 10.1051/0004-6361/201732098. arXiv:1804.02432 [astro-ph.HE].

H. Abdalla et al. The population of TeV pulsar wind nebulae in the H.E.S.S. Galactic Plane Survey. *Astronomy & Astrophysics*, 612:A2, 2018c. doi: 10.1051/0004-6361/201629377. arXiv:1702.08280 [astro-ph.HE].

A. U. Abeysekara et al. Observation of the Crab Nebula with the HAWC Gamma-Ray Observatory. *The Astrophysical Journal*, 843:39, 2017. doi: 10.3847/1538-4357/aa7555. arXiv:1701.01778 [astro-ph.HE].

J. o. Abraham. Observation of the Suppression of the Flux of Cosmic Rays above $4x10^{19}$ eV. *Physical Review Letters*, 101:061101, 2008. doi: 10.1103/PhysRevLett.101.061101. arXiv:0806.4302 [astro-ph].

T. Abu-Zayyad et al. The Cosmic-Ray Energy Spectrum Observed with the Surface Detector of the Telescope Array Experiment. *The Astrophysical Journal Letters*, 768(1):L1, 2013. doi: 10.1088/2041-8205/768/1/L1. arXiv:1205.5067 [astro-ph.HE].

B. S. Acharya et al. Science with the Cherenkov Telescope Array. 2017. arXiv:1709.07997 [astro-ph.IM].

S. Agostinelli et al. Geant4—a simulation toolkit. *Nuclear Instruments and Methods in Physics Research Section A: Accelerators, Spectrometers, Detectors and Associated Equipment*, 506(3):250 – 303, 2003. ISSN 0168-9002. doi: 10.1016/S0168-9002(03)01368-8.

F. Aharonian et al. Observations of the Crab Nebula with H.E.S.S. *Astronomy & Astrophysics*, 457:899–915, 2006. doi: 10.1051/0004-6361:20065351. arXiv:0607333 [astro-ph].

F. Aharonian et al. Discovery of Very High Energy γ-Ray Emission from Centaurus a with H.E.S.S. *The Astrophysical Journal*, 695:L40–L44, 2009. doi: 10.1088/0004-637X/695/1/L40. arXiv:0903.1582 [astro-ph.CO].

M. Ahlers and P. Mertsch. Origin of Small-Scale Anisotropies in Galactic Cosmic Rays. *Progress in Particle and Nuclear Physics*, 94:184–216, 2017. doi: 10.1016/j.ppnp.2017.01.004. arXiv:1612.01873 [astro-ph.HE].

M. Amenomori. Northern sky Galactic Cosmic Ray anisotropy between 10-1000 TeV with the Tibet Air Shower Array. *Astrophysical Journal*, 836(2):153, 2017. doi: 10.3847/1538-4357/836/2/153. arXiv:1701.07144 [astro-ph.HE].

W. D. Apel et al. The spectrum of high-energy cosmic rays measured with KASCADE-Grande. 2012. arXiv:1206.3834 [astro-ph.HE].

J. Arons. Particle acceleration by pulsars. In G. Setti, G. Spada, and A. W. Wolfendale, editors, *Origin of Cosmic Rays*, volume 94 of *IAU Symposium*, pages 175–204, 1981.

W. B. Atwood et al. The Large Area Telescope on the Fermi Gamma-Ray Space Telescope Mission. *The Astrophysical Journal*, 697(2):1071, 2009. doi: 10.1088/0004-637X/697/2/1071. arXiv:0902.1089 [astro-ph.IM].

P. Auger et al. Extensive Cosmic-Ray Showers. *Reviews of modern physics*, 11:288–291, 1939. doi: 10.1103/RevModPhys.11.288.

W. I. Axford, E. Leer, and G. Skadron. The acceleration of cosmic rays by shock waves. *International Cosmic Ray Conference*, 11:132–137, 1977.

W. Baade and F. Zwicky. On Super-novae. *Proceedings of the National Academy of Science*, 20:254–259, 1934. doi: 10.1073/pnas.20.5.254.

A. R. Bell. The acceleration of cosmic rays in shock fronts. I. *Monthly Notices of the Royal Astronomical Society*, 182:147–156, 1978. doi: 10.1086/182658.

C. R. Benn and S. L. Ellison. Brightness of the night sky over La Palma. *New Astronomy Reviews*, 42:503–507, 1998. doi: 10.1016/S1387-6473(98)00062-1.

D. Berge, S. Funk, and J. Hinton. Background Modelling in Very-High-Energy gamma-ray Astronomy. *Astronomy & Astrophysics*, 466:1219–1229, 2007. doi: 10.1051/0004-6361:20066674. arXiv:0610959 [astro-ph].

K. Bernloehr. Simulation of Imaging Atmospheric Cherenkov Telescopes with CORSIKA and sim_telarray. *Astroparticle Physics*, 30:149–158, 2008. doi: 10.1016/j.astropartphys.2008.07.009. arXiv:0808.2253 [astro-ph].

H. J. Bhabha and W. Heitler. The passage of fast electrons and the theory of cosmic showers. *Proceedings of the Royal Society of London A: Mathematical, Physical and Engineering Sciences*, 159(898):432–458, 1937. ISSN 0080-4630. doi: 10.1098/rspa.1937.0082.

R. D. Blandford and J. P. Ostriker. Particle acceleration by astrophysical shocks. *The Astrophysical Journal*, 221:29–32, 1978. doi: 10.1086/182658.

A. M. Brown et al. Discovery of a new extragalactic population of energetic particles. *Physics Review*, D95(6):063018, 2017. doi: 10.1103/PhysRevD.95.063018. arXiv:1603.05469 [astro-ph.HE].

W. C. Davidon. Variable metric method for minimization. 1:1 – 17, 1991. doi: 10.1137/0801001.

A. Daum. First results on the performance of the hegra iact array. 1997. arXiv:9704098 [astro-ph].

E. M. de Gouveia Dal Pino and G. Kowal. Particle Acceleration by Magnetic Reconnection. In A. Lazarian, E. M. de Gouveia Dal Pino, and C. Melioli, editors, *Magnetic Fields in Diffuse Media*, volume 407 of *Astrophysics and Space Science Library*, page 373, 2015. doi: 10.1007/978-3-662-44625-6_13. arXiv:1302.4374 [astro-ph.HE].

M. de Naurois and L. Rolland. A high performance likelihood reconstruction of gamma-rays for Imaging Atmospheric Cherenkov Telescopes. *Astroparticle Physics*, 32:231, 2009. doi: 10.1016/j.astropartphys.2009.09.001. arXiv:0907.2610 [astro-ph.IM].

H. J. de Vega and N. Sanchez. *Extreme Energy Cosmic Rays: Bottom-up vs. Top-down scenarii*, page 433. Kluwer Academic Publishers, 2003. arXiv:0301039 [astro-ph].

B. Degrange. Cherenkov Array at Themis (CAT): A status report. In *International Workshop Towards a Major Atmospheric Cerenkov Detector-III for TeV Astro/Particle Physics Tokyo, Japan, May 25-27, 1994*, pages 305–310, 1994.

H. P. Dembinski et al. Data-driven model of the cosmic-ray flux and mass composition from 10 GeV to 10^{11} GeV. *Proceedings, 35th International Cosmic Ray Conference (ICRC)*, page 533, 2017. arXiv:1711.11432 [astro-ph.HE].

A. Donath et al. Gammapy: An open-source Python package for gamma-ray astronomy. In *34th International Cosmic Ray Conference (ICRC2015)*, volume 34 of *International Cosmic Ray Conference*, page 789, 2015. arXiv:1509.07408 [astro-ph.IM].

L. O. Drury. Origin of Cosmic Rays. *Astroparticle Physics*, 39:52–60, 2012. doi: 10.1016/j.astropartphys.2012.02.006. arXiv:1203.3681 [astro-ph.HE].

R. Fletcher and M. J. D. Powell. A rapidly convergent descent method for minimization. *The Computer Journal*, 6(2):163–168, 1963. doi: 10.1093/comjnl/6.2.163.

I. M. Frank and I. E. Tamm. Coherent visible radiation of fast electrons passing through matter. *Compt. Rend. Acad. Sci. URSS*, 14(3):109–114, 1937. doi: 10.1007/978-3-642-74626-0_2,10.3367/UFNr.0093.196710o.0388. [Usp. Fiz. Nauk93,no.2,388(1967)].

J. F. Glicenstein and M. Shayduk. NectarCAM, a camera for the medium sized telescopes of the Cherenkov Telescope Array. *AIP Conference Proceedings*, 1792(1):080009, 2017. doi: 10.1063/1.4969030. arXiv:1610.04173 [astro-ph.IM].

D. A. Green. A catalogue of 294 Galactic supernova remnants. *Bulletin of the Astronomical Society of India*, 42:47–58, 2014. arXiv:1409.0637 [astro-ph.HE].

K. Greisen. End to the Cosmic-Ray Spectrum? *Physical Review Letters*, 16:748–750, 1966. doi: 10.1103/PhysRevLett.16.748.

T. Hara et al. A 3.8 m imaging cherenkov telescope for the tev gamma-ray astronomy collaboration between japan and australia. *Nuclear Instruments and Methods in Physics Research Section A: Accelerators, Spectrometers, Detectors and Associated Equipment*, 332 (1):300 – 309, 1993. ISSN 0168-9002. doi: 10.1016/0168-9002(93)90774-C.

M. J. Hardcastle and J. H. Croston. Modelling TeV γ-ray emission from the kiloparsec-scale jets of Centaurus A and M87. *Monthly Notices of the Royal Astronomical Society*, 415: 133–142, 2011. doi: 10.1111/j.1365-2966.2011.18678.x. arXiv:1103.1744 [astro-ph.HE].

T. Hassan et al. Monte Carlo performance studies for the site selection of the Cherenkov Telescope Array. *Astroparticle Physics*, 93:76–85, 2017. doi: 10.1016/j.astropartphys.2017.05.001. arXiv:1705.01790 [stro-ph.IM].

T. Hassan et al. Monte carlo performance studies for the site selection of the cherenkov telescope array. *Astroparticle Physics*, 93:76 – 85, 2017. ISSN 0927-6505. doi: https://doi.org/10.1016/j.astropartphys.2017.05.001. arXiv:1705.01790 [astro-ph.IM].

D. Heck et al. *CORSIKA: a Monte Carlo code to simulate extensive air showers.* 1998.

F. Henault et al. Design of light concentrators for Cherenkov telescope observatories. 8834: 883405, 2013. doi: 10.1117/12.2024049. arXiv:1309.4252 [astro-ph.IM].

V. F. Hess. Über Beobachtungen der durchdringenden Strahlung bei sieben Freiballonfahrten. *Physikalische Zeitschrift*, 13:1084–1091, 1912.

A. M. Hillas. Cerenkov light images of EAS produced by primary gamma. *International Cosmic Ray Conference*, 3, 1985.

J. Hinton and W. Hofmann. Teraelectronvolt astronomy. *Annual Review of Astronomy and Astrophysics*, 47(1):523–565, 2009. doi: 10.1146/annurev-astro-082708-101816. arXiv:1006.5210 [astro-ph.HE].

J. A. Hinton. The Status of the H.E.S.S. project. *New Astronomy Reviews*, 48:331–337, 2004. doi: 10.1016/j.newar.2003.12.004. arXiv:0403052 [astro-ph].

A. Hoecker et al. TMVA - Toolkit for Multivariate Data Analysis. *ArXiv Physics e-prints*, pages 103–110, 2007. arXiv:physics/0703039.

W. Hofmann et al. Comparison of techniques to reconstruct vhe gamma-ray showers from multiple stereoscopic Cherenkov images. *Astroparticle Physics*, 122:135–143, 1999. doi: 10.1016/S0927-6505(99)00084-5. arXiv:9904234 [astro-ph].

M. Holler et al. Advanced search for the extension of unresolved TeV sources with H.E.S.S.: First measurement of the extension of the Crab nebula at TeV energies. In *Proceedings, 35th International Cosmic Ray Conference (ICRC)*, 2017. doi: 10.22323/1.301.0676. arXiv:1707.04196 [astro-ph.HE].

F. Israel. Centaurus a – ngc 5128. *The Astronomy and Astrophysics Review*, 8(4):237–278, 1998. ISSN 1432-0754. doi: 10.1007/s001590050011. arXiv:9811051 [astro-ph].

D. Ivanov. TA Spectrum Summary. *Proceedings of Science*, ICRC2015:349, 2016. doi: 10.22323/1.236.0349.

F. James and M. Roos. Minuit - a system for function minimization and analysis of the parameter errors and correlations. *Computer Physics Communications*, 10(6):343 – 367, 1975. ISSN 0010-4655. doi: 10.1016/0010-4655(75)90039-9.

D. Kerszberg et al. The cosmic-ray electron spectrum measured with H.E.S.S. ICRC, 2017.

Knödlseder et al. Towards a common analysis framework for gamma-ray astronomy. *ArXiv e-prints*, 2013. arXiv:1307.5560 [astro-ph.IM].

E. Korosteleva et al. Measurement of cosmic ray primary energy with the atmospheric cherenkov light technique in extensive air showers. *Nuclear Physics B - Proceedings Supplements*, 165:74 – 80, 2007. ISSN 0920-5632. doi: 10.1016/j.nuclphysbps.2006.11.012. Proceedings of the Cosmic Ray International Seminars.

K. Kosack et al. CTA Experimental Pipeline Framework, 2017. URL `https://cta-observatory.github.io/ctapipe/`.

G. F. Krymskii. A regular mechanism for the acceleration of charged particles on the front of a shock wave. *Akademiia Nauk SSSR Doklady*, 234:1306–1308, 1977.

P. O. Lagage and C. J. Cesarsky. The maximum energy of cosmic rays accelerated by supernova shocks. *Astronomy and Astrophysics*, 125:249–257, 1983.

J. H. Lambert. *Photometria, sive De mensura et gradibus luminis, colorum et umbrae*. E. Anding, 1760.

S. Le Bohec et al. A New analysis method for very high definition imaging atmospheric Cherenkov telescopes as applied to the CAT telescope. *Nuclear Instruments and Methods in Physics Research Section A: Accelerators, Spectrometers, Detectors and Associated Equipment*, A416:425–437, 1998. doi: 10.1016/S0168-9002(98)00750-5. arXiv:9804133 [astro-ph].

E. Lebigot. Uncertainties: a python package for calculations with uncertainties, 2010. URL `http://pythonhosted.org/uncertainties/`. Accessed: 2018-01-01.

T.-P. Li and Y.-Q. Ma. Analysis methods for results in gamma-ray astronomy. *The Astrophysical Journal*, 272:317–324, 1983. doi: 10.1086/161295.

M. S. Longair. *High Energy Astrophysics*. Cambridge University Press, 3 edition, 2011.

E. Lorenz and The MAGIC Collaboration. Status of the 17 m MAGIC telescope. *New Astronomy Reviews*, 48:339–344, 2004. doi: 10.1016/j.newar.2003.12.059.

J. E. McEnery et al. The Milagro gamma-ray observatory. *AIP Conference Proceedings*, 558 (1):549–552, 2001. doi: 10.1063/1.1370821.

R. Mirzoyan et al. The first telescope of the HEGRA air Cherenkov imaging telescope array. *Nuclear Instruments and Methods in Physics Research Section A: Accelerators, Spectrometers, Detectors and Associated Equipment*, 351(2):513 – 526, 1994. ISSN 0168-9002. doi: 10.1016/0168-9002(94)91381-1.

P. Montini and S. M. Mari. The bending of the proton plus helium flux in primary cosmic rays measured by the ARGO-YBJ experiment in the energy range from 20 TeV to 5 PeV. 2016. arXiv:1608.01389 [hep-ex].

MoreInput. Radiocena-en.png, 2015. https://commons.wikimedia.org/wiki/File:RadioCenA-EN.png.

Müller Electronik. *LIGHT SOURCE FOR 50–100 W Xe, Hg, Halogen, Deuterium*, 2011. http://www.muller-elektronik-optik.de/es9.pdf.

Newport. *Model 2835-C Multi-Function Optical Meter*, 1994. Rev. D.

Newport. *818 Series Photodetector Guide*, 1999.

A. Okumura, K. Noda, and C. Rulten. ROBAST: Development of a ROOT-Based Ray-Tracing Library for Cosmic-Ray Telescopes and its Applications in the Cherenkov Telescope Array. *Astroparticle Physics*, 76:38–47, 2016. doi: 10.1016/j.astropartphys.2015.12.003. arXiv:1512.04369 [astro-ph.IM].

A. Okumura et al. Prototyping of Hexagonal Light Concentrators for the Large-Sized Telescopes of the Cherenkov Telescope Array. In *Proceeding of the 34th ICRC*, 2015. arXiv:1508.07776 [astro-ph.IM].

R. D. Parsons and J. A. Hinton. A Monte Carlo Template based analysis for Air-Cherenkov Arrays. *Astroparticle Physics*, 56:26–34, 2014. doi: 10.1016/j.astropartphys.2014.03.002. arXiv:1403.2993 [astro-ph.IM].

C. Patrignani et al. Review of Particle Physics. *Chin. Phys.*, C40(10), 2016. doi: 10.1088/1674-1137/40/10/100001.

V. Prosin et al. Tunka-133: Results of 3 year operation. *Nuclear Instruments and Methods in Physics Research Section A: Accelerators, Spectrometers, Detectors and Associated Equipment*, 756:94 – 101, 2014. ISSN 0168-9002. doi: 10.1016/j.nima.2013.09.018.

G. Pühlhofer. The medium size telescopes of the Cherenkov telescope array. In *6th International Symposium on High Energy Gamma-Ray Astronomy*, volume 1792 of *American Institute of Physics Conference Series*, page 080002, 2017. doi: 10.1063/1.4969023. arXiv:1610.02899 [astro-ph.IM].

G. Pühlhofer et al. FlashCam: A fully digital camera for CTA telescopes. *AIP Conference Proceedings*, 1505(1):777–780, 2012. doi: 10.1063/1.4772375. arXiv:1211.3684 [astro-ph.IM].

S. Pürckhauer, G. Hermann, and F. Werner. Evaluation of light concentrators for cameras of the medium-sized telescopes of the cherenkov telescope array. 2017. doi: 10.1016/j.nima.2017.10.064.

K. Rawlins and T. Feusels. Latest Results on Cosmic Ray Spectrum and Composition from Three Years of IceTop and IceCube. *Proceedings of Science*, ICRC2015:334, 2016.

F. M. Rieger and F. A. Aharonian. Variable VHE gamma-ray emission from non-blazar AGNs. *Astronomy & Astrophysics*, 479:L5, 2008. doi: 10.1051/0004-6361:20078706. arXiv:0712.2902 [astro-ph].

F. Schmidt, 2017. https://www.ikp.kit.edu/corsika/.

S. Schoo et al. The energy spectrum of cosmic rays in the range from 10^{14} to 10^{18}eV. *Proceedings of Science*, ICRC2015:263, 2016. doi: 10.1016/S0927-6505(02)00188-3.

K. M. Schure et al. Diffusive Shock Acceleration and Magnetic Field Amplification. *Space Science Reviews*, 173:491–519, 2012. doi: 10.1007/s11214-012-9871-7. arXiv:1203.1637 [astro-ph.HE].

Spectral Products. *Digikröm CM110/CM112 Monochromator/Spectrograph*, 2006. http://www.spectralproducts.com/pdf/cmmanual.pdf.

A. Tamburro. Measurements of Cosmic Rays with IceTop/IceCube: Status and Results. *Modern Physics Letters*, A27:1230038, 2012. doi: 10.1142/S0217732312300388. arXiv:1210.1832 [astro-ph.HE].

The CTA Consortium. Design Concepts for the Cherenkov Telescope Array. *Experimental Astronomy*, 32:193–316, 2011. doi: 10.1007/s10686-011-9247-0. arXiv:1008.3703 [astro-ph.IM].

C. M. Urry and P. Padovani. Unified schemes for radio-loud active galactic nuclei. *Publications of the Astronomical Society of the Pacific*, 107:803, 1995. doi: 10.1086/133630. arXiv:arXiv [astro-ph].

I. Valino. The flux of ultra-high energy cosmic rays after ten years of operation of the Pierre Auger Observatory. *Proceedings of Science*, ICRC2015:271, 2016. doi: 10.22323/1.236.0271.

H. J. Voelk and K. Bernloehr. Imaging Very High Energy Gamma-Ray Telescopes. *Experimental Astronomy*, 25:173–191, 2009a. doi: 10.1007/s10686-009-9151-z. arXiv:0812.4198 [astro-ph].

H. J. Voelk and K. Bernloehr. Imaging Very High Energy Gamma-Ray Telescopes. *Experimental Astronomy*, 25:173–191, 2009b. doi: 10.1007/s10686-009-9151-z. arXiv:0812.4198 [astro-ph].

T. Weekes et al. VERITAS: the Very Energetic Radiation Imaging Telescope Array System. *Astroparticle Physics*, 17(2):221 – 243, 2002. ISSN 0927-6505. doi: 10.1016/S0927-6505(01)00152-9.

T. C. Weekes et al. Observation of TeV gamma rays from the Crab nebula using the atmospheric Cerenkov imaging technique. *The Astrophysical Journal*, 342:379–395, 1989. doi: 10.1086/167599.

F. Werner et al. Performance verification of the FlashCam prototype camera for the Cherenkov Telescope Array. *Nuclear Instruments and Methods in Physics Research A*, 876:31–34, 2017. doi: 10.1016/j.nima.2016.12.056. arXiv:1612.09528 [astro-ph.IM].

R. Winston et al. *Nonimaging Optics*. Elsevier Inc, 2005.

Zaber Technologies. *RSW Series User's Manual*, 2018. https://www.zaber.com/manuals/RSW.

G. T. Zatsepin and V. A. Kuzmin. Upper limit of the spectrum of cosmic rays. *Soviet Journal of Experimental and Theoretical Physics Letters*, 4:78–80, 1966. [Pisma Zh. Eksp. Teor. Fiz.4,114(1966)].

"I've heard it said,
that people come into our lives for a reason,
Bringing something we must learn."

Wicked, *For good*, 2003

Acknowledgement

First and foremost, I want to thank my supervisor Prof. Dr. Jim Hinton for letting me freely pursue my scientific interests within CTA, for his ideas and recommendations on my work and for allowing me to go to the CTA Consortium Meeting in Japan when I had just started in the project. Furthermore, I thank my thesis committee constituted of Prof. Dr. Jim Hinton, Prof. Dr. Werner Hofmann and Prof. Dr. Stefan Wagner for fruitful discussions and valuable feedback on my work over the last 3.5 year. Prof. Dr. Stephan Wagner I additionally thank for being the referee for this thesis. I also acknowledge funding and support by the International Max Planck Research School for Astronomy and Cosmic Physics at the University of Heidelberg (IMPRS-HD) and I especially thank Christian Fendt for creating a PhD programme that not only supports the academic progress of students but also the cultural and encourages scientific exchange between international students of different fields of astrophysics.

My work on light concentrators would never have reached the current state without the supervision of Dr. German Hermann. Thank you, for your constant motivation and your interest in my work, even though our time schedules did not always match. A very cordial thank to Dr. Felix Werner. You always gave the right advice at the right time, helped me to separate the necessary from the unnecessary and never lost your patience with a student who asked the same question over and over again.
I also appreciate the support of Dr. Dan Parsons during my work on ctapipe, because you even dedicated part of your holidays and parental leave to recreate ImPACT templates, fix bugs in the prototype code, proof-read a chapter or two and review final results and because you always made sure that we didn't skip coffee break.
I thank all my colleagues at MPIK for creating a pleasant and productive working environment, especially Vincent Marandon because you always find time to help with scientific questions, Simon Sailer because you bring cheerfulness into the office every day, Armelle Jardin-Blicq as you are always motivated to go for an ice-cream when work gets stuck, Vikas Joshi for some of the most unusual discussions I've every had, Pooja Surajbali for making me organise social events outside of MPIK and Johannes King for your incredible motivation. A very special thank also to Ruth Crespo as you make the work at MPIK run smoothly, not only by clearing our way in the administrative jungle.
Für Unterstützung in allen technischen Fragen möchte ich mich bei den Teams der Elektronikwerkstatt sowie der Mechanikwerstatt bedanken, ohne die vieles am Institut nicht realisierbar wäre. Abgesehen von der fachlichen Hilfe, danke ich insbesondere Christian Föhr für seine wunderschönen Fotos, Thomas Schwab für die Pfälzer Schoko-Schlachtplatte und Frank Garrecht für die Versorgung mit Thorlabs-Süßigkeiten und Jörg Baumgart, weil er nicht die Gedult mit meinem Testaufbau verloren hat.

I thank my fellow IMPRS student for all the Thursday evening dinners, board game and movie nights, especially Neven Tomicic for your amazing lessons on history and politics, Christos Vourellis for listening, Yulong Zhuang because you can still see magic in everyday live, Alex Hygate for introducing a million commas into my thesis (I'm afraid, there are a million more missing), Gigi Leung for your great ideas on how to spent time in Heidelberg and Matthias Samland for sharing my love in Japanese language and supplying me with training material. I also want to thank Benjamin Condon, Emanuele Grimaldo and Felix Niederwanger for your friendship and for a great time at the Astroteilchenschule, Erlangen, and the Gamma16.
Ich danke meinen Freunden aus der Zeit vor meiner Doktorantenzeit: Jennifer Bayer, dafür, dass du regelmäßig angerufen hast, um zu hören, wie es mir gut, und Rabea Baur, weil du sicher stellst, dass ich nicht vergesse, dass es noch ein Leben außerhalb der Physik gibt.

Mein ganz besonderer Dank gilt meiner Familie, die mich nicht nur durch die Zeit der Doktorarbeit begleitet hat: Meiner Mutter Ursula Pürckhauer, für deine Ermutigungen, für dein Verständnis und weil du trotz allem nie aufgegeben hast, meiner Schwester Tanja Schneider, weil du siehst, wo Hilfe benötigt wird und einfach handelst, meinem Schwager Jochen Schneider, dafür, dass du mir deine Fähigkeiten in Computer-Graphiken zur Verfügung gestellt hast, meiner Großmutter Inge Pürckauer, weil du auch mit 93 Jahren noch versuchst, nur das Gute im Leben zu sehen und meiner Tante Evi Pürckhauer für gemütliche Abendessen auf der Terasse. Weiterhin danke ich Gerd Schuhmann und Judit Hoch, weil ihr immer da wart, und Karin Klein, dafür, dass du mich mit Tütensuppen und Guarana-Kakao versorgt hast, damit ich mich in den letzten Wochen ganz auf meine Arbeit konzentrieren konnte.